ISBN: 978-3-95450-267-7 ISSN: 2226-0374 doi: 10.18429/JACoW-COOL2025

Table of Contents

ISBN: 978-3-95450-267-7 ISSN: 2226-0374 doi: 10.18429/JACoW-COOL2025-MOA3

PLASMA-INDUCED COLLECTIVE EFFECTS IN MUON IONIZATION COOLING

K. Yonehara*, Fermilab, Batavia, USA

Abstract

Muon ionization cooling is a critical process that determines the achievable beam brightness and overall performance of a muon collider. In this study, we investigate collective effects induced by high-intensity muon beams inside the absorber, effects that have not been included in previous ionization cooling simulations. We show that beam-induced plasma can neutralize the beam space-charge field, while the self-generated azimuthal magnetic field can introduce additional beam focusing through a z-pinch-like mechanism. We also demonstrate that sufficiently high plasma densities may modify the stopping-power rate. The implications of these plasma-induced phenomena for ionization cooling performance are discussed.

INTRODUCTION

Muon ionization cooling is a key process that establishes the achievable beam brightness, including beam intensity and beam size at the interaction point of a muon collider. Ionization cooling occurs when a muon beam traverses an absorber, losing momentum through ionization while external focusing magnets and RF cavities compress the six-dimensional beam phase space. The RF cavities subsequently restore the lost kinetic energy. The overall process is conceptually analogous to a thermodynamic cycle, in which the focused beam in the absorber behaves similarly to an isothermal compression step.

Simulation studies have demonstrated that ionization cooling can reduce the phase-space volume of muon beams by 10^6 without significant decay loss [1]. At the beam densities required for collider operation, collective effects induced by the beam may become significant. These effects have not been explicitly included in previous cooling simulations. In this paper, we analytically examine possible collective phenomena, such as beam-induced plasma formation and associated self-generated magnetic fields, and evaluate how they may modify the beam dynamics within an absorber.

IONIZATION COOLING FORMALISM

Emittance Evolution

The evolution of the normalized emittance can be derived from the derivative of the normalized phase-space volume,

$$\frac{d\varepsilon_n}{ds} = \beta\gamma\frac{d\varepsilon}{ds} + \varepsilon\frac{d\beta\gamma}{ds}. \tag{1}$$

The first term represents emittance growth from stochastic processes (heating), while the second term corresponds to emittance reduction associated with ionization energy loss (cooling). For the transverse normalized emittance, one obtains

$$\frac{d\varepsilon_n}{ds} = \frac{\beta\gamma}{2}\hat{\beta}_x\sigma_\theta^2 - \frac{\varepsilon_n}{\beta^2 E}\left(\frac{dE}{ds}\right), \tag{2}$$

where $\hat{\beta}_x$ is the transverse betatron function and σ_θ is the rms multiple scattering. Equation (2) shows that small $\hat{\beta}_x$, reduced multiple-scattering σ_θ, and a large stopping-power rate (dE/dx) all contribute to achieving lower beam emittance.

Stopping Power Rate

The stopping cross-section can be written as

$$S = \int T(b)d\sigma, \tag{3}$$

where b is the impact parameter, $T(b)$ is the energy transferred in a collision at b, and $d\sigma$ is the differential cross-section. For Coulomb scattering, the differential cross-section in terms of b is

$$\begin{aligned} d\sigma &= 2\pi b \cdot db \\ &\sim 2\pi\frac{e_1^2 e_2^2}{m_2 v^2}\frac{dT}{T^2}, \end{aligned} \tag{4}$$

where e_1 and e_2 are the charges of the incident and target particles, m_2 is the target mass, and v is the velocity of the incident particle. Integrating over the allowed range of energy transfer gives

$$S = 4\pi\frac{e_1^2 e_2^2}{m_2 v^2}\left[\frac{1}{2}\ln(T^2)\right]_{T_{min}}^{T_{max}}, \tag{5}$$

where T_{max} and T_{min} correspond to the maximum and minimum energy transfer. T_{max} represents a head-on collision with a target electron, while T_{min} reflects the mean excitation energy of atomic electrons of the target particle. The logarithmic term is known as the Coulomb logarithm.

The stopping-power rate is then

$$\left\langle -\frac{dE}{dx}\right\rangle = S \cdot N, \tag{6}$$

where N is the number density of the absorber. Including relativistic and quantum corrections yields the Bethe stopping-power formula. For muon ionization cooling, the typical muon momentum is around 200 MeV/c, and the stopping-power rate becomes

$$\left\langle -\frac{dE}{dx}\right\rangle = K\frac{Z}{A}\frac{z^2}{\beta^2}\left[\frac{1}{2}ln\left(\frac{2m_e c^2\beta^2\gamma^2}{I^2}W_{max}\right) - \beta^2\right], \tag{7}$$

where $K = 0.307075$ MeV mol^{-1} cm^2, Z and A are atomic number and mass of the absorber, z is the charge number of

---

* yonehara@fnal.gov

the incident particle, m_e is the electron mass, and β and γ are the Lorentz factors. The maximum transferable energy in a single collision is

$$W_{max} = \frac{2m_e c^2\beta^2\gamma^2}{1 + 2\gamma(m_e/M) + (m_e/M)^2}, \tag{8}$$

and the mean excitation energy of atomic electrons is

$$I = \exp\left(\frac{\Sigma_i f_i \cdot h\nu_i}{\Sigma_i f_i}\right), \tag{9}$$

where M is the mass of the incident particle, and f_i is the transition probability for the i-th excitation state. The accuracy of the formula is typically a few percent.

Electron Density and Temperature

The electron density and temperature of the beam-induced plasma can be evaluated analytically. The electron-ion pair production energy (W_i) has been observed for various materials. Therefore, the electron density is

$$n_e = \frac{dE/dx}{W_i}. \tag{10}$$

The energy distribution of ionized electrons is provided

$$\begin{aligned}\bar{\epsilon} &= \int E \cdot P(E)dE \\ &= \int K\frac{Z}{A}\frac{\rho}{\beta^2}\frac{1}{E^2}E \cdot dE.\end{aligned} \tag{11}$$

Then the temperature of the ionized electrons is estimated from

$$T_e = \frac{\bar{\epsilon}}{k_B}, \tag{12}$$

where k_B is the Boltzmann constant.

Space Charge Effect

The longitudinal space charge field is obtained by solving

$$\left(\nabla_r^2 - \frac{k^2}{r^2}\right)\phi_k(r) = -\frac{\rho_k(r)}{\varepsilon_0\gamma^2}, \tag{13}$$

where $\rho_k(r) = \lambda(k)\exp(-r^2/2\sigma_r^2)/2\pi\sigma_r^2$ is the beam density, and $\lambda(k) \sim Qz/\sigma_z^2 \exp(-z^2/2\sigma_z^2)$ where Q is the total charge. The boundary condition, $\phi_k(r = r_b) = 0$, is applied, where r_b is the beam pipe radius. The on-axis potential is then

$$\phi_k(0) = \frac{\lambda(k)}{2\pi\varepsilon_0\gamma^2}F(k\sigma_r, kr_b), \tag{14}$$

where F is a form factor. In the long-wavelength limit, e.g. $k\sigma_r \ll 1$, the form factor approaches $F \to 1 + 2\ln(r_b/\sigma_r)$. Therefore, the longitudinal electric field is

$$E_z(z) \sim \frac{eQ}{2\pi\varepsilon_0\gamma^2}\left[1 + 2\ln\left(\frac{r_b}{\sigma_r}\right)\right]\frac{z}{\sigma_z^2}\exp\left(-\frac{z^2}{2\sigma_z^2}\right). \tag{15}$$

The transverse space charge field is also derived from the Poisson equation,

$$\begin{aligned}&\frac{1}{r}\frac{\partial}{\partial r}\left(r\frac{\partial\phi}{\partial r}\right) = -\frac{\rho}{\varepsilon_0} \\ &\to r\frac{\partial\phi}{\partial r} = -\frac{1}{\varepsilon_0}\int_0^{r'} \rho(r')r'dr'.\end{aligned} \tag{16}$$

The corresponding transverse electric field is

$$\begin{aligned}E_r(r) &= -\frac{\partial\phi}{\partial r} \\ &\sim \frac{eQ}{2\pi\varepsilon_0\gamma^2 r}\left[1 - \exp\left(-\frac{r^2}{2\sigma_r^2}\right)\right].\end{aligned} \tag{17}$$

The azimuthal magnetic field is induced by the beam current,

$$\begin{aligned}B_\theta(r) &= \frac{\mu_0 I(r)}{2\pi r} \\ &= \frac{\mu_0}{2\pi r}\int_0^{r'} J_z(r')2\pi r'dr',\end{aligned} \tag{18}$$

where the current density $J_z = \beta c\rho(r)$. Using eqs. (17) and (18), the transverse Lorentz force due to the space charge is

$$f_r = q(E_r - \beta cB_\theta) = qE_r(1 - \beta^2) = \frac{qE_r}{\gamma^2}. \tag{19}$$

Equation (19) indicates that the transverse space charge force is suppressed by $1/\gamma^2$ and becomes small at high beam energies.

CHARGE NEUTRALIZATION AND PLASMA Z-PINCH

The plasma density and temperature generated by a muon beam incident on an absorber are evaluated using eqs. (10) and (12). For example, consider a 200 MeV/c muon beam with bunch intensity 10^{12}, rms bunch length 0.1 ns, and rms beam radius 1 mm is injected into liquid hydrogen. The estimated plasma density is $n_e \sim 3 \cdot 10^{16}$ cm^{-3} and the plasma temperature is $T_e \sim 5 \cdot 10^6$ K. These ionized electrons rapidly thermalize through collisions with neutral hydrogen molecules. The corresponding time constant is typically 1-10 ps [2].

On the other hand, the time constant for electron charge recombination (e.g. $e + H_2^+ \to H_2$) is of order μs because charge recombination via binary collision is a low probability process [3]. As a result, electron-ion mixture persists over the time during which the muon beam traverses the absorber. The space charge fields in eqs. (15) and (17) act on the ionized electrons and shift their spatial distribution so as to neutralize the beam charge, while the azimuthal magnetic field in eq. (18) still exists. This configuration is analogous to a plasma z-pinch, in which the self-generated azimuthal magnetic field compresses the charge-neutralized plasma column [4]. In this case, $J_z(r)$ in eq. (18) is replaced by a Gaussian current distribution, yielding

$$B_\theta(r) = \frac{\mu_0 I}{2\pi r}\left[1 - \exp\left(-\frac{r^2}{2\sigma_r^2}\right)\right]. \tag{20}$$

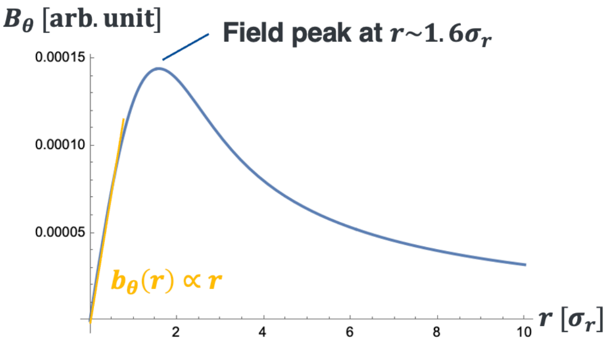

Figure 1: Simulated B_θ as a function of σ_r.

Figure 1 shows the calculated B_θ, which exhibits the expected linear dependence $B_\theta \propto r$ at $r < \sigma_r$.

The focusing strength of the beam-induced magnetic field is evaluated as

$$\begin{aligned} K &= \frac{q}{p}\frac{dB_\theta(r)}{dr} \\ &= \frac{q\mu_0 I}{2\pi p}\left[-\frac{1-\exp(-r^2/2\sigma_r^2)}{r^2}+\frac{\exp(-r^2/2\sigma_r^2)}{\sigma_r^2}\right]. \end{aligned} \tag{21}$$

This suggests that B_θ introduces an additional, self-generated focusing force that is proportional to the beam current density. In this regime, the self-field behaves effectively as an embedded, plasma-induced quadrupole component. For example, consider a muon beam near the final cooling stage with bunch intensity $n_\mu = 10^{12}$ per pulse, pulse length 0.1 ns, and beam spot size $\sigma_r = 0.001$ m. The corresponding current $I = 1.6 \times 10^{-19} \times 10^{12}/10^{-10} = 1.6 \times 10^3$ A. The focusing strength then

$$K \approx \frac{q\mu_0 I}{2\pi p \sigma_r^2} \sim 240\ \mathrm{m}^{-2}. \tag{22}$$

The associated transverse betatron function is $\delta\beta_\perp = \sqrt{K^{-1}} \sim 0.065$ m, which corresponds to approximately 10-20% of the betatron function generated in the cooling lattice.

For $r > 1.6\sigma_r$, the derivative of B_θ becomes negative, implying a weak defocusing force in the beam tail. This suggests that the beam tail is defocused by B_θ. A detailed simulation study is needed to determine whether the net plasma focusing is beneficial or detrimental for ionization cooling.

STOPPING POWER MODIFICATION

The presence of a beam-induced plasma can also modify the stopping-power rate. In this case, the minimum energy transfer is determined by the plasma oscillation frequency rather than atomic excitation. The modified stopping-power rate is

$$\left\langle -\frac{dE}{dx}\right\rangle_{\text{plasma}} = K\frac{z^2}{\beta^2}\left[\ln\left(\frac{T_{Max}}{\hbar\omega_p}\right)-\beta^2\right], \tag{23}$$

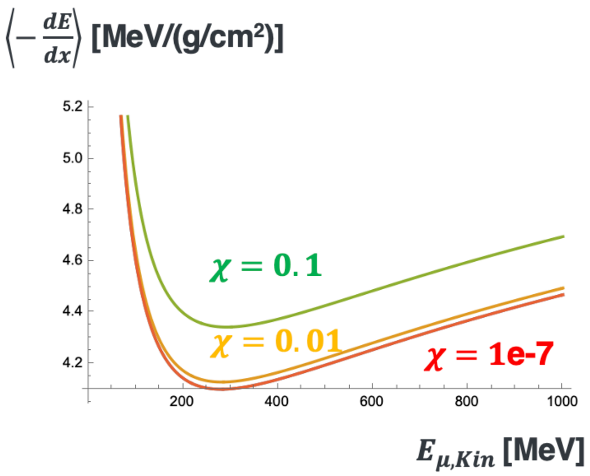

Figure 2: Simulated net stopping power rate with various χ.

where ω_p is the plasma oscillation frequency.

$$\omega_p = \sqrt{\frac{n_e e^2}{\varepsilon_0 m_e}}. \tag{24}$$

The absorber material is partially ionized. We introduce χ to denote the fraction of plasma electrons. The number of bound electrons is then, $n_e^{bound} = (1-\chi)n_e$, and the number of plasma electrons is $n_e^{\text{plasma}} = \chi n_e$. The net stopping-power rate is

$$\left\langle -\frac{dE}{dx}\right\rangle_{\text{net}} = (1-\chi)\cdot\left\langle -\frac{dE}{dx}\right\rangle_{\text{Bethe}} + \chi\cdot\left\langle -\frac{dE}{dx}\right\rangle_{\text{plasma}}. \tag{25}$$

Such plasma-induced modifications to stopping-power have been experimentally observed [5].

Figure 2 shows the estimated stopping-power rate for various plasma fractions χ. It should be noted that the plasma fraction in a nominal cooling channel is $\chi \sim 10^{-7}$. The corresponding change in the stopping-power rate is negligible. If the fraction becomes large, e.g. $\chi \sim 0.01$, the stopping-power rate increases by ~ 1 %. This is favourable for ionization cooling. High plasma densities can be achieved using established ionization techniques. In conventional plasma wakefield accelerators, a high-power laser is used to ionize gaseous hydrogen. Pre-forming the plasma by using an intense proton beam is another option. A more detailed study is planned.

CONCLUSION

Possible collective effects in muon ionization cooling have been evaluated using analytical models. A beam-induced plasma is expected to form in the absorber, leading to partial charge neutralization and the generation of a self-induced azimuthal magnetic field. This field introduces an additional focusing component analogous to a plasma z-pinch, potentially enhancing the effective focusing strength. The plasma chemistry in the absorber has been considered to manipulate

ISBN: 978-3-95450-267-7 ISSN: 2226-0374 doi: 10.18429/JACoW-COOL2025-MOA3

the plasma density and temperature [2, 3]. Further simulation studies have been proposed to quantify these effects in realistic cooling channels [6].

The stopping-power rate can also be modified by the presence of plasma electrons. Although the plasma fraction in a nominal cooling channel is small ($\chi \sim 10^{-7}$), externally pre-ionizing the absorber using either a high-power laser or an intense beam could increase χ to 1-10% level, resulting in a measurable increase in stopping-power rate. These collective effects may provide new opportunities to enhance ionization cooling performance. Numerical simulation studies are planned to further evaluate and validate these models.

ACKNOWLEDGEMENTS

This work was supported by the U.S. Department of Energy, Office of Science, Office of High Energy Physics, through the Fermi National Accelerator Laboratory (Fermilab), which is operated by the Fermi Research Alliance, LLC, under Contract No. DE-AC02-07CH11359.

REFERENCES

[1] D. Stratakis *et al.*, Phys. Rev. Accel. Beams 18, 031003 (2015), `https://journals.aps.org/prab/pdf/10.1103/PhysRevSTAB.18.031003`

[2] M. Chung *et al.*, Phys. Rev. Lett. 111, 184802 (2013), `https://journals.aps.org/prl/pdf/10.1103/PhysRevLett.111.184802`

[3] B. Freemire *et al.*, Phys. Rev. Acc. Beams 19, 062004 (2016), `https://journals.aps.org/prab/pdf/10.1103/PhysRevAccelBeams.19.062004`

[4] Y. Xu *et al.*, AIP Advances 15, 045039 (2025), `https://pubs.aip.org/aip/adv/article/15/4/045039/3345426/Investigation-on-the-dynamics-of-Z-pinch-in`

[5] S. N. Cheng *et al.*, Sci. Rep. 8, 14586 (2018), `https://www.nature.com/articles/s41598-018-32726-2`

[6] K. Yu *et al.*, Phys. Rev. Accel. Beams 20, 032002 (2017), `https://journals.aps.org/prab/pdf/10.1103/PhysRevAccelBeams.20.032002`

The 15th International Workshop on Beam Cooling and Related Topics, New York, USA JACoW Publishing
ISBN: 978-3-95450-267-7 ISSN: 2226-0374 doi: 10.18429/JACoW-COOL2025-MOB3

DEVELOPMENT OF AN ELECTRON COOLER FOR THE HIAF ACCELERATOR*

L. J. Mao†,[1,2], M. R. Li[1], M. X. Li[1,2], H. J. Lu[1], F. Ma[1], X. M. Ma[1], X. P. Sha[1], M. T. Tang[1], K. M. Yan[1], H. Zhao[1], L. X. Zhao[1], Y. B. Zhou[1]
[1] Institute of Modern Physics, CAS, Lanzhou, China
[2] University of Chinese Academy of Sciences, Beijing China

Abstract

The High Intensity heavy-ion Accelerator Facility (HIAF) is a mega scientific infrastructure in China. It consists of a superconducting electron cyclotron resonance ion source (SECR), a superconducting heavy ion linac (iLinac), a fast-ramping rate synchrotron (BRing) and six experimental terminals. One major task is to study atomic physics with internal targets in the spectrometer ring (SRing). An electron cooler was designed and constructed in SRing to boost the internal target experimental luminosities and compensate for energy losses. In this paper, the current status of the cooler was presented.

INTRODUCTION

HIAF is a new accelerator complex hosted by the Institute of Modern Physics (IMP) Chinese Academy of Sciences (CAS) [1]. It is designed to provide intense primary heavy ion beams and produce rare secondary isotopes for nuclear physics, atomic physics and application sciences. The project was proposed in 2011 and approved in 2015. The construction began in 2018 and the first beam commissioning was completed successfully on October 28th, 2025. An aerial view of the HIAF campus is shown in Figure 1.

Figure 1: Aerial view of the HIAF project campus.

SRing is one the of six terminals in the HIAF project. It was designed with different operation modes. The isochronous mass spectrometer (IMS) mode is used to measure short-lived nucleus mass. The internal target mode is used for experiments on the gas target and the electron target. The normal mode is used for ion/isotope accumulation. The electron cooling method is used to improve luminosities for the last two modes.

The HIAF accelerator layout is shown in Figure 2. A typical operation mode can be described as following. Ions provided by SECR and iLinac are accumulated and accelerated in BRing, then be extracted and transferred in HFRS. Secondary beam (highly charged ions or isotopes) can be produced by bombarding a target with the primary beam. The secondary beams (isotopes or highly charged heavy ions) will be injected into SRing and stored for experiments. In the future, a deceleration cavity will be used to prepare low-energy highly-charged ions for atomic physics.

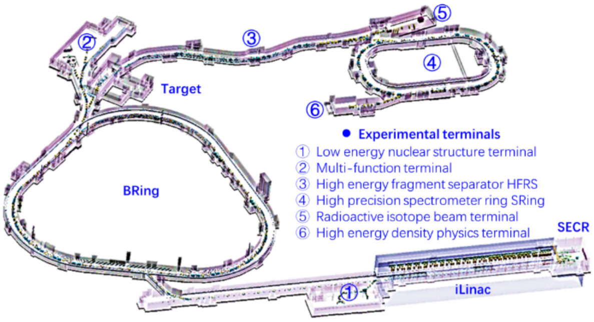

Figure 2: HIAF accelerator layout.

The electron cooler in SRing is a classical magnetized DC cooler [2]. The maximum electron energy and current are 450 keV and 2.0 A, respectively. The cooler was designed based on the existing cooler installed in HIRFL-CSRe at IMP, which was made by collaboration with BINP in 2004. The total cooler assembling was finished in May of 2025. A primary commissioning with few hundreds milliamperes electron beam at 200 keV was achieved successfully. A photo of the cooler assembled in the tunnel is shown in Figure 3.

Figure 3: HIAF electron cooler.

---

* Work supported by National Natural Science Foundation of China (Grants No. 12475162)

† Email address: maolijun@impcas.ac.cn.

BASIC DESIGN FEATURES

The basic parameters of the SRing cooler are listed in Table 1. Calculations of electron cooling effects were performed with an ion beam of 800 MeV/u $^{238}U^{92+}$ for the design work of SRing electron cooler. The initial RMS emittance and momentum spread are 5.0/2.0 π mm·mrad and 5×10^{-4}, respectively. The intra-beam scattering is included as the major heating effect. As shown in Figure 4, the ion beam emittance and momentum spread are effectively decreased within the first 10 seconds, then slowly approach equilibrium because cooling the particles in tail is difficult.

Table 1: Basic Parameters of SRing Cooler

Parameters	Value
Maximum acceleration voltage	450 kV
Voltage ripple	$<5.0\times10^{-5}$
Cathode radius	1.5 cm
Maximum electron current	2.0 A
Gun solenoid field	4.0 kGs
Cooling solenoid field	1.5 kGs
Collector solenoid field	2.0 kGs
Effective cooling length	7.4 m
Vacuum	2.0×10^{-11}
Total power consumption	700 kW

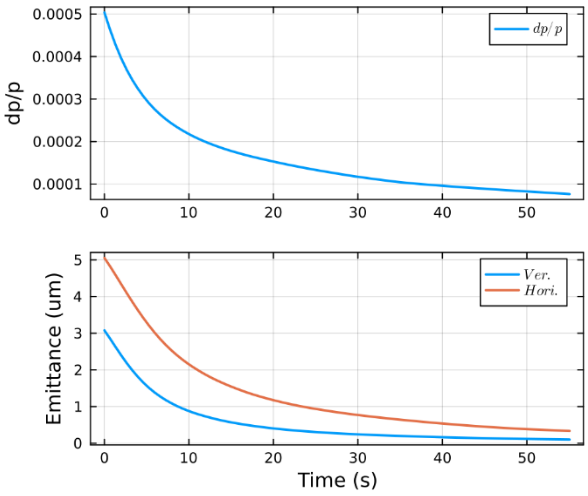

Figure 4: Momentum spread and emittance versus time with electron cooling of 800 MeV/u U^{92+} beam.

A longitudinal magnetic field homogeneity better than 10^{-4} in the cooling section is obtained by pancake structure of the solenoid. The magnetic field axis of coils was measured independently. All coils were installed in the solenoid with a defined sequence according to its field axis data. A compass probe with a laser system is used to measure the field homogeneity. The position and angle of each coil in the solenoid were adjusted in the measurement. Finally, a homogeneity of 4×10^{-5} was obtained for all solenoids in the cooling section. The measurement results of one solenoid are shown in Figure 5.

SRing is a heavy ion storage ring that demands an operating vacuum of 10^{-11} mbar. The vacuum system has similar structure as the straight section in SRing. Ion pumps and titanium sublimation pumps are used to create ultra-high vacuum conditions. NEG coating technology was applied to the vacuum chamber in the cooling section. Figure 6 shows that a vacuum of 1.4×10^{-11} mbar was obtained in the cooling section.

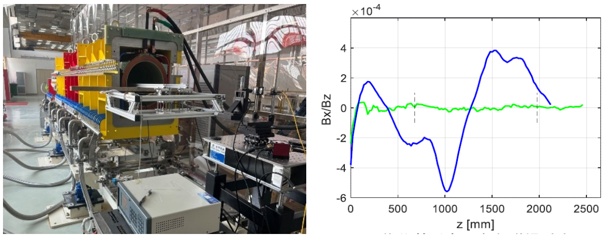

Figure 5: Magnetic field homogeneity measurement and transverse field angle before/after adjustment.

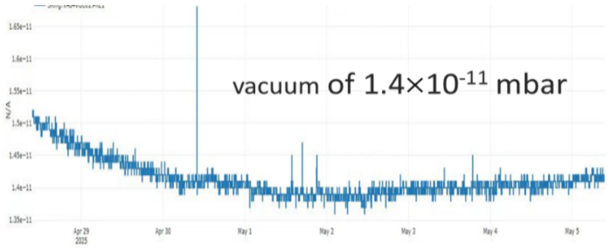

Figure 6: Vacuum of 1.4×10^{-11} mbar in cooling section. A slow increase in pressure could be attributed to the cathode outgassing.

An electron gun with a thermionic cathode is manufactured which is like the guns from BINP. An oxide cathode coated BaSrCa(CO_3) on the surface of Ni base is used [3]. The diameter of cathode is 29 mm. The maximum electron emission current density up to 1.3 A/cm^2 with the temperature of 800°C was achieved at a test bench. After the installation of the gun, degassing of the cathode was carried out during the vacuum baking process. Following the bakeout, cathode activation was performed once the vacuum level reached 2×10^{-11} mbar. The perveance of the electron gun was found to be lower than the design value in the beginning. To thoroughly remove contaminants from the cathode surface, form a uniform cathode emission layer, and achieve a stable and optimal operational state, an extended conditioning process was conducted on the HIAF electron cooling cathode. During conditioning, the cathode was continuously heated, and an electron beam current of 40–70 mA was maintained. As the process progressed, the beam current gradually increased and eventually stabilized. Figure 7 illustrates the daily variation in the electron gun perveance throughout the conditioning process.

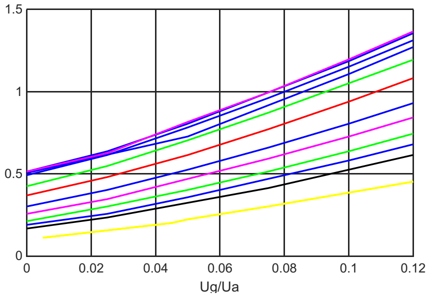

Figure 7: Electron gun perveance increases in commissioning process.

ISBN: 978-3-95450-267-7 ISSN: 2226-0374 doi: 10.18429/JACoW-COOL2025-MOB3

HIGH VOLTAGE SYSTEM

The high voltage system is the key part of the cooling system. A 450 kV high voltage power supply was designed based on a cascade transformer [4]. The gun and collector power supplies with control units are put on the high voltage terminal. The system consists of 15 transformers. An auxiliary coil on each transformer is used to drive the regular -40 kV high voltage section. The main coil on each transformer is used to transmit the electrical energy up to 30 kW from the ground to high voltage terminal. The resonant frequency around 20 kHz was selected depends on the parameters of inductance and capacitors. Figure 8 shows an energy efficiency with different numbers of transformers. The resonant frequency is close to 20 kHz by adjusting the compensative capacitors.

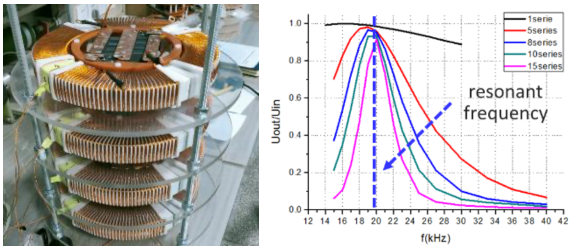

Figure 8: Cascade transformer test bench (left) and the resonant frequency measurement (right).

The stability and ripple are the most important requirement for the high voltage system. Proportional-Integral-Derivative (PID) control is used to compensate the temperature influence. Figure 9(a) shows the stabilities with and without PID control within 72 hours. It is clear to see that an oscillation caused by room temperature can be suppressed efficiently. In addition, a 30 nF capacitor was used in the high voltage section to reduce the ripple. The measured ripple of the high voltage at 400kV is shown in Figure 9(b).

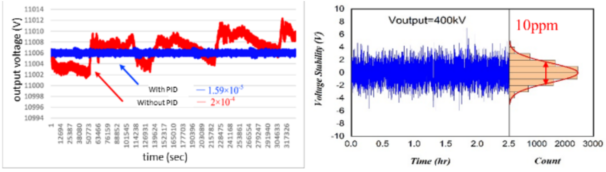

(a) (b)

Figure 9: The output voltage versus time with/without PID control (a) and the ripple measured by oscilloscope (b).

The SF6 gas is used as an electrical insulator in the high voltage tank. A dependence of the total current on the output voltage was measured without load, as shown in Figure 10. Here the total current means the sum of output current of 15 high voltage sections. In the very beginning, the current increases linearly with the voltage, the slope is determined by the internal resistance. Once the voltage exceeds a critical point, the current increases significantly. It depends on the pressure of SF6 in the tank. A stable operation of 400 kV was obtained with the pressure of 2.2 bar, as shown in Figure 10. After installation of the cooler in the tunnel, a commissioning of electron cooler was done with the energy from few keV to more than 200 keV. Figure 11 shows the control panel for the 102 keV, 208 mA electron beam during commissioning.

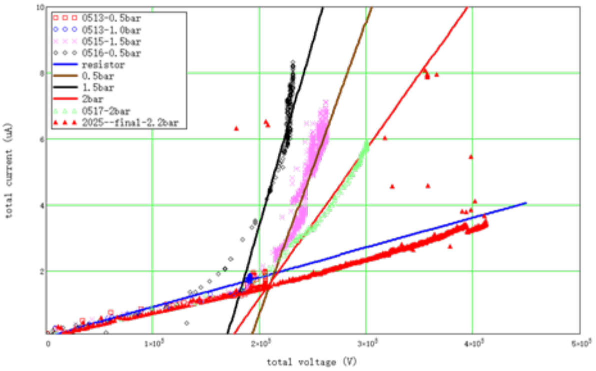

Figure 10: The leakage current versus the output voltage with different gas pressure.

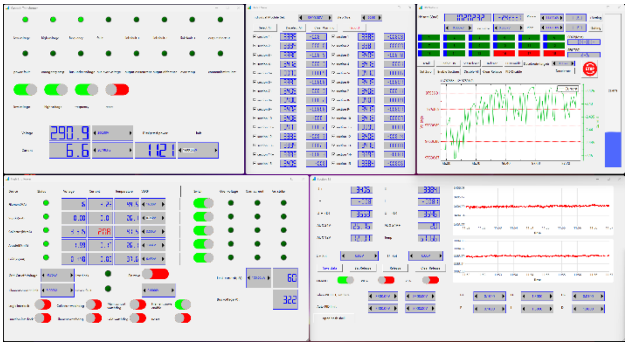

Figure 11: A control panel during the cooler commissioning.

CONCLUSION

The first beam commissioning with $^{18}O^{6+}$ was completed in HIAF successfully. The electron beam for cooling in SRing was also ready for operation. An electron cooling experiment was expected in the beginning of 2026.

ACKNOWLEDGEMENTS

We thank all the colleagues working on the HIAF project for their valuable contributions on this article. The authors would like to thank Dr. Parkhomchuk, Dr. Reva and colleagues from BINP for their supports.

REFERENCES

[1] J. C. Yang *et al.*, *Nucl. Instr. Meth.* B 317, 263, 2013.

[2] L. J. Mao *et al.*, "Development of electron cooler components for HIAF accelerator", in *Proc. 13th Workshop on Beam Cooling and Related Topics (COOL'21)*, Novosibirsk, Russia, Nov. 2021, p. 10-13. doi.org/10.18429/JACoW-COOL2021-S103

[3] Xian heng Liao *et al.*, "Study on the Oxide Cathode for HIRFL-CSR Electron Cooler", in *Proc. 7th Workshop on Beam Cooling and Related Topics (COOL'09)*, Lanzhou, China, Sep. 2009, p. 160-163.

[4] V. V. Parkhomchuk *et al.*, "Cascade transformer for high voltage cooler", in *Proc. 13th Workshop on Beam Cooling and Related Topics (COOL'21)*, Novosibirsk, Russia, Nov. 2021, p. 101-102. doi.org/10.18429/JACoW-COOL2021-P2006

ISBN: 978-3-95450-267-7 ISSN: 2226-0374 doi: 10.18429/JACoW-COOL2025-MOD2

RESEARCH AND DEVELOPMENT OF AN ULTRAHIGH-PRECISION SINGLE-ION IMPLANTER

Y. Yuri[†,1], K. Hosaka[1], N. Miyawaki[1], Y. Ishii[1], S. Hosoya[1], H. Kashiwagi[1],
R. Yamagata[1], S. Onoda[1], K. Muroo[2], K. Ito[2], and H. Okamoto[2]
[1]Takasaki Institute for Advanced Quantum Science, National Institutes for Quantum Science and Technology (QST), Takasaki, Japan
[2]Graduate School of Advanced Science and Engineering, Hiroshima University, Higashi-Hiroshima, Japan

Abstract

Ion implantation is an accelerator-based technology used to create defects and introducing impurities into solid materials. A research and development study is currently underway toward ultrahigh-precision single-ion implantation using laser-cooling techniques at Takasaki Institute, National Institutes for Quantum Science and Technology. To achieve this, we incorporate a linear Paul trap as an ultracold single-ion source, where trapped ions can be made “Coulomb-crystallized” through Doppler laser cooling. In our scheme, nitrogen or silicon ions, useful for ion implantation to create color centers in materials, are sympathetically cooled through Coulomb collisions by co-trapping them with laser-cooled calcium ions to form a two-component crystal. These cold ions are then selectively extracted from the trap to be accelerated and focused through a 50-kV electrostatic bipotential-lens system. Our goal is to achieve beam focusing for ultrahigh-precision implantation on the order of 10 nm. The implanter system has already been assembled, and the commissioning is currently ongoing to enable single-ion extraction using a Coulomb crystal. In these proceedings, we describe the scheme for selective ion extraction and nanobeam focusing based on multiparticle simulations and briefly report recent progress in system implementation.

INTRODUCTION

Improving the focusing and targeting precision of charged-particle beams is an important aspect of accelerator technology. One example is so-called “microbeam (nanobeam) irradiation”, where the transverse spot size of the beam on a target is focused to the micrometer (nanometer) scale. This technique is often employed for pinpoint irradiation in MV-class electrostatic accelerators [1]. In this beam-irradiation method, the beam generated from such a high-energy accelerator is strongly collimated to reduce its effective emittance before final focusing on the target. (Note that this process is not beam cooling as the phase-space density of the beam is not increased.) With fine tuning of the collimator apertures and stronger final focusing, the spot size can, in principle, be further reduced. However, it would be practically more difficult to control single-ion irradiation reliably because of the stochastic nature of ion transmission through collimators in conventional beam-formation methods.

A different approach to obtaining low-emittance beams is beam cooling. Among several cooling methods applicable to fast heavy-ion beams, Doppler laser cooling is the most promising since the lowest attainable temperature is in the mK range [2, 3]. In such an ultralow-temperature state, it is expected that a crystalline-ordered beam, whose emittance is extremely low, can be formed [4, 5]. Although the longitudinal beam temperature of around 1 mK was attained in early laser-cooling experiments [6], transverse cooling to the mK range has not yet been realized (except in very low-beam-energy cases using a circular Paul trap [7]). This is mainly because it is practically quite difficult to maintain high lattice periodicity for avoiding resonance crossing, to accomplish three-dimensional laser cooling, and to compensate for dispersive effects in large-scale storage rings [8].

As a possible method to generate a three-dimensionally ultralow-emittance beam and control single-ion motion reliably, we consider the use of a linear Paul trap (LPT) for several following prominent reasons. It is relatively straightforward to form an ion Coulomb crystal, an ordered state in au ultralow-temperature limit, by applying Doppler cooling to trapped ions [9]. Attainable normalized emittance is on the order of 10^{-15} m·rad or less [10-12]. It is possible to observe the existence of a small number of ions in a crystal and to manipulate them individually under wide-range operating conditions for extraction from the LPT [11-14]. Furthermore, two-component crystals can be formed via sympathetic cooling of various ions co-trapped with laser-coolable ions.

Recently, we have proposed an ultrahigh-precision single-ion implanter for the application of quantum technology [15, 16]. In the following, we present the scheme of single-ion irradiation and nanobeam formation using a Coulomb crystal and report on the progress of ion-trap experiment performed at QST Takasaki Institute.

SINGLE-ION IMPLANTER

We have fabricated a compact ion-implanter system with an LPT at QST Takasaki Institute. As shown in Fig. 1, it mainly consists of an external ion source where various implantation ions (such as N and Si) can be generated, an LPT where a two-component Coulomb crystal is formed by laser cooling of Ca^+ ions (Doppler limit: 0.5 mK) and single-

---

[†] yuri.yosuke@qst.go.jp

ISBN: 978-3-95450-267-7 ISSN: 2226-0374 doi: 10.18429/JACoW-COOL2025-MOD2

ion extraction is controlled, and electrostatic bipotential lenses (BPLs) for nanobeam formation.

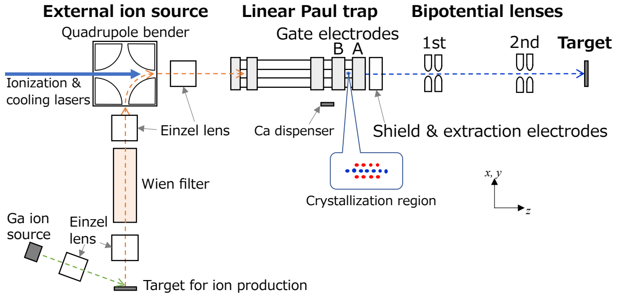

Figure 1: Schematic view of the implanter system. A Coulomb crystal is prepared in the "crystallization region" (6 mm in length) between two Gate electrodes A and B for controlled extraction. The external ion source and the trap are placed on a 50-kV high-voltage platform. Ions extracted from the trap are accelerated and focused on the grounded target through two electrostatic BPLs.

A low-energy (~1 keV for singly-charged ions) ion beam generated by sputtering using a primary Ga liquid-metal ion source is transported to the LPT through a Wien filter, a quadrupole bender, and several Einzel lenses. The beam is properly decelerated due to the electric potential difference when entering the LPT, and then captured by controlling the Gate voltages for the axial confinement. The trapped ions are sympathetically cooled with laser-cooled Ca^+ ions to form a two-component crystal. Once a crystal with a desired spatial configuration is formed, the extraction process is initiated by manipulating the voltages of Gate electrodes A and/or B. In this manipulation, single ions can be selectively extracted from the LPT to the target. The extracted ions are accelerated via the two BPLs to form a nanobeam on the target. For this acceleration, the ion source and LPT are insulated on a 50-kV high-voltage platform. For details of the system, see Ref. [15].

ION-SELECTIVE EXTRACTION

Detailed multiparticle simulations were performed to reveal the feasibility of selective extraction of sympathetically-cooled ions and nanobeam formation of extracted ions. To control singe-ion irradiation (implantation), we have investigated two possible ejection schemes [12, 15]. One is the fast ejection, and the other is the slow adiabatic ejection. Here, we briefly mention the former scheme using a string crystal.

We form a two-component string crystal as shown in Fig. 2 where an implantation ion (here, N^{2+}) is settled at the exit side (at the rightmost side) within the crystal. Otherwise, the lighter nitrogen ion, which can move faster than Ca^+ ions, is easily heated up due to random collisions when passing by them in the extraction process. Experimentally, the location of the nitrogen ion within the crystal must be changed by modulating the trapping axial potential and frequency detuning of cooling lasers.

Once the desired crystal configuration is formed, the ejection process is initiated; here, the voltage V_A of the Gate electrode A is quickly switched off and on so that only the leading N^{2+} ion can exit from the Gate A, while subsequent slow Ca^+ ions are reflected to the LPT by the potential barrier generated again. This was confirmed by multiparticle simulations, as shown in Fig. 3. Switching V_A at a proper timing is necessary for ion-selective ejection. From the results of many independent simulation runs of this single-ion ejection, it has been found that a beam of ejected ions has a normalized root-mean-square (rms) emittance of 3×10^{-14} m·rad, which is one order of magnitude higher than the best cases of Si^+ (instead of N^{2+}) and a shell crystal [15]. A possible reason of this emittance degradation is the fact that the efficiency of sympathetic cooling of N^{2+} is lower due to differences in the mass-to-charge ratio from Ca^+, the number of ions and the crystalline structure.

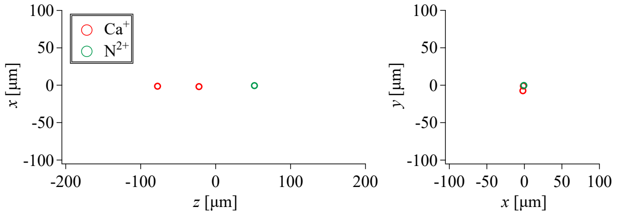

Figure 2: Spatial distribution of a three-ion two-component string Coulomb crystal. The z-coordinate represents the direction of the trap axis while x and y are the transverse directions perpendicular to z. The trapping conditions are as follows: RF voltage applied to quadrupole rods $V_{\mathrm{rf}} = 10$ V, DC voltage applied to two Gate electrodes $V_A = V_B = 0.2$ V, and the driving frequency $f_{\mathrm{rf}} = 2$ MHz. For sympathetic cooling of an N^{2+} ion, two Ca^+ ions are Doppler-cooled by a single axial laser with a peak saturation intensity of 0.1 and detuning of −72 MHz.

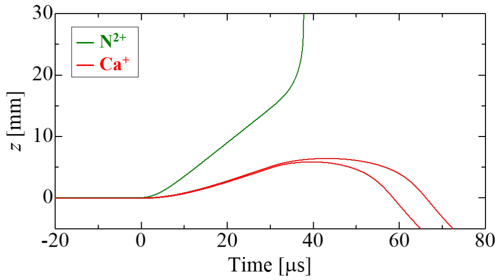

Figure 3: Temporal evolution of the axial position z of the three ions in Fig. 2 during the fast ejection process. The origin of the abscissa is the time when the Gate electrode A is promptly switched off. Only the leading N^{2+} ion is ejected from the LPT toward the target while the two following Ca^+ ions are reflected backward after the Gate A voltage V_A is raised up to 0.5 V at 30 μs.

NANOBEAM FORMATION

Cold single ions extracted from the LPT are transported to the target through the two BPLs to form a nanobeam. We have optimized an operating condition of the BPL voltages as follows: Extraction electrode voltage $V_{\mathrm{ext}} = -2.5$ kV, gap voltages of the two BPLs $G_1 = 12.5$ kV, and $G_2 = 35$ kV, which enables 50-kV acceleration with a sufficiently long working distance of about 80 mm. Note that the final energy is 100 keV on the target for doubly-charged ions.

Figure 4 shows the on-target spatial and phase-space distribution of N^{2+} ions accelerated after the fast ejection in Fig. 3. An rms spot size of 18 nm is achieved although the phase-space shape is slightly deformed due to the lens aberration. Note that a smaller on-target spot size (below 10 nm) is attainable in the above-mentioned cases of Si^+ and a shell crystal [15].

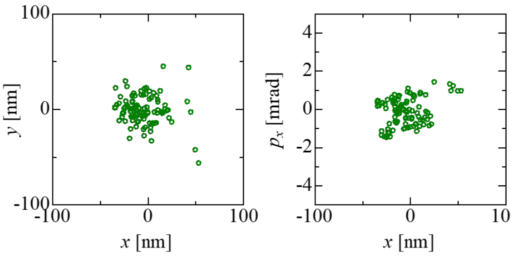

Figure 4: Ion distributions at a focal point. The kinetic energy of the N^{2+} ions is 100 keV. Results of 100 independent simulations on the single-ion extraction are plotted.

ION-TRAP EXPERIMENTS

Our single-ion implanter (Fig. 1) is now in a commissioning stage. We have so far confirmed what follows [16]: Doppler cooling of Ca^+ ions and formation of various Coulomb crystals, sympathetic cooling, extraction of laser-cooled ions from the LPT and its detection, generation of Si ion beams using the Ga ion source and its transport to the target through the LPT, and bipotential acceleration of an ion-source beam. Recent results on ion-trap experiments are briefly reported here.

The LPT is axially segmented into three regions for efficient capture of ions delivered from the external ion source, the ionization of Ca atoms, and the formation of a Coulomb crystal. The minimum distance from the trap axis to quadrupole rods is 3.0 mm. The axial length of the crystallization region is 6.0 mm.

Laser lights of four different wavelengths (390 nm and 423 nm for ionization of neutral Ca atoms, and 397 nm and 866 nm for Doppler cooling of Ca^+ ions) are all introduced along the trap axis from the upstream side of the system (see Fig. 1). Typically, the total power of the 397-nm Doppler-cooling laser is 1~2 mW, and its spot size is 0.9 mm at the crystallization region without tight focusing, which are sufficient for cooling a cloud of initially hot ions and observing laser-induced fluorescence (LIF).

Various structures of Coulomb crystals were formed by Doppler cooling of Ca^+ ions, depending on the number of ions and focusing strength, as shown in Fig. 5. The experimental observations have been well confirmed by the multiparticle simulations.

The extraction of laser-cooled ions from the LPT was investigated recently. We have succeeded in the fast extraction of an entire string crystal and slow single-ion extraction by the manipulation of the Gate voltages finely [17].

SUMMARY

A nanobeam-formation scheme using a Coulomb crystal has been investigated toward the realization of an ultra-high-precision single-ion implanter at QST Takasaki Institute. The detailed simulation results show that it is possible to extract sympathetically-cooled ions selectively from the LPT and form a nanobeam by the BPLs at 100 keV.

According to the multiparticle simulation results, a compact single-ion implanter with the LPT and the laser cooler has been fabricated. Now, we are mainly conducting the ejection experiments of cold ions using a Coulomb crystal toward the nanobeam formation and single-ion irradiation.

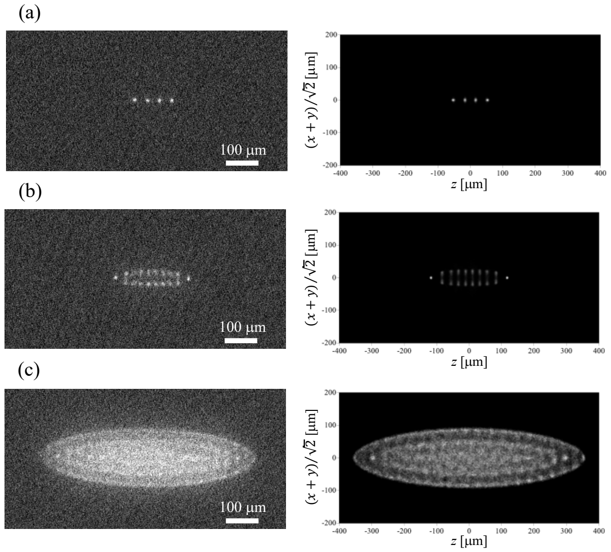

Figure 5: LIF images of $^{40}Ca^+$ Coulomb crystals observed in the LPT (left panels) and corresponding multiparticle simulation results (right panels). (a) A four-ion string, (b) an 18-ion single shell, and (c) a three-layered shell (~300 ions). The trapping conditions are as follows in all cases: $V_{\mathrm{rf}} = 20$ V, $V_A = V_B = 1.0$ V, and $f_{\mathrm{rf}} = 1.91$ MHz.

ACKNOWLEDGEMENTS

This work was supported in part by JST Moonshot R&D Grant Number JPMJMS2062 and JSPS KAKENHI Grant Number JP25K15770.

REFERENCES

[1] R. Hellborg, H. J. Whitlow, and Y. Zhang, eds., Ion Beams in Nanoscience and Technology (Springer Nature, Berlin, Heidelberg, 2010). doi:10.1007/978-3-642-00623-4

[2] T. W. Hänsch and A. L. Schawlow, "Cooling of gases by laser radiation", Opt. Commun. 13, 68 (1975). doi:10.1016/0030-4018(75)90159-5

[3] D. J. Wineland and H. Dehmelt, "Proposed $10^{14}\delta\nu < \nu$ laser fluorescence spectroscopy on Tl^+ mono-ion oscillator", Bull. Am. Phys. Soc. 20, 637 (1975).

[4] A. Rahman and J. P. Schiffer, "Structure of a one-component plasma in an external field: A molecular-dynamics study of particle arrangement in a heavy-ion storage ring", Phys. Rev.

ISBN: 978-3-95450-267-7 ISSN: 2226-0374 doi: 10.18429/JACoW-COOL2025-MOD2

Lett. 57, 1133 (1986). doi:10.1103/PhysRevLett.57.1133

[5] R. W. Hasse and J. P. Schiffer, “The structure of cylindrically confined Coulomb lattice”, Ann. Phys. (N.Y.) 203, 419 (1990). doi:10.1016/0003-4916(90)90177-P

[6] J. S. Hangst *et al.*, “Laser cooling of a stored ion beam to 1 mK”, Phys. Rev. Lett. 67, 1238 (1991). doi:10.1103/PhysRevLett.67.1238

[7] T. Schätz, U. Schramm and D. Habs, “Crystalline ion beams”, Nature 412, 717 (2001). doi:10.1038/35089045

[8] Y. Yuri and H. Okamoto, “Feasibility of beam crystallization in a cooler storage ring”, Phys. Rev. ST Accel. Beams 8, 114201, (2005). doi:10.1103/PhysRevSTAB.8.114201

[9] D. H. E. Dubin and T. M. O’Neil, “Trapped nonneutral plasmas, liquids, and crystals (the thermal equilibrium states)”, Rev. Mod. Phys., 71, 87 (1999). doi:10.1103/RevModPhys.71.87

[10] M. Kano *et al.*, “Ultra-low Emittance Beam Generator Using Coulomb Crystals”, J. Phys. Soc. Jpn., 73, 760 (2004). doi:10.1143/jpsj.73.760

[11] K. Izawa *et al.*, “Controlled Extraction of Ultracold Ions from a Linear Paul Trap for Nanobeam Production”, J. Phys. Soc. Jpn., 79, 124502 (2010). doi:10.1143/JPSJ.79.124502

[12] K. Muroo *et al.*, “Simulation study of ultrahigh-precision single-ion extraction from a linear Paul trap”, Prog. Theor. Exp. Phys., 2023, 063G01 (2023). doi:10.1093/ptep/ptad071

[13] G. Jacob *et al.*, “Transmission Microscopy with Nanometer Resolution Using a Deterministic Single Ion Source”, Phys. Rev. Lett., 117, 043001 (2016). doi:10.1103/PhysRevLett.117.043001

[14] K. Groot-Berning *et al.*, “Fabrication of ^{15}NV^{-} centers in diamond using a deterministic single ion implanter”, New J. Phys., 23, 063067 (2021). doi:10.1088/1367-2630/ac0753

[15] Y. Yuri *et al.*, “Investigating Ultralow-Emittance Nanobeam Formation Using a Coulomb Crystal”, Prog. Theor. Exp. Phys., 2025, 023G01 (2025). doi:10.1093/ptep/ptaf019

[16] Y. Yuri *et al.*, “Research and development study on nanobeam formation using laser-cooled ions for high-precision single-ion irradiation”, in *Proc. IPAC’25,* Taipei, Taiwan, June 2025, pp. 997-1000. doi:10.18429/jacow-ipac2025-tupb026

[17] K. Muroo *et al.*, submitted for publication.

ISBN: 978-3-95450-267-7 ISSN: 2226-0374 doi: 10.18429/JACoW-COOL2025-TUA1

HADRON BEAM COOLING CONCEPT AND COOLER DESIGN STATUS FOR THE EIC *

A.V. Fedotov[†], D. Kayran, S. Seletskiy
Brookhaven National Laboratory, Upton, NY, USA

Abstract

Cooling of hadrons in Electron Ion Collider (EIC) is critical to achieve EIC design parameters and performance. In this paper we summarize current strategy of hadron beam cooling application for the EIC starting with providing strong cooling of proton beam emittances at injection energy and potential subsequent cooling at the top collision energies. We will then discuss requirements, challenges and design status of RF-based electron cooler for 23.8 GeV proton energy.

INTRODUCTION

The Electron-Ion Collider (EIC) project is presently under design at Brookhaven National Laboratory (BNL); a layout of the EIC is shown in Fig. 1. Collisions occur between the hadrons in the Hadron Storage Ring (HSR) and the electrons in the Electron Storage Ring (ESR) [1].

In order to achieve the design emittances of the hadron beam, hadron beams will be injected into the HSR and cooled to the target emittances at injection energy of protons of 23.8 GeV. After the target emittances are achieved, the HSR will be ramped to the collision energy.

Cooling of protons at 23.8 GeV will be done using conventional electron cooling technique which requires 12.5 MeV electron accelerator. The design of such Low-Energy Cooler (LEC) is based on the RF-accelerated electron bunches, similar to the LEReC [2] approach, but scaled to higher energy.

Cooling of heavy ions at collision energies is planned using stochastic cooling technique [3].

Presently, no cooling of protons at collision energies is implemented. However, such high-energy cooling of protons can be considered as future EIC upgrade.

HIGH-ENERGY COOLING

A robust cooling of protons at collision energies in the EIC could significantly increase luminosity in the EIC. However, designing of such High-Energy Cooling (HEC) system for protons is one the most challenging problems in modern accelerator physics.

Recently, significant efforts were devoted to design of such HEC system using stochastic cooling approach but employing electron beam itself as a pick-up, amplifier and kicker, which can extend this technique to much higher bandwidth than possible with conventional microwave technology. A conceptual design study of such an approach based on the micro-bunched Coherent Electron Cooling amplifier was performed [4].

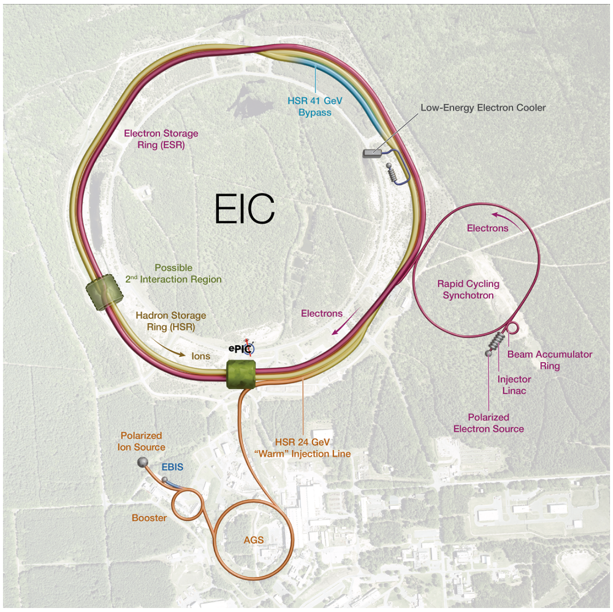

Figure 1: The layout of the Electron-Ion Collider (EIC).

One of the alternative approaches is to use a well-established technique of electron cooling. With such a technique, the cooling rate drops quadratically with energy which makes its extension to high energies challenging. However, the drop of cooling rate with energy can be compensated by an increase in the phase-space density of electron bunches, length of the cooling section and by precooling of hadron beam at lower energies, as cooling rate strongly depends on the divergence of the hadron beam.

Since electron cooling technique has several decades of experience one can provide estimates of the cooling rates and requirements of needed electron beam parameters with very high degree of certainty. What remains is to design required electron accelerator.

Several approaches using conventional electron cooling for the HEC system were considered in the past [5-8]. Most recent R&D studies at BNL were devoted to two approaches: 1) Storage Ring-based Electron Cooler [9] and 2) ERL-based Electron Cooler [10].

While R&D on the HEC continues, immediate focus for the EIC is on the design of the Low-Energy Cooler (LEC).

THE LEC REQUIREMENTS

The LEC design is based on the non-magnetized cooling approach with zero magnetic field on the cathode and no magnetic field in the cooling region [11]. The layout of the LEC accelerator is shown in Fig. 2.

---

*Work supported by the US Department of Energy under contract No. DE-AC02-98CH10886.

[†] fedotov@bnl.gov

ISBN: 978-3-95450-267-7 ISSN: 2226-0374 doi: 10.18429/JACoW-COOL2025-TUA1

To maximize the cooling power and to preserve transverse distribution of hadrons under cooling, the electron beam rms velocity spreads are chosen close to those of the hadron beam. At injection energy in the EIC with γ=25.4, the proton beam with bunch intensities N=2.8×10^{11} will have rms longitudinal momentum spread of about $\sigma_p=7\times10^{-4}$. The requirement for the rms momentum spread of electron beam are < 4×10^{-4}. For the rms normalized emittance of the proton beam around 2 μm and 150 m minimum beta function in the cooling section, the hadron beam rms angular spread in the lab frame is 0.023 mrad. This gives the requirement for the total electrons angular spread in the cooling section to be around 0.025 mrad.

The total angular spread of electrons in the cooling section has several contributions, with the dominant contributions coming from electron beam emittance and electron beam space charge. As a result, special efforts are being made to develop proper electron beam transport to and through the cooling section to ensure that requirements on angular spread are satisfied [12].

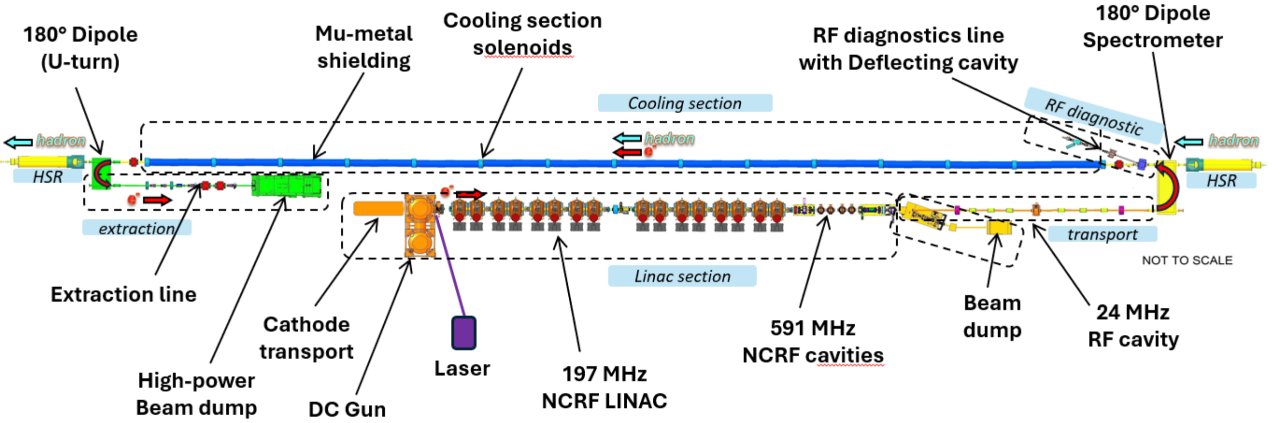

Figure 2: The layout of the LEC accelerator (not to scale).

Table 1: Electron Beam Parameters in the Cooling Section

Relativistic gamma	25.38
Charge per single electron bunch, nC	1.0
Number of bunches in macrobunch	3
Total charge in macrobunch, nC	3
Average current, mA	74
RMS normalized emittance, μm	< 1.5
Angular spread, μrad	< 25
RMS energy spread	<4×10^{-4}
RMS bunch length, cm	4
Beta function, m	150
Length of cooling sections, m	160

With the friction force maximum being located close to the longitudinal rms velocity spread of the electrons, one gets a requirement for matching electron and beam energies to better than the rms velocity spread, which for our parameters is about 3×10^{-4}. Energy stability of the electron beam should be better than this, at about 1×10^{-4} rms. See all parameters in Table 1.

The largest contributions to the angles in the cooling section come from the electron beam emittance and the space charge of electron and proton beams. In addition, to keep the transverse angle of the electron beam trajectory <10 μrad an integral of residual transverse magnetic field in cooling region should be kept below 1 Gauss·cm. A shielding of residual magnetic field to such level will be provided by several concentric cylindrical layers of high permeability alloy [13]. Some cooling section space will be taken up by short solenoids (to control angular spread due to the transverse space charge of electron beam), steering dipoles and beam position monitors to keep the electron and ion beam in close relative alignment.

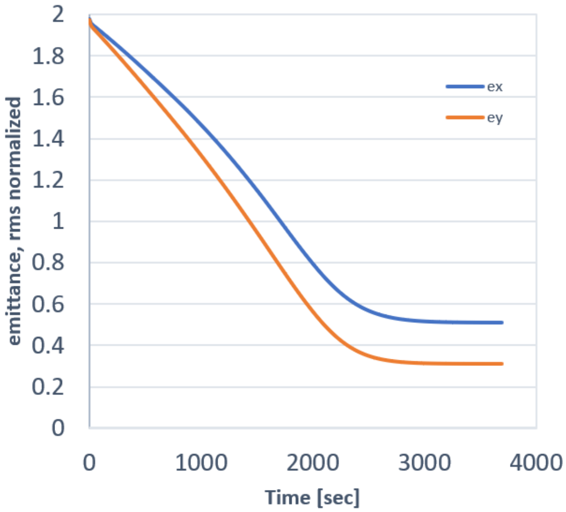

Figure 3: Cooling of protons at γ=25.38, with decoupled transverse motion. Horizontal emittance (top curve, blue) and vertical emittance (bottom curve, orange).

In simulations shown in Fig. 3, we assumed the total angular spread of the electrons in the cooling section to be

25 μrad. Both horizontal and vertical emittances are being cooled to slightly different values due to different IBS rates in the two planes. For optimum cooling performance, cooling should be provided in both transverse planes simultaneously, because the vertical cooling rate is affected by the horizontal angles as well. However, if stability of such cooled proton bunches becomes a problem one can provide heating of the horizontal emittance while cooling vertically, as the goal of the LEC is to achieve small emittance in the vertical plane only, as shown in Fig. 4, for example.

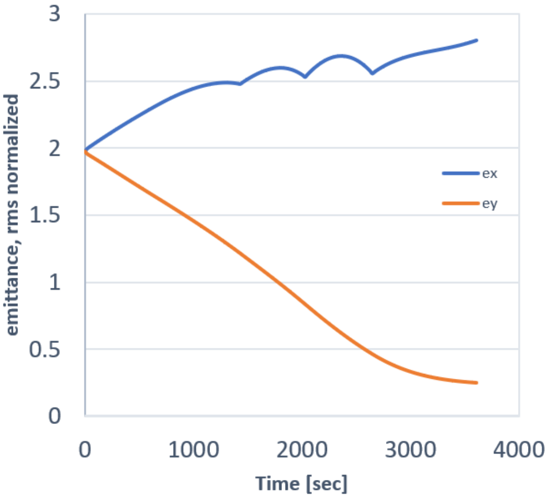

Figure 4: Cooling of protons vertical emittance (bottom curve, orange) while heating of the horizontal emittance (top curve, blue).

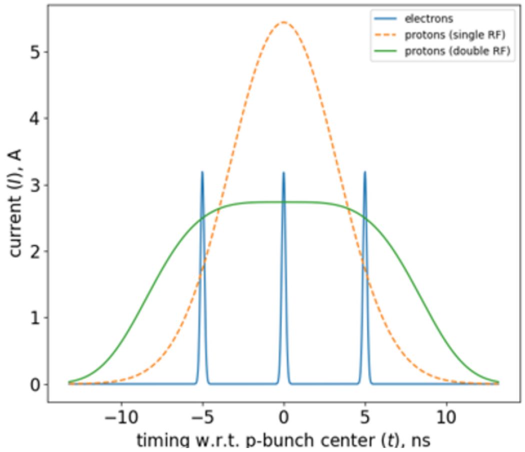

Figure 5: Three electron bunches (blue) spaced by 5.1 ns placed on a single proton bunch (orange dashed line: single RF harmonic; green solid line: double RF harmonic).

To mitigate space-charge effects during cooling the second harmonic RF will be used to produce flattened distribution of proton bunches (green curve in Fig. 5) with peak current reduced by about factor of two compared to a single harmonic RF (orange curve in Fig. 5). With the second harmonic RF and emittances at the end of cooling shown in Fig. 3, space-charge tune shifts for proton beam are estimated to be 0.06 and 0.11, for the horizontal and vertical planes, respectively.

The 197 MHz repetition rate of electron bunches, corresponding to 5.1 ns spacing, allows us to place three electron bunches with 1.0 nC charge each (as shown in Fig. 5) on a single proton bunch to provide total required charge of electrons of 3 nC per proton bunch.

ELECTRON ACCELERATOR

Electron beam will be generated by illuminating a multi-alkali CsK_2Sb photocathode with green light (532 nm) from a laser. The photocathode is inserted into a DC gun with design operational voltage of 350-375 kV. The 197 MHz laser will produce bunch trains with individual electron bunches of about 400 ps full length at 24.6 MHz bunch train repetition frequency. The bunch train repetition rate will be the same as the repetition rate of proton bunches in the HSR at injection energy.

After the gun, an electron beam is accelerated in the 197 MHz linac to the final kinetic energy of 12.46 MeV. The 3^{rd} harmonic RF cavities are used for energy correction. An additional 24.6 MHz RF cavity is used to correct energy spread due to the beam-loading for the macro-bunch of electrons which consists of three electron bunches separated by 5.1 ns. Main parameters of electron accelerator are given in Table 2.

After acceleration to 12.46 MeV kinetic energy, an electron beam is transported to the cooling section in the HSR ring, merged with proton beam, cools protons by propagating together over 160 m of cooling section, turned around and transported to the high-power beam dump.

Simulations of electron beam dynamics show that required electron beam parameters can be achieved with sufficient safety margin [12].

Table 2: Parameters of Electron Accelerator

DC gun voltage, kV	350-375
Final electron kinetic energy, MeV	12.46
Laser repetition frequency, MHz	197
Bunch train repetition frequency, MHz	24.6
Main RF frequency, MHz	197
Number of 197MHz NCRF cavities	17
Voltage per 197MHz RF cavity, kV	850
Energy correction RF frequency, MHz	591
Voltage per 591MHz cavity, kV	380
Number of 591MHz cavities	4
Number of 591MHz deflecting cavities	1
Voltage of deflecting cavity, kV	150
Number of 24.6MHz cavities	1
Voltage of 24.6MHz cavity, kV	10
Average electron current, mA	74
Final beam dump power, kW	922

ISBN: 978-3-95450-267-7 ISSN: 2226-0374 doi: 10.18429/JACoW-COOL2025-TUA1

CHALLENGES

Stable long-term operation of the gun with 74 mA average current is challenging. An ongoing R&D is presently underway to establish such operation.

Extracting 12.46 MeV electron beam with 74 mA current requires 922kW beam dump. Spreading of electron beam inside such beam dump requires special consideration.

The attainment of required low energy spread in the electron bunch relies on RF gymnastics. A tight requirement on impedance budget requires detailed wake fields simulations and special design of every vacuum element including instrumentation devices. Quality of electron beam should be preserved through the entire beam transport and long cooling section.

The achievement of very low transverse angular spread for the electron beam should be addressed by a proper beam transport and design of the cooling sections. The required electron angles in cooling section are about factor of five smaller than achieved in LEReC, which sets strict requirements on the design of the cooling section.

SUMMARY

A robust cooling of protons at collision energies in the EIC could significantly increase luminosity in the EIC. Designing of such high-energy cooling system for protons is very challenging.

While R&D on the high-energy cooling continues, immediate focus for the EIC project is on the design of 12.5 MeV Low-Energy Cooler (LEC), based on the RF acceleration of electron bunches. The LEC is being designed to provide strong cooling of protons at the EIC injection energy of 23.8 GeV. Various challenges are being addressed by a proper physics and engineering design.

ACKNOWLEDGMENTS

We would like to thank members of the EIC team and members of the LEC team who are working on various aspects of the LEC design.

REFERENCES

[1] S. Nagaitsev, "Electron-Ion Collider", in *Proc. IPAC'25*, Taipei, Taiwan, June 2025, pp. 861-865. `doi:10.18429/JACoW-IPAC2025-TUYN1`

[2] A.V. Fedotov *et al.*, "Experimental demonstration of hadron beam cooling using radio-frequency accelerated electron bunches", *Phys. Rev. Lett.*, vol. 124, no. 8., p. 084801, 2020. `doi:10.1103/PhysRevLett.124.084801`

[3] M. Blaskiewicz, "Stochastic cooling for the EIC", these proceedings.

[4] E. Wang *et al.*, "Electron Ion Collider Strong Hadron Cooling design summary", BNL-228488-2025-TECH; also these proceedings.

[5] V. Lebedev *et al.*, "Conceptual design report: A ring-based electron cooling system for the EIC", *J. Instrum.*, vol. 16, p. T01003, 2021. `doi:10.1088/1748-0221/16/01/T01003`

[6] B. Dhital *et al.*, "Dual-energy electron storage ring", *Phys. Rev. Accel Beams*, vol. 27, p. 090101, 2024. `doi:10.1103/PhysRevAccelBeams.27.090101`

[7] S. Benson *et al.*, "Development of a bunched beam electron cooler based on ERL and circulator ring technology", in *Proc. COOL'17*, Bonn, Germany, 2017, pp. 72-76. `doi:10.18429/JACoW-COOL2017-WEM12`

[8] H. Zhao, J. Kewisch, M. Blaskiewicz and A. Fedotov, "Ring-based electron cooler for high energy beam cooling", *Phys. Rev. Accel. Beams*, vol. 24, p. 04350, 2021. `doi:10.1103/PhysRevAccelBeams.24.043501`

[9] S. Seletskiy *et al.*, "Design of ring electron cooler", to be published *Proc. NAPAC'25*, Sacramento, CA, USA, Aug 2025, pp. 1151-1154. `doi:10.18429/JACoW-NAPAC2025-FRAD02`

[10] D. Kayran *et al.*, "Electron cooler for high-energy hadrons based on Energy Recovery Linac", these proceedings.

[11] A. Fedotov *et al.*, "Accelerator physics requirements and challenges of RF-based electron cooler for EIC injection energy", to be published *Proc. NAPAC'25*, Sacramento, CA, USA, Aug 2025, pp. 346-349. `doi:10.18429/JACoW-NAPAC2025-TUP003`

[12] D. Kayran *et al.*, "Beam dynamics studies for low-energy electron cooler for Electron Ion Collider", these proceedings.

[13] S. Seletskiy *et al.*, "Magnetic Shielding of LEReC Cooling Section", in *Proc. NAPAC'16*, Chicago, IL, USA, Oct. 2016, pp. 1030–1032. `doi:10.18429/JACoW-NAPAC2016-WEPOB61`

ISBN: 978-3-95450-267-7 ISSN: 2226-0374 doi: 10.18429/JACoW-COOL2025-TUA2

ELECTRON ION COLLIDER STRONG HADRON COOLING DESIGN SUMMARY

Erdong Wang*, William Bergan, Michael Blaskiewicz, Ferdinand Willeke, Derong Xu
Brookhaven National Laboratory, Upton, NY 11973, USA
Nick Sereno, Kirsten Deitrick, Sadiq Setiniyaz
Thomas Jefferson National Accelerator Facility, Newport News, VA, USA

Abstract

The Electron-Ion Collider (EIC) requires a high-energy cooler to maintain excellent beam quality and achieve high luminosity throughout long collision stores. To meet this requirement, the EIC project has adopted a novel approach known as Coherent Electron Cooling (CeC)—referred to as Strong Hadron Cooling (SHC)—which can provide rapid cooling rates at high energies. The SHC relies on an Energy Recovery Linac (ERL) to provide the intense, high-quality, and low-noise electron beam essential for the cooling process. This talk will overview and summarize the design progress of the Strong Hadron Cooler for the EIC. We will discuss key aspects of the project, including cooling physics, main parameters, the ERL design, risk mitigation strategies, and remaining challenges. Successful outcomes in foundational R&Ds could pave the way for a future proposal to implement SHC as an upgrade to the EIC, unlocking its full luminosity potential.

INTRODUCTION

Hadron Beam cooling is essential for substantially reducing the emittance of the proton or ion beams and preserving these parameters throughout the beam store in the EIC to maintain the average luminosity nearly equal to its peak value of $1.03 \times 10^{34}\ \mathrm{s}^{-1}\ \mathrm{cm}^{-2}$ for e-p collisions at a center-of-mass energy (E_{cm}) of 105 GeV.

Due to high particle densities, conventional stochastic cooling systems for the EIC's proton beams require a 10- to 100-fold increase in bandwidth to provide the cooling rates needed to suppress IBS-induced emittance growth and the corresponding luminosity reduction.

Two primary hadron cooling systems are planned for the EIC: a Low-Energy Cooler (LEC) for hadrons at the injection energy of 24.5 GeV, and a high-energy cooler to maintain luminosity at collision energies of 100 GeV and 275 GeV. The latter is the main Strong Hadron Cooling (SHC) system for the project [1, 2]. This report, follows more detailed design report [3], summarizes the design progress of the SHC.

EIC HIGH ENERGY COOLING REQUIREMENTS AND ROADMAP

The EIC SHC is essential for the EIC to achieve a luminosity of $1 \times 10^{34}\ \mathrm{cm}^{-2}\ \mathrm{s}^{-1}$. The key cooling requirements are:

- Counteract longitudinal and transverse emittance growth during long stores. The cooling time must be less than or equal to the emittance growth time from all diffusion sources. The dominant source is Intra-Beam Scattering (IBS), with longitudinal and horizontal growth times of 2 h to 3 h. The beam-beam diffusion time is approximately 5 h in the vertical plane.
- Provide cooling at top energies (275 GeV for protons, as well as 100 GeV and 41 GeV).
- Ensure the cooling section hardware fits within the available space in the IR-2 tunnel.
- Accommodate various ion species, including protons, ^{3}He, and heavy ions up to gold.

Following a 2020 review, CeC was selected as the primary method for the EIC's high-energy cooler, referred to as SHC in the EIC.

During the 2023 design phase, it became clear that a conventional electron cooler was a desirable addition at the injection energy. This cooler would be integrated into the same ERL to achieve the required beam emittances at lower energies (e.g., the 24 GeV injection energy) and provide a potential path for a 41 GeV storage cooler. Consequently, the EIC hadron cooler scope was updated to include both an SHC and a low energy conventional electron cooler (LEC).

By 2025, significant technical risks associated with the high-energy cooling system remained unresolved, and luminosity studies indicated that even with the SHC scenario, the projected average luminosity would be less than half of the ultimate requirement [4]. Consequently, due to these unresolved risks and performance limitations, the design efforts for advanced high-energy cooling—including both SHC and the storage ring cooler designs, were terminated within the EIC project scope. The mitigation of remaining risks is now being pursued by resources outside of the main project.

STRONG HADRON COOLING DESIGN

The design study for microbunched electron cooling includes the following activities:

- **Cooling Physics Modeling:** Develop and apply physics models and simulation codes to represent the cooling process accurately.
- **Cooling Section Design:** Engineer the lattice, magnets, and diagnostic systems for the complete cooling section.

---

* wange@bnl.gov

ISBN: 978-3-95450-267-7 ISSN: 2226-0374 doi: 10.18429/JACoW-COOL2025-TUA2

- **Luminosity Performance Modeling:** Integrate the cooler model into full collider simulations to project and optimize the machine's luminosity.
- **ERL Design:** Develop the complete design for the ERL, including RF systems, magnets, and beam dynamics.
- **Critical Component R&D:** Conduct targeted research and development for key enabling technologies, such as the high-current electron gun and the amplification system.

The schematic drawing of the SHC facility as well as hadron beamline is shown in the Fig. 1. It consists of Energy Recovery Linac, electron-hadron overlap section, Injector Cooler(precooler) bypass beamline.

Modeling Development and Main Parameter Table

We start modeling the process of microbunched electron cooling(MBEC) by treating the electrons and hadrons as rigid Gaussian discs of charge, with transverse sizes equal to the relevant beam sizes. Detailed expressions and derivations are provided in [2, 5].

An improvement to this paradigm is to use a hybrid model which continues to consider the electrons as discs but treats the hadrons as point particles with arbitrary transverse offsets in the modulator and kicker. This requires only a change to the electron-hadron interaction terms, as detailed in [5]. Later, 3D simulation codes were developed and compared with hybrid model, shows reasonable agreements.

Optimal parameters for cooling 275 and 100 GeV protons were obtained using a multi-objective genetic optimizer followed by manual fine-tuning, and are displayed in Tab. 1. Since the cooling force depends on the local electron current, it is desirable to have a flat-top electron current distribution, which we approximate as a 4th-order supergaussian.

Microbunched electron cooling leading to a factor of roughly 2 improvement in average luminosity. This cooling method works well at cooling the core of the bunch, but does not do a good job of cooling the tails, since those particles overlap less frequently with the cooling electron bunch and have large actions, leading to large delays relative to the wake wavelength and sampling of the nonlinear region of the wake. This contributes to continued particle loss and emittance growth. Detailed luminosity modeling is presented in this workshop.

Hadron Beamline Design

The Insertion Region 2 (IR2) of the Hadron Storage Ring was selected to host the cooling systems, which include a Pre-Cooler operating at injection energy (24 GeV) and a SHC system operating at top energies (100 GeV and 275 GeV). The beam optics was matched to meet the SHC requirements. The hadron lattice have met both 275 GeV and 100 GeV Horizontal and longitudinal cooling. Minor adjustments to the optics can rebalance H/L cooling rate. A vertical cooling lattice can be achieved by using skew quadrupole between dipole in the middle section.

Cooling Section Design

The cooling section consists of three parts: Modulator,Amplifier and Kicker , with a diagram shown in Fig. 1.

The amplification section consists of three chicanes to turn the energy modulation into a density modulation. The electron bunch longitudinal space charge will increase the beam energy spread and lengthen the bunch length when through the cooling section if their R_{56} is not zero and cause the microbunch slippage. This slippage of the modulated micro-bunches will misalign with the same hadrons at the kicker section. One of the methods to solve this problem is reversing sign of R_{56} in one of chicanes in the amplification section and achieve a the total $R_{56} = 0$ [6]. To avoid anti-cooling, the chicane's $R_{56_1} \cdot R_{56_2} \cdot R_{56_3} > 0$, because the hadron chicane provides a positive R_{56}. We have designed chicanes with embedded quadrupoles. It can tune the R_{56} in large range without change the path length. We also evaluated the CSR enhanced microbunch through the chicane. The enhancement factor for microbunching due to CSR is less than one. To achieve the sufficient stability of the longitudinal alignment, the chicane dipole field stabilization must be better than $5e-6$, CSR caused longitudinal shift 140 nm and longitudinal space charge caused shift 56 nm. These noise requirements are very challenging.

It is also necessary for the energy spread in the electron beam to be properly controlled. We see that an electron chicane of strength R_{56} multiplies the impedance by a factor of $\exp[-(kR_{56}\sigma_e)^2/2]$, where k is the wavenumber and σ_e is the electron energy spread. If σ_e is much larger than the design, it will wash out the wake features necessary for cooling, while a too-small σ_e will introduce high-frequency noise into the electron beam, saturating the amplifier.

Another potential challenge is the higher-order path length delays to the electrons. An electron with transverse actions J_x and J_y traveling between points s_1 and s_2 receives phase-averaged delays. We have found that, despite their short lengths, the large Courant-Snyder gammas in the electron chicanes result in those elements providing extra delays to the electrons on the order of the wake wavelength, significantly smearing out the wake function. We addressed it by increasing the beam size through the cooling section. All these effects of cooling wake smearing have been included in the cooling model.

Energy Recovery Linac Design

A design effort was undertaken at JLab, BNL, and Xelera to specify parameters of an Energy Recovery Linac (ERL) located at the 2 o'clock straight of the EIC that can achieve the SHC requirements for the EIC [7]. The primary requirements are high average current up to 100 mA used for pre-cooling the injected HSR beam at 24.5 GeV, and cooling at the hadron beam collision energy of 275 and 100 GeV. The injection and collision beam energies imply required electron beam energies from the ERL of 13, 150 and 55 MeV. The electron beam energies at collision are called modes

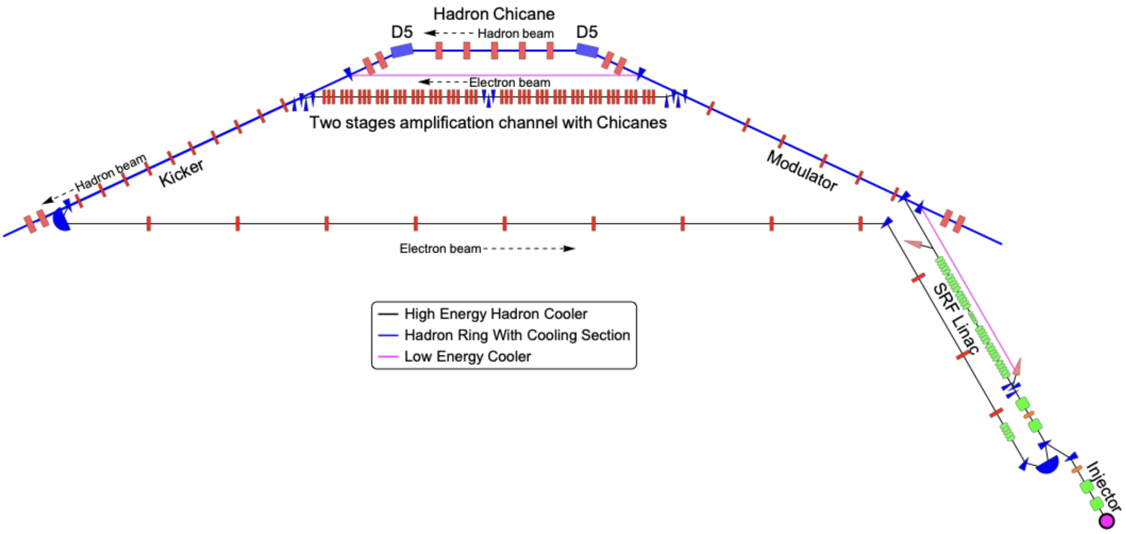

Figure 1: Representative diagram of the ERL with the cooling section at the 2 o'clock straight.

A (150 MeV) and B (55 MeV) respectively. The main ERL design challenges are the relatively low beam energy and high average current which make the machine susceptible to various beam instabilities and losses. Operability also is a challenge in that the machine will have to switch between injection cooling and cooling at collision energy. Multiple talks discussed ERL design in this workshop [10, 12]. Here, we discuss the challenges may impact on cooling performance.

At the end of the Linac, the initial electron beam slice energy spread was non-uniform and too low, which would cause amplifier saturation. A laser heater section is proposed to increase the uncorrelated energy spread and make it uniform. The required 1.1 kW laser is feasible [9]. The long-wavelength noise (1 µm) generated by the heater is not amplified by the amplifier and will not impact cooling.

Maintaining low initial electron beam noise is critical for effective SHC. Shot noise within the electron beam can be amplified by microbunching instabilities, particularly at short wavelengths. This amplified noise can obscure the intended hadron-induced modulation signal, thereby degrading the cooling rate. We performed high-fidelity 3D macroparticle tracking simulations of the shot noise evolution using the IMPACT code [11]. These simulations, which used the real number of electrons, followed the accelerator layout shown in Fig. 1 .

The results show a long-wavelength relative current modulation ($\lambda \approx 280\,\mu\mathrm{m}$) at the linac exit. This wavelength is well outside the amplifier's operational frequency range and thus will not be amplified. After filtering out this modulation, the remaining relative RMS current fluctuation is approximately 7.5×10^{-4}. This level is consistent with the expected noise from a smooth beam distribution, suggesting that the initial high-frequency shot noise is not significantly amplified through the accelerator. Detailed results are presented in [11].

Major Components R&D

Longitudinal Alignment Measurement A significant challenge for the CeC is aligning the hadron and electron beams longitudinally to within the 1 µm to 10 µm wake wavelength over a 100 m path. Measuring the cooling effect directly is too slow (hours) for feedback. A proposed fast diagnostic involves measuring changes in proton radiative power in a downstream dipole [8]. This signal indicates alignment on a sub-second timescale. However, it requires developing a novel, highly sensitive detector for nW-level radiation in the 1 µm to 30 µm wavelength range, which is a significant R&D effort. For 275 GeV, the 5 µm to 8 µm signal is detectable with commercial HgCdTe photodetectors. For 100 GeV, the 30 µm signal requiring non-commercial Si:As BIB detectors at 4 K. An alternative is using optical parametric amplification (OPA) to convert the IR signal to a visible wavelength using a nonlinear crystal (e.g., PPLN or $AgGaSe_2$). Significant R&D is needed, particularly for the 100 GeV case, to either develop the BIB detector system or a prototype wavelength conversion system.

High Current Electron Source SHC requires a high-brightness electron source capable of a 100 mA average current, which is beyond the state of the art.

The selected approach is a high-voltage DC (HVDC) gun, leveraging LEReC and polarized source expertise. The R&D goals include delivering a 98 mA beam at $>$ 500 kV and achieving a long operational lifetime. Novel features focus on cathode cooling, a high-voltage inverted feedthrough, and advanced K2CsSb photocathodes to increase lifetime [13].

SUMMARY AND OUTLOOK

From 2020 to 2024, the EIC strong hadron cooling collaboration made significant progress in designing a high-energy cooler based on CeC. The design effort produced a compre-

Table 1: Parameters for Longitudinal and Transverse Cooling at Store

Case	**100 GeV**	**275 GeV**
Modulator Length (m)	33	33
Kicker Length (m)	33	33
Number of Amplifier Drifts	2	2
Amplifier Drift Lengths (m)	49	49
Proton Parameters		
Protons per Bunch	6.9e10	6.9e10
Fit Proton Bunch Length (cm)	7	6
Proton Fractional Energy Spread	8.5e-4	6.0e-4
Proton Emittance (x/y) (nm)	30 / 2.7	11.3 / 1
Horizontal/Vertical Proton Betas in Modulator (m)	16.6 / 16.4	21.0 / 19.6
Horizontal/Vertical Proton Dispersion in Modulator (m)	0.0036 / 0.096	0.0019 / 0.067
Horizontal/Vertical Proton Dispersion Derivative in Modulator	0.030 / -0.0099	0.030 / -0.0049
Horizontal/Vertical Proton Betas in Kicker (m)	16.6 / 16.4	21.0 / 19.6
Horizontal/Vertical Proton Dispersion in Kicker (m)	0.0036 / 0.096	0.0019 / 0.067
Horizontal/Vertical Proton Dispersion Derivative in Kicker	-0.030 / 0.0099	-0.030 / 0.0049
Proton Horizontal/Vertical Phase Advance (rad)	3.227 / 4.72	3.162 / 4.44
R56 in Proton Chicane (mm)	4.2	0.95
Electron Parameters		
Electron Bunch Charge (nC)	1	1
Equivalent Gaussian Electron Bunch Length (mm)	12	9.4
RMS Electron Bunch Length (mm)	9	7
Electron Peak Current (A)	~ 10	~ 13
Electron Fractional Slice Energy Spread	1e-4	5.9e-5
Horizontal/Vertical Electron Betas in Modulator (m)	20 / 20	21.4 / 21.4
Horizontal/Vertical Electron Betas in Kicker (m)	29.7 / 4.1	7.9 / 7.9
Horizontal/ Vertical Electron Betas in Amplifiers (m)	12.0 / 12.0	4.9 / 4.9
R56 in First Electron Chicane (mm)	23.3	12.0
R56 in Second Electron Chicane (mm)	-16.7	-6.7
R56 in Third Electron Chicane (mm)	-18.2	-6.8
Cooling Times		
Horizontal/Vertical/Longitudinal Initial IBS Times (hours)	2.0 / 4.0 / 2.5	2.0 / - / 2.9
Horizontal/Vertical/Longitudinal Beam-Beam Times (hours)	20.0 / 5.0 / -	20.0 / 5.0 / -
Horizontal/Vertical/Longitudinal Initial Cooling Times (hours)	1.9 / 4.7 / 3.3	1.0 / 13.5 / 1.5

hensive, which is essential for maintaining and improve high luminosity at the EIC. The key achievement includes:

- **Advanced Modeling and Simulation**: Sophisticated 1D, 2D, and full 3D models were developed to understand the cooling physics, including non-linear effects and diffusion. A long-term luminosity evolution code was also created, which incorporated effects like IBS and beam-beam interactions.
- **Comprehensive ERL Design**: A preliminary design for the ERL was established. This included solutions such as a laser heater,uniform current generation, bunch compressive using splitter, wakes evaluation. High-fidelity tracking with the real number of electrons was used to verify amplifier performance and show that initial shot noise is not significantly amplified.
- **Critical R&D Initiatives**: R&D began on the most challenging components. This includes the development of a high-current, high-brightness electron gun and novel detectors for the sub-micrometer scale longitudinal alignment.

While the design studies produced a conceptual framework, we also realized the significant technical risks and performance limitations such as even with a fully functional SHC, the average luminosity would still fall short of the ultimate EIC requirement. Furthermore, critical challenges of beam stability, the high-current ERL operation, cooling measurement instruments could not be fully retired within the project's construction timescale. Successful outcomes in these foundational R&D areas could pave the way for a future proposal to implement SHC as an upgrade to the EIC, unlocking its full luminosity potential.

REFERENCES

[1] D. Ratner, "Microbunched electron cooling for high-energy hadron beams", Phys. Rev. Lett. 111, 084802 (2013)

[2] G. Stupakov, "Cooling rate for microbunched electron cooling without amplification", Phys. Rev. Accel.Beams 21, 114402 (2018)

[3] E. Wang et al, "Electron Ion Collider Strong Hadron Cooling design Summary", Tech. Rep.(Brookhaven National Lab. (BNL), Upton, NY (United States), 2025). `doi:10.2172/2574100`

[4] W. F. Bergan, "EIC Luminosity Models for Various Hadron Cooling Scenarios", in this workshop

[5] W. F. Bergan et al., "Coherent electron cooling physics for the eic", in *Proc. IPAC'24*. (JACoW Publishing, 2024) `doi:10.18429/JACoW-IPAC2024-THYD1`

[6] E. Wang and M. Blaskiewicz, "Longitudinal space charge kick in Coherent Electron Cooling", Tech. Rep.(Brookhaven National Lab. (BNL), Upton, NY (United States), 2020). `doi:10.2172/1725767`

[7] E. Wang *et al.*, "Electron Ion Collider Strong Hadron Cooling Injector and ERL", in *Proc. LINAC'22*, Liverpool, UK, Aug.-Sep. 2022, pp. 7–12. `doi:10.18429/JACoW-LINAC2022-MO2AA04`

[8] W. F. Bergan, M. Blaskiewicz, and G. Stupakov, "Schottky signal modification as a diagnostic tool for coherent electron cooling", Phys. Rev. Accel. Beams 25, 094401 (2022).

[9] E. Wang, J. Qiang, S. Benson, and W. Bergan, "Generating Super-Gaussian distribution and uniform sliced energy spread bunch for EIC strong hadron cooling", in *Proc. IPAC'24*, Nashville, TN, USA, May 2024, pp. 110–113. `doi:10.18429/JACoW-IPAC2024-MOPC23`

[10] K. Detrick et al. "Design of a Microbunched Electron Cooler Energy Recovery Linac", in this workshop

[11] J. Qiang, W. Bergan, and E. Wang, "Simulation of electron beam transport through the coherent electron cooling amplification section using real number of electrons", presented at the IPAC'25, Taipei, Taiwan, Jun. 2025, paper WEPS015, unpublished.

[12] S. Setiniyaz et al., "Transverse BBU Suppression with Feedback for Energy-Recovery Linacs " in this workshop

[13] Wang, Erdong, et al. "High average current HVDC electron gun for EIC hadron cooling." , Jul. 2025. `doi:10.2172/2572417`

ISBN: 978-3-95450-267-7 ISSN: 2226-0374 doi: 10.18429/JACoW-COOL2025-TUA3

EIC LUMINOSITY MODELS FOR VARIOUS HADRON COOLING SCENARIOS[*]

W. F. Bergan[†], Brookhaven National Laboratory, Upton, NY, USA

Abstract

We have developed a simulation to model the evolution of proton and heavy-ion bunches stored in the Electron-Ion Collider's Hadron Storage Ring (HSR) over the course of several hours, taking into account intrabeam scattering, the beam-beam effect, and particle loss. This has enabled us to predict how various cooling schemes, including microbunched electron cooling and microwave stochastic cooling, would impact the collider's luminosity. We discuss the details of this code and show the luminosity evolution for various scenarios.

INTRODUCTION

The Electron-Ion Collider (EIC) is a new collider which will be built at Brookhaven National Laboratory to probe nuclear structure through the collision of electrons with various ion species. In order to improve luminosity, various cooling scenarios are considered, including a low-energy cooler to create initial flat hadron beams [1] as well as stochastic and microbunched electron cooling at store to maintain the beam emittance [2, 3]. Since not all of these systems may be available at startup, it is desirable to have a simulation code which will enable us to quantify the performance of the various cooling systems and operational modes.

To achieve this goal, we have developed a long-term luminosity model. This evolves a bunch of hadrons[1] over the course of the several-hour store and uses this information to compute changes in the luminosity. We discuss the details of this model and the various physical effects included, then show luminosity evolution for various physics cases.

MODEL DETAILS

Our model is an extension of the long-term tracking developed for studies of microbunched electron cooling [3]. We initialize a bunch of hadron macroparticles and then use a small number of transfer matrices to transport them between a handful of key locations in the EIC's hadron storage ring (HSR), allowing the macroparticles to sample their full phase space. We include both 591 and 197 MHz RF cavities to provide sinusoidal energy kicks to the hadrons each turn. We manually add in the interesting dynamic effects, including intrabeam and Touschek scattering, the beambeam effect, and cooling, as will be described in the subsequent subsections. In order to simulate many real turns in a small number of simulated turns, we let each simulated turn represent $N >> 1$ real turns by increasing coherent cooling kicks by a factor N and incoherent kicks by $\sqrt{N}$.

Intrabeam Scattering (IBS)

We calculate intrabeam scattering rates using the formulas in [5]. These are equivalent to the usual Bjorken-Mtingwa formalism [6], but written in terms of elliptic integrals which can be quickly evaluated using the methods of [7]. Due to our explicit implementation of large-amplitude Touschek kicks, as will be discussed later, we restrict the maximum momentum kick in the Coulomb logarithm to be the minimum momentum kick we use for our calculations of Touschek scattering.

As inputs to the IBS calculation, we require the optics around the ring as well as information about the bunch distribution. The optics are simply sampled at 1000 equidistant points of the HSR, with coarser sampling not giving any advantage. The beam transverse emittances are calculated by fitting the distributions of the particles' transverse actions to exponentials, and the bunch length and energy spread are found by fitting the distributions of longitudinal position and energy offset to Gaussians, with the longitudinal bunch positions further constrained to lie within the central 591 MHz RF bucket. This allows us to focus our studies on the core of the beam as opposed to the potentially large tails.

Once the IBS rates are calculated, we apply Gaussian random kicks to each macroparticle in each of the 3 planes in a zero-dispersion location. These kicks have mean 0 and standard deviation chosen to produce the correct heating rates. Additionally, the sizes of the kicks to a given macroparticle are scaled by the square root of the hadron's local density relative to the average density in the 591 MHz RF bucket, since we expect that the heating rate for an individual particle will increase as it moves toward the core of the bunch.

Beambeam Effect

The beambeam effect results in an emittance growth in the hadron beam due to the strong nonlinear force exerted by the electrons. Since this is a complex phenomenon, we simply assume a constant beambeam growth time of 20 hours horizontally and 5 hours vertically for protons and no beambeam growth for heavy ions due to their smaller beambeam parameter [4]. The implementation of the kicks is the same as described for IBS in the previous subsection, except that we do not perform the density scaling, since this is not expected to be the case for beambeam.

Touschek Scattering

While IBS models the emittance growth due to many small-angle scattering events, there is also a non-zero probability that a given hadron will receive a single large energy

---

[*] This work was supported by Brookhaven Science Associates, LLC under Contract No. DE-SC0012704 with the U.S. Department of Energy.

[†] wbergan@bnl.gov

[1] We do not need to do anything special for the electron beam, since its emittance is held constant by radiation damping and the bunches are frequently replaced for polarization reasons [4].

ISBN: 978-3-95450-267-7 ISSN: 2226-0374 doi: 10.18429/JACoW-COOL2025-TUA3

kick that will instantaneously cause a significant change in its phase-space coordinates. The probability of receiving an energy kick of a given size or larger is given by Eq. 41 of [8]. We see empirically that the probability of receiving a kick of at least δ_m scales approximately as δ_m^{-3}. Letting the initial momentum spread of the bunch be δ_0, we calculate the probability P_0 of receiving a momentum kick equal to or greater than δ_0 within a given timestep. Then, at each timestep, we draw a random number in the range $r \in [0, 1)$ for each macroparticle and give it a momentum kick of size $\delta = \pm[-P_0\delta_0^3/\ln(1-r)]^{1/3}$ if $|\delta| > \delta_0$, with both signs having equal probability.

Stochastic Cooling

Stochastic cooling is a well-developed method for cooling low-density hadron beams [9] and has been successfully used at a number of facilities, including the Relativistic Heavy Ion Collider (RHIC) [10]. It uses pickups to measure the positions of the particles in the bunch in 3 dimensions within some bandwidth then uses a kicker to apply momentum kicks to the bunch in order to correct the particle offsets.

We simulate the process directly in our code. At the location of the transverse pickups, we create histograms of the macroparticles' longitudinal positions weighted by either their horizontal or vertical positions. We filter this through the 16 available cavity frequencies, equally spaced between 5 and 8 GHz [10], and apply an appropriate gain factor to obtain the kicks which we then apply at the kicker location. In order to have the transverse offsets at the pickup correspond to transverse angles at the kicker, we ensure that there is a $\pi/2$ phase advance between these locations. For the longitudinal case, we have two pickups separated by 1/6 of a turn. We take the histogram of the longitudinal macroparticle distribution at each location. Since the shift in particle positions between the two pickups is due to their energy offsets, taking the difference in these two distributions gives us information about the momentum distribution of the particles. We then filter this through the 16 available cavity frequencies and apply the appropriate gain and phase shift to get the kick we need to apply at the longitudinal kicker 1/6 of a turn after the second pickup.

Since the noise scales with the bunch population, we need to be careful about how we perform the time and particle-number rescaling. Letting Δp_c be the coherent cooling kick, Δp_h be the diffusive heating kick, g be the amplifier gain, N be the number of macroparticles, and T be the timestep length, we have that $\Delta p_c \propto gT$ and $\Delta p_h \propto g\sqrt{NT}$. Therefore, if we increase the gain by some constant R and decrease the number of macroparticles by this same factor R, we see that it is equivalent to increasing the length of the timestep by R, allowing an effective time rescaling [11].

Microbunched Electron Cooling

For the dense proton bunches planned to be stored in the EIC, stochastic cooling will not work due to its limited bandwidth. Coherent electron cooling is a method of cooling such dense proton bunches which operates by using a co-propagating beam of electrons as both the pickup and kicker. The protons provide energy kicks to nearby electrons, producing energy fluctuations which are then amplified and turned into density fluctuations. These provide energy kicks to the protons which tend to fix their initial phase space actions [12].

Microbunched electron cooling (MBEC) is a specific implementation of coherent electron cooling which amplifies the electron density fluctuations using the microwave instability [13]. Details of the design for the EIC can be found in [3] and the references provided therein.

We once again simulate this process directly. We compute the wake function which tells us the energy kick that a proton receives in the kicker as a function of its phase space coordinates in modulator and kicker. We also can compute a diffusion term which tells us the size of the random kick it would receive due to the wakes of the other protons and due to noise in the electron beam. We then simply track the proton macroparticles directly between the modulator and kicker using the relevant transfer matrix and apply the appropriate cooling kick and a Gaussian random heating kick, with RMS value given by the diffusion term,. Further details are given in [3].

Particle Losses and Initialization

In order to simulate particle losses, we define an ellipse in the 6-dimensional phase space and eliminate particles which fall outside the ellipse. Specifically, a macroparticle with actions in the three planes equal to J_x, J_y, and J_z is removed if $J_x/J_{x,max} + J_y/J_{y,max} + J_z/J_{z,max} > 1$, where the maximum transverse actions $J_{x,max}$ and $J_{y,max}$ are those which would bring a particle to transverse coordinates 6 times the beam's initial transverse size and $J_{z,max}$ is defined by the RF bucket. We use the full 197 MHz bucket for the heavy ions, but limit the protons to stay within the 591 MHz bucket due to their larger sensitivity to the beambeam effect [14].

In order to get a realistic distribution of particles filling the RF bucket, we seed the particles longitudinally using the rejection algorithm. We randomly place a trial macroparticle within some area of z-pz phase space including the entire RF bucket. It is then kept with probability $(1 - J_z/J_{z,max})^2$, so that macroparticles at the bucket center are always kept and those near the edges are rarely retained. This is repeated until the desired number of macroparticles has been seeded.

Beta-Function Rescaling

During the store, the emittances of the beam will change, and so we adjust the beta functions at the interaction point (IP) in order to maintain a number of constraints. First, we must rescale the beta functions of the electrons so that their beam size matches that of the hadrons. We also will have forward detectors near the IP to measure particles which are scattered at very small angles. In order to keep backgrounds here low, we need to tightly constrain the divergence of the beam at the IP. Therefore, if the hadron beam emittance

ISBN: 978-3-95450-267-7 ISSN: 2226-0374 doi: 10.18429/JACoW-COOL2025-TUA3

would increase above its initial value, we increase the corresponding beta function at the IP to maintain the divergence equal to the initial divergence. Conversely, if the hadron emittance is reduced (primarily due to cooling), we also increase the corresponding beta function at the IP to avoid needing to shrink the beta functions of the electron beam below their initial values.

Since the hadron beam may have a non-Gaussian profile, particularly due to the effects of cooling, we need to define the emittance appropriately when evaluating the above constraints. Since we care about the tails for the divergence constraint, we compute the emittance as the average of the particle actions for that case, while we compute the emittance using an exponential fit to the actions when evaluating the other two constraints related to matching beam sizes, since we care there mainly about the core of the bunch.

Crabbing

The EIC will collide electrons and hadrons with a 25 mrad crossing angle [4]. Without any correction, the particles in the two bunches will have poor overlap during the collision, significantly reducing the luminosity. In order to help fix this issue, we will install crab cavities which provide a transverse kick to particles in the two beams as a function of their longitudinal coordinate, effectively rotating the bunches so that they collide head-on. However, during early operations, we may not yet have any cavities for the electron beam and only the 197 MHz cavities for the hadrons, which will have a significant nonlinear x-z distribution.

Luminosity Evaluation

In order to evaluate the luminosity, we make use of Eq. 1 from [15], evaluated in the limit when the electron and hadron beams have negligible transverse momenta,

$$\mathcal{L} = 2cf_{rep}\int d^3\vec{x}dt\rho_+(\vec{x},t)\rho_-(\vec{x},t) \tag{1}$$

where c is the speed of light, f_{rep} is the frequency of bunch crossings, and $\rho_\pm(\vec{x},t)$ are the densities of the hadrons and electrons.

In order to evaluate this integral numerically, we use a transfer matrix to bring the hadron bunch to the IP, backtrack them some distance upstream, provide a z-dependent transverse kick to model the effect of the crab cavities, and then track them as they move forward across the IP. We assume that the electron beam is perfectly Gaussian, potentially with a tilt due to the crab cavities. While tracking the hadron macroparticles across the IP, we can analytically determine the local electron density that each of them sees. We then need only numerically integrate this over the time that the hadron macroparticle is near the IP, average over the macroparticles, and multiply by the relevant prefactors to recover the instantaneous luminosity.

SELECTED RESULTS

We show here plots of luminosity and integrated luminosity for 3 potential operational modes, discussed in detail below. Since the experimentalists care about the integrated luminosity over real time, ie, including the downtime between stores, we include plots of average luminosity as a function of store length. This is computed by dividing the integrated luminosity up to that time by the length of the store plus some amount of turnaround time to account for the time needed to ramp down the machine, refill the hadrons, do low-energy cooling, and ramp to collision energy. We additionally set the luminosity to zero during the first 15-30 minutes of the store, since this is the time when we would be filling electrons and turning on the detector. However, the hadron beam still deteriorates during this time. We assume that the turnaround time is 1 hour for heavy ions without low-energy cooling, 1.5 hours for heavy ions with low-energy cooling, and 2 hours for protons, to account for the time needed for low-energy cooling and the necessity of slowing down the ramp due to the presence of the Siberian snakes [16]. For the heavy ions, where we only have 290 electron bunches to fill, we assume that filling the electrons and turning on the detector takes 15 minutes, while we assume 30 minutes for the protons, when we have 1160 bunches. We do not directly simulate low-energy cooling, but simply adjust the initial emittances of the beam.

For the first year of EIC operation, we are exploring the use of heavy ions such as niobium which have charge-to-mass ratios which will let us store them in the center of the beampipe with the dipole magnets at their maximum strength. We assume that only the 197 MHz crab cavities are installed for the ions, and none for the electrons. Plots of instantaneous and average luminosity are shown in Fig. 1 with and without low-energy cooling and/or stochastic cooling. We see that the inclusion of each of these roughly doubles the average luminosity.

We show in Fig. 2 luminosities for the highest energy heavy ion collisions foreseen for the EIC, 110 GeV/u gold colliding with 18 GeV electrons with or without stochastic cooling. In this case, we assume that low-energy cooling and all crab cavities are installed. Once again, we see that stochastic cooling doubles the average luminosity.

Finally, we consider the highest luminosity case for the EIC: 275 GeV protons colliding with 10 GeV electrons. We show in Fig. 3 the luminosity for this mode with or without microbunched electron cooling at store. Again, low-energy cooling and all crab cavities are assumed to be operational. We once again see that cooling at store doubles the average luminosity we can expect.

CONCLUSION

We have developed a simulation program which allows us to model the evolution of hadron bunches stored in the EIC with a wide variety of physical effects included, and in particular see the effects of stochastic cooling and microbunched electron cooling at store and the impact of the initial emittances which could be achieved with a low-energy cooler. For the parameters shown here, including cooling either at injection or at store roughly doubles the average

ISBN: 978-3-95450-267-7 ISSN: 2226-0374 doi: 10.18429/JACoW-COOL2025-TUA3

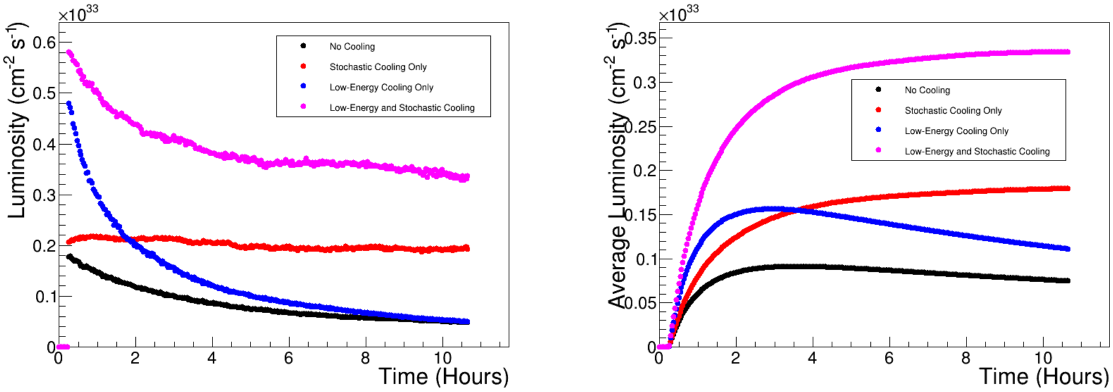

Figure 1: Instantaneous (left) and average (right) luminosity for 121 GeV/u niobium on 10 GeV electrons. We achieve an average luminosity of at most $0.9 \times 10^{32}\text{cm}^{-2}s^{-1}$ without any cooling, but this increases to $1.8 \times 10^{32}\text{cm}^{-2}s^{-1}$ with stochastic cooling alone, $1.6 \times 10^{32}\text{cm}^{-2}s^{-1}$ with low-energy cooling alone, and $3.3 \times 10^{32}\text{cm}^{-2}s^{-1}$ with both methods.

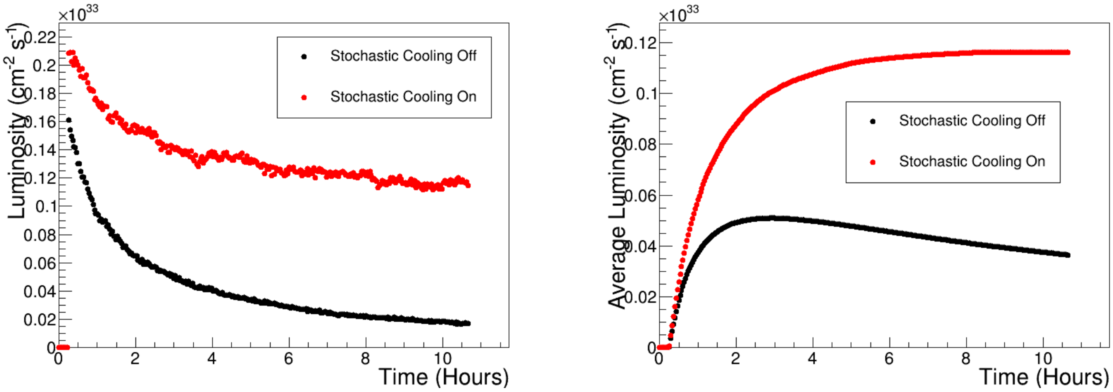

Figure 2: Instantaneous (left) and average (right) luminosity for 110 GeV/u gold on 10 GeV electrons. We see that adding stochastic cooling increases the average luminosity from 0.5 to $1.2 \times 10^{32}\text{cm}^{-2}s^{-1}$.

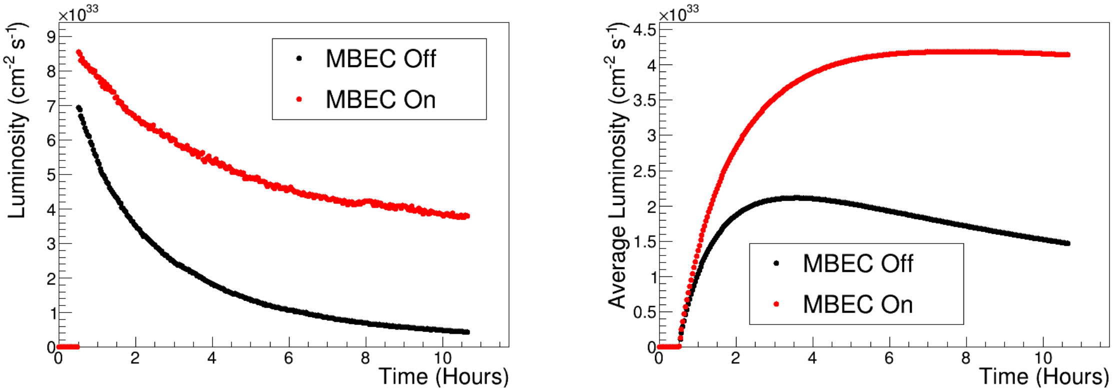

Figure 3: Instantaneous (left) and average (right) luminosity for 275 GeV protons on 10 GeV electrons. We see that adding microbunched electron cooling increases the average luminosity from 2.1 to $4.2 \times 10^{33}\text{cm}^{-2}s^{-1}$.

luminosity we can achieve, and including both quadruples the average luminosity. While we have only included detailed models of microbunched and stochastic cooling, we can in principle extend this code to handle other methods, such "regular" electron cooling.

ACKNOWLEDGMENTS

I would like to thank Mike Blaskiewicz, Erdong Wang, Vadim Ptitsyn, Elke Aschenauer, Yun Luo, and Alexei Blednykh for many useful discussions.

ISBN: 978-3-95450-267-7 ISSN: 2226-0374 doi: 10.18429/JACoW-COOL2025-TUA3

REFERENCES

[1] A. Fedotov *et al.*, “Accelerator physics requirements and challenges of RF based electron cooler for EIC injection energy”, in *Proc. NAPAC2025*, Sacramento, CA, USA, Aug. 2025, pp. 346-349. `doi:10.18429/JACoW-NAPAC2025-TUP003`

[2] M. Blaskiewicz, “Stochastic cooling for the EIC”, in *Proc. COOL’25, this conference*, slides TUB3, Stony Brook, NY, USA, Oct. 2025.

[3] W. F. Bergan *et al.*, “Coherent electron cooling physics for the EIC”, in *Proc. IPAC’24*, Nashville, TN, USA, May 2024, pp. 2937-2942. `doi:10.18429/JACoW-IPAC2024-THYD1`

[4] Electron-ion collider at Brookhaven National Laboratory, conceptual design report 2021, `https://www.bnl.gov/EC/files/EIC_CDR_Final.pdf`

[5] S. Nagaitsev, “Intrabeam scattering formulas for fast numerical evaluation”, *Phys. Rev. ST Accel. Beams*, vol. 8, p. 064403, 2005. `doi:10.1103/PhysRevSTAB.8.064403`

[6] J. D. Bjorken and S. K. Mtingwa, “Intrabeam scattering”, *Part. Accel.*, vol. 13, pp. 115-143, 1983.

[7] B. C. Carlson, “Computing elliptic integrals by duplication”, *Numer. Math.*, vol. 33, pp. 1-16, 1979.

[8] A. Piwinski, “The Touschek effect in strong focusing storage rings”, DESY-98-179, 1998. `https://doi.org/10.48550/arXiv.physics/9903034`

[9] S. van der Meer, “Stochastic cooling and the accumulation of antiprotons”, *Rev. Mod. Phys.*, vol. 57, p. 689, 1985. `doi:10.1103/RevModPhys.57.689`

[10] M. Blaskiewicz, J. M. Brennan, and F. Severino, “Operational stochastic cooling in the relativistic heavy-ion collider”, *Phys. Rev. Lett.*, vol. 100, p. 174802, 2008. `doi:10.1103/PhysRevLett.100.174802`

[11] M. Blaskiewicz, private communication.

[12] V. N. Litvinenko and Ya. S. Derbenev, “Coherent electron cooling”, *Phys. Rev. Lett.*, vol. 102, p. 114801, 2009. `doi:10.1103/PhysRevLett.102.114801`

[13] D. Ratner, “Microbunched Electron Cooling for High-Energy Hadron Beams”, *Phys. Rev. Lett.*, vol. 111, p. 084802, 2013. `doi:10.1103/PhysRevLett.111.084802`

[14] Y. Luo, private communication.

[15] M. A. Furman and M. S. Zisman, “Luminosity”, in *Handbook of Accelerator Physics and Engineering*, 2nd Ed., edited by A. W. Chao, K. H. Mess, M. Tigner, and F. Zimmermann, pp. 311-318 (2013).

[16] V. Ptitsyn, private communication.

ISBN: 978-3-95450-267-7 ISSN: 2226-0374 doi: 10.18429/JACoW-COOL2025-TUB1

DEVELOPMENT OF STORAGE RING ELECTRON COOLER FOR HIGH ENERGY APPLICATIONS *

S. Seletskiy†,[1], J. Kewisch [1], A. Fedotov [1], Y. Jing [1], D. Kayran[1], J. Unger[2], G. Hoffstaetter[2]
[1]Brookhaven National Laboratory, Upton NY, USA
[2]Cornell University, Ithaca NY, USA

Abstract

Electron cooling at high energy requires large average current in the cooling section (CS), which can be achieved by reusing the same electron beam on many passes through the CS. One of the options to realize such a cooling scheme is to use an electron storage ring with electrons being cooled by dedicated radiation damping wigglers. We will discuss the conceptual design of the 150 MeV Ring Electron Cooler as a potential future application for the Electron Ion Collider.

INTRODUCTION

Cooling of protons in the Electron Ion Collider (EIC) [1] at top energy ($\gamma = 293$) to counteract the IBS-driven emittance growth will be needed to achieve the design average luminosity at EIC. Electron Cooling [2] can provide such a capability.

Extending electron cooling to the high energies requires substantial electron current in the cooling section. To relax requirements to an injector, one can reuse the same electron beam on multiple turns. In this paper we consider a multi-turn electron cooling based on the Ring Electron Cooler.

In REC, electron bunches are stored in a dedicated storage ring, and the same e-bunches are reused for the cooling on multiple turns. The electrons' emittances are preserved during the storage cycle by counteracting heating caused by various scattering mechanisms with radiation damping facilitated by dedicated damping wigglers.

The REC utilizes a non-magnetized RF-based electron cooling, which was successfully applied at LEReC [3-6] during RHIC operation in 2019-2021 runs.

RING ELECTRON COOLER

The Ring Electron Cooler must be compatible with the EIC Low Energy Cooler (LEC) [7] and must share the cooling section with the LEC.

While the LEC "precools" the protons at the injection energy to the design emittances (Table 2), the REC's preserves the emittances at the collision energy by providing horizontal and longitudinal cooling times of 2 and 3 hours respectively.

REC Layout and Lattice

The REC layout is shown in Fig. 1. The REC lattice is shown in Fig. 2.

The electron storage ring is a trapezoidal shape "racetrack" with the CS and damping wigglers occupy most it.

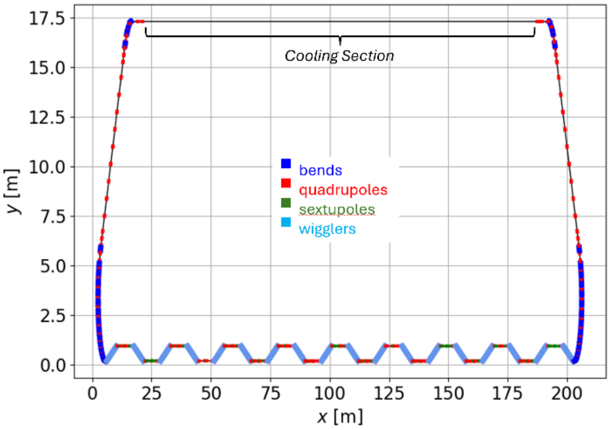

Figure 1: The Ring Electron Cooler layout.

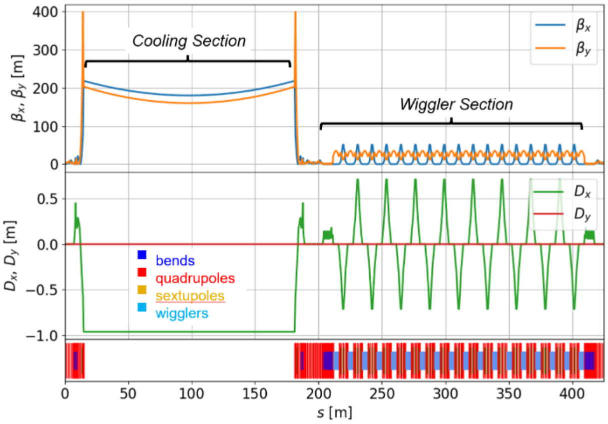

Figure 2: The Ring Electron Cooler lattice.

The cooling section is 170 m long. It is shielded by several layers of μ-metal, which provides at least factor of 1000 attenuation of ambient magnetic fields. The BPMs and trajectory correctors are located every 12 m in the CS.

About one meter of electron dispersion in the cooling section is needed to provide the required cooling times.

A wiggler section is opposite to the cooling section. It contains 18 damping wigglers. The wigglers must provide enough radiation cooling of the electron bunches to counteract the effects of the electrons intra-beam scattering (IBS) and beam-beam scattering (BBS) of electrons on protons in the CS.

The arcs connecting the wiggler section and the CS contain 10 m long straight sections with adjustable optics suitable for placement of injection and RF systems.

REC Parameters

The REC parameters are listed in Tables 1 and 2.

---

* Work supported by Brookhaven Science Associates, LLC under Contract No. DE-SC0012704 with the U.S. Department of Energy

† seletskiy@bnl.gov

Table 1: The REC Parameters (Electron Storage Ring)

Parameter	Value	Units
Relativistic γ	293	
Ring Circumference	426	m
CS length	170	m
Horizontal dispersion in CS	1	m
CS β-function (x,y)	180, 160	m
Momentum compaction	$-1.5 \cdot 10^{-3}$	
Geometric emittance (x,y)	7.8, 7.8	nm
Relative momentum spread	$9.8 \cdot 10^{-4}$	
FWHM bunch length	34	cm
Charge per bunch	21	nC
Peak current	17.5	A
Number of bunches	140	
Average current	2	A
Space charge tune shift x/y	0.14, 0.14	
Beam-beam parameter x/y	0.04, 0.09	
Number of wigglers	18	
Wiggler field	2.4	T
Wiggler length	4.2	m
Wiggler gap	2	cm
Wiggler period	23	cm
Damping rate (x,y,z)	31, 31, 62	s^{-1}
IBS rate (x,y,z)	31, 31, 48	s^{-1}
BBS rate (x,y,z)	0.8, -0.3, 12	s^{-1}
Main RF frequency	98.6	MHz
Main RF voltage	50	kV
2nd harmonic RF voltage	25	kV

Table 2: The REC Parameters (Protons in the CS)

Parameter	Value	Units
Relativistic γ	293	
Protons per bunch	$6.9 \cdot 10^{10}$	
Geometric emittance (x,y)	11.3, 1	nm
Relative momentum spread	$6 \cdot 10^{-4}$	
rms bunch length	6	cm
CS β-function (x,y)	300, 700	m
Horizontal dispersion in CS	2.1	m
Cooling time (x,y,z)	**2, 4, 3**	**hrs**

The following sections explain various aspects of obtaining the REC parameters.

More details of the REC design process can be found in [8].

COOLING OPTIMIZATION

The exact formulas used to calculate and optimize the REC cooling rates are given in [8]. Here, we give a rough scaling relations between the rate and beam parameters:

$$\lambda \propto \frac{N_e L_{CS}}{\gamma^2\left(\frac{\varepsilon_{ne}}{\beta_e}+\frac{\varepsilon_{ni}}{\beta_i}\right)(\varepsilon_{ne}\,\beta_e+\varepsilon_{ni}\,\beta_i)\sqrt{\sigma_{\delta e}^2+\sigma_{\delta i}^2}\sqrt{\sigma_{ze}^2+\sigma_{zi}^2}} \quad (1)$$

While cooling rate drops quadratically with beam energy, it grows linearly with number of electrons N_e and length of the cooling section L_{CS}. Smaller ion emittance ε_{ni}, energy spread $\sigma_{\delta i}$ and bunch length σ_{zi}, as well as smaller e-bunch phase space volume (defined by its emittance ε_{ne}, energy spread $\sigma_{\delta e}$ and length σ_{ze}), farther increase the cooling rate.

The proton bunch parameters are defined by the EIC design and are obtained by the LEC.

Electron bunch parameters in the REC are determined by an equilibrium between the radiation damping rate (λ_{damp}) and the overall heating rate characterized by the IBS rate (λ_{IBS}), the BBS rate (λ_{BBS}), and quantum excitations ($C_q = \lambda_{damp}\varepsilon_{nat}$), where ε_{nat} is a natural emittance. The equilibrium emittance is found from an iterative equation:

$$\varepsilon_{new} = \frac{\lambda_{rad}+\lambda_{IBS}(\varepsilon_{old})+\lambda_{BBS}(\varepsilon_{old})}{\lambda_{damp}} \quad (2)$$

A dedicated code [9] based on solving Eq. (2) was created to find equilibrium electron beam parameters. The details of relevant calculations can be found in [8,10,11].

Optimal cooling requires redistribution of cooling decrements between longitudinal and horizontal directions. This is achieved by introducing electron and proton horizontal dispersions in the REC CS [8, 12].

An iterative multiparametric optimization of cooling in the REC comprises the following steps:

- Choosing field profile of damping wigglers.
- Solving Eq. (2) for equilibrium parameters.
- Choosing e- and p-bunches parameters in the CS.
- Checking resulting cooling rates, BBS rate and beam-beam effect and beam lifetime.
- Optimizing the REC dynamic and momentum apertures and adjusting the REC lattice.

An example of one of the steps on a final iteration is demonstrated in Fig. 3. Here, the electron bunch β-functions and horizontal dispersion in the CS are kept constant, the longitudinal cooling time is kept at $\tau_z = 3$ hours and for each combination of ions β-functions the horizontal cooling time is minimized by varying ions' horizontal dispersion (D_i) in the CS.

After each iteration the equilibrium e-beam parameters were recalculated and the beam-beam effect on electrons' emittance [13] was checked.

The red dot in Fig. 3 shows the choice of protons Twiss parameters which maximize the cooling rate while keeping tolerable BBS rate and beam-beam effect.

Optimization of dynamic and momentum apertures is discussed in detail in [14]. The optimization includes choosing a proper field profile for damping wigglers, fine-

ISBN: 978-3-95450-267-7 ISSN: 2226-0374 doi: 10.18429/JACoW-COOL2025-TUB1

tuning a phase advance over the ``wiggler-sextupoles blocks", using two families of octupoles to reduce the non-linear motion, and adjusting the betatron tunes. The resulting apertures of $A_x = 10\sigma_x$, $A_y = 9\sigma_y$, and $A_\delta = 0.5\%$ are shown in Fig. 4.

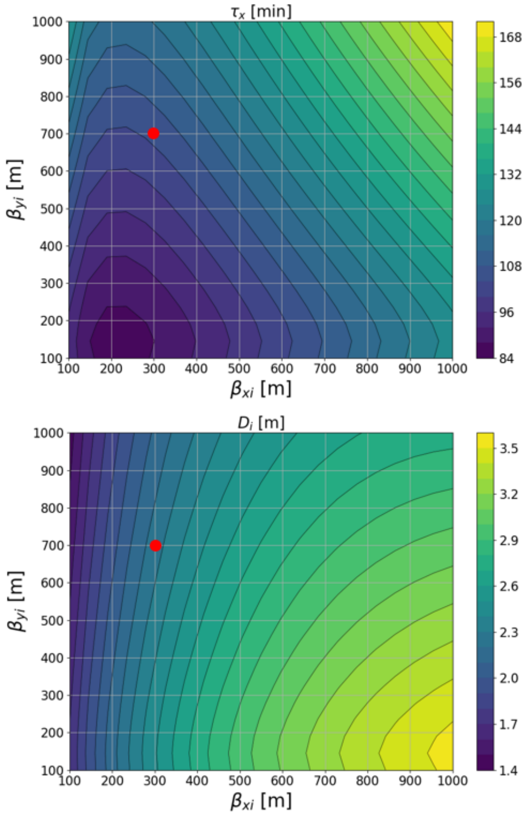

Figure 3: Optimization of protons parameters in the REC cooling section.

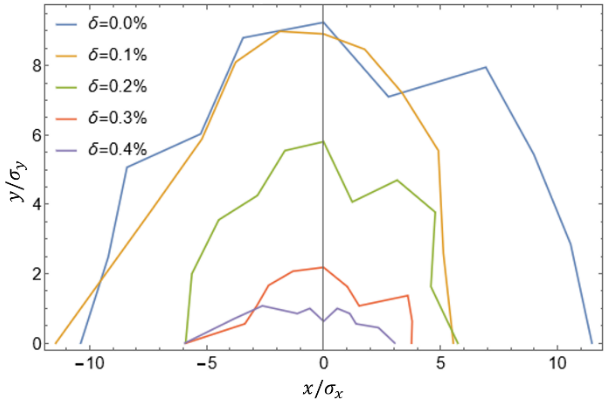

Figure 4: Dynamic aperture at various relative momenta.

REC SYSTEMS

Damping Wigglers

The wigglers parameters are listed in Table 1. The wigglers are inclined with respect to the axis of the wiggling section with an angle alternating in sign. This design produces dispersion in between the wigglers, which allows placing sextupoles for controlling chromatic effect.

Wigglers have small D_x and large D_x'. Thus, keeping small $\beta_x = 30$ cm allows to minimize H-function, respectively minimizing the IBS-driven emittance growth.

Figure 5 shows lattice and schematic layout of a part of the wiggler section.

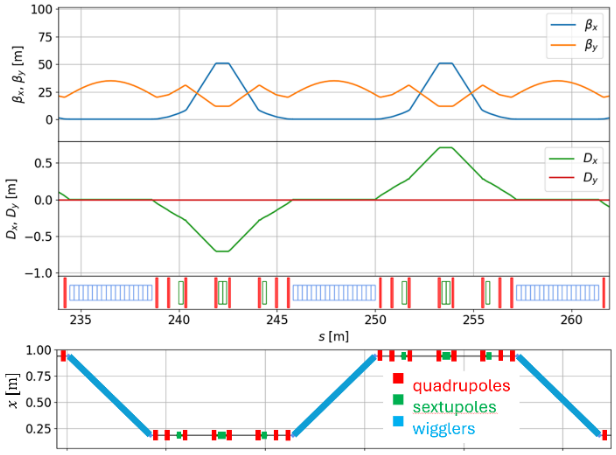

Figure 5: Lattice and magnets layout in the wiggler section.

A proper choice of wiggler field profile allowed us to minimize their contribution to the REC chromaticity.

Details of the wigglers design are given in [8,15,16].

RF system

The REC is utilizing a double RF system. Its main parameters are given in Table 1.

The REC RF produces a flat-top electron bunch, thus reducing its peak current and limiting the space charge effects. Simulations of beam dynamics with the REC double RF are described in [8].

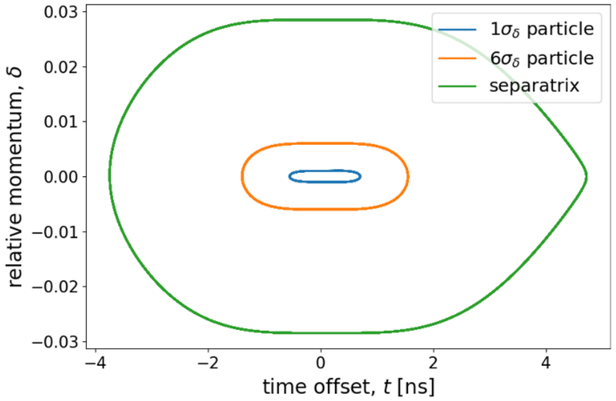

Figure 6: The REC RF bucket.

To compensate for the radiation loss of 6 kV/turn, the fundamental phase of the RF is shifted by 7.24 degrees. The resulting RF bucket is shown in Fig. 6. It corresponds to a flat-top e-bunch with FWHM length of 34 cm and $\sigma_\delta = 9.8 \cdot 10^{-4}$, as Fig. 7 demonstrates.

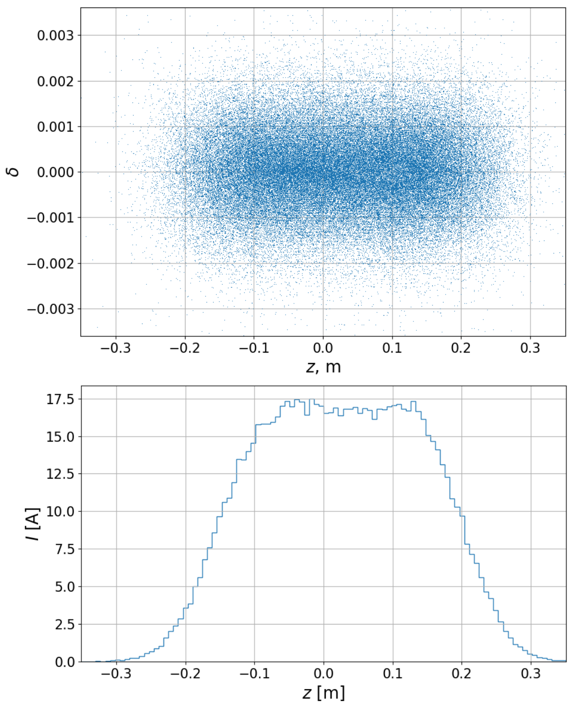

Figure 7: Longitudinal phase space and distribution of electron bunch in the REC RF bucket.

Injection System

The REC uses a top-off injection with a pulsed septum delivering the injected beam, and a closed four-bump fast kick moving the stored beam closer to the injected one (see Fig. 8). The overall length of the injection system is 2.5 m.

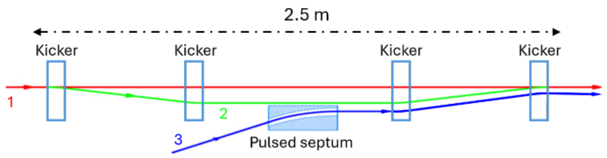

Figure 8: Schematic layout of the REC injection: 1 is an undisturbed stored beam, 2 is a stored beam with kickers on, 3 is an injected beam.

Parameters of the injection magnets are listed in Table 3.

Table 3: The REC Injection System

Parameter	**Kicker**	**Septum**
Maximum field [G]	760	7000
Magnetic length [m]	0.2	0.38
Pulse shape	trapezoid	sin
Rise/fall time [ns]	200	N/A
Flat-top duration [ns]	284	N/A
Wavelength [us]	N/A	200
Repetition rate [Hz]	3-5	

The injection time structure is driven by the beam lifetime, which is defined by the elastic scattering and is equal to 16.2 s (for 0.5 nTorr residual gas pressure). The top-off injection will be done into 1/5 of the ring with 3 Hz frequency.

The initial injection will have a 5 Hz frequency. The injector will provide 100 MHz trains of 28 bunches with charge of 1.75 pC per bunch.

Parameters of the injected and stored beams in the injection section are listed in Table 4.

Table 4: Stored and Injected Beam Parameters

Beam Parameter	**Stored**	**Injected**
β-function at septum [m]	60	20
Geometric emittance [nm]	8	5
Bunch charge [nC]	21	1.75

Transverse phase space of injected and stored beams, as well as transverse acceptance of the storage ring, are shown in Fig. 9.

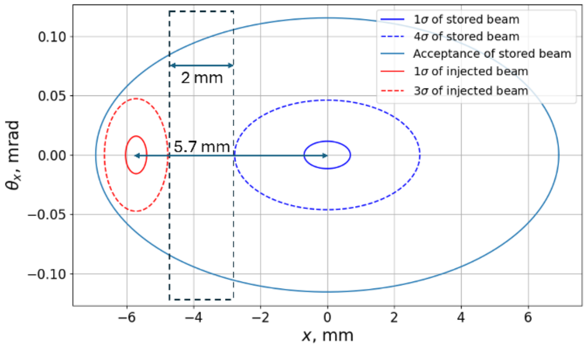

Figure 9: Injected and stored beams.

CONCLUSION

The Ring Electron Cooler is designed to cool the EIC proton beam at the top energy.

Optimization of the REC parameters allowed us to reduce electron bunch charge and average current by a factor of 2.3 as compared to [9], which helps with collective effects significantly. The space charge effect was farther reduced by employing a double RF system producing a flat-top electron bunch.

The realistic lattice for the REC compatible with the EIC Low Energy Cooler was developed and optimized. Good dynamic and momentum apertures were obtained for the lattice. The damping wigglers with realistic fields and optimized chromaticity contribution were developed.

Conceptual design of the injection system was devised. A detailed study of collective effects in the REC is left for future work.

REFERENCES

[1] S. Nagaitsev, “Electron-Ion Collider”, presented at the NAPAC'25, Sacramento, California, USA, Aug. 2025, paper MOXP01.

[2] G. I. Budker et al., “Experimental study of electron cooling”, Part. Accel. 7, 197 (1976). `https://cds.cern.ch/record/1021068/files/p197.pdf`

[3] S. Seletskiy et al., “Accurate setting of electron energy for demonstration of first hadron beam cooling with RF

ISBN: 978-3-95450-267-7 ISSN: 2226-0374 doi: 10.18429/JACoW-COOL2025-TUB1

accelerated electron bunches", Phys. Rev. Accel. Beams **21**, 111004 (2019). doi.org/10.1103/PhysRevAccelBeams.22.111004

[4] A. Fedotov et al., "Experimental demonstration of hadron beam cooling using radio frequency accelerated electron bunches", Phys. Rev. Lett. **124**, 084801 (2020). doi.org/10.1103/PhysRevLett.124.084801

[5] D. Kayran et al., "High brightness electron beams for linac based bunched beam electron cooling", Phys. Rev. Accel. Beams **23**, 021003 (2020). doi.org/10.1103/PhysRevAccelBeams.23.021003

[6] S. Seletskiy et al., "Obtaining transverse cooling with non-magnetized electron beam", Phys. Rev. Accel. Beams **23**, 110101 (2020). doi.org/10.1103/PhysRevAccelBeams.23.110101

[7] A. Fedotov, D. Kayran, S. Seletskiy, J. Kewisch, Y. Jing, and G. Wang, "Accelerator physics requirements and challenges of RF based electron cooler for EIC injection energy", in Proc. NAPAC'25, Sacramento, California, USA, Aug. 2025, pp. 346-350. doi:10.18429/JACoW-NAPAC2025-TUP003

[8] S. Seletskiy et al., "Ring Electron Cooler for Electron Ion Collider", BNL-228463-2025-TECH, 2025. https://www.osti.gov/servlets/purl/2573763

[9] H. Zhao et al., "Ring-based electron cooler for high energy beam cooling", Phys. Rev. Accel. Beams 24, 043501 (2021). doi.org/10.1103/PhysRevAccelBeams.24.043501

[10] S. Nagaitsev, "Intrabeam scattering formulas for fast numerical evaluation", Phys.Rev. STAccel.Beams 8, 064403 (2005). doi.org/10.1103/PhysRevSTAB.8.064403

[11] H. Zhao, M. Blaskiewicz, "Electron Heating by Ions in Cooling Rings", TUPLM24, NAPAC2019, Lansing, MI, USA, 2019. doi:10.18429/JACoW-NAPAC2019-TUPLM24

[12] S. Seletskiy, "Redistribution of cooling rates for electron bunch with nonuniform density", BNL-223860-2023-TECH, 2023. https://technotes.bnl.gov/PDF?publicationId=223860

[13] S. Seletskiy, "Beam-beam effects in EIC electron coolers", ICFA workshop: Beam-Beam Effects in Circular Colliders BB24, Lausanne, Switzerland, 2024. https://indico.global/event/9305/contributions/90682/attachments/41498/77715/eCoolBeamBeam.pdf

[14] J. Unger, A. Fedotov, G. Hoffstaetter, J. Kewisch, and S. Seletskiy, "Dynamic aperture correction for Ring Electron Cooler", in *Proc. NAPAC'25*, Sacramento, California, USA, Aug. 2025, pp. 426-429. doi:10.18429/JACoW-NAPAC2025-TUP031

[15] S. Seletskiy et al., "Optical properties of wigglers for EIC Ring Electron Cooler", BNL-225896-2024-TECH, 2024. https://technotes.bnl.gov/PDF?publicationId=225896

[16] S. Seletskiy, D. Kayran, G. Hoffstaetter, J. Unger, and J. Kewisch, "Optical properties of wigglers with high field-to-energy ratio", in Proc. NAPAC'25, Sacramento, California, USA, Aug. 2025, pp. 535-539. doi:10.18429/JACoW-NAPAC2025-TUP073

ISBN: 978-3-95450-267-7 ISSN: 2226-0374 doi: 10.18429/JACoW-COOL2025-TUC3

UV LASER SYSTEMS FOR COOLING RELATIVISTIC BUNCHED ION BEAMS AT THE SIS100

D. Schwarz[1], T. Grunwitz[1,2], J. Gumm[1], B. Langfeld[1,2], S. Klammes[3], D. Winters[3], T. Walther*[1,2]
[1] Institute of Applied Physics, Technical University of Darmstadt, Germany
[2] HFHF Campus Darmstadt, Department for Atomic and Plasma Physics, Germany
[3] GSI Helmholtzzentrum für Schwerionenforschung Darmstadt, Germany

Abstract

In this contribution, we present two high power ultraviolet (UV) laser systems and their integration for laser cooling at the heavy ion synchrotron SIS100 at FAIR (Facility for Antiproton and Ion Research).

The tunable continuous wave (cw) laser system operates at 257 nm, generated through two consecutive stages of second-harmonic generation (SHG), is optimized for long-term stability and high UV output power. Employing elliptical focusing in the second enhancement cavity, an output power exceeding 2.8 W in the UV could be demonstrated. Stable long-term UV generation is achieved at 2 W, ensuring reliable operation for extended experimental runs.

The pulsed laser system, also based on two frequency conversion stages, delivers more than 5 W of UV output power at 257 nm with a tunable frequency range exceeding 3 THz. The duration of the pulses is adjustable between 46–734 ps with repetition rates of 1–10 MHz, enabling synchronization with ion bunches.

Overall, we anticipate the use of three laser systems; the two detailed here as well as a second pulsed laser provided by the University of Dresden group. We present a scheme for precise spatial, temporal and energetic overlap of the three laser systems with the bunched ion beams.

INTRODUCTION

Laser cooling is a promising technique for achieving narrow longitudinal momentum distributions in relativistic, bunched ion beams, which is essential for high-precision experiments at modern accelerator facilities such as the heavy ion synchrotron SIS100 at FAIR. For the SIS100, laser cooling is the only intended beam cooling method.

In theory, relative longitudinal momentum spreads of $\Delta p/p = 10^{-7}$ can be achieved [1]. Laser cooling has been successfully demonstrated at the Experimental Storage Ring (ESR) at GSI using both continuous wave (cw) and pulsed laser systems individually [2, 3]. For fast and efficient cooling, three laser systems will be operated simultaneously [4]. The two pulsed lasers, with spectral widths of several hundred GHz, will cover a broad range of ion velocities. The cw laser, with an instantaneous linewidth of less than 1 MHz, will cool the ions near their ideal velocity [5].

Reliable operation of these systems requires broad tunability of the laser frequencies as well as high and stable output powers in the green (514 nm) and UV (257 nm), as both wavelengths can be used for laser cooling at the SIS100 [5].

CONTINUOUS WAVE LASER SYSTEM

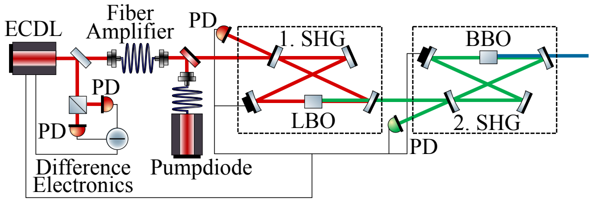

Figure 1: Simplified setup of the cw laser system.

The cw laser system (cf. Fig. 1) consists of an external cavity diode laser (ECDL) emitting a fundamental wavelength of 1028 nm. To avoid mode hops of the ECDL, a polarization based locking scheme adapting the current is implemented [6]. The infrared (IR) light is amplified in an ytterbium doped fiber amplifier up to 37 W, which is only limited by the fiber damage threshold.

Frequency conversion is employed to convert the IR light into the green and then the UV spectral range. The first second-harmonic generation (SHG) is realized in a spherical enhancement cavity in a bow-tie configuration employing a 15 mm long lithium triborate (LBO) crystal non-critically phase-matched by temperature. With up to 95 % mode-matching efficiency and a Pound-Drever-Hall (PDH) locking scheme [7] implemented using the open source software PyRPL [8], an output power of 25.2(6) W at 514 nm is achieved with conversion efficiencies up to 70 %. To ensure reliable operation, an automated relocking system is embedded.

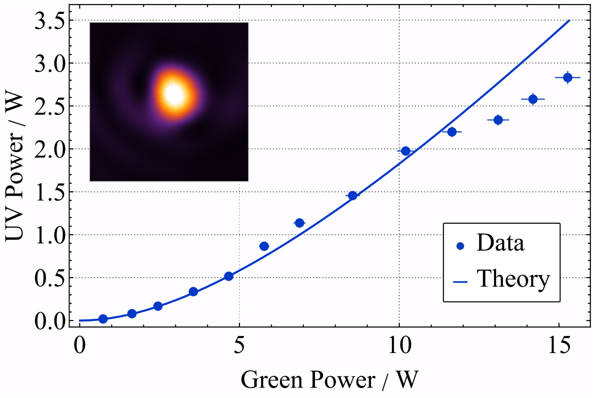

Figure 2: UV output power of the elliptical focusing enhancement cavity against the power of the fundamental green light. The dots mark the measured data, the line the corresponding theory according to Steinbach et al. [9]. The inset shows the corresponding beam profile at 2 W in the UV.

---

* thomas.walther@physik.tu-darmstadt.de

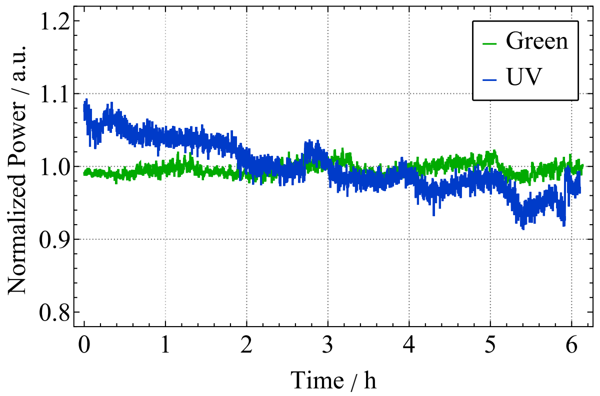

Figure 3: Long-term normalized power measurement of the cw laser over 6 h with mean powers of 15 W in the green and 2 W in the UV.

The second enhancement cavity uses an elliptical focus in a 10 mm long β-barium borate (BBO) crystal, which is one of the most common nonlinear media for frequency conversion into the UV spectral range. BBO crystals are prone to irreversible degradation due to two-photon absorption (TPA) scaling with the square of the intensity [10]. To decrease this effect, we developed an elliptical focusing enhancement cavity to reduce the intensity inside the crystal while maintaining a high conversion efficiency [11]. The focus is 21 µm in the non-walk-off direction and 577 µm in the walk-off direction of the BBO crystal. In addition, the BBO crystal is heated to 150 °C and has a protective anti-reflective coating. Hence an output power of 2.83(7) W in the UV spectral range is achieved, as shown in the power slope in Fig. 2. The measured data agrees with the theory for output powers up to 2.2 W, the slight deviations for higher output powers arise from thermal effects due to the high circulating power in the cavity. The heating of the crystal and the output coupler causes a slight misalignment of the cavity and thus a loss of output power. Systems with a spherical focus regularly experience degradation of the crystal with much less power [12].

The strong elliptical focus in the BBO crystal results in an elliptical beam profile in the UV spectral range. This is compensated by cylindrical lenses (cf. beam-profile at 2 W in the UV; inset of Fig. 2).

The long-term stability at high output powers is an essential characteristic of the cw laser system in order to ensure reliable laser cooling. In the green spectral range, a stable average power of 15 W with a standard deviation of 0.8 % is maintained over about 6 h, as shown in Fig. 3 (normalized data). Figure 3 shows the UV output of 2 W over 6 h. The standard deviation is slightly higher compared to the green spectral range with 3.5 % due to the decrease of power over time. This decrease is caused by thermal dephasing caused by the high circulating power in the cavity, as described before. At 2.7 h and 5.9 h the cavity performs an automatic relock and the UV power increases as a result of the missing heating effect. This behavior confirms the thermal effects within the UV cavity and shows that the BBO crystal is not degrading [13].

PULSED LASER SYSTEM

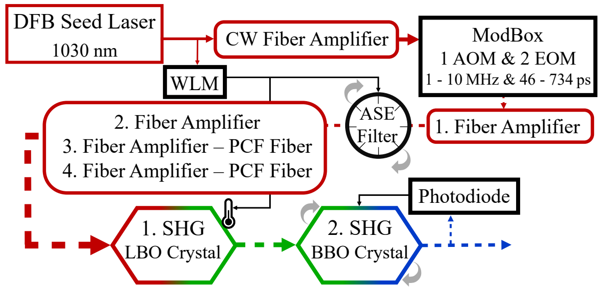

Figure 4: Schematic setup of the pulsed laser system.

The pulsed laser system consists of a cw distributed-feedback (DFB) laser diode allowing mode hop free tuning over 3 nm with a central wavelength of 1029.6 nm by adjusting the temperature of the diode in combination with a wavelength meter (WLM).

After a cw fiber amplifier stage, pulses are generated in a Modulator Box (ModBox) using an acousto-optic modulator and two electro-optic modulators driven by an arbitrary function generator (AFG). This setup provides adjustable pulse durations between 46 ps and 734 ps with repetition rates from 1 MHz to 10 MHz, with optimal operation at 112 ps and 10 MHz [14]. The Fourier-transform limited pulses are further amplified in four consecutive fiber amplifier stages, two of which use photonic crystal fibers (PCF), to an average power of about 57 W of IR light at a repetition rate of 10 MHz, independent of the pulse duration. Two narrow-band filters after the first pulsed amplifier suppress amplified spontaneous emission (ASE).

Frequency conversion is performed in two single-pass SHG stages. The first stage is a 15 mm long non-critically phase matched LBO crystal, producing up to 34(1) W of average green power, depending on the pulse duration at 10 MHz (see Table 1). In the second critical phase matched SHG stage, averaged UV output powers of up to 5.3(1) W can be obtained using a dual BBO setup implemented for frequency tuning, whereas the setup with one 10 mm long crystal leads to 4.1(1) W average power with an elliptical focus of 25.5 µm×622 µm to avoid degradation of the crystal.

Continuous tuning requires several adjustments throughout the pulsed laser system [15]. When the wavelength is tuned, the narrow-band filters for the ASE suppression must be realigned, using a motorized stage operated in a feed-forward control-loop.

Table 1: Output powers for different pulse durations of the pulsed laser system with a fundamental IR power of approximately 57 W and 10 MHz repetition rate.

Pulse Duration	Average Power	
	514 nm	257 nm
734 ps	17.1(4) W	0.60(2) W
112 ps	34(1) W	5.3(1) W
46 ps	30.4(9) W	2.10(5) W

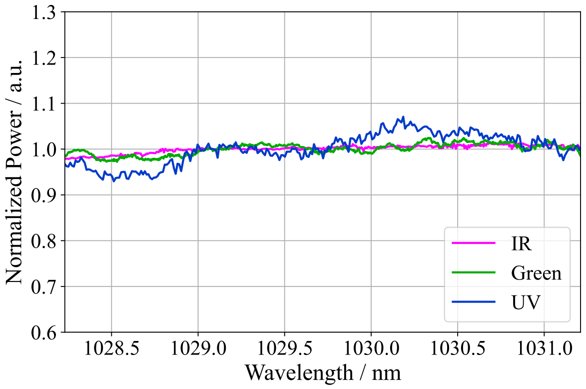

Figure 5: Normalized power in the IR, green and UV spectral range when tuning the pulsed laser system over 3.4 THz in the UV. The mean powers are 28.3 W in the green and 1.4 W in the UV.

Since for the frequency conversion, both crystals are phase-matched for a fixed wavelength, detuning leads to a phase mismatch and therefore less output power. For the non-critically phase-matched LBO crystal, the temperature is adapted using a feed-forward control-loop based on the measured IR wavelength, enabling a tuning rate of 0.02 nm/s across the 3 nm range in the IR. In the second SHG stage, the BBO crystal angle is actively optimized using a gradient algorithm with the UV output power as the feedback signal. With these adjustments, a tuning range of 3.4 THz in the UV is reached while maintaining a stable output power over the whole range (see Fig. 5). The UV power has a standard deviation of 3.3 %, primarily caused by fluctuations of the green power and the quadratic dependency of the conversion.

Beam displacement in the UV remains a challenge during wavelength tuning due to the change of the angle of the BBO crystal. A setup using two 7 mm long BBO crystals with inverted optical axes (see Fig. 6) compensates the displacement introduced by the first BBO crystal [16]. This configuration not only leads to an improved beam stability but also provides a maximum UV output of 5.3(1) W average power compared to 4.1(1) W obtained with a single BBO crystal due to the higher effective crystal length.

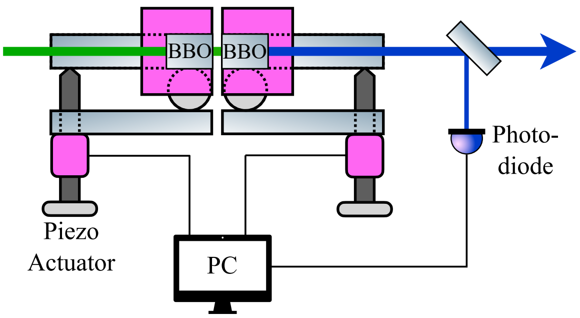

Figure 6: Schematic setup of the second SHG stage using two BBO crystals to reduce the beam displacement during frequency tuning of the pulsed laser.

ALIGNMENT FOR OPERATION AT THE SIS100

Efficient and effective laser cooling at the SIS100 requires the simultaneous operation of three laser systems [4]. It is crucial to align these laser systems in terms of energy, timing, and space to achieve effective laser cooling. The photon energy is set by tuning the frequency of the laser system and then locking the system to a wavelength meter. Proper timing between laser pulses and ion bunches is achieved by driving the pulsed lasers with an AFG synchronized to the bunching frequency. Finally, the three laser beams must overlap spatially with the ion beam. This is particularly critical at the SIS100, where even a small misalignment causes significant differences in the beam position due to the large distance of 60 m between the laser systems and the 22 m long interaction zone. Therefore, the overlap of three laser beams was characterized in a mock set-up in our laboratory, using both green and UV light simulating the large distance by folding the beam with the help of several mirrors. The different wavelengths require different setups due to different available powers and ion saturation intensities [1].

For either wavelength, two laser beams were combined via polarization, while the third was overlapped geometrically at a small angle of about 0.01°. The main difference lies in the beam size in the interaction zone, so that for the UV spectral range higher intensities can be attained. Figures 7 and 8 show the overlap regions of the lasers (pink) and the 22 m long interaction zone with the ions (gray). The diameters of the green laser beams matches the diameter of the ion beams, which is about 1 cm, and cover almost the whole interaction zone. The UV laser beams have a focus of 2–3 mm in diameter in the interaction zone. Considering the long-term stable output power of 2 W of the cw laser system, this leads to an intensity of 64 W/cm^2 in the focus. The pulsed laser system has a UV power of about 5 W leading to an intensity of 160 W/cm^2 in the interaction zone. Higher intensities can be reached by reducing the focus size in the interaction zone, but the sweet spot between high laser intensity and a good

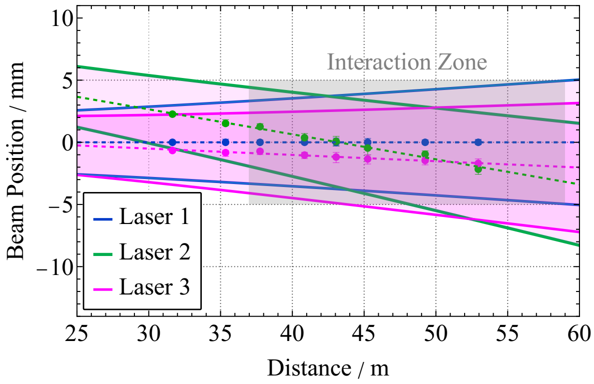

Figure 7: Spatial overlap using three green laser beams. The data and dashed lines mark the relative center position of each laser beam, the solid lines mark the Gaussian beam profile of each laser beam. Both were determined using a WinCam. Note the different scales on x- and y-axes.

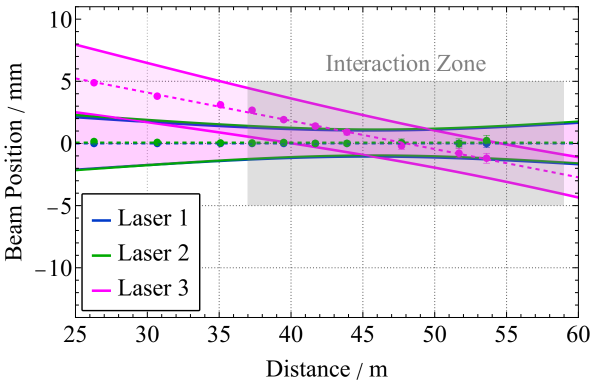

Figure 8: Measured spatial overlap using three laser beams in the UV. The measurement procedure was as described in Fig. 7. Please note the different scales on *x*- and *y*-axis.

spatial overlap needs to be determined experimentally, since the smaller the laser beams the worse the spatial overlap.

As well as the spatial overlap, the spatial stability of the laser beams is important. Even though the pulsed laser system has a reduced beam displacement with the dual BBO setup, there are still fluctuations in the beam position due to temperature fluctuation, air pressure variations and mechanical movements. The fluctuations can be reduced using a commercial active beam stabilization system by about 75 % at a distance of 50 m in our mock setup [13].

CONCLUSION

The cw laser system provides high output powers in the green and UV spectral range with long-term stability. In the green spectral range, a standard deviation of only 0.8 % at an average power of 15 W demonstrates highly stable operation. In the UV spectral range, the long-term stability at 2 W with a standard deviation of 3.5 % is only limited by thermal effects due to the high circulating power in the cavity, rather than by degradation of the BBO crystal. Using the elliptical focusing enhancements cavity, a UV power of 2.83(7) W is achieved without degradation of the crystal.

The pulsed laser system provides Fourier-transform limited pulses with adjustable pulse durations from 46 ps to 734 ps and repetition rates between 1 MHz and 10 MHz, with optimal performance at 112 ps and 10 MHz. It generates about 57 W of IR power independent of the pulse duration. Output powers of up to 34(1) W in the green and 5.3(1) W in the UV spectral range are reached. Additionally, the system demonstrates a stable output over a tuning range of 3.4 THz in the UV, reducing the beam displacement employing a dual BBO setup with an active control.

Future work will focus on improving the long-term stability of both laser systems. For the cw laser, this will require reducing thermal dephasing further in the second enhancement cavity. For the pulsed system, additional measures like a different focus in the BBO crystal will be implemented to enhance long-term output stability.

ACKNOWLEDGMENTS

The authors would like to thank the Bundesministerium für Forschung, Technologie und Raumfahrt (funding ID: 05P21ROFA1 and 05P24RD5) as well as HFHF Darmstadt for the funding of this project.

REFERENCES

[1] L. Eidam, O. Boine-Frankenheim, and D. Winters, “Cooling rates and intensity limitations for laser-cooled ions at relativistic energies”, *Nucl. Instrum. Methods Phys. Res. A*, vol. 887, pp. 102–113, 2018. `doi:10.1016/j.nima.2018.01.038`

[2] D. Winters *et al.*, “Laser cooling of relativistic heavy-ion beams for FAIR”, *Phys. Scr.*, vol. T166, p. 014 048, 2015. `doi:10.1088/0031-8949/2015/T166/014048`

[3] B. Langfeld, “Breitbandige Laserkühlung relativistischer Ionenstrahlen: Erste Experimente und Weiterentwicklung des UV-Lasers”, Dissertation, Technische Universität Darmstadt, 2025.

[4] D. Winters *et al.*, “Laser cooling taken to the extreme: Cold relativistic intense beams of highly-charged heavy ions”, in *Proc. IPAC’23*, pp. 1314–1318, 2023. `doi:10.18429/JACoW-IPAC2023-TUOGA2`

[5] SPARC Collaboration, “Technical report for the design, construction and commissioning of the SPARC laser systems for laser cooling at the FAIR SIS100”, Tech. Rep., 2020.

[6] T. Führer, S. Euler, and T. Walther, “Model for tuning an external-cavity diode laser by polarization locking”, *J. Opt. Soc. Am. B*, vol. 28, pp. 508–514, 2011. `doi:10.1364/JOSAB.28.000508`

[7] R. Drever *et al.*, “Laser phase and frequency stabilization using an optical resonator”, *Appl. Phys. B*, vol. 31, pp. 97–105, 1983. `doi:10.1007/BF00702605`

[8] L. Neuhaus *et al.*, “PyRPL (Python Red Pitaya Lockbox) — an open-source software package for FPGA-controlled quantum optics experiments”, in *Proc. CLEO/Europe–EQEC*, 2017. `doi:10.1109/CLEOE-EQEC.2017.8087380`

[9] A. Steinbach, M. Rauner, F. Cruz, and J. Bergquist, “CW second harmonic generation with elliptical Gaussian beams”, *Opt. Commun.*, vol. 123, pp. 207–214, 1996. `doi:10.1016/0030-4018(95)00626-5`

[10] M. Rumi and J. Perry, “Two-photon absorption: An overview of measurements and principles”, *Adv. Opt. Photonics*, vol. 2, pp. 451–518, 2010. `doi:10.1364/AOP.2.000451`

[11] J. Gumm, D. Schwarz, and T. Walther, “High power UV lasers employing elliptically focusing enhancement cavities”, *Rev. Sci. Instrum.*, vol. 96, p. 033 003, 2025. `doi:10.1063/5.0253513`

[12] D. Preißler, D. Kiefer, T. Führer, and T. Walther, “Evolutionary algorithm-assisted design of a UV SHG cavity with elliptical focusing to avoid crystal degradation”, *Appl. Phys. B*, vol. 125, p. 220, 2019. `doi:10.1007/s00340-019-7333-6`

[13] J. Gumm, “Leistungsfähiger Dauerstrich UV Laser zur Kühlung hochrelativistischer Ionen”, Dissertation, Technische Universität Darmstadt, 2025.

[14] D. Kiefer, S. Hepp, and T. Walther, “High average power transform limited picosecond laser with flexible repetition rate and pulse duration”, *Opt. Lett.*, vol. 45, pp. 4488–4491, 2020. `doi:10.1364/OL.397893`

[15] B. Langfeld, T. Grunwitz, and T. Walther, “High-power, tunable ps-UV-laser system for laser cooling of relativistic ion beams”, *Opt. Lett.*, 2025.

[16] S. C. Kumar, J. Casals, J. Wei, and M. Ebrahim-Zadeh, “High-power, high-repetition-rate performance characteristics of β-BaB_2O_4 for single-pass picosecond ultraviolet generation at 266 nm”, *Opt. Express*, vol. 23, no. 21, pp. 28 091–28 103, 2015. `doi:10.1364/OE.23.028091`

ISBN: 978-3-95450-267-7 ISSN: 2226-0374 doi: 10.18429/JACoW-COOL2025-TUD1

SCHOTTKY SPECTRA OF LASER-COOLED BUNCHED ION BEAMS: SIMULATIONS AND RECENT EXPERIMENTAL RESULTS FROM THE CSRe*

H. B. Wang[1,2], D. Y. Chen[3], Y. J. Yuan[1,2], W. Q. Wen[1,2,†], Z. K. Huang[1,2], D. C. Zhang[4], D. Winters[5], S. Klammes[5], D. Kiefer[6], Th. Walther[6,7], M. Loeser[8], M. Siebold[8], U. Schramm[8,9], L. J. Mao[1,2], J. Li[1,2], M. T. Tang[1,2], J. X. Wu[1,2], Q. Wang[1,2], X. L. Yan[1,2], D. Y. Yin[1,2], J. C. Yang[1,2], M. Bussmann[8,10], and X. Ma[1,2,‡]

[1] Institute of Modern Physics, Chinese Academy of Sciences, Lanzhou, China
[2] University of Chinese Academy of Sciences, Beijing, China
[3] School of Physics and State Key Laboratory of Nuclear Physics and Technology, Peking University, Beijing, China
[4] School of Optoelectronic Engineering, Xidian University, Xi'an, China
[5] GSI Helmholtzzentrum für Schwerionenforschung GmbH, Darmstadt, Germany
[6] Institut für AngewandtePhysik, Technische Universität Darmstadt, Darmstadt, Germany
[7] Helmholtz Research Academy Hesse for FAIR, Campus Darmstadt, Darmstadt, Germany
[8] Helmholtz-Zentrum Dresden-Rossendorf, Dresden, Germany
[9] Technische Universität Dresden, Dresden, Germany
[10] Center for Advanced Systems Understanding, Görlitz, Germany

Abstract

Schottky spectra of longitudinal bunched ion beams are not as well studied as those of coasting ion beams. Much less is known about what they actually exhibit and how this should be interpreted. At the storage ring CSRe, we have systematically studied the longitudinal dynamics of O^{5+} ion beams by means of Schottky analysis. Besides, a multi-particle tracking code using a differential equation model has been developed to simulate the longitudinal Schottky spectra of bunched ion beams. Based on the experimental and simulation results, we propose a novel method to extract the longitudinal momentum distribution from the Schottky spectra of the bunched ion beams. In addition, we have systematically investigated the Schottky spectra of bunched Kr^{30+} ion beams both experimentally and by simulations, and provide a detailed interpretation of the extremely strong central peak caused by the coherent effect.

INTRODUCTION

In storage rings, longitudinal bunched ion beams are produced by applying a sinusoidal voltage through an RF-buncher, which longitudinally modulates the coasting ion beams. This bunching process is essential for manipulating the longitudinal properties of ion beams, such as accelerating or decelerating beam energy, reducing their longitudinal spatial size, and achieving higher spatial density and luminosity [1]. Nowadays, bunched ion beams have been widely used for experiments at storage rings, such as precision laser spectroscopy experiments [2, 3] and collision experiments [4, 5].

In these experiments, a Schottky detector plays a major role in measuring the longitudinal momentum spread of the bunched ion beams [6], which is one of the most important parameters for beam cooling and precision spectroscopy experiments. However, Schottky spectra of bunched ion beams are very complex, and many simulations have been performed to understand such Schottky spectra. For instance, Betz et al. theoretically analyzed the characteristics of longitudinal Schottky spectra for bunched ion beams recorded at the LHC [7]. Lasocha et al. provide a method to extract the longitudinal and transverse bunch characteristics in the LHC using Schottky-based diagnostics [8,9]. Boine-Frankenheim and Hofmann et al. simulated the Schottky spectra of high-intensity bunched ion beams by considering the influence of the space charge effects [10, 11]. Bussmann et al. simulated Schottky spectra of laser-cooled weakly coupled ion beams in the equilibrium state between heating due to intra-beam scattering and cooling by a laser force [12]. Hasse and Danared et al. successfully explained the anomalous reduction of the longitudinal temperature and Schottky-noise power for the very weak ion beam during the electron cooling process [13, 14]. Even though these simulations provide the fundamental basis for understanding the Schottky spectrum of bunched ion beams, there are still some open questions, such as what causes the greatly enhanced power of the central peak in Schottky spectra and how to extract the momentum distribution of the bunched ions from a Schottky spectrum.

In this paper, we present our experimental and simulation studies to answer these open questions. Both O5+ and Kr30+ ions were used to study the Schottky spectrum of longitudinal bunched ion beams at the experimental Cooler Storage Ring (CSRe) [15]. A multi-particle tracking code

---

* Work supported by NSFC No. 12375152, No.11905269, the Center for Advanced Systems Understanding (CASUS) which is financed by Germany's Federal Ministry of Education and Research (BMBF), and the Saxon state government out of the State budget approved by the Saxon State Parliament.

† wenweiqiang@impcas.ac.cn
‡ x.ma@impcas.ac.cn

ISBN: 978-3-95450-267-7 ISSN: 2226-0374 doi: 10.18429/JACoW-COOL2025-TUD1

using the differential equation model was developed to simulate the longitudinal Schottky spectra of stored bunched relativistic ion beams at storage rings. Based on the simulations, the coherent effect was systematically studied, and a novel method was proposed to extract the longitudinal momentum distribution from the Schottky spectrum of the bunched ion beams.

EXPERIMENTAL SETUP

Laser cooling experiment of bunched O5+ ion beams was carried out at the storage ring CSRe at the Institute of Modern Physics (IMP) in Lanzhou, China [15]. The schematic view of the laser cooling experimental setup and parameters is shown in Fig. 1. The beam energy is 275.7 MeV/u, corresponding to an ion velocity of about 64% of the speed of light. The O5+ ion beams were longitudinally modulated by a multi-harmonic RF-buncher. A counter-propagating CW laser beam with a wavelength of 220 nm was employed to resonantly excite the 2s1/2 - 2p1/2 transition of O5+ ions, and achieve laser cooling by combining with the RF-buncher. The longitudinal Schottky spectra were recorded by employing a Schottky resonator, as shown in Fig. 1(a), to investigate the laser cooling process and measure the momentum distribution of the laser-cooled bunched O5+ ion beams.

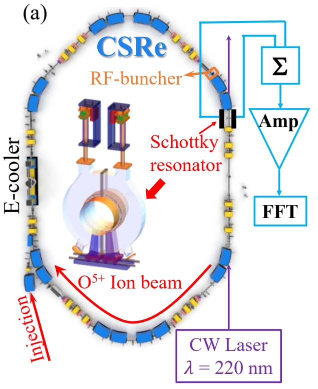

(b)

CSRe parameters	
Circumference	128.80 m
Ion species	$^{16}O^{5+}$
Beam energy	275.7 MeV/u
Relativistic β, γ	0.636, 1.296
Revolution frequency $f_{\rm rev}$	1.48 MHz
Transition energy γ_t	2.626
Slip factor η	0.45
Beam lifetime	~35 s
Bunching harmonic h_b	33
cw laser system	
Laser wavelength	$\lambda_{\rm laser} = 220$ nm
Laser power	$P_{\rm laser} = 40$ mW
Cooling transition	
$2s_{1/2} \rightarrow 2p_{1/2}$	$\lambda_{\rm rest} \approx 103.76$ nm

Figure 1: (a) Schematic view of the storage ring CSRe, showing the RF-buncher, the Schottky resonator, and the laser beam. Schematic drawing of the Schottky resonator is shown in the center of the figure. (b) Parameters for the laser cooling experiment of O^{5+} ion beams at the CSRe.

SIMULATION METHOD

The longitudinal motion of each individual ion in the bunch can be tracked by using the following set of coupled differential equations [16]:

$$\begin{cases} \dot{\delta} = \frac{frev}{\beta^2 E} \cdot qeU_b \cdot (\sin\varphi - \sin\varphi_s) \\ \dot{\varphi} = 2\pi h_b f_{rev} \eta \delta \end{cases} \quad (1)$$

where δ is the relative momentum difference of the ion compared to the synchronous ion, f_{rev} the revolution frequency of the ion, β the the relativistic factor, E the kinetic energy of the ion, qe the charge of the ion, U_b the effective bunching voltage, φ the rf phase of the ion, φ_s the rf phase for a synchronous particle, h_b the RF-bunching harmonic, η the slip factor. The momentum and phase at any time can be calculated by solving Eq. (1) with a given initial momentum and phase distribution.

We have developed a simulation code based on the multi-particle tracking method to simulate the longitudinal Schottky spectra of bunched ion beams. The flow chart of the simulation code is shown in Fig. 2. The first step is to input all the parameters relevant to the storage ring, the ion beam, and the RF-buncher. The second step is to initialize the momentum and phase for each ion. These input parameters are based on the laser cooling experiment of O5+ ions at the CSRe [15]. The third step is to solve the differential equations (1) to obtain the momentum and phase for each ion in each period until reaching the final period. Following this, the phase space is divided into several sections with equal intervals, and the number of ions in each section is counted to obtain the phase distribution of all ions. Subsequently, a Kaiser window is applied to reduce the spectral leakage caused by the finite length in the time region, and an FFT is performed to generate the Schottky spectrum of bunched ion beams. Then the final result is output.

The simulation code is written in MATLAB, and the simulation code is parallel to minimize the simulation time. In the simulation, the ions number is chosen to be 50000, the revolution number is 218 turns, and each revolution period is divided into 211 parts for FFT. To decrease the fluctuations caused by the random distribution generator used in the simulation code, we averaged the simulation results 20 times.

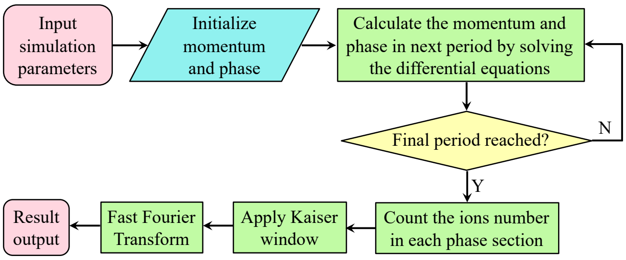

Figure 2: Flow chart of the simulation code for the longitudinal Schottky spectrum of bunched ion beams.

Based on this simulation code, we simulated the longitudinal Schottky spectra of bunched O5+ ion beams with different phase-space distributions, and the results are shown in Fig. 3. The ion distributions in phase space are shown in Figs. 3(a1) & (a2). The synchronous oscillation time amplitudes within the bucket are assumed to follow a Rice distribution, which was proved in the previous experiment [8]. The center value is chosen to be 0 ns, and the standard deviations σ are 0.5 ns and 2 ns, respectively. The phases of the ions are randomly distributed from 0 to 2π. With the standard deviation σ increasing from Figs. 3(a1) to (a2), the phase space density decreases, and the relative momentum spread of the ion beams becomes broader, as shown in Figs. 3(b1) & (b2). The corresponding simulated Schottky spectra are plotted in Figs. 3(c1) & (c2). Multi-bunches (33 bunches) in the storage ring, with all the ions randomly distributed in these bunches, are used in the simulation. The observation frequency of the Schottky resonator is chosen to be 242758 kHz, which is the 164th harmonic of the revolution frequency (1.48 MHz) of the O5+

ISBN: 978-3-95450-267-7 ISSN: 2226-0374 doi: 10.18429/JACoW-COOL2025-TUD1

ions in the CSRe. The Schottky observation frequency is non-integer multiples of the bunching frequency, resulting in the central peaks not coherently enlarged [17, 18].

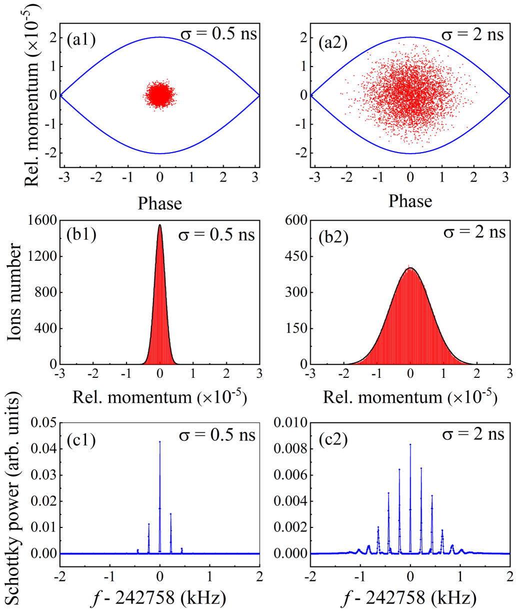

Figure 3: Simulated longitudinal Schottky spectra of bunched O^{5+} ion beams with different phase-space distributions. (a) The distribution of the ions (red points) in phase space, and the blue line is the separatrix of the RF-bucket. (b) The relative momentum distributions of the ion beams. (c) The corresponding simulated Schottky spectra.

SCHOTTKY SPECTRA OF LASER-COOLED O^{5+} ION BEAMS

Systematic investigations of longitudinal dynamics of the laser-cooled bunched ion beams are shown in Fig. 4. Figs. 4(a1)-(a3) are the experimentally measured Schottky spectra. The width of the Schottky sideband distributions clearly narrows as the laser gets closer to the center of the bucket, as shown in these figures. Therefore, the momentum spread of the ion beam also decreases in this process. The simulated Schottky spectra shown in Figs. 4(b1)-(b3) have a similar shape to the experimentally measured ones, helping us understand the laser cooling process and the real laser cooling effects for different cooling parameters.

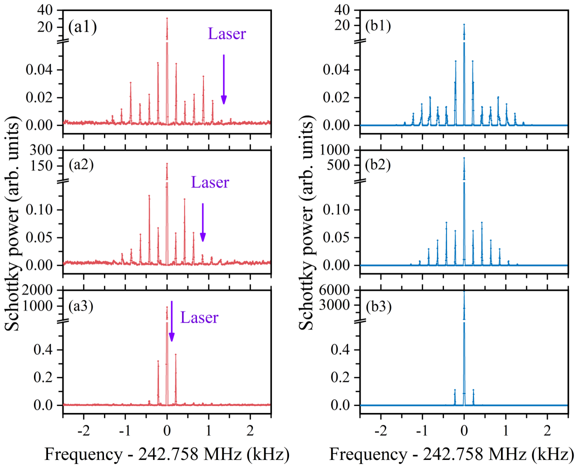

Figure 4: (a) Experimental measured Schottky spectra with different laser positions. (b) Simulated Schottky spectra by using the corresponding parameters in figure (a).

NOVEL METHOD TO EXTRACT THE MOMENTUM DISTRIBUTION

Precise measurement of the longitudinal relative momentum distribution is extremely important in beam cooling experiments since it will help achieve optimal cooling effect and thus obtain better experimental results. The most commonly used method in previous works [10, 19] was to fit the envelope of the Schottky sidebands, normally using a Gaussian fitting. The comparison between the relative momentum distributions and the fitted envelope of the simulated Schottky sidebands is shown in Fig. 5. In Fig. 5(a), the fitted envelope reproduces the relative momentum distribution fairly well, indicating that the envelope-fitting method can provide a reasonable extraction of the relative momentum distributions. When the relative momentum distributions become broader, as shown in Fig. 5(b), the fitted envelope is narrower than the relative momentum distributions, and this deviation is very significant. Consequently, the envelope-fitting method is only suitable for quick and approximate extraction of the momentum distributions for bunched ion beams.

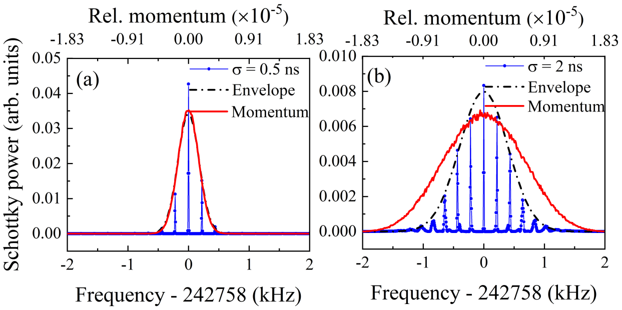

Figure 5: Comparison of the envelope (black dash dotted line) of simulated Schottky spectra (blue dotted line) and the momentum distributions (red line) of bunched O^{5+} ion beams. A Gaussian fit is applied in these figures to illustrate the envelope of the Schottky sidebands in a straightforward manner. For direct comparison with the relative momentum distribution, the upper horizontal axis of each spectrum is additionally labeled in units of longitudinal momentum. The Schottky spectra are from Figs. 3(c1) & (c2), and the relative momentum distributions are from Figs. 3(b1) & (b2).

We propose a novel method to precisely extract the momentum distributions by calculating the total Schottky power of each sideband [20]. The sketch map of this method is shown in Fig. 6. By adding up the Schottky power of all the points in each sideband, as shown in Fig. 6(a), a distribution between the total Schottky power of each sideband and the relative momentum could be given as shown in Fig. 6(b). Fig. 7 presents a comparison of the calculated results and the corresponding actual relative momentum distributions used in the simulation. The close agreement between these two curves demonstrates that the relative momentum distribution of the bunched ion beams

ISBN: 978-3-95450-267-7 ISSN: 2226-0374 doi: 10.18429/JACoW-COOL2025-TUD1

can be accurately described by the novel method we proposed. Due to its simplicity and accuracy, it is the most ideal method for extracting momentum spread, and therefore well suited for detailed studies of cooling dynamics and for the optimization of cooling efficiency in future beam cooling experiments. Here, we need to mention that in real experiments, the non-cooled background ions and the ions outside of the rf-bucket will also affect the measured Schottky spectra, and thus should be carefully taken into account. Systemically studies of the influence of these ions are in progress.

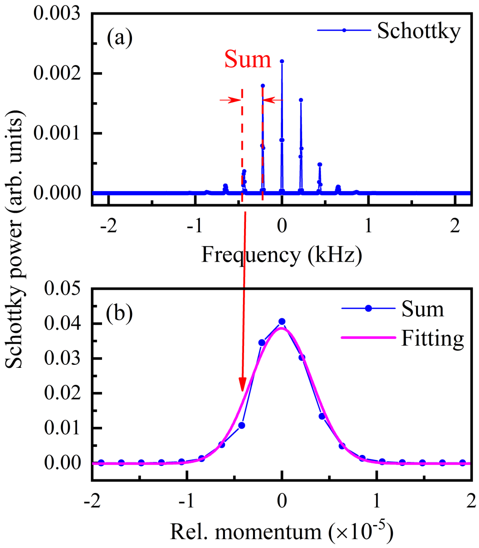

Figure 6: The sketch map of the novel method we proposed to extract the relative momentum distribution (b) from the Schottky spectrum (a) of the bunched O^{5+} ion beams by calculating the total Schottky power of each sideband. Each Schottky sideband in figure (a) is summed and shown as a blue point in figure (b).

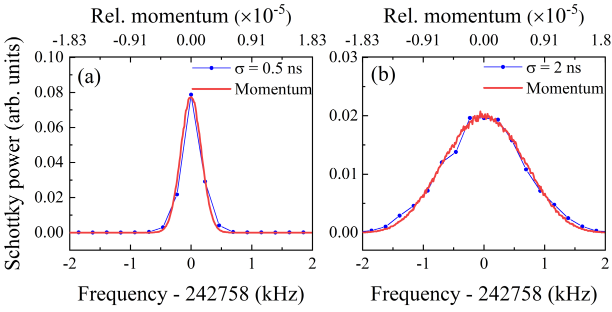

Figure 7: Comparison of the total Schottky power of each sideband (blue dotted line) calculated from Fig. 3(c1) & (c2) and the relative momentum distributions (red line) of bunched O^{5+} ion beams from Fig. 3(b1) & (b2).

COHERENT EFFECT OF LONGITUDINAL BUNCHED Kr^{30+} ION BEAMS

The Schottky spectra of bunched ion beams has a very puzzling phenomenon: the power of the central peak exhibits significant variability, sometimes being orders of magnitude higher than that of the sidebands, e.g. in the laser cooling experiment of bunched O5+ ions at the storage ring CSRe [15], while at other times, this difference is absent, such as in the experiments of bunched C3+ ions at both the ESR and CSRe [12, 21]. A similar phenomenon was observed in the stochastic cooling experiments at Fermilab [22] and RHIC [23], where the powerful central peak only appeared on the rf-bunching frequency harmonics. To interpret this phenomenon, systematic experimental and simulation studies of Schottky spectra for bunched Kr30+ ion beams with an energy of 100 MeV/u were performed at CSRe. The mean revolution frequency of the Kr30+ ions in the CSRe was 1.00 MHz. The observation frequency of the Schottky resonator was chosen to be the 240th harmonic of the revolution frequency, while the RF-bunching harmonics were 40, 42, 48, and 49, respectively.

We compared the temporal decay of the experimental Schottky power of both the central peak and the sidebands with the beam current, as shown in Fig. 8(a). In Fig. 8(a1), the observation harmonic is an integer multiple of the bunching harmonic - a condition we refer to as the coherent case. In this situation, the square root of the Schottky power of the central peak and the Schottky power of the sidebands exhibit nearly identical decay trends to that of the beam current. This behavior confirms that the power of the central peak scales with the square of the number of ions (N2), while the sideband power scales linearly with N. In contrast, when the observation harmonic is not an integer multiple of the bunching harmonic - the incoherent case, as shown in Fig. 8(a2), the Schottky power of both the central peak and the sidebands follows the same decay trend as the beam current, indicating a linear dependence on the number of ions (N).

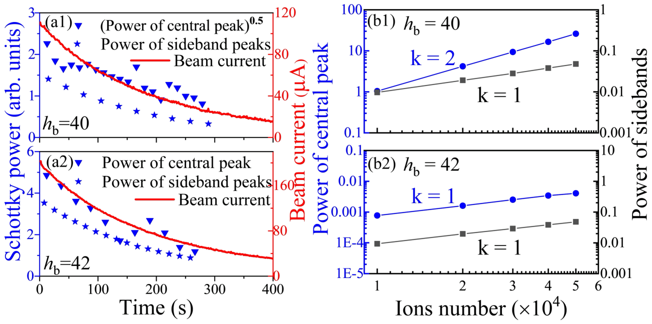

Figure 8: (a1) The comparison of the decay tendencies of the square root of the power of the central peak and the total power of sideband peaks in the Schottky spectrum at the bunching harmonic = 40 with respect to the beam current over storage time, respectively. (a2) The decay tendencies of the power of the central peak and the total power of sideband peaks in the Schottky spectrum at the bunching harmonic = 42 with respect to the beam current over storage time, respectively. (b1) & (b2) Dependence of the Schottky power for the central peak and the total power of sideband peaks on the number of ions for different bunching harmonics. Here k is the exponent in N^k, where N is the number of ions. Therefore, k = 2 means that the power scales quadratically with the number of ions ($P \propto N^2$), while k = 1 means that the power scales linearly with the number of ions ($P \propto N$). The observation harmonic in these figures is chosen to be 240.

ISBN: 978-3-95450-267-7 ISSN: 2226-0374 doi: 10.18429/JACoW-COOL2025-TUD1

To further illustrate this behavior, we simulated the dependence of the Schottky power of both the central peak and the sidebands on the number of ions for both coherent and incoherent cases, as shown in Fig. 8(b). In Fig. 8(b1), where the bunching harmonic hb = 40 and the observation harmonic is an integer multiple of hb, the power of the central peak scales quadratically with the number of ions (N2), while the power of the sidebands increases linearly with N. In Fig. 8(b2), where the hb = 42 and the observation harmonic is not an integer multiple of hb, the power of both the central peak and the sidebands exhibits a linear dependence on the number of ions (N). These results demonstrate that the Schottky power of the central peak follows an N2 scaling only when the observation harmonic is an integer multiple of the bunching harmonic. Otherwise, it scales linearly with N. In contrast, the sidebands always scale linearly with the number of ions, independent of the harmonic relationship. More detailed results could be found in [24].

CONCLUSION

We have developed a multi-particle tracking code to simulate the longitudinal Schottky spectra of bunched ion beams in storage rings. Based on the simulation results, we propose a novel method to extract the longitudinal momentum distribution from the Schottky spectrum of the bunched ion beams by calculating the envelope of the total Schottky power of each sideband. Unlike the previously used methods, this is a very simple and precise way for real-time monitoring of the momentum distribution during beam cooling experiments at the storage rings. Besides, we have systematically studied the dependence of the Schottky power on the number of stored ions in different bunching and observation harmonics. The greatly enhanced central peak phenomenon caused by the 'coherent effect' is fully interpreted.

REFERENCES

[1] Y.S. Yuan, et al., High-intensity effects on longitudinal bunch merging in hadron synchrotrons, Phys. Rev. Accel. Beams, 26 (2023) 024201. http://dx.doi.org/10.1103/PhysRevAccelBeams.26.024201

[2] J. Ullmann, et al., High precision hyperfine measurements in Bismuth challenge bound-state strong-field QED, Nat. Commun., 8 (2017) 15484. http://dx.doi.org/10.1038/ncomms15484

[3] M. Horst, et al., Storage-ring laser spectroscopy of accelerator-produced hydrogen-like $^{208}\mathrm{Bi}^{82+}$, Nat. Phys., (2025) 1057–1063. http://dx.doi.org/10.1038/s41567-025-02885-x

[4] L. di Lella, and C. Rubbia, The Discovery of the W and Z Particles, Adv. Ser. Direct. High Energy Phys., 23 (2015) 137-163. http://dx.doi.org/10.1142/9789814644150_0006

[5] E. Accomando, et al., Physics with e+e− linear colliders, Phys. Rep., 299 (1998) 1-78. http://dx.doi.org/10.1016/S0370-1573(97)00086-0

[6] D. Boussard, Schottky noise and beam transfer function diagnostics, CAS - CERN Accelerator School: 5th Advanced Accelerator Physics Course, (1995) 749-782. http://dx.doi.org/10.5170/CERN-1995-006.749

[7] M. Betz, et al., Bunched-beam Schottky monitoring in the LHC, Nucl. Instrum. Methods A, 874 (2017) 113-126. http://dx.doi.org/10.1016/j.nima.2017.08.045

[8] K. Lasocha, and D. Alves, Estimation of longitudinal bunch characteristics in the LHC using Schottky-based diagnostics, Phys. Rev. Accel. Beams, 23 (2020) 062803. http://dx.doi.org/10.1103/PhysRevAccelBeams.23.062803

[9] K. Lasocha, D. Alves, Estimation of transverse bunch characteristics in the LHC using Schottky-based diagnostics, Phys. Rev. Accel. Beams, 25 (2022) 062801. http://dx.doi.org/10.1103/PhysRevAccelBeams.25.062801

[10] O.B. Frankenheim, and T. Shukla, Space charge effects in bunches for different rf wave forms, Phys. Rev. ST Accel. Beams, 8 (2005) 034201. http://dx.doi.org/10.1103/PhysRevSTAB.8.034201

[11] I. Hofmann, and G. Kalisch, Space-charge-dominated bunched beams in the frequency domain, Phys. Rev. E, 53 (1996) 2807-2811. http://dx.doi.org/10.1103/PhysRevE.53.2807

[12] M. Bussmann, et al., The dynamics of bunched laser-cooled ion beams at relativistic energies, J. Phys.: Conf. Ser., 88 (2007) 012043. http://dx.doi.org/10.1088/1742-6596/88/1/012043

[13] R.W. Hasse, Theoretical verification of Coulomb order of ions in a storage ring, Phys. Rev. Lett., 83 (1999) 3430-3433. http://dx.doi.org/10.1103/PhysRevLett.83.3430

[14] H. Danared, et al., Model and Observations of Schottky-Noise Suppression in a Cold Heavy-Ion Beam, Phys. Rev. Lett., 88 (2002) 174801. http://dx.doi.org/10.1103/PhysRevLett.88.174801

[15] W.Q. Wen, et al., Laser cooling of stored bunched relativistic Li-like oxygen ions, Phys. Rev. A, 110 (2024) L010803. http://dx.doi.org/10.1103/PhysRevA.110.L010803

[16] S.Y. Lee, Accelerator Physics, 4th ed., World Scientific, Singapore, 2019. http://dx.doi.org/10.1142/11111

[17] J. Wei, Coherent Signals of the Bunched beam at High Frequency, Technique Report ADAP-23, (1991).

[18] J.M. Byrd, Bunched beam signals in time and frequency domain, in: Beam Measurement, World Scientific, 1999, pp. 233-262. http://dx.doi.org/10.1142/9789812818003_0010

[19] U. Schramm, et al., Combined Laser and Electron Cooling of Bunched C^{3+} Ion Beams at the Storage Ring ESR, AIP Conf. Proc., 821 (2006) 501-509. http://dx.doi.org/10.1063/1.2190157

[20] H.B. Wang, et al., Novel method for extraction of momentum distribution from longitudinal Schottky spectra of bunched ion beams at heavy-ion storage rings, submitted to Nucl. Instrum. Methods A.

[21] H.B. Wang, et al., Measurement of the lifetime and the proportion of $^{12}\mathrm{C}^{3+}$ ions in stored relativistic ion beams as a preparation for laser cooling experiments at the CSRe, Nucl. Instrum. Methods B, 408 (2017) 280-284. http://dx.doi.org/10.1016/j.nimb.2017.03.096

[22] G. Jackson, et al., Bunched Beam Stochastic Cooling in the Fermilab Tevatron Collider, PAC1993, 5 (1993) 3533-3535. http://dx.doi.org/10.1109/PAC.1993.309708

[23] J.M. Brennan, et al., Possibilities for stochastic cooling at RHIC, Nucl. Instrum. Methods A, 532 (2004) 335-339. http://dx.doi.org/10.1016/j.nima.2004.06.113

[24] H.B. Wang, et al., Investigation of coherent effect in longitudinal Schottky spectrum of bunched krypton ion beams at a heavy-ion storage ring, to be submitted to Nucl. Instrum. Methods A.

ISBN: 978-3-95450-267-7 ISSN: 2226-0374 doi: 10.18429/JACoW-COOL2025-TUD2

ELECTRON AND LASER COOLING OF STORED ION BEAMS AT CERN: XSUITE SIMULATIONS AND MEASUREMENTS*

P. Kruyt [1,2], G. Franchetti [1,2,3,4], D. Gamba [2], J. Romain [2,5]
[1] Goethe University, Frankfurt, Germany; [2] CERN, Meyrin, Switzerland; [3] GSI, Darmstadt, Germany;
[4] HFHF, Frankfurt am Main, Germany; [5] Grenoble INP Phelma, Grenoble, France

Abstract

Electron and laser cooling are key techniques for improving the quality of stored beams in synchrotrons. This contribution summarises the main advancements in electron and laser cooling simulations and measurements at CERN, with emphasis on benchmarked Xsuite models and on their application to present and future facilities. On the electron–cooling side, we present the implementation and validation of the Parkhomchuk model in Xsuite and its application to LEIR, ELENA, and to the design of the new AD electron cooler. On the laser–cooling side, we discuss simulations for the Gamma Factory proof–of–principle experiment in the SPS. The interplay between cooling and intrabeam scattering (IBS) is addressed, and we outline operational scenarios and open questions.

INTRODUCTION AND MOTIVATION

Beam cooling is routinely used in several CERN rings. Stochastic and electron cooling provide the deceleration and delivery of high-quality antiproton beams at the Antimatter Factory (AD/ELENA) [1], while electron cooling in LEIR is an essential component of the heavy–ion injector chain feeding the LHC and fixed–target experiments [2]. Ongoing initiatives such as the Gamma Factory proof–of–principle (PoP) experiment in the SPS [3] create a unique opportunity to test laser cooling at unprecedented energies. A unified, predictive simulation environment is therefore needed to study cooling and its interplay with heating mechanisms such as intrabeam scattering (IBS) and space charge in a consistent and quantitative manner.

Xsuite is the current production toolkit for beam dynamics at CERN, gradually replacing a landscape of legacy codes [4]. It provides a modern Python interface, supports heterogeneous computational back-ends (multi-threaded CPUs and GPUs), and follows an agile, community-driven development model with frequent releases. The framework hosts physics modules covering the full range from low-energy hadron rings to high-energy lepton colliders, allowing a wide variety of effects to be simulated within coherent coordinates and conventions. This significantly simplifies combining multiple physical mechanisms and accelerates both the setup and execution of complex simulations.

For these reasons, electron and laser cooling have been implemented directly within Xsuite, taking advantage of its fast development cycle and existing heating modules (e.g. IBS). This enables realistic start-to-end studies of cooling in operational and future CERN machines.

This work provides a concise overview of recent progress in this effort and continues the developments presented in Refs. [5–8]. A more detailed and comprehensive description will be available in the PhD thesis of P. Kruyt [9].

ELECTRON COOLING IN XSUITE

All CERN electron coolers operate in the magnetised regime, with relatively low-energy ($\lesssim$ 30 keV) DC electron beams (currents up to ~ 2.5 A) and longitudinal guide fields in the range of a few hundred gauss (100 G to 750 G). For this reason, the empirical Parkhomchuk friction-force model [10] was implemented in Xsuite, after revisiting the physics as implemented in BETACOOL [11], to ensure correctness and full documentation. A detailed re-analysis of the BETACOOL source code revealed several issues: (i) minor bugs in the handling of space-charge neutralisation; (ii) an inversion of the sign convention for the electron-beam rotation; and (iii) an undocumented coupling between the rotation and the transverse electron temperature. The first two effects have been corrected in the publicly available BETACOOL source [12], while the third was *not* imported into Xsuite, pending further theoretical clarification. Additional details will be provided in [9].

The resulting Xsuite implementation was validated against BETACOOL benchmarks using LEIR-like parameters and scanning a wide set of cooler conditions, including deliberately extreme—and sometimes non-physical—values to stress-test the algorithms. An example is shown in Fig. 1, where the cooling performance is compared over a scan of the cooler magnetic field, probing different regimes contained within the Parkhomchuk model. The agreement between the two codes is remarkable, with only minor deviations attributable to statistical differences in the generated particle distributions. These results provide confidence that the Xsuite implementation is ready to replace BETACOOL for magnetised electron-cooling simulations based on the Parkhomchuk model.

ELENA, AD, AND LEIR APPLICATIONS

The validated Xsuite electron-cooling model has been applied to several CERN accelerator rings.

For ELENA, Xsuite has been used to interpret both longitudinal and transverse cooling measurements, including the characterisation of transverse cooling at the extraction momentum of 13.7 MeV c_0^{-1}. A detailed account of these

---

* Work supported by Physics Beyond Colliders Study Group (PBC) and partially supported by the European Union's Horizon 2020 Research and Innovation program under Grant Agreement No. 101004730 (iFAST)

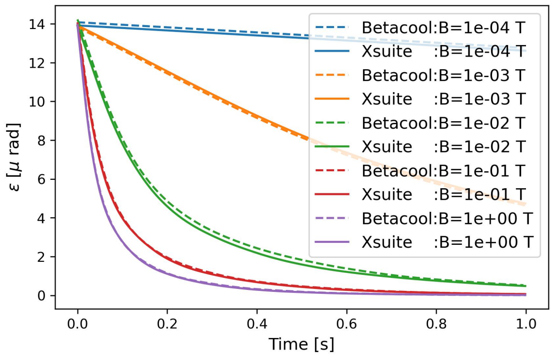

Figure 1: Evolution of transverse beam emittance as a function of time in the presence of electron cooling in LEIR, simulated with BETACOOL (dashed) and Xsuite (solid) for various assumed values of the cooler magnetic field.

measurements and the corresponding simulations is given in [9, 13].

After more than forty years of operation, the AD electron cooler is being replaced by a new device designed at CERN [7, 14]. The new cooler must ensure reliable operation of the Antimatter Factory for the next decade and beyond, while addressing known limitations of the present system and integrating modern technologies. A key limitation concerns the required magnetic-field quality, which was assessed through dedicated Xsuite simulations documented in [9]. These studies provided quantitative guidance for the cooler design and the tolerances associated with magnetic-field errors, indicating a target field quality of order rms $\lesssim 10^{-4}$, consistent with previous specifications obtained from empirical formulas [7, 15].

In LEIR, studies to characterise the longitudinal cooling were performed as a continuation of previous measurements, documented in [16]. Longitudinal cooling-force measurements follow a standard sequence: the circulating beam is pre-cooled, a step is applied to the electron-gun voltage (and hence to the electron energy), and the derivative of the ion momentum evolution is inferred from the longitudinal Schottky signal.

Figure 2 shows an example of the Schottky signal evolution during such a measurement. Two injections, spaced by approximately 220 ms, are visible, followed by a pre-cooling period after which the electron energy is abruptly changed, and the ions are dragged towards the new equilibrium.

This procedure in LEIR has two intrinsic limitations: (i) the actual electron-energy step is not instantaneous, as the power-supply and system capacitance response have a finite rise time; (ii) the momentum evolution inferred from Schottky diagnostics has limited time resolution. To overcome these limitations, Xsuite simulations were set up to model the full transient, including the dynamic evolution of the electron energy derived from the measured electron gun voltage. The observable used for benchmarking between measurements and simulations was the ion momentum at a fixed time after the voltage step.

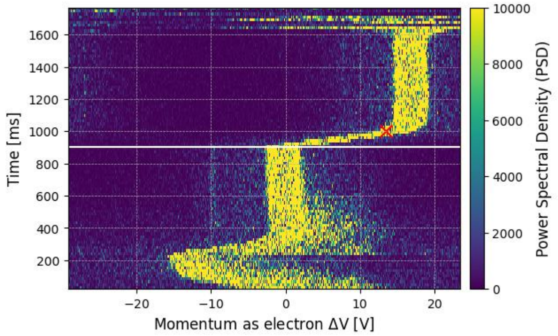

Figure 2: Example waterfall plot of the longitudinal Schottky power spectral density (PSD) as a function of the equivalent electron kinetic-energy deviation ΔV and time. The horizontal white line marks the moment when the electron energy is changed by 17 V, while the red cross indicates the reconstructed ion momentum deviation at a given time after the voltage step.

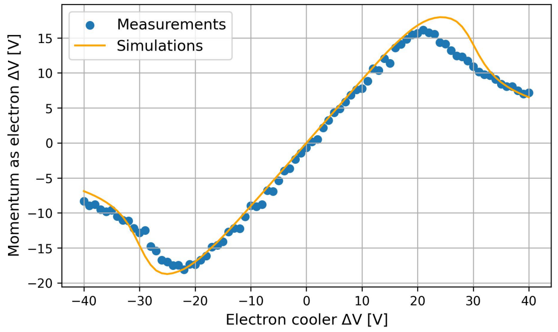

Figure 3: Example of longitudinal friction-force characterisation in LEIR with Pb^{54+}. The ion-beam momentum deviation—expressed, as an equivalent electron-gun voltage deviation—measured 75 ms after the electron energy is changed, is shown for measurements (blue points) and Xsuite simulations (orange line) as a function of the applied electron-gun voltage step.

First measurements with Mg^{7+} showed limitations due to incomplete pre-cooling and unmeasured beam parameters [2]. Subsequent Pb^{54+} studies achieved markedly improved agreement once electron-beam neutralisation and ion-optics constraints were measured or bounded as accurately as possible. Figure 3 compares the measured friction-force response with the corresponding Xsuite simulations for the Pb^{54+} case, showing excellent agreement. Details of the measurement configuration and simulation parameters can be found in [9].

During a measurement with Mg^{7+}, an exotic fast runaway was observed, as shown in Fig. 4: after the ion beam had reached equilibrium with the new electron energy, the beam suddenly increased in energy and was subsequently lost on the machine aperture, without any change in machine parameters.

This phenomenon was investigated using Xsuite by combining the effects of electron space charge, machine dis-

ISBN: 978-3-95450-267-7 ISSN: 2226-0374 doi: 10.18429/JACoW-COOL2025-TUD2

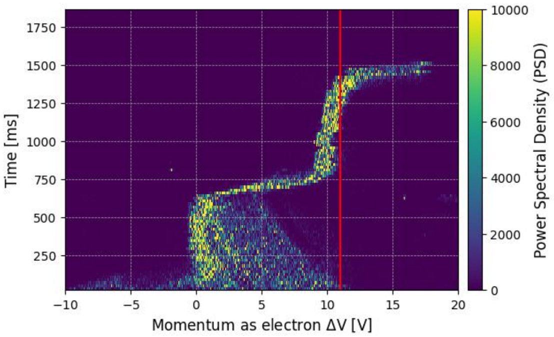

Figure 4: Example waterfall plot of the longitudinal Schottky power spectral density (PSD) in which a fast runaway was observed with Mg^{7+}. After an initial equilibrium is reached, the ion-beam energy rapidly increases before the beam is lost.

persion, orbit offsets, and transverse heating arising from the intrinsic rotation of the electron beam. Although unrealistically large dispersion would be required to fully reproduce the measured behaviour, the simulations highlight the importance of improved machine control and refined modelling [9].

LASER COOLING AND THE GAMMA FACTORY POP

The laser-cooling module in Xsuite solves optical Bloch equations for macro-particles interacting with continuous-wave and Fourier-limited pulsed lasers, including realistic laser bandwidth, beam size, and timing effects [6, 8]. Multi-threading and GPU back-ends are essential to cover the long time-scales and the large macro-particle samples required for these simulations.

The implemented module was benchmarked against published continuous-wave laser-cooling experiments conducted in Lanzhou [17, 18] on an O^{5+} beam at 275.70 MeV/u. Figure 5 shows an example simulation using a zero-emittance beam, illustrating that the laser–ion interaction follows the excitation probability expected from the laser parameters and interaction bandwidth.

To obtain realistic estimates matching the observed magnitude of the momentum dips, a careful treatment of the emittance-induced Doppler spread and of the laser–beam overlap is required. Using realistic laser and optics parameters at the interaction point, Xsuite reproduces the main experimental trends within the uncertainties of the experimental conditions, as summarised in Table 1, in agreement with independent simulation results reported in [18]. These results give confidence in the Xsuite implementation, which can therefore be used to explore other scenarios.

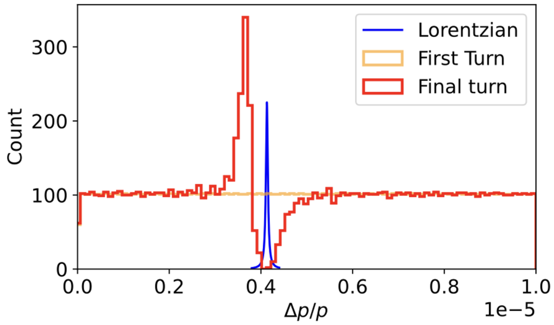

Figure 5: Ion-beam momentum-deviation distribution before (orange) and after (red) 10^4 turns with excitation by a CW laser, simulated in Xsuite. The expected Lorentzian excitation-probability distribution is shown for comparison (blue).

Table 1: Comparison of FWHM $\Delta p/p$ dip generated in the overall beam distribution from experiment [18], and Xsuite estimate.

	Exp. [18]	**Xsuite**
FWHM $\Delta p/p$	5.7×10^{-6}	$[2\times10^{-6}, 7\times10^{-6}]$

The Gamma Factory concept aims at producing intense high-energy photon beams by exciting partially stripped ions (PSIs) with lasers and exploiting the double Doppler boost of the absorption and emission processes. The proposed GF PoP experiment in the SPS would also provide the first demonstration of laser cooling at such high energies and is a natural testbed for the laser-cooling capabilities developed in Xsuite. In high-energy synchrotrons, laser cooling acts primarily in the longitudinal plane, while transverse cooling can be achieved by coupling the longitudinal and transverse dynamics through lattice dispersion. Operationally, the interplay between the optics functions, the laser–ion displacement at the interaction point (IP), and the beam energy must be carefully tuned to obtain the desired cooling rate in a given plane. A full optimisation therefore involves exploiting dispersion and transverse–longitudinal coupling, and scanning over ion species, charge states, transition energies, and available laser parameters — all of which can now be performed with the developed module in Xsuite.

Figure 6 shows an example of the expected cooling performance for selected ion species. A more exhaustive survey of ion species, laser parameters, and optics configurations, including predicted photon yields and spectra, can be found in [8, 9].

In parallel, studies are ongoing for the design of the Fabry–Perot cavity that will eventually need to be installed in the SPS, and a start-to-end scenario for the SPS PoP is being assembled in Xsuite. This includes compatibility with nominal SPS beams, steering margins with realistic corrector strengths and apertures, and possible commissioning sequences.

INTERPLAY OF COOLING WITH INTRABEAM SCATTERING

IBS acts as a diffusive heating mechanism that slows down the net cooling and sets a lower bound on the achievable equilibrium emittances. In Xsuite, IBS and cooling can be

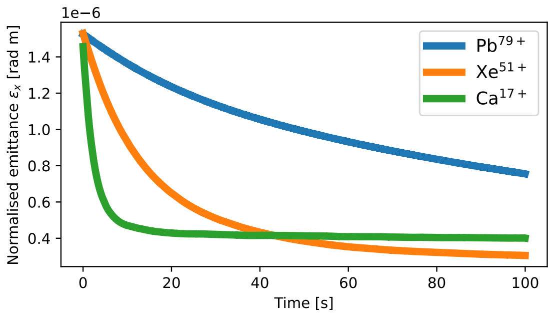

Figure 6: Simulated evolution of transverse emittance as a function of time under the effect of optimized laser cooling conditions at the SPS Gamma Factory PoP for different foreseeable ions.

combined consistently within the same tracking framework, using the same optics and lattice descriptions employed in other studies.

Figure 7 shows the evolution of the transverse emittance and beam-energy spread under the effect of laser cooling in the PoP experiment with Pb for different starting points with IBS included, and — at the design starting point — with and without IBS. The non-accessible region indicated in Fig. 7 is computed by evaluating, on a grid in the $(\varepsilon_x, \sigma_p/p)$ phase space, the IBS growth rates and the laser cooling rates corresponding to the configuration optimised for the design starting point. The contour is drawn when the local cooling rate cancels out the local IBS growth rate, which is done separately for both the longitudinal and horizontal planes. Notably, full simulations that integrate both effects appear to respect these boundaries.

Care must be taken, however, because laser cooling generally produces non-Gaussian beam distributions, which can strongly affect the computation of the rms σ_p/p and rms emittances, and can introduce numerical artifacts in IBS calculations, whose models typically assume Gaussian beams. For this reason, we report the 15–85% percentile σ_p/p values rather than rms quantities, as the percentile-based measure was found to be significantly more robust. Further details will be provided in [8, 9].

SUMMARY AND OUTLOOK

We have integrated and validated the Parkhomchuk magnetised electron-cooling model in Xsuite, which has been benchmarked against BETACOOL and found consistent with measurements in ELENA and LEIR, with electron space-charge effects being essential to reproduce observed behaviour. The model was also used to provide specifications for the new AD cooler field quality requirements.

Laser-cooling modules (CW and pulsed) are nearing completion for inclusion in an upcoming Xsuite release. The present code has been used to validate SPS PoP performance estimates, as well as to provide cooling estimates for future ions that could increase the luminosity in operations of HL–LHC.

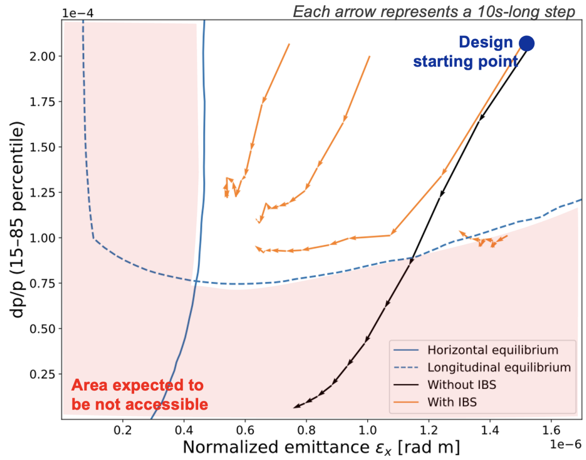

Figure 7: Evolution of transverse emittance and momentum spread with IBS (orange) and without IBS (black) for different starting points. Each arrow corresponds to 10 s of cooling. The blue curves indicate locations in phase space where the computed IBS growth rate balances the laser-cooling rate.

The interplay between cooling and IBS has been studied, suggesting the use of the percentile emittance metrics for more accurate and physical predictions in combined cooling–heating simulations. The unified treatment of cooling and heating effects within a single supported framework will provide a bright perspective for predictive simulation in future applications. In this regard, the forthcoming SPS PoP and the new AD cooler will provide further validation opportunities after LS3.

A key motivation for this work is to support operational decision–making for current and future CERN accelerators. For the SPS GF PoP, a start–to–end scenario has been assembled in Xsuite, including compatibility with nominal SPS beams, steering margins with realistic corrector strengths and apertures, and potential commissioning sequences. The impact of different laser configurations, optics choices, and ion species on both cooling and IBS can be assessed within the same simulation framework. For the AD, the new cooler design benefits directly from the field–quality tolerance studies, which translate into specifications for magnets and alignment. In ELENA and LEIR, the combination of measurements and simulations enables data–driven optimisation of cooler settings and provides a basis for future upgrades.

Xsuite now hosts production modules for magnetised electron cooling and for laser cooling with continuous–wave and Fourier–limited pulsed lasers, and developments towards chirped–laser support and extended IBS models are ongoing [4, 6].

REFERENCES

[1] L. Ponce, "The CERN Antimatter Factory: Performance and Perspectives", in *Proc. COOL2025*, Stony Brook, USA, 2026.

ISBN: 978-3-95450-267-7 ISSN: 2226-0374 doi: 10.18429/JACoW-COOL2025-TUD2

[2] M. Slupecki, R. Alemany Fernandez, S. Albright, D. Almeida, *et al.*, “CERN Ion Injector Complex Performance During 2024 Magnesium Test”, *CERN-ACC-NOTE-2025-0006*, 2025. `https://cds.cern.ch/record/2929494`

[3] M. W. Krasny *et al.*, “Gamma Factory Proof-of-Principle Experiment”, CERN, Tech. Rep., 2019. `https://cds.cern.ch/record/2690736`

[4] G. Iadarola *et al.*, “Xsuite: An Integrated Beam Physics Simulation Framework”, in *Proc. HB’23*, Geneva, Switzerland, pp. 73–80, 2024. `doi:10.18429/JACoW-HB2023-TUA2I1`

[5] A. E. Borucka, D. Gamba, and A. Latina, “Comparison of Available Models of Electron Cooling and their Implementations”, in *Proc. COOL’21*, Novosibirsk, Russia, pp. 74–77, 2021.

[6] P. M. Kruyt, G. Franchetti, and D. Gamba, “Advancements and Applications of Cooling Simulation Tools: A Focus on Xsuite”, in *Proc. COOL2023*, Montreux, Switzerland, pp. 49–53, 2024. `doi:10.18429/JACoW-COOL2023-THPOSRP02`

[7] D. Gamba, A. Rossi, G. Russo, and P. Kruyt, “Specifications for a New Electron Cooler of the Antiproton Decelerator at CERN”, in *Proc. IPAC’23*, Venice, Italy, pp. 2241–2244, 2023. `doi:10.18429/JACoW-IPAC2023-TUPM027`

[8] P. Kruyt, D. Gamba, and G. Franchetti, “Simulation Studies of Laser Cooling for the Gamma Factory Proof-of-Principle Experiment at the CERN SPS”, in *Proc. IPAC’24*, Nashville, TN, USA, pp. 832–835, 2024. `doi:10.18429/JACoW-IPAC2024-MOPS50`

[9] P. M. Kruyt, “Laser and Electron Cooling for Particle Accelerators”, PhD thesis, under publication, Ph.D. dissertation, Goethe University Frankfurt, 2026.

[10] V. Parkhomchuk, “New Insights in the Theory of Electron Cooling”, *Nucl. Instrum. Meth. A*, vol. 441, no. 1, pp. 9–17, 2000. `doi:10.1016/S0168-9002(99)01100-6`

[11] A. O. Sidorin, I. N. Meshkov, I. A. Seleznev, A. V. Smirnov, E. M. Syresin, and G. V. Trubnikov, “BETACOOL Program for Simulation of Beam Dynamics in Storage Rings”, *Nucl. Instrum. Meth. A*, vol. 558, pp. 325–328, 2006. `doi:10.1016/j.nima.2005.11.041`

[12] *Un-official repository of BETACOOL code by A. Smirnov et al.* `https://github.com/dgamba/betacool`

[13] P. Kruyt, D. Gamba, and G. Franchetti, “Measurements and simulations of the e-cooling performance in ELENA”, in *Proc. IPAC’24*, Nashville, TN, USA, pp. 836–839, 2024. `doi:10.18429/JACoW-IPAC2024-MOPS51`

[14] A. Rossi *et al.*, “Specifications and Status of the New Electron Cooler for the CERN Antiproton Decelerator (AD)”, in *Proc. COOL2023*, Montreux, Switzerland, pp. 5–10, 2024. `doi:10.18429/JACoW-COOL2023-MOPPM1R3`

[15] H. Poth, “Electron Cooling: Theory, Experiment, Application”, *Phys. Rep.*, vol. 196, no. 3, pp. 135–297, 1990. `doi:10.1016/0370-1573(90)90040-9`

[16] A. Latina *et al.*, “Electron Cooling Simulation and Experimental Benchmarks at LEIR”, in *Proc. IPAC’18*, Vancouver, Canada, Apr.-May 2018, pp. 776–779. `doi:10.18429/JACoW-IPAC2018-TUPAF039`

[17] W. Q. Wen *et al.*, “Laser Cooling of Stored Bunched Relativistic Li-like Oxygen Ions”, *Phys. Rev. A*, vol. 110, no. 1, p. L010803, 2024. `doi:10.1103/PhysRevA.110.L010803`

[18] D. Chen *et al.*, “Explanation for the Observed Wide Deceleration Range on a Coasting Ion Beam by a CW Laser at the Storage Ring CSRe”, *Nucl. Instrum. Meth. A*, vol. 1047, p. 167 852, 2023. `doi:10.1016/j.nima.2022.167852`

ISBN: 978-3-95450-267-7 ISSN: 2226-0374 doi: 10.18429/JACoW-COOL2025-TUD3

SIMULATION OF LONGITUDINAL ELECTRON COOLING OF 20 GeV PROTON BEAM AT EicC*

X. D. Yang†, He Zhao, Institute of Modern Physics, CAS, Lanzhou, China

Abstract

The longitudinal electron cooling processes of a 20 GeV proton beam were simulated using a code at the Electron-Ion collider in China. The longitudinal cooling time was obtained for different parameter configurations of the storage ring, proton beam, electron cooling device, and electron beam. From the simulated results, the longitudinal cooling time of the 20 GeV proton beam is over 100 seconds. The longitudinal cooling time can be shortened with the help of proper configuration of the parameters.

INTRODUCTION

Based on the HIAF (the Heavy Ion High-Intensity Accelerator Facility, approved in 2015 in China), a high luminosity polarized Electron-Ion Collider facility in China (EicC) has been proposed to study hadron structure and the strong interaction to carry out the frontier research on both nuclear and particle physics.

EicC will be constructed in two phases, EicC-I and EicC-II. In the first phase, a proton beam with energy between 15–20 GeV will collide with an electron beam with energy between 2.8–5 GeV. Both electron and proton beams are polarized. The luminosity is expected to reach $2–4\times10^{33}$ $cm^{-2}\cdot s^{-1}$.

In the second phase, the energy of the proton will be upgraded to 60–100 GeV, and the energy of the electron beam will be increased to 5–10 GeV, with luminosity expected to reach 1×10^{35}. The primary design and some initial parameters of EicC are found in Ref. [1].

To obtain the expected luminosity in the collider, the polarized proton beam will be cooled by various cooling methods throughout the entire operational energy range. Especially in the case of high-intensity energy proton beams, the intra-beam scattering effect should be considered in the collider design. The transverse electron cooling and intra-beam scattering were presented in the Ref. [2]. Some preliminary simulations of longitudinal electron cooling are presented in this contribution.

SIMULATION OF ELECTRON COOLING

The longitudinal electron cooling time depends not only on the lattice parameters of the storage ring, such as the Betatron function, dispersion of the cooling section, parameters of proton beam including energy, initial emittance, and momentum spread, but also on the construction parameters of electron cooling device, including the strength of magnetic field, the parallelism of magnetic field in the cooling section, the effective cooling length, and the parameters of electron beam, such as radius, density and transverse temperature of electron beam. These parameters are determined by the storage ring and the technology limitation, on the other hand, they are influenced and restricted by each other.

Among these parameters, the first type of parameter determines whether the proton beam under such parameters can be cooled down, playing a decisive role. The second type of parameter determines the length of cooling time for the proton beam under such parameters, playing an optimization role.

Using the electron cooling simulation code SIMCOOL [3, 4], the longitudinal electron cooling time of the proton beam was extensively simulated in various parameters in the EicC, including proton beam energy, initial transverse emittance, and momentum spread. The influence of the machine lattice parameters such as the Betatron function and dispersion function the cooling time was investigated. The parameters of the electron beam and cooling devices were taken into account, such as effective cooling length, magnetic field strength and parallelism in the cooling section, and electron beam current.

The different performances in transverse and longitudinal directions were observed compared with the traditional low-energy electron cooling.

The variation of momentum spread over time does not follow an exponential decay form, making it impossible to fit the cooling time. During the fitting process, either the decay curve does not match, or the final equilibrium value does not match. It decays faster than the exponential decay.

The fitting can only be performed on the first half of the data, while the second half corresponds to the scattering process. The other time it takes for momentum spread to reach its minimum.

As mentioned in the previous paragraph, the proton beam was cooled in the transverse direction. The longitudinal cooling process differs from the transverse one. During the initial cooling, the momentum spread drops rapidly and then gets to the minimum. And then the momentum spread starts to grow, rebounding from its minimum. The proton beam was not cooled when the energy shift of the electron beam was larger than a certain value.

In the longitudinal direction, due to the cooling happened first, and then scattering happened later. So only the cooling part was fitted. The longitudinal cooling time was replaced by the time when the momentum spread reached its minimum.

Proton Beam Parameters

Typical longitudinal cooling processes are illustrated in Figure 1 (left).

The right diagram of Figure 1 shows the longitudinal electron cooling time as a function of the particle number in the proton beam. In the case of other parameters that

---

* Work supported by NSFC No. 12275325, 12275323, 12205346.

† yangxd@impcas.ac.cn

ISBN: 978-3-95450-267-7 ISSN: 2226-0374 doi: 10.18429/JACoW-COOL2025-TUD3

were fixed, the longitudinal electron cooling time decreases with the particle number in the proton beam.

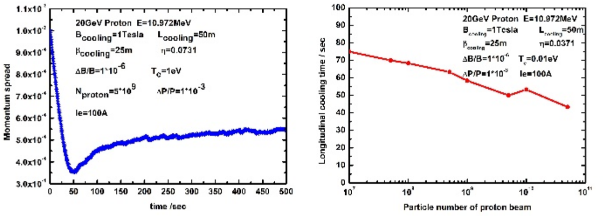

Figure 1: The momentum spread as a function of the time (left). The longitudinal electron cooling time as a function of the particle number in the proton beam (right).

Electron Beam Parameters

When the electron transverse temperature was 100 eV, the magnetic field parallelism was 10^{-5}, and the electron beam current was 10 A, the proton beam was not cooled. When the electron transverse temperature was 1 eV, the magnetic field parallelism was 10^{-6}, and the electron beam intensity was 10 A, the proton beam was cooled.

Parameters related to the longitudinal direction play a dominant role and are more sensitive to electronic cooling.

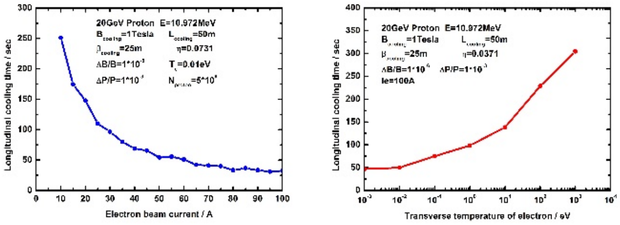

Figure 2: The longitudinal cooling time as a function of the electron beam current (left) and the transverse temperature of electron beam (right).

To decrease the longitudinal cooling time, the current of the electron beam and the length of the cooling section were set as a larger value. The left diagram of Figure 2 presents the longitudinal cooling time as a function of the electron beam current. The right diagram of Figure 2 indicates the longitudinal cooling time depends on the transverse temperature of the electron beam. In the case of other parameters that were fixed, the longitudinal cooling time decreases with the increasing electron beam current and decreasing transverse temperature of the electron beam.

Magnetic Field Parameters

The left plot of Figure 3 shows the longitudinal cooling time as a function of the magnetic field strength in the cooling section, and the right plot of Figure 3 presents the longitudinal cooling time as a function of the parallelism of the magnetic field in the cooling section. In the case of other fixed parameters, the longitudinal cooling time decreases with the magnetic field strength in the cooling section. The longitudinal cooling time decreases with the increasing parallelism of the magnetic field in the cooling section. From Figure 3, one can see the magnetic field parallelism strongly influences the cooling time. The cooling time becomes shorter when the magnetic field parallelism is higher in the cooling section.

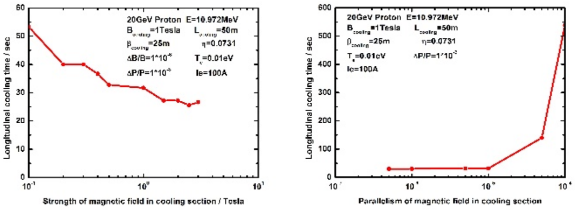

Figure 3: The longitudinal cooling time as a function of the magnetic field strength (left) and the parallelism of magnetic field (right) in the cooling section.

Electron Cooling Device Parameters

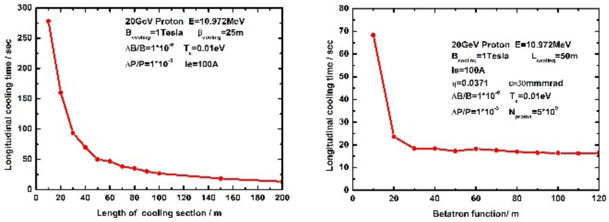

Figure 4: The longitudinal electron cooling time as a function of the length of the cooling section (left) and the Betatron function in the cooling section (right).

The left plot of Figure 4 shows the longitudinal cooling time varies as a function of the length of the cooling section. In the case of other parameters that were fixed, the longitudinal cooling time decreases with the length of the cooling section. The length of the cooling section strongly influences the longitudinal cooling time. The right plot of Figure 4 presents the longitudinal cooling time as a function of the Betatron function in the cooling section. The longitudinal cooling time decreases with the Betatron function in the cooling section.

Minimum and Final Momentum Spread

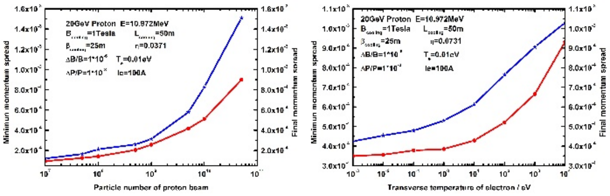

Figure 5: The minimum momentum spread and final momentum spread as a function of the particle number (left) and transverse temperature of electron (right).

The left plot of Figure 5 shows the minimum and final momentum spread as a function of the particle number. The right plot of Figure 5 presents the minimum and final momentum spread as a function of the transverse temperature of the electron. The minimum and final equilibrium momentum spread was mainly dominated by the particle number in the proton beam and the transverse temperature of the electron.

ISBN: 978-3-95450-267-7 ISSN: 2226-0374 doi: 10.18429/JACoW-COOL2025-TUD3

The left plot of Figure 6 shows the minimum and final momentum spread as a function of the parallelism of the magnetic field in the cooling section. The right plot of Figure 6 presents the minimum and final momentum spread as a function of the magnetic field strength in the cooling section. The minimum and final momentum spread were mainly dominated by the strength and quality of the magnetic field in the cooling section.

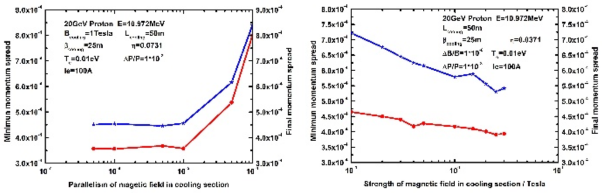

Figure 6: The minimum momentum spread and final momentum spread as a function of the parallelism of magnetic field (left) and the magnetic field strength (right) in the cooling section.

DISCUSSION

The difference in electron cooling behavior between the longitudinal and transverse directions should be investigated carefully. The reason why the proton beam was cooled first and then scattered later should be revealed clearly. In the case of high-energy conditions, the solution to solve this problem of longitudinal cooling followed by scattering should be explored.

In the case of high-energy electron cooling, the longitudinal velocity of the electron beam was much greater than the transverse velocity. In the cooling simulation, the same time interval was used for both transverse and longitudinal. Electron beams travelled at different path lengths during the same time interval in the transverse and longitudinal directions. This may be the cause of the unexpected results in the simulations.

At high energy, the longitudinal velocity of the proton beam is much greater than the transverse velocity, therefore, the deviation of the longitudinal velocity is also much greater than that of the transverse velocity. Due to longitudinal velocity mismatch or magnetic field parallelism, the projection of longitudinal velocity in the transverse direction will also be much greater than the transverse velocity of the electron beam. Therefore, in the longitudinal direction, the parameter requirements are more precise and the matching degree is high.

Additionally, the cooling forces vary with the absolute value of velocity difference between electron and proton, not relative value.

Cooling force is a nonlinear force [5], and when the relative velocity is small, the cooling force is weak. When the relative speed is high, the cooling force is strong. The maximum cooling force is only achieved when the relative velocity reaches a certain value.

In electron cooling, the transverse cooling rate usually differs from the longitudinal cooling rate, especially at high energies. Dispersive cooling [6] is the way to redistribute cooling force, it can redistribute the cooling rate between longitudinal and transverse planes.

SUMMARY

From the simulated results, the longitudinal cooling time of the proton beam with 20 GeV is over 100 seconds. The longitudinal cooling time can be shortened with the help of proper configuration of the parameters, such as smaller initial emittance and electron transverse temperature, higher magnetic field strength, parallelism of magnetic field in the cooling section, longer length of electron cooling section, stronger electron beam current, and proper beta function in the cooling section.

The longitudinal cooling behavior is different from the transverse one. After the balance is achieved in the transverse direction, the emittance remains unchanged. However, the longitudinal momentum spread shrinks rapidly at the beginning and then bounces back from the bottom.

In the interest of achieving the required luminosity from physics experiments, the parameters of the proton beam, electron cooling device, and storage ring should be optimized carefully and compromise each other, and the different configurations from the point of view of realizable technical solutions.

The emittance, particle number, and longitudinal bunch length of the proton beam should be optimized and compromised carefully to obtain the required luminosity. Additionally, the cooling strategy is important too, such as multi-stage cooling [7] at different energy or different periods. The emittance and momentum spread should be cooled to the required value by the stronger electron beam in the first stage, and then the smaller emittance and momentum spread will be maintained by the weaker electron beam.

High-intensity proton beam and short bunch length were expected to store in a collider with a long lifetime and less loss. To increase the lifetime of the proton beam and decrease the loss, a longitudinal hollow electron beam [8] will be attempted to suppress the intra-beam scattering. The traditional DC electron beam in the electron cooler will be modulated into shorter electron bunches with different longitudinal distributions. The stronger cooling was expected in the tail of the proton beam and the weaker cooling was performed in the core of the proton beam. The proton loss will be decreased and the lifetime will be increased. The intensity of the proton beam in the collider will be kept and maintained for a long time.

For the sake of obtaining and keeping enough particle number, smaller emittance, and shorter bunch length in the case of a proton beam with energy 20 GeV, the cooling should counteract the scattering at the different situations and periods, and provide high-quality proton beam for the higher luminosity in the storage ring. The detailed and exact simulation will be necessary for the real lattice design of the EicC storage ring in the future.

ISBN: 978-3-95450-267-7 ISSN: 2226-0374 doi: 10.18429/JACoW-COOL2025-TUD3

REFERENCES

[1] Xu Cao, Lei Chang, Ningbo Chang et al., "Electron ion collider in China". *Nuclear Techniques*, vol. 43, no. 2, 2020, p. 020001 1–59.
`doi:10.11889/j.0253-3219.2020.hjs.43.020001`

[2] X. D. Yang, "Simulation of transverse electron cooling and IBS of 20 GeV proton beam at EicC", in *Proc. COOL2021*, Novosibirsk, Russia, Nov. 1–5, 2021, pp. 70–73. `doi:10.18429/JACoW-COOL2021-P1002`

[3] Vasily Parkhomchuk and Ilan Ben-Zvi, "Electron cooling for RHIC", *BNL C-A/AP/47*, April 2001.

[4] A.V. Fedotov, I. Ben-Zvi, Yu. Eidelman et al., "Simulation of high-energy electron cooling", in *Proc. PAC2005*, Knoxville, Tennessee, USA, May 16–20, 2005, paper TPAT090, pp. 4251–4263.

[5] A.V. Fedotov, D.L. Bruhwiler, and A.O. Sidorin, "Analysis of the magnetized friction force", in *Proc. HB2006*, Tsukuba, Japan, May 29 – Jun. 2, 2006, paper WEAY04, pp. 210–214.

[6] He Zhao, Lijun Mao, Meitang Tang et al., "Theoretical and simulation study of dispersive electron cooling", *Phys. Rev. Accel. Beams*, vol. 27, p. 033501, Mar. 2024.
`doi: 10.1103/PhysRevAccelBeams.27.033501`

[7] H. Zhang, Y. Zhang, Ya. Derbenev et al., "Multi-stage electron cooling scheme for JLEIC", in *Proc. IPAC2018*, Vancouver, BC, Canada, Apr. 29 – May 4, 2018, paper MOPML006, pp. 397-399.
`doi:10.18429/JACoW-IPAC2018-MOPML006`

[8] X. D. Yang, "Longitudinal hollow electron beam", in *Proc. IPAC2025*, Taipei, Taiwan, 1–6, Jun. 2025, paper MOPS004, pp. 588–591.
`doi:10.18429/JACoW-IPAC25-MOPS004`

ISBN: 978-3-95450-267-7 ISSN: 2226-0374 doi: 10.18429/JACoW-COOL2025-WEA1

VERSATILE PLATFORM FOR RELATIVISTIC ELECTRON COOLING AND OTHER EXPERIMENTS

K. Aulenbacher *[1], Th. Beiser[1], J. Dietrich[1], W. Klag[1]
Helmholtz-Institut Mainz, Mainz, Germany
[1]also at GSI Helmholtzzentrum für Schwerionenforschung GmbH, Darmstadt, Germany

Abstract

At Helmholtz-Institut Mainz (HIM) a high voltage platform for high intensity electron beams has been installed. This apparatus is intended as a scalable, modular system for high energy magnetized DC-beam cooling. On the one hand, the system can be used as a prototype for antiproton beam cooling for the planned HESR storage ring at FAIR. On the other, because the HESR will be delayed, we have the opportunity to use the device for other applications. We present recently realized technical progress and how these can be applied for different new experiments during the time until the initially intended application becomes possible.

INTRODUCTION

Helmholtz-Institut Mainz (HIM) is a joint venture of the Johannes Gutenberg-University in Mainz and the national research lab GSI (GSI Helmholtzzentrum für Schwerionenforschung GmbH, Darmstadt, Germany). The latter is presently installing several accelerators of the FAIR (Facility for Antiproton and Ion Research) complex on its premises.

At the beginning of the 2010-decade, HIM had taken over responsibilities for a relativistic electron cooler which is to be used at the High Energy Storage Ring (HESR), where the majority of the antiproton experiments at FAIR are planned. This will happen in particular by interaction with a fixed target within the $\overline{\text{P}}$ANDA experiment. The strong interaction with its target necessitates magnetized electron cooling with a very high intensity at kinetic energy of almost 8 MeV. A cooperation between Budker Institute Novosibirsk (BINP) and HIM was started to investigate the challenges associated with this task.

An important part of the developments done at HIM has been concentrated on a sustainable floating power supply for the magnetization solenoids in the acceleration/deceleration channel of the cooler. A gas turbine based system has been installed at HIM which solves this problem producing power of several kilowatts at high potential, see for instance [1]. The next goal was a prototype device which has two 600 kV units in order to demonstrate the scalability comprising two identical HV-platforms, each containing a single gas-turbine [1]. These platforms were to be produced by BINP, but only one has been delivered before the war in Ukraine has stopped the cooperation.

Another important point to take into account is that the construction of the HESR-building has not yet begun, which means that HESR will not be operated within the present decade. This opens up the question which research can be done at HIM in the meantime while not compromising the goals relevant for electron cooling.

In the next sections we will first describe the present status of the cooler activities and then present two projects which will permit us to sustain competences and knowledge until the timeline for electron cooling at HESR becomes more predictable. A first one which is already producing promising results is using high power electron beams of similar intensity as in the cooler for medical purposes. Another potential project is to use the existing cooler-prototype to develop techniques which can be used to make precision measurements of a possible electric dipole moment (EDM) of electrons.

STATUS OF THE ELECTRON COOLER PROTOTYPE

The power for the solenoids which magnetize the beam is provided by a turbo-generator which expands 3 bar nitrogen gas. The gas is used in a closed circuit which is driven by a screw compressor. All units of the circuit are commercial devices. The gas circuit was designed by Prof. M. Wirsum from the institute for gas driven power stations at RWTH Aachen. After setting the mass flows with regulation valves at constant load, the system runs stable without further intervention. The turbine gas-system is separate from the pressure tank. In summer 2025 the tank itself was sealed and filled with 3 bar of nitrogen. Leak rate was observed to be about 0.1 bar/week which is no limit for present experimentation but needs to be improved if typical insulation gases such as SF_6 would be used.

The communication with the HV-platform is based on software delivered by BINP. After some trial and error, communication could be set up. The turbo-generator permitted to power the solenoid on the platform and also the Cockcroft Walton HV-generator. This voltage could not be increased to more than 80 kV, we suspect an internal hardware safety limit. No sign of corona discharges was observed at this voltage. This seems reasonable since the air gap between the inner wall of the tank and the outer radius of the platform is about 50 cm (see Fig. 1), which should provide sufficient insulation for even the maximum voltage of the HV-generator (600 kV) at our 3 bar nitrogen pressure. The next step is to "reverse engineer" the control of the Cockcroft-Walton to circumvent the present limit.

Summarizing the situation, it can be stated that the device is now ready for experimentation which can go in several directions, for instance to demonstrate the scalability of the

---

* aulenbac@uni-mainz.de

ISBN: 978-3-95450-267-7 ISSN: 2226-0374 doi: 10.18429/JACoW-COOL2025-WEA1

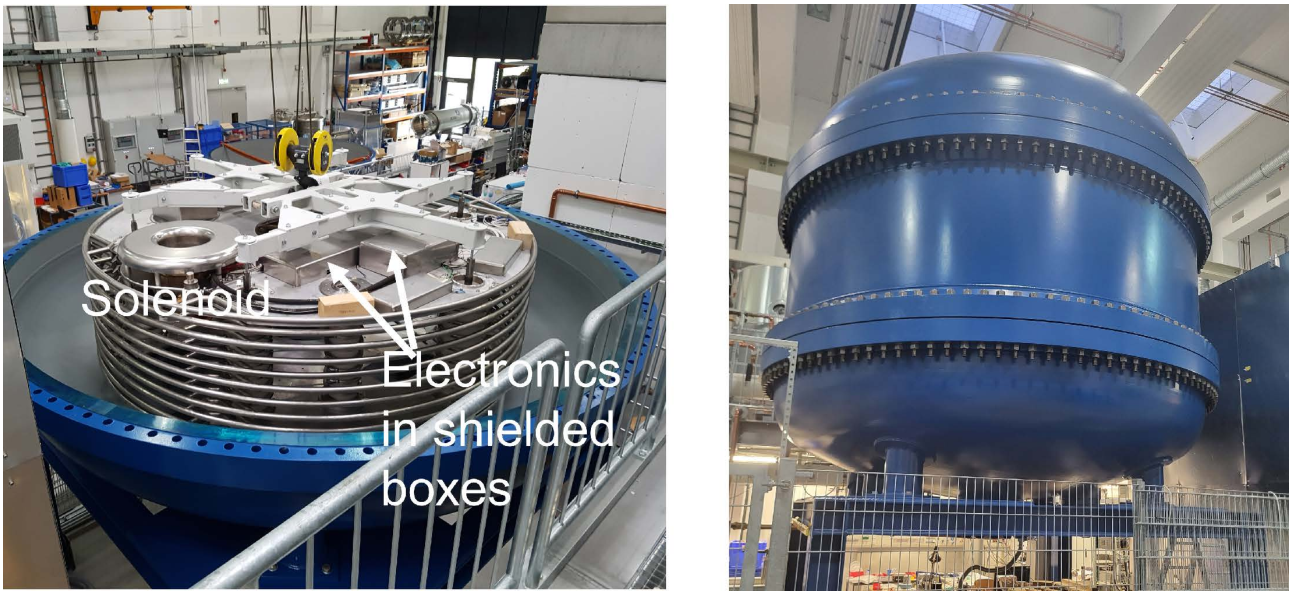

Figure 1: Left: Open tank during assembly of the 600 kV platform which is hanging on a crane. On the upper plane of the platform a solenoid can be identified, the rectangular boxes contain power supplies and communication devices. The right panel shows the tank after tightening all flanges. The inner diameter of the tank is 3.98 m, the outer diameter of the platform is 2.86 m [2].

turbine/platform concept or to start tests with an electron beam. Since the cooperation with BINP was suspended, such attempts need considerable additional personnel resources. Taking into account the unclear timeline of the HESR project it is even more difficult to justify such measures. Therefore our strategy is to "hibernate" knowledge within a different project and/or to find a science related project for which the existing cooler set-up could be used. This will be described in the next two sections.

HIGH POWER ELECTRON BEAM FOR THE LINE FOCUS X-RAY TUBE

In parallel to the developments described above we have commissioned a 30 kV magnetized "test-cooler" which delivers 1 A beam [3]. This experience has enabled us to develop an electron-source with high current density for a medical device, the so-called Line Focus X-ray Tube (LFXT). The line focus on the X-ray anode permits more electron beam power and even power density than in conventional X-ray tubes. This is because the range of secondary electrons is larger than size of the beam spot making heat transfer depending on the speed of these electrons and not on the speed of sound as usual [4]. Since a small emittance is only needed in one direction, this results in the additional advantage that a line emitter can be used (see Fig. 2) which reduces the necessary current density. At the required current of 300 mA a current density of 6 A/cm^2 is needed which can be handled by commercial Barium-Oxide dispenser cathodes. An intermediate state of the project was already communicated at COOL23 [1]. Meanwhile the computer-simulated beam parameters have been demonstrated and first medical tests with animals have been performed with good success [5].

During the next years we will work on R&D aspects of the project, in particular how to suppress the outgassing from the X-ray anode which limits presently the operation time. We therefore have a research program which will keep our competences in the field of high power electron beams alive. A commercialization of our technology is intended and in a few years time it will become clear if this "spin-off" from cooler developments can be used in clinical practice. This time period could fit to the anticipated time frame for the construction of the HESR buildings when our focus could be redirected to cooler activities for HESR/FAIR.

USING THE COOLER PROTOTYPE FOR AN EDM STUDY

Storage rings for spin-polarized particles such as the proton are extremely sensitive instruments to search for possible electric dipole moments (EDMs) of fundamental particles. Such experiments have been pursued for instance at the storage ring COSY [6] which unfortunately was shut down recently.

If a non-zero EDM exists, it leads to an additional spin-precession which can be observed as occurrence of a component of the polarization vector that cannot be explained by the magnetic moment of the particle. The challenge of such experiments is to control systematic uncertainties which may be caused, for instance, by small unwanted magnetic field contributions. These can be suppressed by using a purely electrostatic storage ring. Another measure is to use counter-rotating beams. Moreover, the $g-2$ precession of the particles in the lab frame should be avoided which can be achieved by operating at a so-called "magic momentum" which depends on the anomalous magnetic momentum

Figure 2: Left: Cathode assembly of the electron cooler test-stand at HIM. Circular cathode with 1 cm diameter. Upper right: Cathode assembly with linear emitter for LFXT. Dimensions 0.3×15 mm. Lower right: emitter in operation.

of the particle. Unfortunately, the magic momentum for protons is 700 MeV/c and for electrons 14.8 MeV/c which would require a huge investment for the development of such an electrostatic ring, even for electrons. The $g-2$ precession can also be switched off by bending the beam in a periodic orbit which has a figure-of-8, since the rotation of the particle switches its sign during a single turn. This would however also cancel the EDM precession. To avoid this, Suleiman et al. propose [7] to operate an electrostatic figure-of-8 storage ring at two different total energies, ($\gamma_1 = 2.6, \gamma_2 = 1.4$) which corresponds to kinetic energies of 800 keV and 200 keV respectively.

The dimensions estimated by Suleiman et al. can be seen in the right panel of Fig. 3. These dimensions fit into the framework of the cooler set-up shown in Fig. 1.

The storage ring needs a 200 keV polarized electron source for injection. Such a source is presently used in our institute for the MESA-accelerator [8]. With its cylindrical size (< 500 mm in height and diameter) it could be installed on the platform (see Fig. 1). This platform also offers sufficient space — note that the existing tank has a height that is sufficient for two stacked platforms — for the power supplies needed, these supplies can get their (floating) supply from the turbo-generator which offers ample power.

After injection, the beam can be accelerated by 600 kV to ground potential where the more demanding 800 keV electrostatic bends can be installed. It is by chance that the desired acceleration voltage matches the capability of our HV-generator. The lower energy fits to the optimum sensitivity range of a classical Mott-polarization detector, which decreases strongly with energy.

Suleiman et al. estimate the final sensitivity for the EDM of the electron to be below 1×10^{-28} e · cm. However, the standard model predicts much lower electron EDMs and measurements in molecules like hafnium fluoride have already indicated that the electron EDM is below 1×10^{-29} e · cm. It is therefore not very likely that a major particle physics breakthrough can be obtained with the cooler. This could be, on the other hand, expected from a measurement of the proton EDM. It may be useful to optimize the techniques to be used in a proton EDM storage ring at this small scale installation that could be realized by a small collaboration within a comparatively short timescale.

REFERENCES

[1] K. Aulenbacher *et al.*, “Sustaining competences for electron cooling at HESR,” in *Proc. COOL’23*, Montreux, Switzerland, Oct. 2023, paper THPAM1R2. `doi:10.18429/JACoW-COOL2023-THPAM1R2`

[2] Budker Institute of Nuclear Physics, “Interim design report for HIM,” unpublished, 2020.

[3] Th. Beiser *et al.*, “Investigation of ion trapping and beam-induced fluorescence at the electron cooler test-bench at HIM,” in *Proc. COOL’23*, Montreux, Switzerland, Oct. 2023, paper THPOSRP13. `doi:10.18429/JACoW-COOL2023-THPOSRP13`

[4] S. Bartzsch and U. Oelfke, “Linefocus x-ray tubes—a new concept to produce high brilliance x-rays,” *Phys. Med. Biol.*, vol. 62, p. 8600, 2017. `doi:10.1088/1361-6560/aa910b`

[5] Ch. Petrich *et al.*, “Commissioning, characterization, and first high-dose-rate irradiations at a compact x-ray tube for microbeam and minibeam radiation therapy,” *Int. J. Radiat. On-*

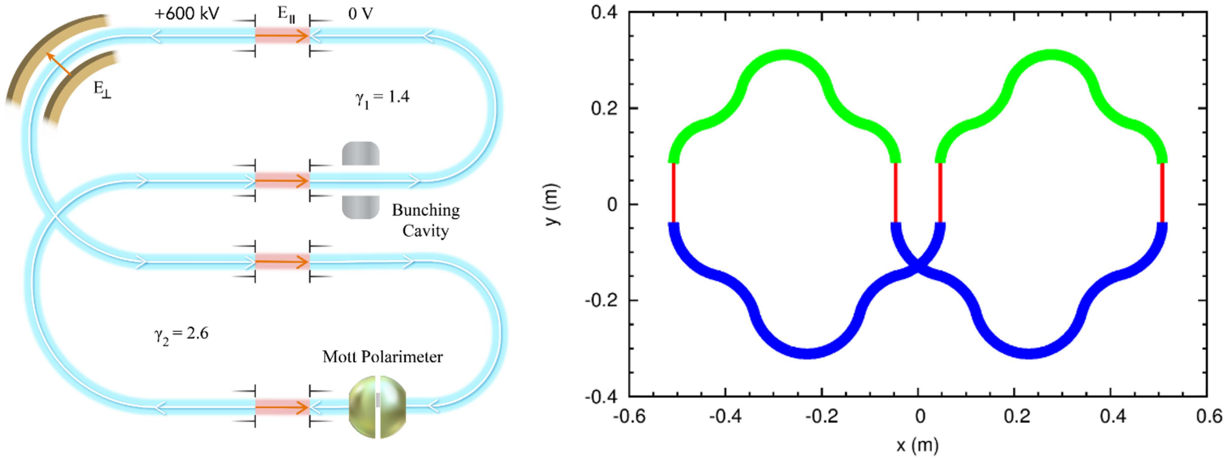

Figure 3: Left: Scheme of a "Figure of eight" electrostatic storage ring for counter-propagating spin-polarized electrons. Right: Spatial dimension of this storage ring. Figures taken from Suleiman et al. [7].

col. Biol. Phys. vol. 124, no. 4, pp. 1137–1146, Mar. 2026. `doi:10.1016/j.ijrobp.2025.10.012`

[6] R. Gebel *et al.*, "Spin physics at COSY (2021–2024) and beyond," arXiv:2108.13933, 2021. `doi:10.48550/arXiv.2108.13933`

[7] R. Suleiman *et al.*, "On possibilities of high precision fundamental physics experiments in spin-transparent storage rings of low energy polarized electron beams," arXiv:2105.11575, 2023. `doi:10.48550/arXiv.2105.11575`

[8] S. Friederich *et al.*, "The small thermalized electron source at Mainz (STEAM)," in *Proc. ERL'17*, Geneva, Switzerland, Jun. 2017, paper MOPSPP005. `doi:10.18429/JACoW-ERL2017-MOPSPP005`

ISBN: 978-3-95450-267-7 ISSN: 2226-0374 doi: 10.18429/JACoW-COOL2025-WEA2

GUN AND COLLECTOR DEVELOPMENT ON THE ELECTRON COOLER TEST STAND (ECTS)

G. Khatri*, J. Cenede, A. Frassier, A. Rossi, G. Tranquille
CERN, Geneva, Switzerland

Abstract

The electron cooler of the Antiproton Decelerator (AD) at CERN, that can operate with an electron beam of up to 2.4 A at 27 keV, is scheduled for replacement during the upcoming Long Shutdown 3 (LS3). A newly designed electron gun and collector—optimized for enhanced reliability, efficiency, and operational performance—are undergoing rigorous testing and validation at the dedicated Electron Cooler Test Stand (ECTS). The new electron collector features a re-engineered cooling system, where the water circuit is fully decoupled from the vacuum environment, significantly reducing the risk of vacuum leaks. The new electron gun operates at high perveance in the range of 2.2 to 2.5 $\mu A \cdot V^{-3/2}$ and employs a magnetic beam expansion by a factor of two. This expansion lowers the transverse temperature of the electron beam, thereby enhancing the cooling efficiency. This paper will present the ongoing research, key design considerations, and the latest experimental results from the ECTS, contributing to the successful implementation of the new AD electron cooler.

INTRODUCTION

Electron cooling, first introduced by G. Budker in 1966 [1], is a standard technique for reducing beam emittance and improving beam quality. The present AD electron cooler originates from the Initial Cooling Experiment (ICE) at CERN [2], was later adapted for LEAR [3] and finally integrated into the Antiproton Decelerator [4]. After decades of operation many components have reached end-of-life and critical spares are no longer available, motivating the development of a new electron cooler for the AD [5, 6].

A new high-performance electron gun has therefore been designed, prototyped and tested. Its geometry was derived from detailed electron-beam simulations to meet the requirements of 2.4 A at 27 keV. This paper focuses on the development, optimisation and characterisation of this gun and its integration with the redesigned collector. A description of the legacy gun and collector used in the existing AD cooler can be found in Refs. [7, 8].

EXPERIMENTAL SETUP

The characterization of the prototype electron gun and the validation of the redesigned collector were performed on the Electron Cooler Test Stand (ECTS), a dedicated high-voltage platform developed at CERN for testing electron cooler components at DC high voltages of up to –80 kV, see Fig. 1. A detailed description of the facility is available in Ref. [9]; only a short summary is given here.

The ECTS consists of a fully enclosed Faraday cage on an elevated high-voltage platform, powered by an 80 kV / 50 kW three-phase isolation transformer. All gun and collector power supplies are located on the HV platform, while magnet power supplies and supervisory computers remain at ground potential. Communication is via optical fibre links and Wi-Fi. The system is operated through a Python/LabVIEW-based control suite providing slow control, data logging, vacuum diagnostics and interlock handling.

The test line includes a 1.5 m solenoid capable of generating up to 900 G, a squeeze coil at the collector entrance, and a magnetic shield surrounding the collector chamber to minimise electron losses. Current and voltage measurements are performed using precision shunt resistors on the gun and collector return lines. Vacuum is maintained by a combination of a turbomolecular pump backed by a dry scroll pump, an ion pump, a NexTorr pump and a titanium sublimation pump, reaching base pressures of a few 10^{-10} mbar at the collector after bakeout. During hot-cathode operation and beam extraction, the pressure typically rises into the low 10^{-8} mbar range.

A dedicated low-conductivity cooling-water circuit removes heat from the electron collector during beam dump. The loop includes resin filters and continuous purification to maintain low conductivity for high-voltage operation and to minimise leakage currents to ground. The redesigned collector has already been tested and validated [10]; the present work concentrates on the prototyping and iterative development of the new electron gun.

GUN PROTOTYPE AND TESTS

Informed by detailed particle-tracking simulations in EGUN, TRAK and CST [12, 13, 15], a high-perveance electron gun was developed to meet the specifications of the new AD electron cooler: 2.4 A at 27 keV in a 2400 Gauss magnetic field at the gun, matched to a ~ 600 Gauss field in the cooling region. This yields a magnetic expansion of the beam radius by a factor two, from 12.5 mm at the cathode to 25 mm in the cooling section. Several cathode surface shapes—flat, concave and convex—were investigated in simulations to minimise transverse temperature while preserving perveance in the range 2.2 $\mu A/V^{1.5}$ to 2.5 $\mu A/V^{1.5}$.

Guided by these results, a first prototype gun was designed and built with the aim of validating the electrodes geometry, demonstrating emission at 27 keV and 2.4 A, checking insulation up to 30 kV with a hot cathode and identifying

---

* gunn.khatri@cern.ch

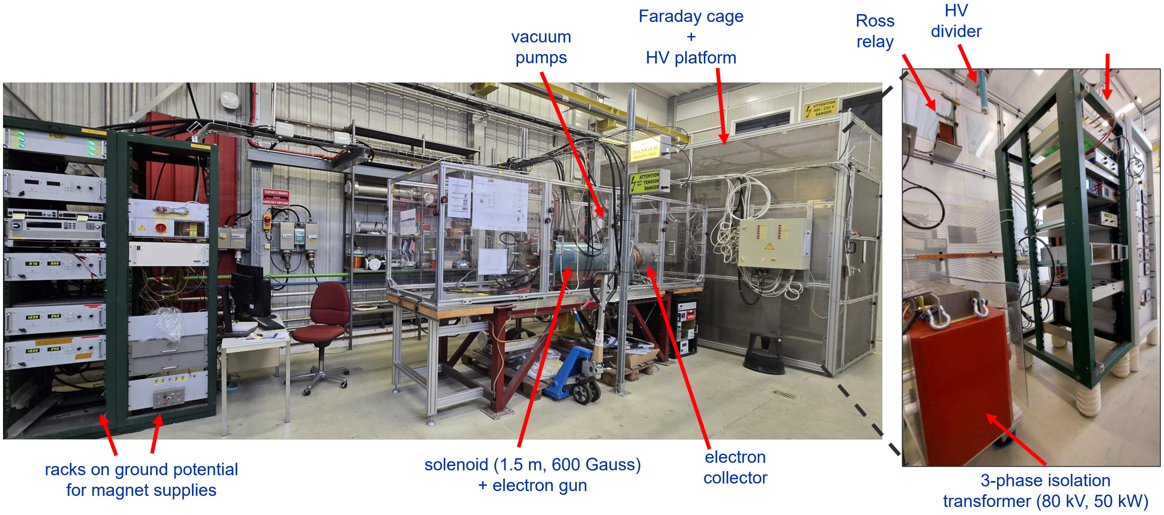

Figure 1: Test bench layout and main elements of the ECTS.

thermo-mechanical weaknesses before committing to a final design.

Mechanical Design Choices

The prototype uses a modular, low-cost architecture based on off-the-shelf components. Electrodes can be exchanged with minimal rework, enabling rapid iteration. The gun consists of three main electrodes (anode, grid and Pierce electrode), with the cathode recessed inside the Pierce geometry; all electrodes are machined from bulk stainless steel.

The cathode and Pierce electrode must operate close to 1000°C while maintaining high-voltage insulation. The cathode is held by a 12 cm ceramic support, while the grid electrode is mounted on three axial rods, each carrying a radial ceramic spacer. On the grid side, the ceramics are rigidly attached to the grid electrode but slide inside slots at the rod ends, a scheme derived from thermo-mechanical simulations [14] to avoid hyperstatic constraints and prevent ceramic fracture. Macor and high-purity alumina were both produced for the cathode and grid ceramics in the first iteration of the gun design. A schematic of the prototype gun assembly is shown in Fig. 2.

High-Voltage and Cathode Heating Tests

At room temperature each electrode was biased up to 30 kV with respect to ground and no measurable leakage current was observed, confirming sufficient insulation margins. Cathode heating was then tested under vacuum using a viewport and a pyrometer. The measured I–V–T characteristics, shown in Fig. 3, closely followed the SpectraMat cathode data sheet, demonstrating correct heater performance and emissive behaviour up to about 1000°C. After repeated heating cycles the gun was opened and no thermo-mechanical damage of the ceramic supports or electrodes was observed.

First Iteration: Beam Extraction and Limitations

The gun was then installed on the ECTS for the first beam-extraction campaign. It was placed in the existing 1.5 m solenoid providing up to 900 G, well below the nominal 2400 G foreseen at the gun in the final cooler. Since dedicated grid and cathode supplies were not yet available, the grid was held at ground potential and the cathode–Pierce assembly biased negatively, so that the applied voltage defined both extraction field and beam energy.

Beam extraction up to 5 kV was achieved, with beam currents of about 700 mA and a perveance of 2.15 $\mu A/V^{1.5}$. However, the total loss current—including leakage through ceramics and water-cooled structures and true beam interception—reached about 2 mA. For comparison, when the same collector was tested with the legacy AD gun the total losses remained below 300 µA, indicating that the additional losses originated from the prototype gun.

During these tests the cathode and grid ceramics became very hot. The cathode-support ceramic resistance dropped

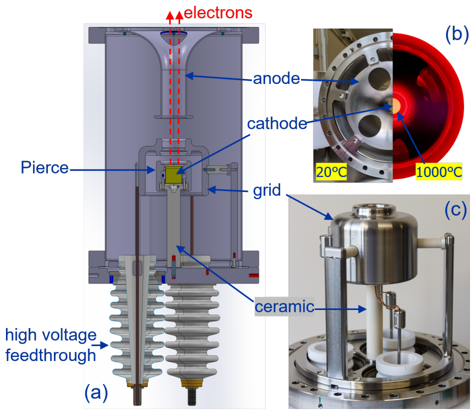

Figure 2: Prototype electron gun design: (a) 3D model, (b) hot/cold cathode and (c) without the vacuum chamber.

ISBN: 978-3-95450-267-7 ISSN: 2226-0374 doi: 10.18429/JACoW-COOL2025-WEA2

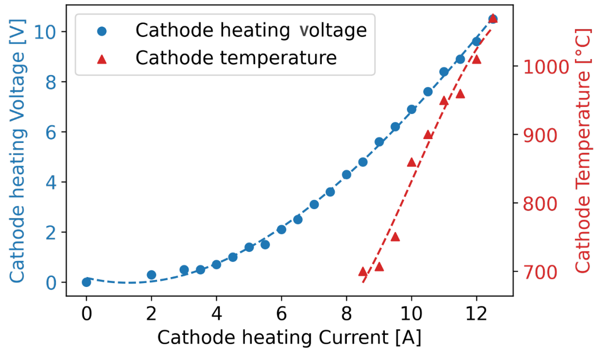

Figure 3: Measured cathode heating characteristics (I–V–T curve).

to ~ 0.5 MΩ, while the grid-support ceramics stayed around 10 MΩ. The reduced resistance led to significant leakage current through the cathode support, further heating the ceramic and driving a thermal-runaway process. The collector pressure reached about 10^{-7} mbar, implying substantially worse pressure in the gun region, above the 10^{-6} mbar limit recommended by the cathode manufacturer. Under these conditions stable operation above 5 kV was not possible.

Second Iteration: Thermal Mitigation

A second iteration of the prototype focused on reducing the thermal load on the cathode-support ceramic. Two main changes were implemented, see Fig. 4: the original 12 cm ceramic was replaced by a 6 cm ceramic plus a 6 cm stainless-steel extension tube, reducing conductive heat flow, and two layers of tantalum foil were installed around and behind the cathode to improve radiative shielding and temperature uniformity. Thermal simulations indicated a drop of the average ceramic temperature from about 800°C to roughly 500°C.

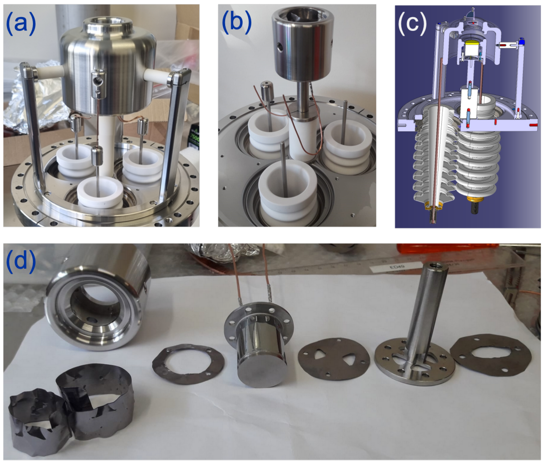

Figure 4: Prototype gun assembly: (a) first iteration with 12 cm cathode ceramic, (b,c) second iteration with 6 cm ceramic + 6 cm stainless-steel (ss) extension and (d) tantalum foils along with Pierce, cathode and ss extension.

With these modifications the cathode-ceramic resistance increased from about 0.5 MΩ to ~ 30 GΩ, and the grid-ceramic resistance from ~ 10 MΩ to ~ 7 GΩ. The leakage current at high voltage was greatly reduced and the HV supply could reach 27 kV without reaching its current limit.

In this configuration full beam extraction was demonstrated: 27 keV, 2.4 A and a measured perveance of about 2.1 μA/V$^{1.5}$, close to the design value, see Fig. 5. Operation at these parameters was sustained for about 10 minutes. The total loss current, however, remained around 4.3 mA and the collector pressure about 2×10^{-7} mbar, indicating that further work is needed to understand and reduce the loss budget.

Choices and Positioning of Ceramics

For the 6 cm cathode support three ceramic materials were evaluated: alumina, Macor and Shapal. Alumina and Macor both allowed extraction of 2.4 A at 27 keV with perveance around 2.1 μA/V$^{1.5}$; leakage currents and thermal behaviour were similar. Alumina was selected as baseline due to its superior mechanical strength, while Macor is more fragile.

Shapal (aluminium nitride), although a good electrical insulator, has much higher thermal conductivity. Heat was rapidly conducted from the cathode to the gun structure, causing strong outgassing and preventing stable high-voltage or beam operation; Shapal is therefore not suitable.

Operational experience also showed the importance of ceramic positioning with respect to the magnetic field and beam/ion trajectories. Ceramic surfaces directly exposed along field lines can be coated by sputtered metal or evaporated cathode material and become partially conductive. In one incident, overheating of the cathode led to molybdenum evaporation; X-ray fluorescence confirmed molybdenum deposits on ceramic surfaces and the resistance of an affected feedthrough dropped from the TΩ range to about 200 GΩ at room temperature. The main design rules derived are therefore: keep ceramics cold and avoid exposing them directly to electron or ion trajectories. Both principles are already implemented in the historical gun produced at BINP in Dubna (from here referred as Novosibirsk gun) used in the current AD cooler [8].

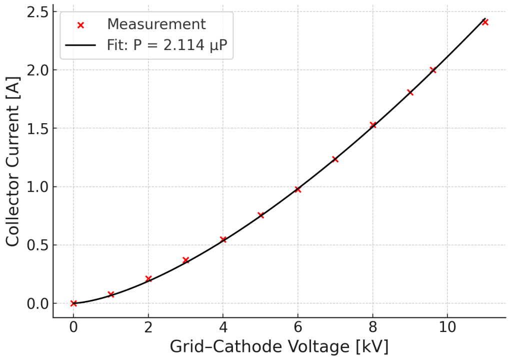

Figure 5: Gun perveance from 2$^{\text{nd}}$ iteration tests.

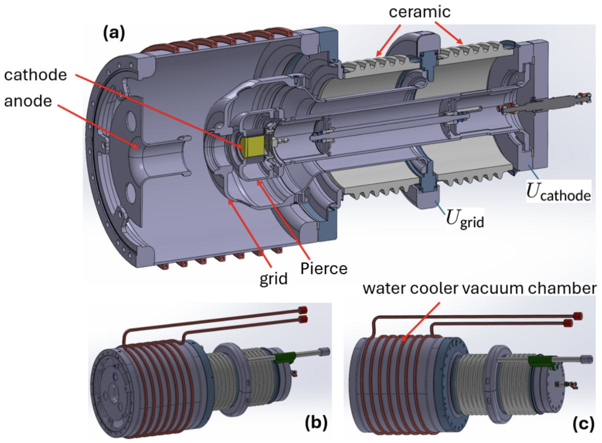

Figure 6: 3D model of the final gun design, combining the validated prototype optics with an externally mounted ceramic layout and cooling circuit.

FINAL GUN DESIGN AND FUTURE TESTS

Combining the validated electrode geometry from the prototype with the proven thermal and insulation concepts of the legacy Novosibirsk gun, a final gun design for the new AD electron cooler has been developed, see Fig. 6. The final gun reuses the high-perveance electrode shapes that demonstrated 2.4 A at 27 kV, while adopting a more conservative ceramic layout inspired by the Novosibirsk gun design [8].

In the final configuration all main ceramics are located outside the vacuum envelope, cooled by air and shielded from direct radiation and sputtering. Their external surfaces are ribbed and profiled to increase the creepage path for surface flashover, and several layers of tantalum shielding surround the cathode region. The gun chamber includes a dedicated water-cooling circuit.

The final gun is in production and will be tested on the ECTS in an upgraded configuration. A new expansion solenoid, providing up to 2400 Gauss at the gun, will be installed upstream of the existing 1.5 m solenoid (operated around 600 G), see Fig. 7. This will allow adiabatic expansion of the beam radius from 12.5 mm to 25 mm, reproducing the AD cooling section. A squeeze coil will be placed just upstream of the final collector. Note that the final collector will have minor differences compared to the collector already validated [10], namely (1) larger vacuum chamber and (2) individual electrodes biasing scheme for improved reliability.

The test bench is now enclosed in a plexiglass box interlocked with the high-voltage cage: opening the enclosure immediately triggers an HV shutdown and returns exposed parts to ground potential. The first comprehensive test campaign of the final gun in this configuration is planned for 2026 and will characterise DC and pulsed operation, high-current and high-voltage limits, stability and cathode lifetime.

Beyond the AD cooler project, the ECTS is evolving into a versatile test facility for high-voltage electron-beam components at CERN. It can be used to qualify guns, collectors and diagnostics (e.g. beam-gas curtain monitors) for other electron coolers and related systems.

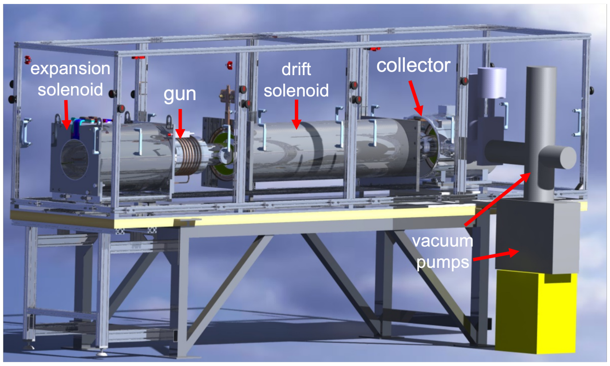

Figure 7: Upgraded ECTS configuration with the final gun inside an expansion solenoid, followed by the long solenoid and the validated collector.

CONCLUSION AND OUTLOOK

The prototype electron gun for the new AD electron cooler has confirmed the validity of the high-perveance electrode geometry, demonstrating beam extraction up to 27 keV, 2.4 A and perveance consistent with simulations. Equally, the tests revealed the dominant limitations related to thermal loading of the ceramic supports, showing that high ceramic resistance, effective shielding, and careful positioning are essential for stable high-voltage operation. These lessons directly informed the final gun design by combining the validated prototype optics with a more robust ceramic layout inspired by the legacy Novosibirsk gun.

The final gun is now in production and will undergo comprehensive testing on the upgraded ECTS, equipped with a 2400 G expansion solenoid and improved safety and vacuum systems. The final collector, featuring a larger vacuum chamber and revised biasing scheme, will also be tested, but is expected to perform similarly to the already validated one. These tests will establish the operating margins, long-term stability and cathode lifetime required for LS3 installation. With these upgrades, the ECTS is becoming a versatile facility for characterizing electron-beam components at CERN, supporting future developments beyond the AD electron cooler.

ACKNOWLEDGEMENTS

The authors thank A. Pikin and F. Wenander for discussions on test results; C. Accettura and T. Hernandez for thermo-mechanical studies; V. Maire, N. Chritin and W. Andreazza for mechanical design; C. Petrone and C. Tsiolakis for magnet testing; and the CERN AD-CONS project team for their continued collaboration.

ISBN: 978-3-95450-267-7 ISSN: 2226-0374 doi: 10.18429/JACoW-COOL2025-WEA2

REFERENCES

[1] G. I. Budker *et al.*, "Experiments on cooling by electrons", *Soviet Atomic Energy*, Vol. 40, pages 50–54, 1976. `doi:10.1007/BF01119392`

[2] F. Krienen, "Initial Cooling Experiments (ICE) at CERN" in *11th International Conference on High-Energy Accelerators*, CERN, Geneva, Switzerland, 7 - 11 Jul 1980, pp.781-93. `doi:10.1007/978-3-0348-5540-2`

[3] H. Poth *et al.*, "First Results of Electron Cooling Experiments at LEAR", *Zeitschrift für Physik*, vol. A332, 1987. `doi:10.1007/BF01289773`

[4] G. Tranquille, "40 years of electron cooling at CERN", *IPAC2018*, Vancouver, BC, Canada, 2018. `doi:10.18429/JACoW-IPAC2018-MOZGBF3`

[5] M. Lamont *et al.*, "AD e-cooler Consolidation Strategy", presented at the 259th IEFC meeting, CERN, Geneva, Switzerland, Dec. 2019, unpublished. `https://indico.cern.ch/event/868354`

[6] D. Gamba *et al.*, "Specifications for a new electron cooler of the antiproton decelerator at CERN", *IPAC 2023*, Venice, Italy, 7 - 12 May 2023. `doi:10.18429/JACoW-IPAC2023-TUPM027`

[7] J. Bosser *et al.*, "The new collector for the electron cooling device at LEAR", *Nucl. Instr. and Meth. A*, vol. 311, no.3, pages 465-471, 1992. `doi:10.1016/0168-9002(92)90642-H`

[8] I. N. Meshkov *et al.*, "The variable current gun: the parameter tests and the results of the first electron cooling experiments at LEAR" *Nucl. Instr. and Meth. A*, Vol. 355, Issues 2-3, pages 208-222, 1995. `doi:10.1016/0168-9002(94)01151-6`

[9] G. Khatri *et al.*, "A test bench for characterizing electron cooler components at up to -80 kVDC", To be published in *COOL'23 workshop*, Montreux, Switzerland, 8-13 Oct. 2023. `doi:10.18429/JACoW-COOL2023-THPOSRP06`

[10] G. Khatri *et al.*, "Development of high-power electron gun and collector for the new antiproton decelerator electron cooler", *IPAC 2024*, Nashville, TN, USA, 19-24 May. 2024. `doi:10.18429/JACoW-IPAC2024-TUPS19`

[11] M. Furman *et al.*, "Probabilistic model for the simulation of secondary electron emission", *Phys. Rev. Spec. Top. Accel. Beams* 5, 124404 2002. `doi:10.1103/PhysRevSTAB.5.124404`

[12] A. Pikin *et al.*, "Simulation of electron guns for electron cooler", presented at an internal CERN meeting on 10 Jan. 2019. `https://indico.cern.ch/event/774322/`

[13] G. Tranquille *et al.*, "Electron Gun and Collector status - EGUN simulation", presented at an internal CERN meeting on 12 Feb. 2024. `https://indico.cern.ch/event/1379735/`

[14] C. Accettura *et al.*, "Gun thermo-mechanical calculations", presented at an internal CERN meeting on 03 Nov. 2022. `https://indico.cern.ch/event/1208848/`

[15] G. Khatri *et al.*, "AD E-Cooler joint E-BEAM meeting on e-beam simulations", presented at an internal CERN meeting on 03 Nov. 2023. `https://indico.cern.ch/event/1339640/`

[16] L. Joergensen, "The collector issues in 2018 & general spares situation", presented at *AD Electron Cooler Consolidation Review* meeting on 26 March 2019. `https://indico.cern.ch/event/797056/`

ISBN: 978-3-95450-267-7 ISSN: 2226-0374 doi: 10.18429/JACoW-COOL2025-WEA3

PROGRESS TOWARDS A FIELD EMISSION ELECTRON GUN FOR THE ELENA ELECTRON COOLER

G. A. Tranquille*, CERN, Geneva, Switzerland
E. Welker†, TU Wien, Vienna, Austria

Abstract

Field emission-based cathodes have been shown to be an attractive alternative to thermionic sources for the generation of electron beams. Their low transverse energy spread, and low power consumption make them an ideal replacement for the thermionic cathode currently used on the electron cooler of the Extra Low ENergy Antiproton (ELENA) ring.

We have investigated the use of carbon nanotubes (CNT) as the field emitting source, studying the emission characteristics and lifetime of various patterned structures. Fowler-Norheim analysis of our samples has given us a better understanding of the limiting factors of such sources, especially the influence of the conditioning process on the emitted current.

A double-gridded electron gun has also been tested with CNT samples of various sizes up to 4×4 cm. The measured current density for the larger samples was somewhat lower that expected and showed a larger beam divergence than what was predicted by the simulations. This discrepancy is currently under investigation as well as improvements to the gun design to obtain stable and reproducible beams.

INTRODUCTION

In ELENA, electron cooling is fundamental to reduce the emittance blow-up of the antiproton beam so that a focused and bright beam can be delivered to the experiments [1]. Presently, the electron gun relies on thermionic emission, where a tungsten-doped barium oxide (BaO) source is heated to 1200 °C. However, this imposes several limitations on the transverse beam energy and the required magnet system. A cold emission-based electron gun might overcome these constraints, as field emission relies solely on high electric fields to both generate and control the electron beam.

WHY CARBON NANOTUBES?

Despite field emission being a known effect since 1928 when first proposed by Fowler and Nordheim [2], it has only recently become a flourishing field of research thanks to the technological progress that has opened to the possibility of creating 2D nano-structures. 2D nano-materials can have greatly enhanced field emission properties and allow to extract relatively high currents (usually tens of mA/cm^2) at relatively low applied electric field (some V µm^{-1}) [3]. This is possible thanks to a field enhancement at the nano-structure surface, usually described by means of the so-called field enhancement factor β.

For our development, CNTs have been chosen due to their remarkable properties in this field. They are nowadays considered among the most promising material for field emission, reaching high current densities, being largely chemically inert and having a good emission stability. Several groups have reported promising results using arrays of vertically aligned CNTs. Such an arrangement minimizes the screening effect which usually severely affects the performance of forests and disordered structures.

EXPERIMENTAL SETUP

The Cold-Cathode-Test-Bench (see Fig. 1) has undergone a major upgrade since the initial measurements and now encompasses the gun assembly installed in a vacuum tank mounted on a 6-way cross. Three flanges are dedicated for the Edwards Vacuum Pump and Pfeiffer TPG 362 Dual Gauge, a Vacom Novion vacuum sensor and a PHOTONIS Ion Beam Profiler (IBP). A three sample holder is installed on the final flange for testing the emission characteristics of individual carbon nanontube structures.

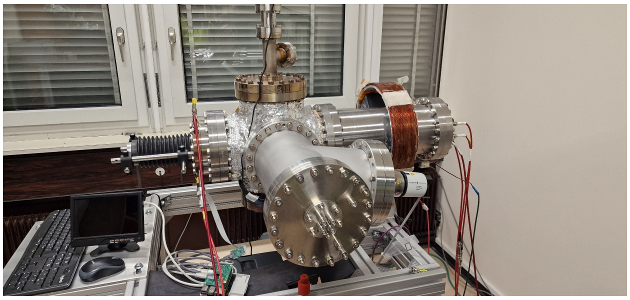

Figure 1: Cold Cathode Test Bench (CCTB)

CNT SAMPLE MEASUREMENTS

In previous studies we investigated the emission stability and lifetime of patterned CNT arrays purchased from NanoLab Inc. [4]. We concluded that hexagonal structures were best suited for our application, giving relatively high emission currents with good long-term stability.

A new set of CNTs of various dimensions was obtained from the International Iberian Nanotechnology Laboratory (INL, `https://inl.int/`) in Braga, Portugal. Hexagonal CNT arrays of 10 µm side and 20 µm height spaced by 3 µm (see Fig. 2) were grown by chemical vapour deposition (CVD) on silicon wafers and diced to the required dimensions [5]. Samples were first conditioned and characterised on the measurement flange and then transferred to the gun for beam profile measurements. The conditioning consists in slowly ramping the voltage to a fixed value whilst monitoring

---

[*] gerard.tranquille@cern.ch
[†] elisabeth-sena.welker@outlook.com

ISBN: 978-3-95450-267-7 ISSN: 2226-0374 doi: 10.18429/JACoW-COOL2025-WEA3

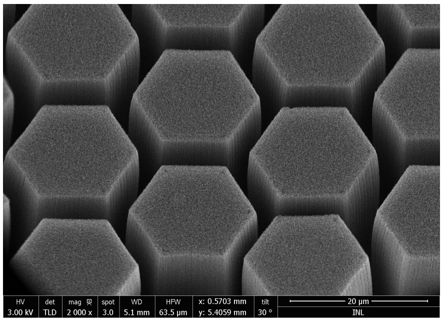

Figure 2: SEM image of the hexagonal CNT array

the vacuum level and emission current. When the emission has stabilised and the vacuum fully recuperated, the electric field is slowly ramped to a higher level. This is performed three or four times until it is deemed that breakdowns due to gas ionisation is no longer an issue.

Fowler Nordheim (FN) Analysis

After vacuum conditioning, the emission properties of different samples as a function of the applied voltage was studied. The first sample to be measured was the 4 cm × 4 cm large area CNT which was expected to emit a current density equivalent to what is needed for cooling in ELENA. The first ramp (see Fig. 3, navy blue curve) shows a very random behaviour of the emitted current. This is probably due to an incomplete conditioning of the sample resulting in an alteration of the field emitter tips. The subsequent ramps display a more normal emission following the classical Fowler-Nordheim equation:

$$J = \frac{AE_L^2}{\phi} \mathrm{e}^{\left(\frac{-B\phi^{3/2}}{E_L}\right)} \tag{1}$$

where J is the current density, A $=1.54 \times 10^6$ A eV V^{-2}, B $=6.83 \times 10^9$ eV$^{-3/2}$ V m^{-1}, ϕ is the work function of the material, and E_L is the local field at the emitting tip. $E_L = \beta E$, with E being the applied electric field and β the field enhancement factor [6, 7].

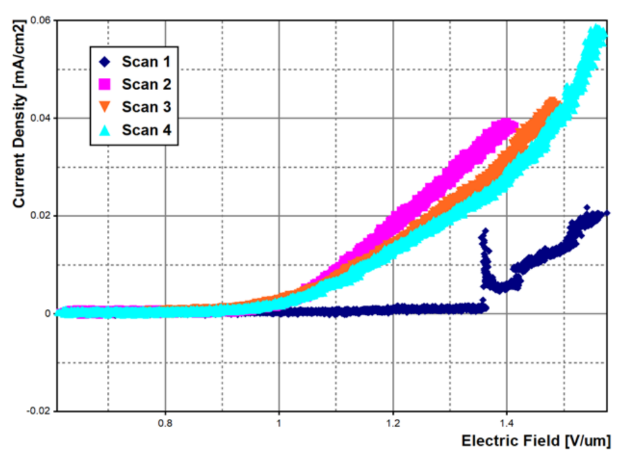

Figure 3: Four FN scans of the 4x4 CNT sample

To fit the data, we used the generalised Fowler-Nordheim equation (2) due to its streamlined form compared to equation (1). It describes the emission behaviour well enough for most emitters:

$$J(E) = AE^2 \mathrm{e}^{\left(\frac{-B}{E}\right)} \tag{2}$$

The applied electric field E can be approximated, using the anode-cathode voltage V and inter-electrode separation d, by $E \approx V/d$. Constants A and B are defined by the material properties and experimental conditions. By fitting data to this exponential curve, it is possible to determine key parameters for evaluating emission performance and comparing different emitters or conditioning methods.

Seppen-Katamuki (SK) Plots

To further analyse the contributions of β and ϕ to the field emission performance, a Seppen-Katamuki (SK) plot is commonly used. The exponential relationship described in equation (2) is used to plot $\ln(J/E^2)$ versus $1/E$. In an ideal FN process, this plot is linear, confirming that quantum tunnelling dominates the emission, where as deviations indicate additional adverse influences. In an SK plot, the abscissa represents intercept of the FN plot, while the ordinate represents the slope m.

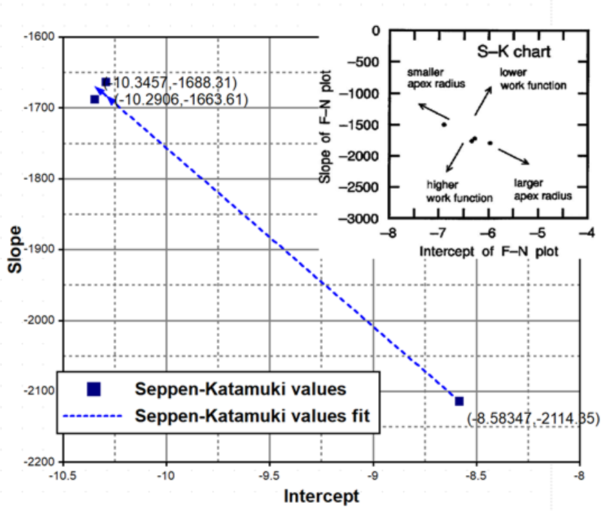

Figure 4: SK plot of three scans for the 4 × 4 cm CNT sample

The SK plot for three scans (scans 2 to 4) of the 4 cm × 4 cm sample is shown in Fig. 4. One clearly sees an evolution of the SK values indicating a change in the tip apex radius for each ramp up of the electric field. FN scans have also been performed on samples of different sizes. Their behaviour is similar to what was observed with the 4 cm × 4 cm sample. We believe that the main cause of the initial degradation is Joule heating which is enhanced because of the low intertube spacing. Once the tips have burnt-off, the sample emits more uniformly but the screening effect eventually results in localised heating which in turn causes peeling of the CNTs from the substrate surface.

ISBN: 978-3-95450-267-7 ISSN: 2226-0374 doi: 10.18429/JACoW-COOL2025-WEA3

FIELD EMISSION CNT (FECNT) GUN MEASUREMENTS

Gun Design

We have developed a dual-gridded electron gun based on a cold cathode CNT sample. It relies on a triode configuration where the extracting anode and the third electrode are referred to as grid 1 and grid 2. In this configuration the silicon wafer, on whose surface the CNTs are grown, is used as a cathode with a negative applied voltage. The voltage on grid 1 is responsible for creating the local electric field that extracts the electrons from the CNTs. Grid 2 is usually grounded so that the electrons can be transported downstream with the required beam energy (for ELENA operation 355 eV). The two grids were manufactured by MicroCreate BV using a highly n-doped round silicon wafer with a thickness of 100 µm and a diameter of four inches. The wafer was thinned down to 50 µm in a central area where a rectangular hole pattern measuring 3 × 3 cm was created. The mesh consists of 15 µm square holes separated by 3 µm walls. Additionally, two MACOR ring-shaped spacers are used for insulation between cathode/grid 1 and grid 1/grid 2. The spacers inner diameter limits the beam size and act as a short drift tube for the beam. The final component is a focusing electrode; an aluminium ring with a triangular-shaped cross-section. It is designed to maintain straight field lines and keep the transverse energy of the emitted beam low. All edges of metal surfaces exposed to high voltage are rounded, to reduce the risk of electrical discharges and arcing. HV coaxial feedthroughs in the upstream flange were used to make electrical connections to the power supplies or multimeters. All these components, collectively referred to as the “emitter region”, are stacked and secured with peek screws. After the focusing electrode, the beam is directed through an Einzel lens system onto the beam profile monitor.

Figure 5: electron gun (left),CNT holder (middle),emitter region (right)

Source Test

The first tests with a 4 × 4 cm CNT sample proved to be inconclusive. We only managed to observe a bright signal filling the whole observation window. As a result it was decided to switch to a 1 × 1 cm CNT sample previously validated with an emission current density close to 1 mA cm^{-2}. The Einzel lens was also removed such that the emitted electrons could be visualised directly on the monitor window. An electron beam current of 0.52 mA was obtained but the beam spot seen on the screen (see Fig. 6) was much larger than expected from the CST simulations [8], indicating a large beam divergence at the source. It was also noted that the beam was deviated to the top right hand side of the monitor. We suspected that only part of the CNT source was effectively emitting which was confirmed with COMSOL simulations.

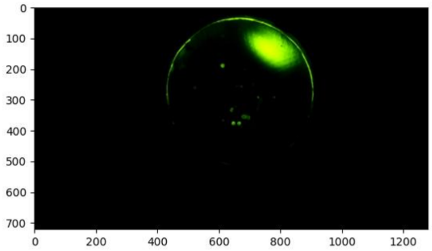

Figure 6: 520 µA beam spot observed on the IBP

Gun Tests With Einzel Lens

Having seen beam for the first time on the IBP, the Einzel lens was reinserted into the system and the trajectory was tuned to steer the beam onto the IBP. A short solenoid was installed around the source to focus the beam at the source exit and the the Einzel lens electrodes were scanned over a range of voltages from -200 V to +150 V. The final setting for the solenoid was 0.7 A (giving a longitudinal field of only 3.8 Gauss) and -130 V on the middle Enzel lens electrode (the other two were set to 0 V). This enabled us to transport a 260 µA electron beam to the monitor. Using small permanent magnets the beam could also be scanned across the window without any loss in beam intensity.

Long-Term Stability Measurements

Following the successful generation and transport of a beam from the FECNT electron gun, a long-term stability test was conducted. The aim was to measure if the CNT could emit a stable current continuously over a long period of time. Figure 7 shows the beam current intensity and fluctuations over 28 days, corresponding to approximately 670 hours. As the vacuum improves in the setup, one also sees that the intensity fluctuations stabilise.

CONCLUSION

We have demonstrated that an electron source based on field emission is a viable alternative to a thermionic source for eventual use in a low energy electron cooler. A double-gridded gun has been prototyped and has shown very promising results. The design of the source focussing electrode needs to be addressed as the emitted beam is clearly too divergent. Alternative field emission sources should also

ISBN: 978-3-95450-267-7 ISSN: 2226-0374 doi: 10.18429/JACoW-COOL2025-WEA3

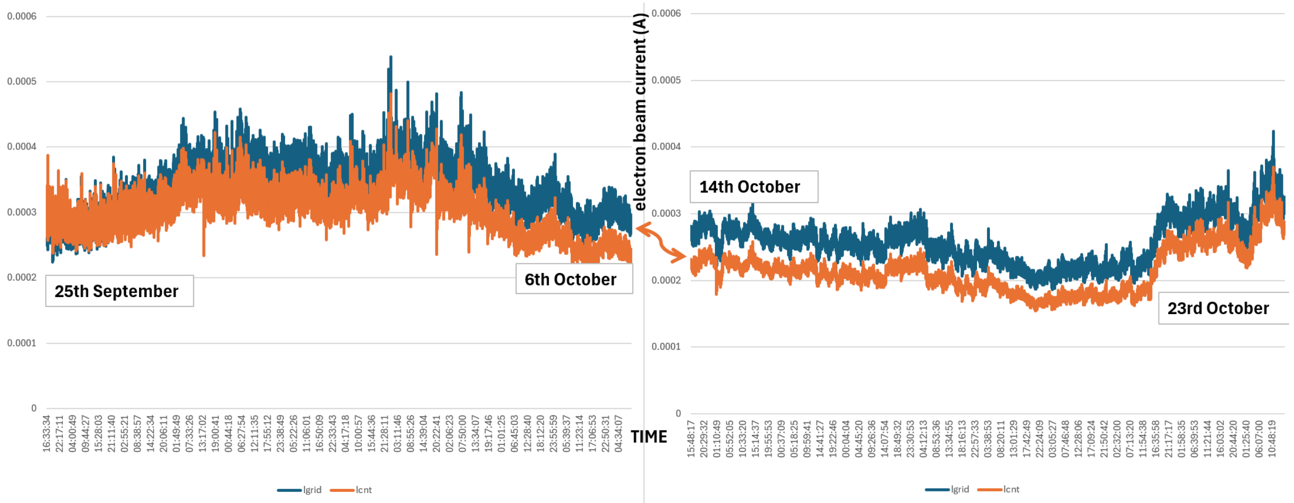

Figure 7: Long-term stability measurement of a 0.64 cm^2 CNT source

be investigated as the performance of large-area CNTs is very dependent on the growth process. Gated FE arrays such as Spindt cathodes [9] could be the way forward to obtaining the required performance not only in intensity but also long-term stability.

REFERENCES

[1] S. Maury, W. Oelert, W. Bartmann, P. Belochitskii, H. Breuker, F. Butin, C. Carli, T. Eriksson, S. Pasinelli, and G. Tranquille. "ELENA: the extra low energy antiproton facility at CERN." in Hyperfine Interact **229** (2014).

[2] R.H.Fowler and L.Nordheim. "Electron Emission in Intense Electric Fields." in Proceedings of the Royal Society of London. Series A, Containing Papers of a Mathematical and Physical Character 119.781 (1928), issn: 09501207. `http://www.jstor.org/stable/95023`

[3] Yahachi Saito. Carbon Nanotube and related field emitters: Fundamentals and applications. Wiley-VCH, 2010. isbn: 978-3-527-32734-8.

[4] `https://www.nano-lab.com/`

[5] L.Sun, G.Yuan, L.Gao, J.Yang, M.Chhowalla, M.H.Gharahcheshmeh, K.K.Gleason, Y.S.Choi, B.H.Hong, and Z.Liu. "Chemical vapour deposition." in Nature Reviews - Methods Primers (2021)1:5 (2021).

[6] S.Parveen et al. "Fowler Nordheim theory of carbon nanotube based field emitters." in Physica B: Condensed Matter 505 (2017), issn: 0921-4526. `https://doi.org/10.1016/j.physb.2016.10.031`

[7] G.S.Bocharov and A.V.Eletskii. "Theory of Carbon Nanotube (CNT)-Based Electron Field Emitters." in Nanomaterials 3.3 (July 17, 2013), `https://doi.org/10.3390/nano3030393`

[8] G.Tranquille et al. "Development of a Field Emission Electron Gun for Low Energy Electron Cooling." Proceedings COOL23 (October 8th - 13th, 2023), `https://doi.org/10.18429/JACoW-COOL2023-THPOSRP10`

[9] C.A.Spindt, I.Brodie, L.Humphrey, and E.R.Westerberg. "Physical properties of thin-film field emission cathodes with molybdenum cones." in J. Appl. Phys. 47, 5248–5263 (1976), `https://doi.org/10.1063/1.322600`

STOCHASTIC COOLING ENHANCED STEADY-STATE MICROBUNCHING

Xiujie Deng*, Institute for Advanced Study, Tsinghua University, Beijing, China

Abstract

In this paper, we propose to combine two promising research topics in accelerator physics, i.e., optical stochastic cooling (OSC) and steady-state microbunching (SSMB). Our study shows that such an OSC-SSMB storage ring with a circumference of 50 m and beam energy of several hundred MeVs using present technology can deliver kilowatt radiation at 100 nm wavelength. A more ambitious application of OSC in an SSMB ring can push the radiation wavelength to an even shorter wavelength, such as EUV and soft X-ray. Such a powerful compact light source could benefit fundamental science research and industry applications.

INTRODUCTION

Steady-state microbunching (SSMB) [1–3] scales the bunching mechanism in a storage ring from the conventional microwave or radio-frequency (RF) region to optical wavelengths to generate ultrashort electron bunches on a turn-by-turn basis for high-power short-wavelength coherent radiation generation, and its proof-of-principle experiment has been successfully conducted recently at the MLS storage ring [4, 5]. Optical stochastic cooling (OSC) [6, 7] is a scaling of the conventional stochastic cooling scenario from the microwave to optical frequency range to speed up the damping of particle beam emittance. Its mechanism has also been demonstrated recently in the IOTA storage ring [8, 9]. One interesting idea is then to combine them, which hopefully can relax the technical requirements and enhance the capabilities of an SSMB radiation source.

SSMB SCENARIOS

SSMB is a general concept and there are several specific scenarios for its realization. Here we group these scenarios into two categories, i.e., globally microbunching schemes and locally microbunching schemes.

Globally Microbunching / Longitudinal Focusing

For globally microbunching or longitudinal focusing schemes, it means the electron beam is microbunched all around the ring. Generally, these SSMB schemes require the storage ring to work in a quasi-isochronous or low-alpha mode. The laser modulators are used in a way similar to that of RF cavities in a conventional storage ring, i.e., to longitudinal focus the electron beam to make it become microbunched. The microbunches are thus separated with a distance of the modulation laser wavelength. Note that due to the impact of local phase slippage factor and transverse-longitudinal coupling [2], the microbunch length can vary significantly around the ring. The microbunching here therefore more accurately refers to microbunching in phase space. Depending on the strength and mechanism of longitudinal focusing, we have developed three such SSMB scenarios in the past years, namely longitudinal weak focusing (LWF), longitudinal strong focusing (LSF) and generalized longitudinal strong focusing (GLSF) [10, 11], as schematically shown in Fig. 1. For a comprehensive analysis of their beam physics, the readers can refer to Ref. [11].

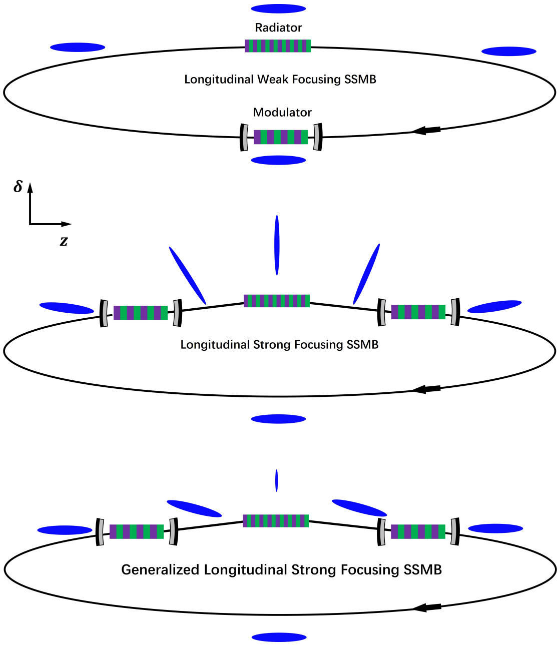

Figure 1: Schematic layouts of a longitudinal weak focusing (top), longitudinal strong focusing (center) and generalized longitudinal strong focusing (bottom) SSMB storage ring.

For globally microbunching schemes, the key is to realize a small equilibrium beam emittance. At least one of the three eigen emittances should be ultra-low to realize ultra-short electron bunch with a mild requirement on the modulation laser power. For LWF and LSF SSMB, it is the longitudinal emittance, while for GLSF SSMB it is the vertical emittance.

Locally Microbunching / Reversible Modulation

For locally microbunching schemes, it means microbunching appears only in a limited section in a storage ring. Outside that limited region, the electron beam is just a conventional bunch, which means it can be an RF bunch, or even a coasting beam. A representative method to realize locally microbucnhing is using a downstream reverse laser modulation to cancel the modulation imprinted in the upstream laser modulator, and microbunching only appears at the radiator in between [12, 13]. By invoking such a

---

* dengxiujie@mail.tsinghua.edu.cn

ISBN: 978-3-95450-267-7 ISSN: 2226-0374 doi: 10.18429/JACoW-COOL2025-WEB1

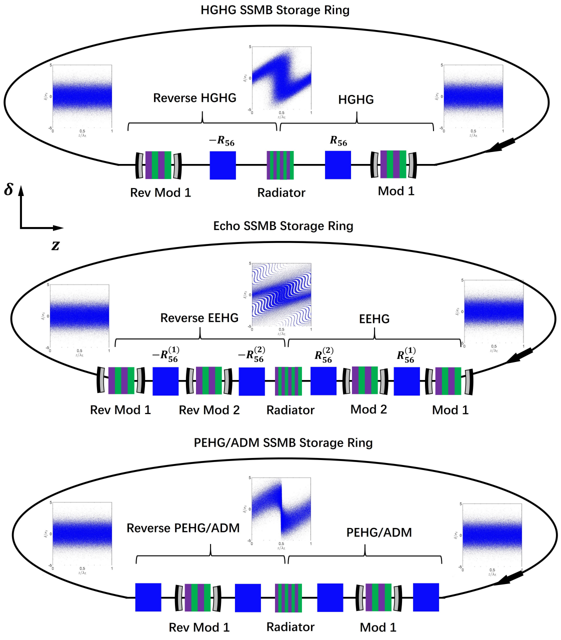

Figure 2: Schematic layouts of a reversible HGHG (top), reversible EEHG (center) and reversible PEHG/ADM (bottom) SSMB storage ring.

reversible modulation scheme, the storage ring does not need to be quasi-isochronous. Depending on the laser-induced microbunching technique, for example HGHG [14], EEHG [15], PEHG/ADM [16, 17], we can have HGHG SSMB, Echo SSMB, PEHG/ADM SSMB as shown in Fig. 2. For a comprehensive analysis of beam physics of these reversible microbunching schemes, especially that of the Echo SSMB scenario, the readers can refer to Ref. [13].

The key of reversible microbunching is to realize perfect modulation cancellation such that the equilibrium beam parameters can preserve and the microbunching process can repeat turn-by-turn. However, in reality, due to various physical effects, the modulation cancellation cannot be perfect. One critical issue is the longitudinal coordinate deviation of a particle Δz from its ideal location between the upstream laser modulator and downstream reverse laser modulator,

$$\Delta\delta = \frac{h}{k_L}\{\sin[k_L(z+\Delta z)] - \sin(k_L z)\}, \tag{1}$$

with k_L the laser wavelength and h the energy chirp strength around zero-crossing phase. The sources of Δz include effects like quantum excitation, intrabeam scattering (IBS), coherent radiation, linear optics mismatch and lattice nonlienarities [13]. A non-perfect cancellation will result in a growth of the energy spread, and when $|\Delta z| \ll \lambda_L$, we have $\Delta\sigma_\delta^2 = (h\sigma_{\Delta z})^2/2$. And if the modulators are placed at dispersive locations, like that in PEHG/ADM SSMB, it will also lead to a growth of transverse emittance.

For HGHG and Echo SSMB, the key parameter is the energy spread. For PEHG/ADM SSMB, it is the vertical emittance. A growth of these parameters means the required modulation laser power will be even higher to realize a given coherent radiation wavelength. Our analysis has revealed a universal criterion for the tolerance of rms value of Δz [13]

$$\sigma_{\Delta z} \lesssim \frac{\lambda_R}{\pi}\sqrt{2/N_{z,\mathrm{damp}}}, \tag{2}$$

where λ_R is the target radiation wavelength, and $N_{z,\mathrm{damp}}$ is the longitudinal damping time in unit of revolution numbers.

Motivation of a Faster Damping

A faster damping in an SSMB storage ring can help to obtain a smaller equilibrium beam emittance, energy spread, increase the tolerance of non-perfect modulation cancellation, and fight against collective effects. This can mitigate the technical challenges and enhance the potential of an SSMB source. While damping wiggler seems to be a straightforward choice to enhance damping, an OSC section has the advantage of a more compact setup and a higher efficiency of wall-plug electricity to user desired radiation.

OSC BASICS

After a brief introduction of SSMB, here we present some basics of OSC to make our paper more self-contained.

Cooling Mechanism and Damping Rate

The cooling mechanism of an OSC section is to use each electron's radiation generated in the pick-up undulator to correct its own momentum deviation in the kicker undulator. The kickes of nearby electrons' radiations in the radiation slippage length is a heating effect. Assume that the corrective energy kick due to each particle's own radiation is given by

$$\Delta\delta_{\mathrm{O}} = -A\sin(k_{R\mathrm{O}}\Delta z_{\mathrm{O}}). \tag{3}$$

And if $\Delta z_{\mathrm{O}} = R_{56}\delta$ with R_{56} the momentum compaction between the pick-up and kicker undulator, then the longitudinal damping rate is

$$\alpha_{L\mathrm{O}} = Ak_{R\mathrm{O}}R_{56}/2. \tag{4}$$

For the analysis of damping rates in a general coupled lattice, the readers can refer to Ref. [18]. Considering the sinusoidal waveform of the kick, the damping rate is actually amplitude-dependent. And to ensure damping for majority of the particle beam, we need a sufficient cooling range [9].

Bandwidth Limit

The bandwidth W of an OSC section is limited by the ability of identifying each electron, which is determined by the OSC undulator radiation slippage length $N_{u\mathrm{O}}\lambda_{R\mathrm{O}}$. So $W = f_{R\mathrm{O}}/N_{u\mathrm{O}}$, with $f_{R\mathrm{O}}$ and $N_{u\mathrm{O}}$ the OSC undulator radiation frequency and period number, respectively. Assume perfect mixing and appropriate amplifier applied, the theoretical optimal damping rate is $\frac{1}{\tau} = \frac{W}{N}$, with N the total number of particles in the ring. For a coasting beam, we have the optimal damping time in unit of revolution

$$N_{z,\mathrm{damp,opt}} = \text{No. of } e \text{ in the OSC radiation slippage}. \tag{5}$$

To get a fast damping in OSC, a short radiation slippage length is required. In this sense, a shorter OSC undulator radiation wavelength is desired, for example EUV [19].

ISBN: 978-3-95450-267-7 ISSN: 2226-0374 doi: 10.18429/JACoW-COOL2025-WEB1

Mixing Condition

A central problem in stochastic cooling is the mixing. Loosely, a good mixing means the particles in the OSC radiation slippage length update turn-by-turn. More accurately, it means the overlap of particles' Schottky bands in the feedback system bandwidth. Since reversible SSMB scenarios do not require a small momentum compaction for the ring, the mixing condition can be straightforwardly satisfied in these schemes, as long as we have

$$|\sigma_{\delta}\eta C_0| \gg N_{uO}\lambda_{RO}, \tag{6}$$

with σ_δ the beam energy spread, η and C_0 the phase slippage factor and circumference of the ring. In this paper we only discuss the application of OSC in a reversible SSMB ring.

The mixing condition in globally microbunching schemes is more subtle. And the combination of these schemes with OSC will be reported elsewhere in the future.

Radiation Kick Strength

The OSC radiation kick strength A in Eq. (3) is determined by the details of pick-up, kicker, optical system and amplifier if there is one. Assume identical pick-up and kicker planar undulator, and the optical system is refractive. And assume a perfect linear amplifier. The radiation kick strength is [9]

$$A = \frac{1}{4\pi\varepsilon_0}\frac{(e\gamma K k_u)^2}{3\gamma m_e c^2}2L_u[JJ]F_h(K,\gamma\theta_m)\sqrt{G}, \tag{7}$$

with θ_m the angular acceptance of the focusing lens, G the radiation power amplification factor and for $0 \le K \le 4$ we have $F_h(K,\infty) \approx 1/\left(1+1.13K^2+0.04K^3+0.37K^4\right)$.

Equilibrium Energy Spread

If we consider the combined affects of OSC, radiation damping, quantum excitation and other diffusion-like effects, the equilibrium energy spread is given by,

$$\sigma_{\delta\mathrm{O}} = \frac{1}{2}\sqrt{\left(\Delta\sigma^2_{\delta\mathrm{O}}+\Delta\sigma^2_{\delta\mathrm{QE}}+\Delta\sigma^2_{\delta\mathrm{other}}\right)/(\alpha_{L\mathrm{O}}+\alpha_{L\mathrm{RD}})}. \tag{8}$$

where $\Delta\sigma^2_{\delta\mathrm{O}} = \frac{I_P}{ec}\frac{N_{u\mathrm{O}}\lambda_{R\mathrm{O}}}{3}A^2$ is the heating effect of nearby particles' radiation kick in the OSC, $\Delta\sigma^2_{\delta\mathrm{QE}} = 4\alpha_{L\mathrm{RD}}\sigma^2_{\delta0}$ is the natural quantum excitation with $\sigma_{\delta0}$ the natural energy spread and $\alpha_{L\mathrm{RD}}$ the longitudinal radiation damping rate, $\Delta\sigma^2_{\delta\mathrm{other}}$ is from the other energy spread growth effects, for example that due to the non-perfect cancellation in a reversible SSMB ring. With other parameters fixed, there is an optimal A to minimize the equilibrium energy spread.

COMBINE OSC WITH REVERSIBLE SSMB

Schematic Setup and Parameters List

Now we use the application of OSC in a reversible HGHG SSMB ring to increase the longitudinal damping rate as an example to demonstrate the benefit of implementing OSC in an SSMB storage ring. A schematic layout of such an OSC-HGHG-SSMB storage ring is shown in Fig. 3, and an example parameters list is given in Tab. 1. In this example, the desired radiation wavelength is assumed to be the 8-th harmonic of the modulation laser, i.e., λ_R = 100 nm with λ_L = 800 nm. The envisioned ring consists of two arcs and two straight sections. The circumeference of such a ring is about 50 m. The two straights are about 2×15 m, and the two arcs are about 2 × 10 m. The OSC section is implemented in one straight section, while the other is used for HGHG and reverse HGHG. The average modulation laser power is set to be 1 MW, which is close to the state-of-art value reachable in an optical enhancement cavity [20]. All the parameters in Tab. 1 should be feasible from a practical viewpoint.

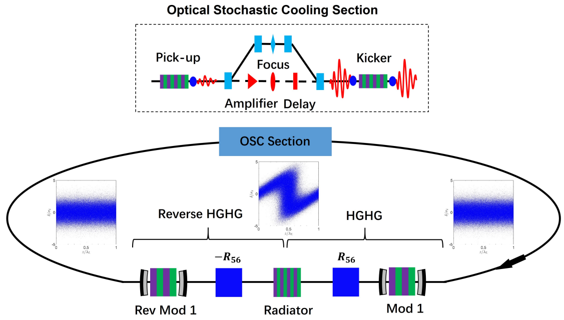

Figure 3: Schematic layout of applying OSC in a reversible HGHG SSMB storage ring.

Induction Linac and Barrier Bucket

To mitigate collective effects like IBS, the peak current we applied is not too high, namely 1 A. While for a high-average-power output radiation, we hope for a high average beam current. Therefore, we may use induction linac as the energy compensation system to get a costing beam with a large filling factor for example 50% in the ring. Assuming the repetition rate of the induction linac is the same as the particle revolution frequency in the ring, which is 6 MHz. The acceleration voltage $V_{\mathrm{acc}} \approx 2$ kV, considering that the incoherent radiation loss in dipoles and coherent radiation loss in radiator undulator are each about 1 keV per electron. To form the barrier bucket, we let the acceleration voltage have two edge slopes as shown in Fig. 4. The barrier bucket half-height formed by these two slopes is $\Delta\delta = \sqrt{\frac{eV_0}{E_0}/\frac{\eta C_0}{c\Delta t}}$, with V_0 and Δt the magnitude and time duration of the slope.

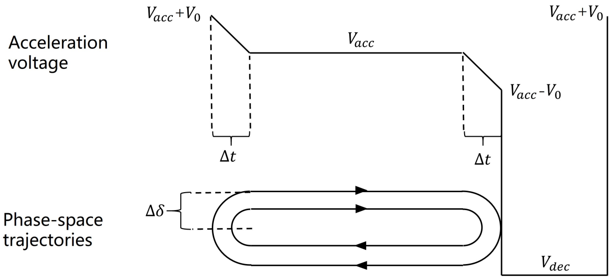

Figure 4: The schematic layout of applying an induction linac for energy compensation and barrier bucket formation.

ISBN: 978-3-95450-267-7 ISSN: 2226-0374 doi: 10.18429/JACoW-COOL2025-WEB1

Table 1: An example parameters set of an OSC-HGHG-SSMB ring for high-power 100 nm radiation generation.

Para.	Value	Description
E_0	300 MeV	Beam energy
C_0	50 m	Circumeference
η	1×10^{-3}	Phase slippage factor
$I_P(I_A)$	1 A (0.5 A)	Peak (Average) current
B_{ring}	1.25 T	Bending field of dipoles
$\sigma_{\delta 0}$	2.9×10^{-4}	Natural energy spread
$\tau_{\delta\text{RD}}$	55.8 ms	Longitudinal R.D. time
$\frac{\alpha_{L\text{O}}}{\alpha_{L\text{RD}}}$	10	Ratio of two damping
$\sigma_{\delta\text{O}}$	1.9×10^{-4}	Energy spread with OSC
$\tau_{\delta\text{O}}$	5.1 ms	Damping time with OSC
$\tau_{\delta,\text{IBS}}$	$\gtrsim$ 100 ms	IBS diffusion time
λ_L	800 nm	Laser wavelength
h	9425 m^{-1}	Liner energy chirp strength
λ_u	4.5 cm	Modulator undulator period
B_0	1.13 T	Modulator peak field
L_u	3.15 m	Modulator undulator length
$P_{L,A}$	1 MW	Laser average power
$\sigma_{\Delta z}$	0.2 nm	rms Δz between LMs
$\Delta\sigma^2_{\delta\text{ins}}$	1.8×10^{-12}	$\Delta\sigma^2_\delta$ per pass of insertion
$\Delta\sigma^2_{\delta\text{O}}$	1.9×10^{-12}	$\Delta\sigma^2_\delta$ per pass of OSC
$\Delta\sigma^2_{\delta\text{QE}}$	1×10^{-12}	$\Delta\sigma^2_\delta$ quantum excitation
$\lambda_{R\text{O}}$	266 nm	OSC radiation wavelength
$\lambda_{u\text{O}}$	3 cm	OSC undulator period
$B_{0\text{O}}$	1.14 T	OSC undulator field
$L_{u\text{O}}$	15 cm	OSC undulator length
N_s	2.77×10^4	No. of e in a slippage length
G	178	Power amplification factor
R_{56}	179 µm	R_{56} between two undulators
$\frac{\mu_{01}}{k_{R\text{O}} R_{56} \sigma_{\delta\text{O}}}$	3	Cooling range
λ_R	100 nm	Radiation wavelength
b_8	0.1	Bunching factor
$\epsilon_\perp$	6 nm	Transverse emittance
$\sigma_\perp$	~100 µm	Transverse beam size
λ_u	2 cm	Radiator undulator period
B_0	1.18 T	Radiator peak field
L_u	6 m	Undulator length
P_P	1 kW	Peak radiation power
P_A	0.5 kW	Average radiation power

If $E_0 = 300\,\text{MeV}$, $C_0 = 50\,\text{m}$, $\eta = 1\times10^{-3}$, $\Delta t = 20\,\text{ns}$, then to realize a bucket half-height of $\Delta\delta = 0.02$ which means about $100\sigma_{\delta\text{O}}$ given in the table, then we need $V_0 = 1$ kV. Such a requirement on induction linac should be feasible. We point out that it is also possible to realize a large beam filling factor by using the combination of different RF harmonic cavities to lengthen the RF bunch in a RF bucket.

Intrabeam Scattering

To minimize the IBS diffusion rate, we have used a transversely round electron beam, with a large transverse emittance of $\epsilon_\perp = 6$ nm. The IBS diffusion of energy spread for a transversely round beam ($\epsilon_x = \epsilon_y$) is [21] $\tau^{-1}_{\delta,\text{IBS}} \approx \frac{\Psi_0 I_P r_e^2 L_C}{8e\gamma^3\sigma_\delta^2\langle\sigma_x\rangle\epsilon_\perp}$, where Ψ_0 is a constant depending on the lattice optics around the ring. Here for an order of magnitude estimation, we put in some numbers, $\Psi_0 = 1$, Columb Log $L_c = 10$, average transverse beam size around the ring $\langle\sigma_x\rangle = \sqrt{6\text{ nm} \times 10\text{ m}} \approx 250\,\mu\text{m}$, $\sigma_\delta = 1.9 \times 10^{-4}$, $I_P = 1$ A, we have $\tau_{\delta,\text{IBS}} = 169$ ms, which is more than one order of magnitude longer than the OSC damping time. For the transverse dimension $\tau_{\perp,\text{IBS}} = \frac{\epsilon_\perp}{\sigma_\delta^2\langle\mathcal{H}_\perp\rangle}\tau_{\delta,\text{IBS}}$. When $\langle\mathcal{H}_\perp\rangle \lesssim 0.2$ m, it is acceptable for the transverse dimensions.

Coherent Undulator Radiation

The radiator is assumed to be an undulator. The radiation power at the fundamental resonance frequency from a transversely-round electron beam in a planar undulator is [2]

$$P_{\text{peak}}[\text{kW}] = 1.183 N_u \chi [JJ]^2 FF_\perp(S) |b_z|^2 I_P^2 [\text{A}], \quad (9)$$

where $[JJ]^2 = [J_0(\chi) - J_1(\chi)]^2$, with $\chi = \frac{K^2}{4+2K^2}$ and K being the undulator parameter, and the transverse form factor is $FF_\perp(S) = \frac{2}{\pi}\left[\tan^{-1}\left(\frac{1}{2S}\right) + S\ln\left(\frac{(2S)^2}{(2S)^2+1}\right)\right]$, with $S = \frac{\sigma_\perp^2 \frac{\omega}{c}}{L_u}$ is the diffraction parameter and $\sigma_\perp$ the rms transverse electron beam size, b_z is the bunching factor at the radiation wavelength, and I_P is the peak current. For the radiation power of a helical undulator, there is no $[JJ]^2$ factor and the power can roughly be about a factor of 2 larger. The power given in the table assumes a helical undulator radiator. Similarly we can also use a helical undulator as the modulator to lower the required modulation power by a factor of 2 compared to a planar undulator as modulator.

Remaining Issues

Feasible in principle, there are important issues to be resolved before such an OSC-HGHG-SSMB ring becoming a reality. For example, is the required amplifier of OSC radiation available at such short wavelength? We recognize that we may also do OSC without an amplifier. Is it challenging to realize the required phase-locking of electron and its own radiation in OSC, especially when we want to shorten the radiation wavelength to increase the bandwidth for a faster damping? How to realize the phase locking of the two optical cavities, or more accurately locking of the downstream laser modulator to the electron beam arrival time to ensure perfect modulation cancellation?

SUMMARY

Both OSC and SSMB have great potential, here we propose to combine them for an even brighter and longer future. The application of OSC in a reversible SSMB ring for a 1 kW 100 nm radiation source has been presented. Such a compact source (circumference ~ 50 m) can be built in universities and institutes with a reasonable cost, and be useful for basic science research. The work on application of OSC in global microbunching SSMB scenarios is ongoing and will be reported in the future. This work is supported by the National Natural Science Foundation of China (NSFC Grant No. 12522512) and Tsinghua University Dushi Program.

ISBN: 978-3-95450-267-7 ISSN: 2226-0374 doi: 10.18429/JACoW-COOL2025-WEB1

REFERENCES

[1] D. F. Ratner, and A. W. Chao. “Steady-state microbunching in a storage ring for generating coherent radiation," Phys. Rev. Lett., vol. 105, no. 15, p. 154801, Oct. 2010. doi: 10.1103/PhysRevLett.105.154801

[2] X. Deng. *Theoretical and experimental studies on steady-state microbunching*. Springer Nature, 2024.

[3] Tang, C. X. et al. “Physics of steady-state microbunching." to be published in Springer Series Synchrotron Light Sources and Free-Electron Lasers.

[4] X. Deng *et al.*, “Experimental demonstration of the mechanism of steady-state microbunching," Nature, vol. 590, no. 7847, pp. 576-579, Feb. 2021. doi: 10.1038/s41586-021-03203-0

[5] A. Kruschinski *et al.*, “Confirming the theoretical foundation of steady-state microbunching," Commun. Phys., vol. 7, no. 1, p. 160, May 2024. doi: 10.1038/s42005-024-01657-y

[6] A. A Mikhailichenko, and M. S. Zolotorev. “Optical stochastic cooling," Phys. Rev. Lett., vol. 71, no. 25, p. 4146, Dec. 1993. doi: 10.1103/PhysRevLett.71.4146

[7] M. S. Zolotorev, and A. A. Zholents. “Transit-time method of optical stochastic cooling," Phys. Rev. E , vol. 50, no. 4, p. 3087, Oct. 1994. doi: 10.1103/PhysRevE.50.3087

[8] J. Jonathan *et al.*, “Experimental demonstration of optical stochastic cooling," Nature, vol 608, no. 7922, pp. 287-292, Aug. 2022. doi: 10.1038/s41586-022-04969-7

[9] V. Lebedev *et al.*, “The design of optical stochastic cooling for IOTA," JINST, vol 15, no. 05, p. T05002, May 2021. doi: 10.1088/1748-0221/16/05/T05002

[10] Z. Li *et al.*, “Generalized longitudinal strong focusing in a steady-state microbunching storage ring," Phys. Rev. Accel. Beams, vol. 26 no. 11, p. 110701, Nov. 2023. doi: 10.1103/PhysRevAccelBeams.26.110701

[11] X. J. Deng *et al.*, “Steady-state microbunching based on transverse-longitudinal coupling," Nucl. Sci. Tech. vol. 37 no. 2. Dec. 2025. doi: 10.1007/s41365-025-01855-5.

[12] D. Ratner, and A. Chao. “Reversible seeding in storage rings," Proc. of the 33th International Free-electron Laser Conference. 2011.

[13] Deng, X. J., Pan Z. L., Zhao J. Y., Chao, A. W., Tang, C. X. "Reversible microbunching in an electron storage ring." submitted to PRAB, Apr. 2025.

[14] L. H. Yu, “Generation of intense uv radiation by subharmonically seeded single-pass free-electron lasers," Phys. Rev. A, vol. 44, no. 8, pp. 5178–5193, Oct. 1991. doi: 10.1103/PhysRevA.44.5178

[15] G. Stupakov, “Using the beam-echo effect for generation of short-wavelength radiation," Phys. Rev. Lett., vol. 102, no. 7, p. 074801, Feb. 2009. doi: 10.1103/PhysRevLett.102.074801

[16] H. Deng, and C. Feng. “Using off-resonance laser modulation for beam-energy-spread cooling in generation of short-wavelength radiation," Phys. Rev. Lett., vol. 111, no. 8, p. 084801, Aug. 2013. doi: 10.1103/PhysRevLett.111.084801

[17] C. Feng, and Z. Zhao. “A storage ring based free-electron laser for generating ultrashort coherent EUV and X-ray radiation," Sci. Rep., vol. 7, no. 1, p. 4724, Jul. 2017. doi: 10.1038/s41598-017-04962-5

[18] X. Deng. "Optical Stochastic Cooling in a General Coupled Lattice." Proceedings of the 67th ICFA Adv. Beam Dyn. Workshop Future Light Sources, Luzern, Switzerland (JACoW, Geneva, 2023), p. TU4P30.

[19] A. Zholents, L. Rebuffi, and X. Shi. “Stochastic cooling of electrons and positrons with EUV light," Phys. Rev. Accel. Beams, vol. 24 no. 2, p. 022803, Feb. 2021. doi: 10.1103/PhysRevAccelBeams.24.022803

[20] X. Y. Lu *et al.*, “710 kW stable average power in a 45,000 finesse two-mirror optical cavity," Opt. Lett. vol. 49, no. 23, pp. 6884–6887. Dec. 2024. doi: 10.1364/OL.543388

[21] Lebedev, V. Handbook of accelerator physics and engineering, 2nd ed. (World scientific, Singapore, 2013) pp. 155–159.

ISBN: 978-3-95450-267-7 ISSN: 2226-0374 doi: 10.18429/JACoW-COOL2025-WEB2

ION MACHINE-GUN EXPERIMENT AT HIROSHIMA UNIVERSITY*

K. Muroo[1]†, K. Ito[1], H. Okamoto[1], K. Hosaka[2], Y. Yuri[2], N. Miyawaki[2]
[1]Graduate School of Advanced Science and Engineering, Hiroshima University, Higashihiroshima, Japan
[2]Takasaki Institute for Advanced Quantum Science, National Institutes for Quantum Science and Technology (QST), Takasaki, Japan

Abstract

Ion beams with micrometer-order spot size, so-called "microbeams," have been utilized in a variety of fields. These include the biological response of radiation in cells and the single event effects of a semiconductor, etc. On the other hand, certain applications, such as the creation of a color center in a diamond, require an ion beam with not only the higher precision of a nanometer-order diameter but also the ability to implant ions one by one. The ion machine gun (IMG) is the possible choice for the realization of this distinctive ion beam. It is mainly composed of a linear Paul trap (LPT) and Doppler-cooling lasers. Ions laser-cooled to nearly absolute zero in the LPT reach a "Coulomb crystalline state." If we extract ions in this state without heating, a unique ion beam can be attained. Most ion species, even if they cannot be directly laser-cooled, can be cooled sympathetically and crystallized through Coulomb collisions with laser-cooled ions simultaneously confined in the LPT. At Hiroshima University, we conduct proof-of-principle experiments of the IMG using laser-cooled calcium ions and sympathetically cooled nitrogen ions. Here we discuss the fundamental principle and experimental results of this study.

INTRODUCTION

Various types of charged-particle beams, differing in particle species, kinetic energy, or intensity, are used depending on their purpose. Among these is the *microbeam*, which is focused down to the micrometer scale. Microbeams are used, for example, in studies of biological response to radiation in cells [1] or in research into errors caused by charged particles entering semiconductors [2]. Generally, microbeams achieve a micrometer-order spot size by narrowing the beam using collimators or focusing lenses. How tightly the beam can be focused is determined by the beam's emittance. The emittance is defined as a volume in the 6D phase space occupied by particles constituting the beam. The lower the particle beam's emittance, the smaller the particles' positional and momentum divergence, which means the better the beam's quality.

Reducing the emittance with a dissipative force is called *cooling* because it is physically equivalent to lowering the beam temperature. If ions are cooled to near absolute zero, the Coulomb interaction between each ion and the external confinement force reaches equilibrium, and the relative position of each ion does not change. This state is called *Coulomb crystal*, which is the ultimate low-emittance state of the ions. Among beam-cooling techniques, *laser cooling* is the only one that can crystallize ions so far. However, crystallizing a beam rapidly circulating in an accelerator is difficult because the laser cooling force is not very effective in the direction perpendicular to the laser, and a strong dispersive heating effect occurs due to bending magnets.

On the other hand, crystallizing ions confined in an ion trap is much easier than a beam in an accelerator. The "Ion Machine Gun (IMG)," which utilizes a Coulomb crystal in an ion trap as a beam source, is a possible choice for realizing an ultra-low-emittance beam [3]. Coulomb crystals form different structures depending on their line density. At low line densities, ions line up in a single row along the axis of the trap, forming what is called *string* crystal. As the line density increases, they form a *zigzag* crystal, and with an even higher density, they become a *shell* crystal structure. If ions are extracted from an ion trap one by one without serious heating, we can obtain a unique beam whose emittance is on the order of femtometers or less, and the spot size can be focused on the nanometer scale [4, 5].

Although laser cooling can only be applied to a limited number of ion species with specific energy levels, any ion species can, in principle, be sympathetically cooled through Coulomb interactions with laser-coolable ions. A European research team conducted an experiment to extract a nitrogen molecular ion ($^{14}N_2^+$) from a Coulomb crystal composed of a laser-coolable calcium ion ($^{40}Ca^+$) and sympathetically cooled a $^{14}N_2^+$ ion [6].

We are conducting research and development to extract a single nitrogen ion with very low emittance, applying the IMG idea. In what follows, we introduce our experimental system employing a linear Paul trap (LPT) and a new extraction method employing a shell Coulomb crystal. We also report the results of some numerical tests and experiments for proof-of-principle of the method.

PAUL-TRAP ION SOURCE

Experimental Setup

The LPT used in the experiment has a conventional structure with quadrupole rods and three end-plate electrodes. Figure 1 shows an image of the LPT. Each rod electrode measures 6.88 mm in diameter, 88 mm in length, and 3 mm from the trap axis. The amplitude of radiofrequency (rf) voltage (V_{rf}) is 30 V or lower, with an operating frequency of 2 MHz. Three end-plate electrodes (End-A, End-B, and End-C) with a uniform thickness of 12 mm are

---

* Work supported in part by JSPS KAKENHI Grant No. JP24KJ1723 and JP25K15770, and by JST, the establishment of university fellowships towards the creation of science technology innovation, Grant No. JPMJFS2129, and Moonshot R&D Grant No. JPMJMS2062.

† muroo-kento@hiroshima-u.ac.jp

biased at a few volts DC voltage (V_A, V_B, and V_C) and create two axial potential wells. To avoid contamination, the ion confinement region where ions crystallize (between End-A and End-B) is separated from the ion generation region where neutral atoms or molecules are ionized (between End-B and End-C). End-B is placed apart from End-A at 7.1 mm, resulting in a nearly parabolic potential. When extracting ions from the LPT, we manipulate the voltage applied to the End electrode. Extracted ions are detected by a channel electron multiplier (CEM) placed 4.5 mm away from the exit of the LPT.

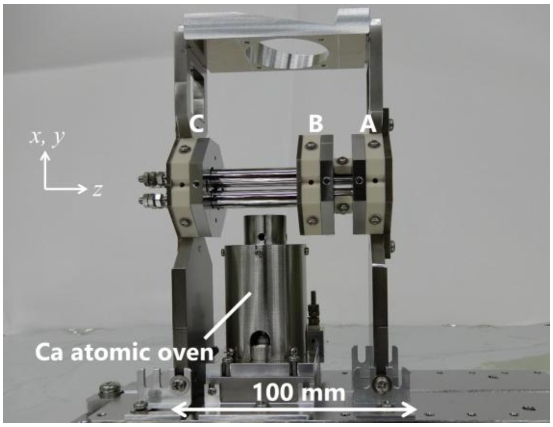

Figure 1: Linear Paul trap used in the experiments. The Ca atomic oven is installed under the ion generation region. After crystallizing in the ion confinement region, ions are ejected toward the right side in this figure.

We choose $^{40}Ca^+$ ions as the coolant and $^{14}N_2^+$ ions as the sympathetically cooled ions for the experiment. Calcium atoms are introduced from an atomic oven placed under the LPT. The $^{40}Ca^+$ ions can be cooled by two semiconductor lasers: a cooling laser (397 nm) for the transition of $4s^2S_{1/2}$–$4p^2P_{1/2}$ and a repumping laser (866 nm) for excitation from the metastable state ($3d^2D_{3/2}$) to the upper state ($4p^2P_{1/2}$). The lower temperature limit for laser-coolable ions, referred to as the Doppler cooling limit T_D, is expressed as $T_D = \hbar\Gamma/2k_B$, where Γ, $\hbar$ and k_B represent the natural width of the excited state, the reduced Plank constant and the Boltzmann constant, respectively. For $^{40}Ca^+$ ions, Γ is 22.5 MHz; thus, T_D is estimated to be 0.54 mK. Nitrogen gas is introduced via a variable leak valve installed at the top of the vacuum chamber. Nitrogen is chosen as the sympathetically cooled ion because, if a precise nitrogen beam can be generated, it can be applied to quantum technologies, such as the creation of nitrogen-vacancy centers in diamond [6], and it is also easy to introduce nitrogen gas into equipment. The calcium atoms and nitrogen molecules are ionized by electron bombardment. The base pressure in the vacuum chamber is maintained below 5×10^{-8} Pa using a turbomolecular pump.

The laser-induced fluorescence (LIF) from $^{40}Ca^+$ ions is observed in real-time by a CCD camera. A few examples of LIF images from Coulomb crystals in past experiments at Hiroshima University are shown in Fig. 2. The structure of a Coulomb crystal changes depending on its line density, as mentioned above. Figure 2(a) shows an image of a shell crystalline structure observed in the case of a high line density. Figure 2(b) shows a string crystal with a lower density, which consists of five $^{40}Ca^+$ ions and one different ion accidentally confined in the trap. Because there is a particularly large gap between the first and second dots on the left side of the picture, we hypothesize that an ion that does not release LIF is trapped in the gap.

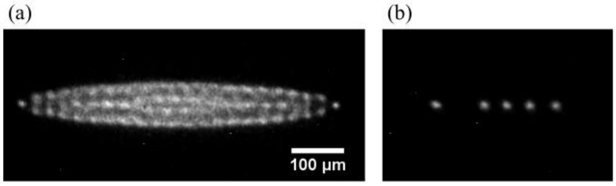

Figure 2: Coulomb crystals detected using a CCD camera. Each bright dot represents the LIF emitted from a single $^{40}Ca^+$ ion. (a) Shell crystal. (b) Two-component string crystal.

Slow Extraction Method

The previous IMG experiments [6-8] have involved forming a *string* crystal and rapidly switching the voltage applied to the electrode generating the axial potential barrier to eject the ions—this can be described as a “fast extraction.”

However, the fast extraction method has strict conditions regarding the order of ions. When extracting ions from a two-component string crystal using this method, a lighter $^{14}N_2^+$ ion is ejected at higher speeds than a heavier $^{40}Ca^+$ ion. As a result, a $^{14}N_2^+$ ion can collide with the preceding $^{40}Ca^+$ ions and be heated during extraction, unless it is placed at the head of the crystal. In actual experiments, since the position of each ion in the crystal is a matter of chance, it is difficult to intentionally place a $^{14}N_2^+$ ion at the head. Moreover, in this scheme, to remove the $^{40}Ca^+$ ions used as a coolant extracted at the same time, a filtering system is required. Here, we propose a method that utilizes a shell crystal for precise extraction. When generating a two-component shell crystal with different kinds of ions, ions with a smaller mass-to-charge ratio gather near the trap axis because the transverse focusing force acting on them in an LPT is stronger. An example of the result of a numerical simulation is shown in Fig. 3. In this simulation, a two-component shell crystal consisting of $^{40}Ca^+$ and $^{14}N_2^+$ ions is formed. The lighter $^{14}N_2^+$ ions aligned in a row along the axis of the trap, surrounded by heavier $^{40}Ca^+$ ions. With this type of crystal, it is always possible to ensure that a $^{14}N_2^+$ ion is positioned at the head.

Figure 4 illustrates the method for extracting nitrogen ions located at the head of a two-component shell crystal. After generating a two-component shell crystal, we eject the ions at the head toward a target by increasing the voltage applied to the electrode opposite the target. The “slow extraction method” not only eliminates the need for a filter system but also enables the extraction of a single ion by appropriately controlling the voltage.

ISBN: 978-3-95450-267-7 ISSN: 2226-0374 doi: 10.18429/JACoW-COOL2025-WEB2

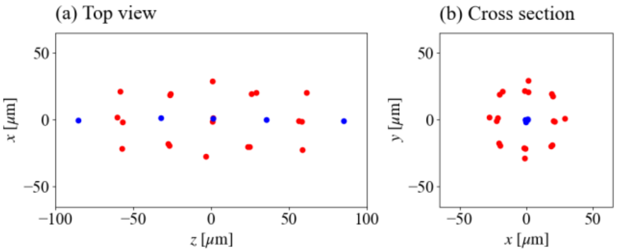

Figure 3: Two-component Coulomb crystal consisting of twenty $^{40}Ca^+$ ions (red) and five $^{14}N_2^+$ ions (blue) in the simulation.

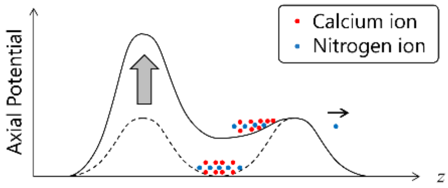

Figure 4: Scheme of slow extraction.

NUMERICAL SIMULATION

Before moving on to the details of the experiment, let us first confirm through numerical simulations that a single $^{14}N_2^+$ ion can be extracted from a Coulomb crystal.

For the simulation, we employed a 3D molecular dynamics (MD) simulation code developed in our laboratory. The potential is calculated by the software “CST Studio Suite” [9], assuming the structure of the trap used in the experiment. A detailed description of the MD simulation method is provided in Ref. [4]. Under $V_{rf} = 30$ V and $V_A = V_B = 3$ V, a Coulomb crystal consisting of twenty $^{40}Ca^+$ ions and five $^{14}N_2^+$ ions, as depicted in Fig. 3, is created inside the LPT. While V_A maintains its initial value, V_B begins to increase at $\Delta t = 0$. At $\Delta t = 10$ ms, V_B reaches 142.35 V and maintains its value, to extract only the single nitrogen ion at the head.

Figure 5 shows the ion extraction process. As the voltage is increased, the entire crystal is stretched in the axial direction of the trap, and only the frontmost $^{14}N_2^+$ ion is ejected. We perform 100 independent simulations with different random seeds and obtain the distribution of $^{14}N_2^+$ ions at the front of the CEM. The normalized root-mean-squared emittances evaluated from the horizontal or vertical phase-space distributions are on the order of 10^{-16} m·rad in both directions. This slow extraction method enables the extraction of a single nitrogen ion with an extremely low emittance.

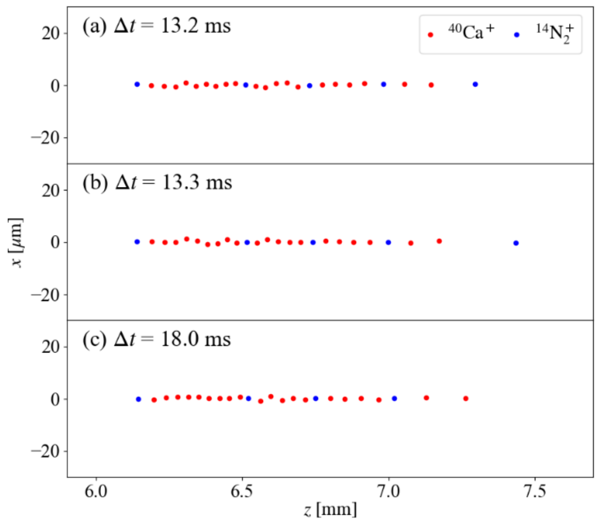

Figure 5: Time evolution of the extracted two-component crystal. (a) $\Delta t = 13.2$ ms, (b) $\Delta t = 13.3$ ms, and (c) $\Delta t = 18.0$ ms. The abscissa represents the distance from the center of the ion confinement region.

EXPERIMENT

Generation of a Two-component Coulomb Crystal

We confirm the generation of a two-component Coulomb crystal consisting of $^{40}Ca^+$ and $^{14}N_2^+$ ions [10]. Pure nitrogen gas is introduced into the vacuum chamber via a variable leak valve to reach a pressure of 5×10^{-7} Pa. In this environment, calcium atoms are emitted from an atomic oven, and both calcium atoms and nitrogen molecules are ionized by electron impacts. Subsequently, $^{40}Ca^+$ ions are cooled by lasers, and $^{14}N_2^+$ ions are sympathetically cooled through Coulomb interactions with the $^{40}Ca^+$ ions. As the cooling process proceeds, a two-component Coulomb crystal is formed. A CCD camera observes the crystal formation process. The applied voltages are fixed at $V_{rf} = 20$ V and $V_A = V_B = 1.5$ V in this experiment.

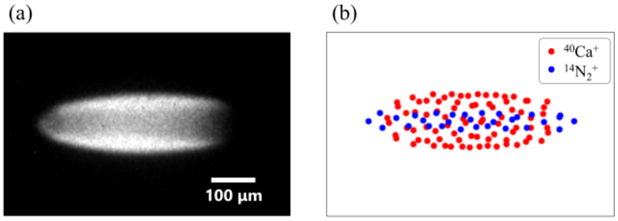

Figure 6: (a) CCD image of the two-component crystal. (b) Two-component crystal consisting of eighty $^{40}Ca^+$ ions and thirty $^{14}N_2^+$ ions in the simulation.

Figure 6(a) shows the CCD image obtained in this experiment. A crystal with a dark central region is produced. The bright white area represents the LIF from the $^{40}Ca^+$ ions. The darkened area is considered to contain the sympathetically cooled $^{14}N_2^+$ ions because they do not emit fluorescence and have a smaller mass-to-charge ratio than $^{40}Ca^+$ ions. From these observations, it is expected that a

ISBN: 978-3-95450-267-7 ISSN: 2226-0374 doi: 10.18429/JACoW-COOL2025-WEB2

two-component shell crystal consisting of $^{40}Ca^+$ and $^{14}N_2^+$ ions is successfully produced.

By comparing with numerical simulations, we estimate the number of ions composing the crystal. We adjust the numbers of $^{40}Ca^+$ and $^{14}N_2^+$ ions in the simulation to reproduce the ion distribution captured by the camera. As shown in Fig. 6(b), the crystal structure roughly matches when there are eighty $^{40}Ca^+$ ions and thirty $^{14}N_2^+$ ions, although correcting the end-plate voltage to $V_A = V_B = 1.1$ V is necessary. We assume that the difference in the end-plate voltages between the experiment and simulation is attributed to the mechanical error of the LPT.

Partial Extraction of a Shell Crystal

The key principle for single-ion extraction is controlling the number of ions extracted from a Coulomb crystal. We confirm the controllability of ejected ions in the slow extraction method using a shell crystal of pure $^{40}Ca^+$ ions. After generating a shell crystal consisting of approximately 80 $^{40}Ca^+$ ions in $V_{rf} = 30$ V and $V_A = V_B = 0.5$ V, V_B increases at a constant rate of 2.95 V/ms until V_B reaches a set value. We change the final value of V_B to control the number of ions extracted from a shell crystal. The CEM is biased to −2.19 kV to gain energy of ions.

Figure 7 shows the number of detected ions at each final voltage of V_B. When the final V_B is below 5.0 V, no ions are detected, as they are confined within the potential well of the LPT. Over 5.5 V, the number of observed ions increases significantly. At 6.2 V or above, the measured ion count stabilizes at approximately eighty. This is because ions constituting the shell crystal are completely extracted. This result demonstrates that the number of ions ejected from a shell crystal can be controlled by adjusting the post-raise voltage, allowing for selective extraction of only the ion located near the leading part of a two-component crystal.

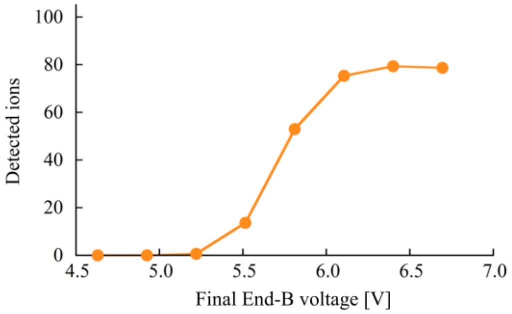

Figure 7: Partial extraction from a shell Coulomb crystal. The horizontal axis represents the voltage after raising, and the vertical axis represents the number of detected ions. The experiment is conducted three times for each voltage, and the average number of detected ions in each case is plotted.

SUMMARY AND FUTURE PLANS

We have investigated methods for achieving the extraction of a single nitrogen ion using a Coulomb crystal. The "slow extraction method," which involves slowly raising the voltage on the end-plate electrode opposite the extraction direction and halting it at a suitable voltage, shows promise as a technique capable of extracting single ions of any species with extremely low emittance. Through numerical simulations, we have confirmed that high-precision extraction of a single nitrogen ion is feasible using the slow extraction scheme from a two-component shell crystal. We have conducted experiments to produce a two-component shell crystal and to demonstrate partial extraction of a shell crystal employing the slow extraction scheme. Recently, we successfully extracted a single $^{40}Ca^+$ ion from a string crystal using the slow extraction method [11]. We plan to continue our research toward one of our objectives: the single extraction of a nitrogen ion.

REFERENCES

[1] N. Guo *et al.*, "Live cell imaging combined with high-energy single-ion microbeam", *Rev. Sci. Instrum.*, vol. 87, pp. 034301, 2016. doi:10.1063/1.4943257

[2] K. M. Prise, G. Schettino, B. Vojnovic, O. Belyakov, and C. Shao, "Microbeam Studies of the Bystander Response", *J. Radiat. Res.*, vol. 50, pp. A1, 2009. doi:10.1269/jrr.09012S

[3] M. Kano, S. Masuda, A. Ogata, K. Okabe and H. Okamoto, "Ultra-low Emittance Beam Generator Using Coulomb Crystals", *J. Phys. Soc. Jpn.*, vol. 73, pp.760, 2004. doi:10.1143/jpsj.73.760

[4] K. Muroo, H. Okamoto, N. Miyawaki, and Y. Yuri, "Simulation study of ultrahigh-precision single-ion extraction from a linear Paul trap", *Prog. Theor. Exp. Phys.*, vol. 2023, pp. 063G01, 2023. doi:10.1093/ptep/ptad071

[5] Y. Yuri *et al.*, "Investigating Ultralow-Emittance Nanobeam Formation Using a Coulomb Crystal", *Prog. Theor. Exp. Phys.*, vol. 2025, pp. 023G01, 2025. doi:10.1093/ptep/ptaf019

[6] K. Groot-Berning, G. Jacob, C. Osterkamp, F. Jelezko, and F. Schmidt-Kaler, "Fabrication of $^{15}NV^-$ centers in diamond using a deterministic single ion implanter", *New J. Phys.*, vol. 23, pp. 063067, 2021. doi:10.1088/1367-2630/ac0753

[7] W. Schnitzler *et al.*, "Deterministic ultracold ion source targeting the Heisenberg limit", *Phys. Rev. Lett.,* vol. 102, pp. 070501, 2009. doi:10.1103/PhysRevLett.102.070501

[8] K. Izawa, K. Ito, H. Higaki, and H. Okamoto, "Controlled extraction of ultracold ions from a linear Paul trap for nanobeam production", *J. Phys. Soc. Jpn.* vol. 79, pp. 124502, 2010. doi:10.1143/JPSJ.79.124502

[9] CST Studio Suite is a commercially available software. For more detail, see https://www.3ds.com/products/simulia/cst-studio-suite

[10] K. Muroo, K. Ito and H. Okamoto, "An ultimate single-ion source using a Coulomb crystal in a Paul trap", *in Proc. IPAC'24*, Nashville, TN, May 2024, pp. 606-609. doi:10.18429/JACoW-IPAC2024-MOPR71

[11] K. Muroo, K. Hosaka, Y. Yuri, K. Ito, and H. Okamoto (submitted for publication).

ISBN: 978-3-95450-267-7 ISSN: 2226-0374 doi: 10.18429/JACoW-COOL2025-WEB3

PROPOSED ULTRALOW-EMITTANCE BEAM SOURCE FOR HIGH-LUMINOSITY HADRON COLLIDERS*

S.J. Brooks†, Brookhaven National Laboratory, Upton, NY, USA

Abstract

Laser Doppler cooling of ion bunches in a Paul trap is a demonstrated method of achieving millikelvin bunch temperatures, with the ions forming a Coulomb crystal with a solid-like structure. This is proposed as a source for accelerators that would be a factor 10^5 lower in emittance than conventional plasma sources. Methods to transport the crystalline bunch while limiting emittance growth are examined, including a novel ring in which the bunch maintains a fixed orientation relative to the outside world (i.e. does not rotate with the ring as usual). In this geometry, magnetic focussing can confine all three dimensions of the bunch without RF. This ring can circulate a 3D crystalline bunch with heating rates of less than 1 K/s.

LASER COOLED ION TRAPS

Laser Doppler cooling is an established method for studying atoms and ions at low temperatures [1]. Several trap geometries can be used with this method but the linear Paul ion trap, with DC electrostatic confinement longitudinally and ~MHz range RF quadrupole transversely, has been used for accelerator applications. The SPOD experiment [2] at Hiroshima University has prepared Ca^+ Coulomb crystals at rest, where the individual ions have vibration velocities of a few m/s and can be seen in a fixed lattice via their fluorescence light during cooling [3]. A Paul trap without cooling has also been built for accelerator physics reasons in the IBEX experiment [4] at Rutherford Appleton Laboratory, where the resonances of the ion cloud under space charge forces can be studied.

Cooling Simulation

A simulation code that runs on the GPU using OpenCL has been written to simulate cooled ion traps. 4th order Runge–Kutta steps in the trap potential are interleaved with pairwise space charge kicks. The ions have a ground and an excited state, the transitions between them governed by a statistical model whose rates agree with the quantum description of a two-level atom in a laser beam. These excitations and de-excitations come with appropriate $\Delta p = \hbar k$ momentum kicks, where it is important to apply the events at truly random points within each timestep, so the short periods where the Doppler process is active are not jumped over.

The results of such a simulation are shown in Figure 1, where the eventual configuration of ions was a long Coulomb crystal several ions wide. Two phases of cooling can be seen: the first occurs before formation of a solid Coulomb crystal core from the initially gas-like ions, while the second ends when the small fraction of remaining ions ‘orbiting’ the solid core eventually lose enough momentum to merge with it. The final temperature is a small multiple of the predicted Doppler limit ($T_D = 0.552\,\mathrm{mK}$ here). The RF nature of the transverse focussing excites some vibrations that take the temperature above the limit.

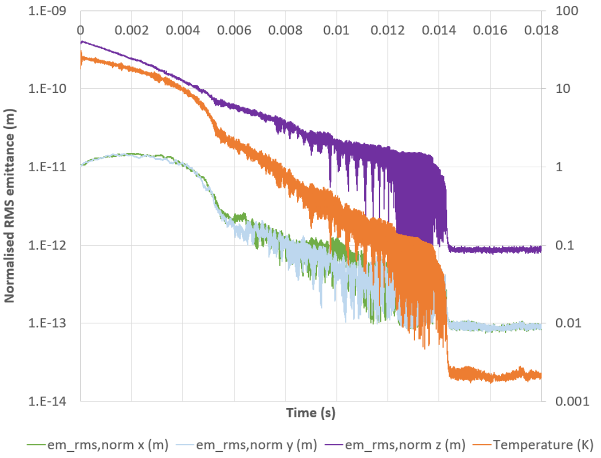

Figure 1: Laser Doppler cooling simulation with $N = 500$ ions.

The final emittances are very small. For a shorter trap producing a spherical bunch, the scaling

$$\frac{\sigma_{x,y,z}}{N^{1/3}} \simeq 25\,\mu\mathrm{m},$$

$$\frac{\epsilon_{x,y}}{N^{1/3}} \simeq 7\times 10^{-14}\,\mathrm{m}, \qquad \frac{\epsilon_z}{N^{1/3}} \simeq 4\times 10^{-14}\,\mathrm{m}$$

was observed in simulations from $N = 100$ to 81920 ions, where ϵ denotes normalised RMS emittance. The crystal temperature was consistently ~3 mK. This emittance is related to temperature via $\epsilon \simeq \sigma_x \frac{\sigma_v}{c} = \frac{\sigma_x}{c}\sqrt{\frac{k_B T}{m}}$.

Increasing Throughput

The maximum possible ion population in existing traps is around 10^7 [2, 5]. With the cooling time of up to 20 ms, a 50 Hz repetition rate source would give an average current of only 80 pA. However, existing sources are not optimised for throughput. The trapping electrode voltages are typically 150 V or lower, which could be increased by two orders of magnitude with a high voltage setup, allowing 10^9 ions to be trapped. A more drastic improvement would be possible using a linear cooling channel, where multiple bunches move along at ~10 km/s so that by the end of a ~200 m-long (possibly coiled) channel they would have completed cooling. This channel would resemble an RFQ but operate at

---

* Work supported by Brookhaven Science Associates, LLC under Contract No. DE-SC0012704 with the U.S. Department of Energy.

† sbrooks@bnl.gov

ISBN: 978-3-95450-267-7 ISSN: 2226-0374 doi: 10.18429/JACoW-COOL2025-WEB3

lower frequencies and velocities; it would also be immersed in the cooling laser light, which is not particularly intense (48 mW/cm^2) and not completely absorbed by the ions, so could be reused multiple times with mirrors. Maximum repetition rates would be of the order 1 MHz, corresponding to ~1 cm bunch spacing in the channel and producing an average current of 160 µA of ultra-low emittance beam.

Related Studies

Extraction from the trap through a non-linear field has been simulated in [6], where relatively simple changes to the extraction system can limit 6D emittance growth below a factor of two. Creation of a high density focal point from an ultra-low emittance bunch, correcting for optical aberrations, was studied in [7] with computer optimisation.

LUMINOSITY ESTIMATE

Parameters of an ion trap bunch are compared to those of a typical plasma ion source in Table 1.

Table 1: Simplified Luminosity Estimate

Parameter	**Ion source**	**Ion trap**
N	10^9	10^5
$\epsilon_{\text{norm,rms}}$	10^{-7} m	3.2×10^{-12} m
Initial condition:		
σ_x	1 mm	1.2 mm
σ_v	30 km/s	0.8 m/s
T	4.3 MK	3.2 mK
At focus:		
σ_x^*	9.4 nm	0.3 pm
σ_θ^*	10 mrad	10 mrad
L/bunch	9×10^{28} cm^{-2}	8.8×10^{29} cm^{-2}

The ion trap bunch can be focussed far smaller than the conventional bunch, albeit with a lower population of particles. Luminosity per bunch calculated via $L = \frac{N_1 N_2 f N_b}{4\pi\sigma_x\sigma_y} \Rightarrow L/\text{bunch} = \frac{N_1 N_2}{4\pi\sigma_x\sigma_y}$ shows that the low emittance bunch produces almost ten times the luminosity despite having 10^4 times fewer ions. This increase in specific luminosity would enable highly energy efficient linear or ERL colliders, with lower beam currents giving reduced power consumption and collective effects. The picometre-level focal point does not require stronger focussing magnets because σ_θ^* is the same as the conventional case. Stabilising against vibrations would be the main challenge, while optical aberration correction and longitudinal compression for a point-like focus are discussed in [7].

From the total Ca-Ca cross section $\sigma_{tot} = 0.9\times10^{-24}$ cm^2, a straightforward estimate would predict 8×10^5 events from colliding the ion trap bunches. This exceeds the bunch population of 10^5, so the interaction point operates in the opaque bunch regime where the entire beam is consumed in one pass. This means a collider ring is not needed, although rings may be used to reduce the cost of acceleration relative to linacs. Taking instead the saturated luminosity per bunch crossing of $2N/\sigma_{tot} = 2.1\times10^{29}$ cm^{-2}, a 1 MHz bunch repetition rate would give $L = 2.1\times10^{35}$ cm^{-2}s^{-1} from 16 nA of beam current.

BEAM TRANSPORT

A solid phase material such as a Coulomb crystal only has one velocity at any given position, whereas a gas has a velocity distribution. Figure 2 shows this difference: the gas is an area in phase space whereas the solid is just a line.

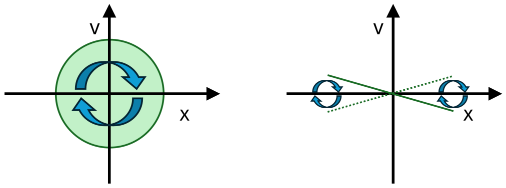

Figure 2: Phase space of a gas phase beam (left) and solid phase beam (right) being transported in a beamline.

The usual phase space rotation in beamlines is not appropriate for a solid, since at 90 degrees phase advance the line would be vertical, corresponding to the particles smashing through each other in that axis. This is desired at the final collision point but not before because it would cause intra-beam scattering. Roughly zero net phase advance is therefore required, by balancing the external focussing forces with space charge repulsion (i.e. operating at the space charge limit). Divergence from the emittance itself is suppressed by the strongly coupled solid structure. Small errors in bunch size cause the dynamics shown on the right of Figure 2, where the bunch ‘breathes’ around a stable size.

Since the crystal has an internal structure in which forces are balanced, changing the aspect ratio by more than a few percent causes heating (although uniform scaling is allowed). This can be accommodated with a gentle focussing structure, either low phase advance cells or weak focussing in a ring.

STORAGE RING

A storage ring is desired with a low heating rate, so that a Coulomb crystal injected into it will survive as long as possible even without cooling. Okamoto has shown [8] that trying to cool from a gaseous beam to a solid in a ring requires going through a peak IBS heating regime and thus requires powerful cooling. This paper proposes that injecting an already cold crystal will alleviate this problem and reduce cooling requirements in the ring. (Acceleration in such a ring will be studied in future work.)

Field Model

Consider motion of equal-energy particles in a uniform vertical magnetic field. All orbits are equal radius circles and are translated copies of each other, so relative positions of particles in the bunch are constant *in the lab frame* rather

ISBN: 978-3-95450-267-7 ISSN: 2226-0374 doi: 10.18429/JACoW-COOL2025-WEB3

than rotating with the direction of travel. If space charge were zero, this motion keeps a crystalline structure stable and avoids rotation, which at relativistic speeds may require large changes in particle momentum.

To this constant field, M small azimuthal oscillations can be added to provide focussing. The midplane field

$$B_z(r, \theta, 0) = B_0 + \sum_{j=0}^{n_c-1} c_j r^{M+2j} \sin(M\theta)$$

provides a form of this that has a simple Maxwellian extension off the midplane [9]. The transverse field of the oscillations $b(r) = \sum_{j=0}^{n_c-1} c_j r^{M+2j}$ can be made any shape locally by increasing n_c, the number of c_j values chosen.

As the bunch does not rotate with the ring, focussing at the ring radius R (from $b'(R)$) will first act on the 'North-South' axis of the bunch and then on the 'East-West' axis 90 degrees further around the ring, while the vertical focussing is always active.

Definitions of Bunch Temperature

Temperature is often defined via average kinetic energy as $\frac{3}{2}k_B T = \langle E_k \rangle = \frac{1}{2}m\langle|\mathbf{v}|^2\rangle$ but accelerator bunches may be travelling at high speed, making the naive temperature $\sim 10^{12}$ K, or be changing shape due to the lattice. To measure only 'random' movement of particles and not these collective motions, define

$$T_n = \frac{m}{3k_B}\langle|\mathbf{v} - \mathbf{p}_n(\mathbf{x})|^2\rangle$$

where $\mathbf{p}_n(\mathbf{x})$ is the n^{th} order polynomial least squares fit to $\mathbf{v}(\mathbf{x})$. This means that T_0 removes bunch average velocity. T_1 also removes linear optics motion, giving a quantity similar to the emittance-based definition in [8]. T_2 also removes 2^{nd} order motion, but setting n too high relative to the number of particles will start to 'overfit' and subtract random motion.

Tracking Results

Table 2: Simulation Parameters

Parameter	Value	Unit
Number of ions N	2560	
Ion species	Ca^+	
Bunch size $\sigma_{x,y}, \sigma_z$	481, 265	μm
Kinetic energy per mass	3.257	MeV/u
Main field B_0	1	T
Mean radius R	10.38448	m
Oscillations per turn M	20	
Oscillation terms n_c	1	
Oscillation amplitude $c_0 R^M$	0.081665	T

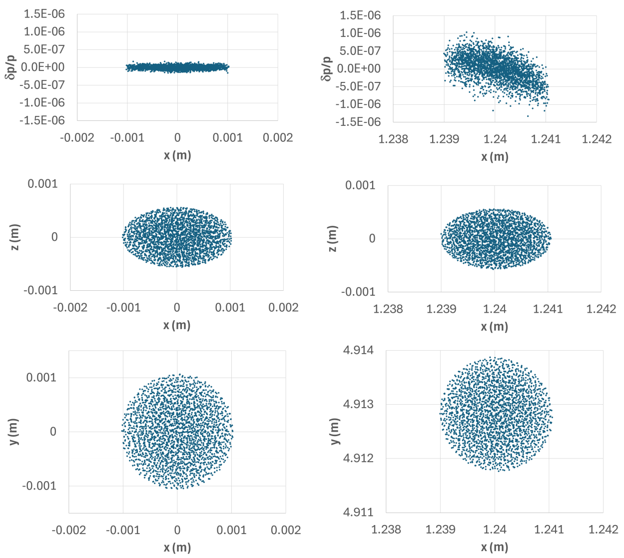

Figure 3: Particle distribution at injection (left) and t = 63.3 ms (right).

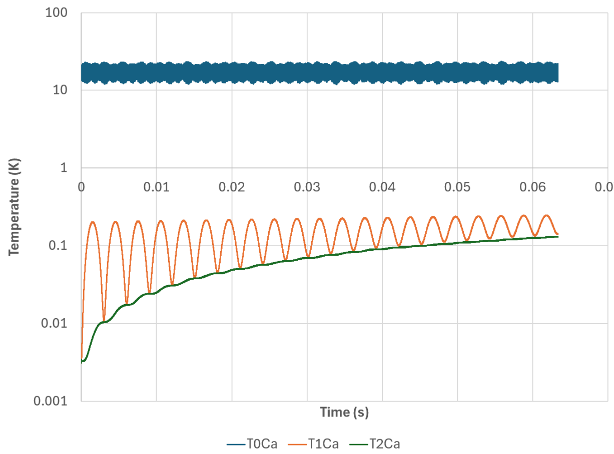

Figure 4: Bunch temperatures $T_{0,1,2}$ over time.

It was found that the simplest case with $n_c = 1$ and oscillation field $b(r) \propto r^M$ produced stable dynamics for a ring with parameters given in Table 2. The bunch shown on the left of Figure 3 was formed in an ion trap cooling simulation and placed in the ring tracking simulation. After 63.3 ms (24170 turns) it was still solid as shown on the right of the figure. The temperature evolution is plotted in Figure 4 with interesting second-order oscillatory behaviour making $T_2 < T_1$. The lattice motion makes $T_0 > 10$ K.

Changing the shape of the bunch with different ion trap parameters reduced the heating rate further, as shown in Figure 5 using a vertically taller bunch. This shape may make it less sensitive to dispersive effects in the horizontal plane. A heating rate of 0.8353 K/s was observed over 5 ms.

First Order Stability Analysis

In some cases, when the oscillation field profile $b(r)$ was changed from that in the previous section, velocity distribution parameters (and the temperature) showed exponential growth over ~100 turn time scales.

ISBN: 978-3-95450-267-7 ISSN: 2226-0374 doi: 10.18429/JACoW-COOL2025-WEB3

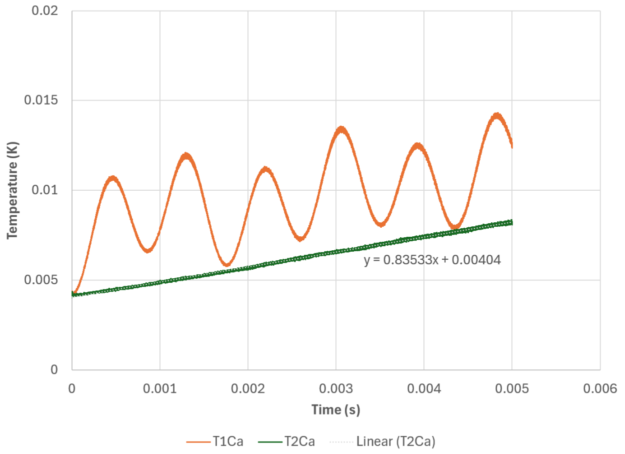

Figure 5: Reduced heating rate achieved with $\sigma_{x,y}$ =229 µm, σ_z =432 µm bunch.

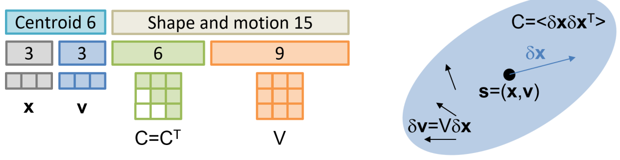

Figure 6: Parameters of the ellipsoid bunch model.

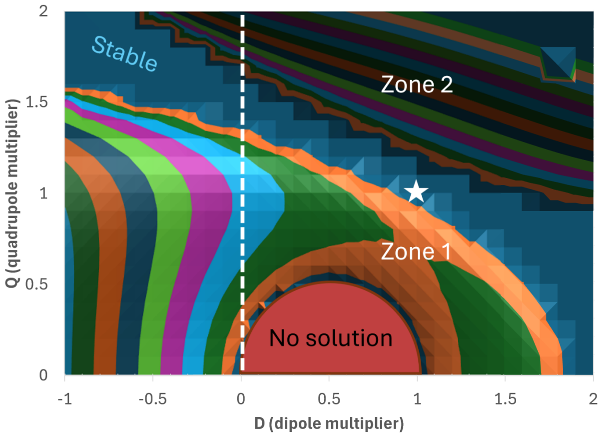

Figure 7: Growth rate in the first order model as D and Q are varied, $S = 1$. Colour contours are every 0.002 turns^{-1}.

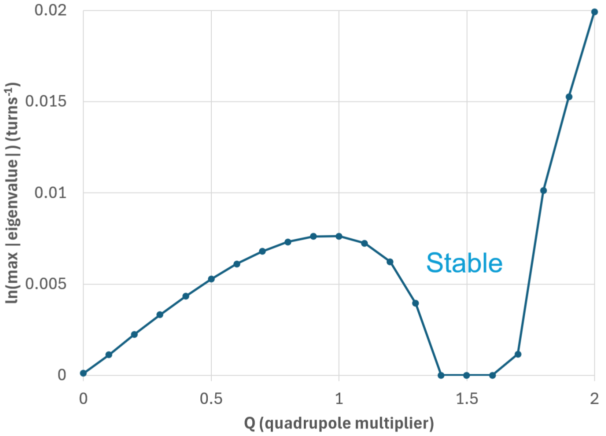

Figure 8: Model growth rate as Q is varied, $D = 0$, $S = 1$.

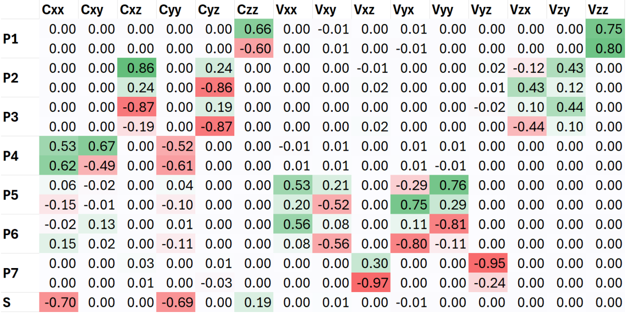

	Cxx	Cxy	Cxz	Cyy	Cyz	Czz	Vxx	Vxy	Vxz	Vyx	Vyy	Vyz	Vzx	Vzy	Vzz
P1	0.00	0.00	0.00	0.00	0.00	0.66	0.00	-0.01	0.00	0.01	0.00	0.00	0.00	0.00	0.75
	0.00	0.00	0.00	0.00	0.00	-0.60	0.00	0.01	0.00	-0.01	0.00	0.00	0.00	0.00	0.80
P2	0.00	0.00	0.86	0.00	0.24	0.00	0.00	0.00	-0.01	0.00	0.00	0.02	-0.12	0.43	0.00
	0.00	0.00	0.24	0.00	-0.86	0.00	0.00	0.00	0.02	0.00	0.00	0.01	0.43	0.12	0.00
P3	0.00	0.00	-0.87	0.00	0.19	0.00	0.00	0.00	0.00	0.00	0.00	-0.02	0.10	0.44	0.00
	0.00	0.00	-0.19	0.00	-0.87	0.00	0.00	0.00	0.02	0.00	0.00	0.00	-0.44	0.10	0.00
P4	0.53	0.67	0.00	-0.52	0.00	0.00	-0.01	0.01	0.00	0.01	0.01	0.00	0.00	0.00	0.00
	0.62	-0.49	0.00	-0.61	0.00	0.00	0.01	0.01	0.00	0.01	-0.01	0.00	0.00	0.00	0.00
P5	0.06	-0.02	0.00	0.04	0.00	0.00	0.53	0.21	0.00	-0.29	0.76	0.00	0.00	0.00	0.00
	-0.15	-0.01	0.00	-0.10	0.00	0.00	0.20	-0.52	0.00	0.75	0.29	0.00	0.00	0.00	0.00
P6	-0.02	0.13	0.00	0.01	0.00	0.00	0.56	0.08	0.00	0.11	-0.81	0.00	0.00	0.00	0.00
	0.15	0.02	0.00	-0.11	0.00	0.00	0.08	-0.56	0.00	-0.80	-0.11	0.00	0.00	0.00	0.00
P7	0.00	0.00	0.03	0.00	0.01	0.00	0.00	0.00	0.30	0.00	0.00	-0.95	0.00	0.00	0.00
	0.00	0.00	0.01	0.00	-0.03	0.00	0.00	0.00	-0.97	0.00	0.00	-0.24	0.00	0.00	0.00
S	-0.70	0.00	0.00	-0.69	0.00	0.19	0.00	0.01	0.00	-0.01	0.00	0.00	0.00	0.00	0.00

Figure 9: Stable eigenvectors for $D = Q = S = 1$.

To search for collective instability modes, the model in Figure 6 was used. Here, the bunch is approximated by a uniform ellipsoid of charge with zero temperature. It is parameterised by its centroid $\mathbf{s} = \langle(\mathbf{x}, \mathbf{v})\rangle$, covariance matrix $C = \langle \delta\mathbf{x}\delta\mathbf{x}^T \rangle$ and velocity distribution V where $\delta\mathbf{v} = V\delta\mathbf{x}$. The centroid **s** evolves as a single particle while the 15 parameters (C, V) have time derivatives calculated in [10]. This captures the dynamics spatially to first order, so higher-order modes and heating of phonon motion are not included.

The oscillation field was changed by using $n_c = 3$ terms and defining multipole strength multipliers $D = b(R)/b_s(R)$, $Q = b'(R)/b'_s(R)$ and $S = b''(R)/b''_s(R)$ where $b_s(r)$ is the stable oscillation field used in the previous section. Combinations of $c_{0,1,2}$ can be found to produce any desired (D, Q, S).

For each (D, Q, S) setting, matched values of (C, V) were found that are unchanged after one turn. The Jacobian $\frac{\partial(C,V)_{out}}{\partial(C,V)_{in}}$ is a 15×15 matrix showing the effect of small perturbations to the bunch shape or velocity distribution. If it has an eigenvalue with modulus greater than one, there is an instability with growth rate given by the logarithm of that modulus. The effect of scanning D and Q on stability is shown in Figures 7 and 8. The previous stable solution is shown by a star at $(1, 1, 1)$ and lies between two unstable zones labelled in Figure 7.

Figure 9 shows the full set of eigenvectors for the Jacobian matrix of the stable solution. Seven pairs with complex eigenvalues are written as their two real combinations, which span the plane that periodic oscillations take place in. Zone 1 corresponds to eigenvector pairs P5 and P6 becoming unstable, which involve velocity in the horizontal plane. Zone 2 corresponds to pair P7 becoming unstable, involving velocity coupling between the horizontal and vertical planes.

For the stable solution, the seven eigenvalue pairs $e^{\pm 2\pi i f}$ have $f = \frac{1}{13.9}, \frac{1}{19.6}, \frac{1}{21.4}, \frac{1}{179}, \frac{1}{485}, \frac{1}{709}, \frac{1}{958}$ turns^{-1} for P1 through P7 respectively. The remaining single eigenvector S has eigenvalue 1 and comes about because the model has an odd number of dimensions (15). This unit eigenvalue allows multiple matched solutions where the vertical bunch aspect ratio $\sigma_z/\sqrt{\sigma_x\sigma_y}$ can be freely chosen within a range.

REFERENCES

[1] H. J. Metcalf and P. van der Straten, “Laser Cooling and Trapping of Neutral Atoms”, in The Optics Encyclopedia, Vol. 38, pp.847–853 (Wiley-VCH Verlag GmbH & Co. KGaA, Weinheim, Germany, 2007).

[2] R. Takai, H. Enokizono, K. Ito, Y. Mizuno, K. Okabe and H. Okamoto, “Development of a Compact Plasma Trap for Experimental Beam Physics”, *Japan. J. Appl. Phys.* **45**, No. 6A pp.5332–5343 (2006).

[3] K. Izawa, K. Ito, H. Higaki and H. Okamoto, “Controlled Extraction of Ultracold Ions from a Linear Paul Trap for Nanobeam Production”, *J. Phys. Soc. Japan* Vol. **79**, No. 12, p.124502 (2010).

[4] S. L. Sheehy, E. J. Carr, L. K. Martin, K. Budzik, D. J. Kelliher, S. Machida and C. R. Prior, “Commissioning and First Results of the IBEX Linear Paul Trap”, in *Proc. IPAC 2017*, Copenhagen, Denmark, May 2017, pp.4481–4484. `doi:10.18429/JACoW-IPAC2017-THPVA027`

[5] L. K. Martin, S. Machida, D. J. Kelliher and S. L. Sheehy, “A study of coherent and incoherent resonances in high intensity beams using a linear Paul trap”, New J. Phys. **21** 053023 (2019).

[6] S. J. Brooks, “Extraction of Coulomb Crystals with Limited Emittance Growth”, in *Proc. IPAC 2024*, Nashville, TN, May 2024, pp.460–463. `doi:10.18429/JACoW-IPAC2024-MOPR04`

[7] S. J. Brooks, “Ultra-Low Emittance Bunches from Laser Cooled Ion Traps for Intense Focal Points”, in *Proc. HB2023*, Geneva, Switzerland, Oct. 2023. `doi:10.18429/JACoW-HB2023-TUC3I1`

[8] H. Okamoto, H. Sugimoto and Y. Yuri, “Coulomb Coupling and Heating of Charged Particle Beams in the Presence of Dispersion”, J. Plasma Fusion Res. SERIES, Vol. **8**, pp.950–954 (2009).

[9] S. J. Brooks, “Maxwellian Fields for a Ring derived from Multipole End Fields”, note BNL-227922-2025-TECH, available from `https://www.osti.gov/biblio/2530893` (2024). `doi:10.2172/2530893`

[10] S. J. Brooks, “First Order Transport of a Cold Uniform Ellipsoid of Charge”, note BNL-229092-2025-TECH, available from `https://www.osti.gov/biblio/3000537` (2025). `doi:10.2172/3000537`

ISBN: 978-3-95450-267-7 ISSN: 2226-0374 doi: 10.18429/JACoW-COOL2025-THA1

ELECTRON BEAM DYNAMICS SIMULATION IN COHERENT ELECTRON COOLING

Yichao Jing[†,1], Nikhil Bachhawat[2], Alexei Fedotov[1], Dmitry Kayran[1], Vladimir N. Litvinenko[2],
Jun Ma[1], Igor Pinayev[1], Sergei Seletskiy[1], Gang Wang[1]
[1]Collider-Accelerator Department, Brookhaven National Laboratory, Upton, NY 11973
[2]Physics Department, Stony Brook University, NY 11794

Abstract

New scheme with lower electron beam energy together with lower peak beam current has been proposed for the Coherent electron cooling (CeC) proof of principle experiment in RHIC Run 25 [1]. Such new operation mode appears to be a better candidate in providing a high-quality beam for cooling performance. In this paper we will present our results to achieve the low slice emittance/low slice energy spread electron beam and discuss the progress in achieving better uniformity in both average slice energy and slice peak current to minimize potential anti-cooling effect.

INTRODUCTION

The CeC beamline (Figure 1) consists of low energy beam transport (where electron beam is prepared and accelerated to a total energy of 10 MeV), a dogleg section to transport the beam to a common section where the electron beam is co-propagating with the hadron beam. In the common section, the electron beam is matched to beam requirements in cooling section where the electron beam co-propagates with the hadron beam.

The performance of the cooling is highly dependent on the electron beam's quality. Thus, a self-consistent start to end (S2E) simulation of the accelerator section is crucial in determining the amplifier's performance and in predicting the machine setups to characterize the cooling.

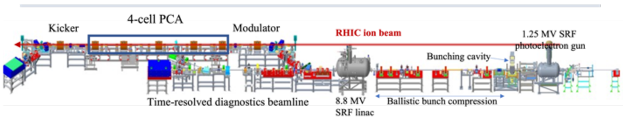

Figure 1: Engineering drawing of CeC beamline (electron beam travels from right to left).

LOW ENERGY BEAM DYNAMICS

There are three RF systems in the CeC's accelerator section – a quarter-wave SRF gun cavity (1.25 MeV, 113 MHz), a NC bunching cavity (tunable for different peak current, usually at about 140 to 160 keV, 500 MHz) and a 5-cell SRF linac (up to 13.5 MeV, 704 MHz). All three RF systems are operated at harmonics of a global clock, 78 kHz – the RHIC's revolution frequency. In between cavities, 6 solenoids are used for electron beam's phase space manipulation and beam size control. More specifically, the solenoid in between gun cavity and the linac is used to perform emittance compensation, i.e., provide optimal transverse focusing to minimize emittance growth from space charge effect of low energy electron beam, which is illustrated in Fig. 2. After the beam gains energy chirp from bunching cavities and experiences ballistic compression in long straight section (~ 10 m to linac), the beam current increases to ~ 20 amps prior to entrance into linac where the space charge effect is dominating. In additional, we alternate the polarity of the 5 solenoids in this 10-m long drift to control any systematic field errors and maintain the initial coordinate systems so that the lowest order chromatic effect introduced by misalignments in magnets is compensated. The beam size is focused and matched to optimal beam conditions at the entrance of the linac.

There are many different beam dynamics in the beam line that could potentially affect beam qualities severely, namely space charge, wakefields, shielding effect from vaccum chamber etc. Doing all beam dynamics in one simulation code is unimaginable. We used many dedicated codes to calculate these effects before importing the simulated results into the IMPACT-T [2] to track particles' 6D evolution along the beamline. We benchmarked our calculated beam properties (like beam envelope, phase space distributions, energy evolutions) in IMPACT-T with many other well established beam dynamics codes e.g., GPT/PARMELA/ASTRA.

We recessed our cathode position in the gun cavity so that the initial RF field provides a strong transverse focusing to the beam. With adjusted cathode recess position, the proper focusing force can be selected to better suit beam dynamics in the gun.

As mentioned above, we used a bunching cavity to provide energy chirp in the low energy beam (~ 1.25 MeV kinetic energy) for the beam to undergo a ballistic compression in the long beam transport prior to getting a major boost in energy in the 704 cavity (~ 8.4 MeV kinetic energy gain). The energy distribution in different beam slices will have different rotation in solenoids which are used to provide focusing. Such process smears out the transverse phase space and by carefully tuning up the solenoids, the longitudinal slices along the beam are aligned in the phase space to reduce the projected emittance as well as the variation of the optics functions along the slices at the end of the low energy beam line. Detailed plots of the transverse phase space evolution can be visualized from particle tracking in IMPACT-T shown in Figure 2.

[†] yjing@bnl.gov

ISBN: 978-3-95450-267-7 ISSN: 2226-0374 doi: 10.18429/JACoW-COOL2025-THA1

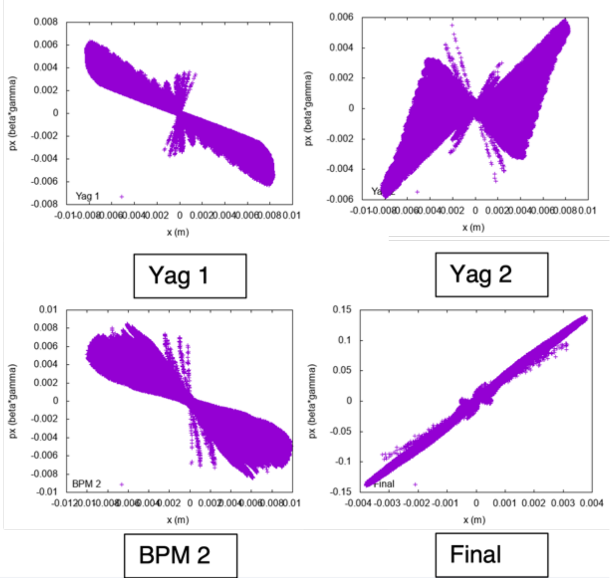

Figure 2: Solenoidal fields were adjusted and optimized in the low energy beam transport so that at the end of the beam line, all longitudinal slices along the beam are aligned in the phase space to reduce the projected emittance.

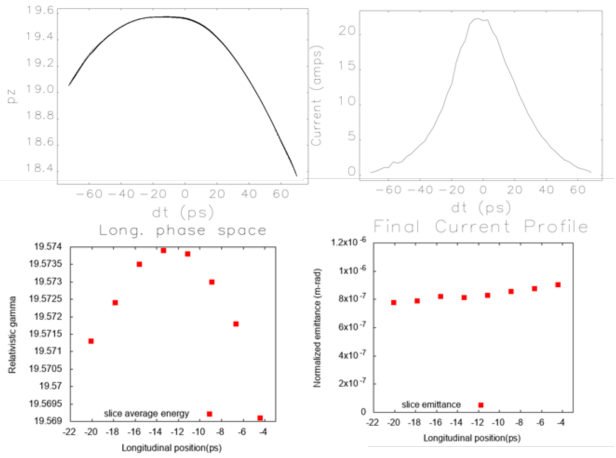

Figure 3: The electron beam at the end of linac reaches very high 6D brightness: transverse emittances (slice) less than 1 um while peak current higher than 20 A and sliced fractional energy spread is less than 2e-4.

Optimization in IMPACT-T takes all beam line components as variables (magnets, cavities…). The optimization goals were to achieve high peak current for core part of the beam while keep the projected emittance as well as sliced emittances low. Figure 3 shows the longitudinal phase space of electron beam at the end of linac (@ 13.6 meters from cathode). For a beam with bunch charge 0.8 nC, the peak current of the beam is compressed more than 8-fold reaching 20 A after the low energy line and sliced energy spread after linac is lower than 2e-4.

BENCHMARK WITH EXPERIMENT

To verify what we achieved in simulation experimentally, we benchmarked our findings in IMPACT-T of the evolution of beam envelope, emittance, energy, bunch length, etc, with measurements using diagnostics implemented through the beamline. A beam image on one of the YAG profile monitors can be seen in Figure 4.

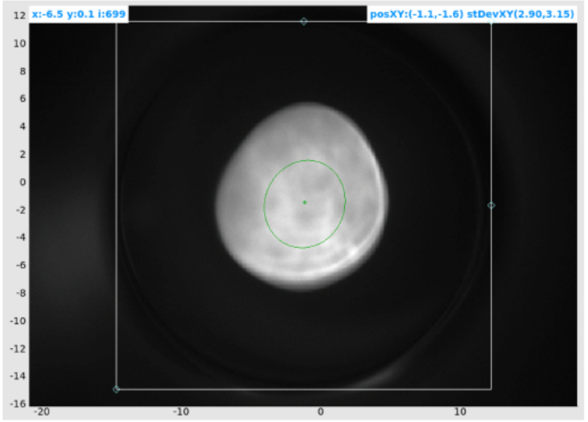

Figure 4: Beam image taken after buncher cavity on a YAG profile monitor. Beam size, position and distributions are extracted and compared with simulation.

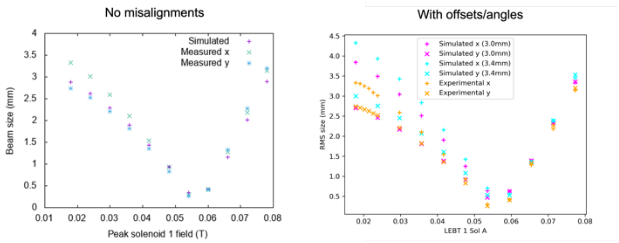

Figure 5: Measured beam sizes dependence on SRF solenoid and one of the LEBT solenoids have very good agreement with simulated envelopes.

Using the multi-stage beam diagnostics, including YAG viewers, bpms, pepper pot etc (details can be found in Fig. 1), we can benchmark our simulation results with experiment and thus gain better understanding of our physics models and possible missing factors in the simulation setup.

As shown in Figure 5, in one of the dedicated benchmark experiments, where we scanned couple of solenoids in the beamline and measured beam size dependence downstream, which to be compared with simulation predictions. The agreement is excellent.

With the help of understanding the important effects to include in simulations (field errors, magnet misalignments etc), we can set up simulation to experiment comparison along the beam line at various diagnostics, details can be found in Figure 6. We have not only good predictions on the overall beam qualities (sizes, spreads, etc) but also have qualitatively good understandings on the uncommon beam patterns developed along the beamline.

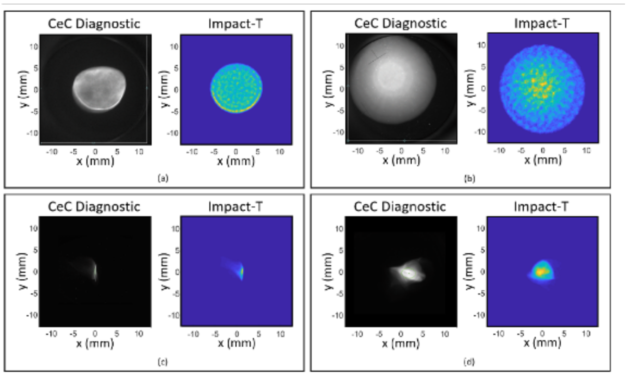

Figure 6: Comparison of beam profile on profile monitors along the beam line has very close resemblance with simulation prediction.

These patterns are largely coming from the non-zero offset through strong solenoids and misalignment of the orbit into the linac cavity. In normal operation, we perform beam-based alignment to minimize these effects.

QUADSCAN FOR SPACE CHARGE DOMINATED BEAM

It is well known that space charge effect plays an important role in a strongly focused lattice. Such effect does not only exist in the low energy transport line (which was carefully considered in beam line design mentioned above), but also in the experiment where quadrupole magnets are scanned to measure beam optical functions and emittances at relatively higher energy. Figure 7 shows a simulated quad-scan process using CeC beam parameters. In such simulation, the vertical plan has much stronger space charge effect (beam size is much larger when space charge effect is turned on) because the initial vertical emittance is about half of the horizontal one (smaller vertical phase space volume thus higher charge density).

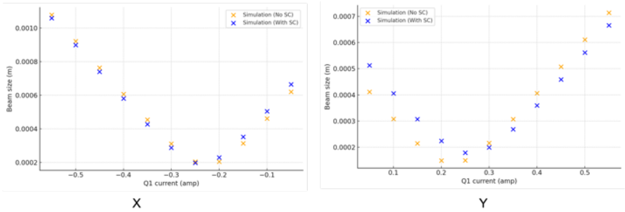

Figure 7: simulation using CeC beam parameter shows strong space charge effect on beam envelope when beam is focused (and over focused).

Under such scenario (where space charge effect is non-negligible), quad-scan measured beam quantities can no longer be used to characterize the beam and to match the beam into later sections for beam cooling. To solve this issue, we set up simulations with varying initial conditions to match to the beam sizes measured in experiments. We can then derive the real beam properties from the initial conditions that provide the best match to the envelope, with consideration of space charge effect.

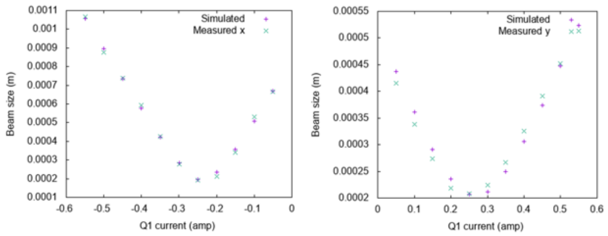

Figure 8: beam sizes with varying quadrupoles for both simulation and experiment. The simulation is used to identify the initial conditions to best match the experiments, with space charge, and thus derive the beam quality.

Figure 8 shows the best match after several iterations and the derived beam parameters, together with parameters directly calculated from quad-scan, are listed in Table 1.

Table 1: The derived TWISS functions as well as beam parameters are quite different from calculated directly using quad-scan approach, with strong space charge in existence. The real (simulated) beam parameters tend to have smaller emittances and larger beta functions.

	Simulated	Exp (quad scan)
Beta x/y, m	7.34/4.03	5.21/2.79
Alpha x/y	-5.74E-02/ 4.86E-02	-1.85/-0.29
Emittance x/y, um	1.5/0.72	2.08/1.01
Peak current, A	21.78	22.3

CONCLUSION

We designed and performed the S2E simulation in a space charge dominated beam and studied various beam dynamics issues. The beam properties are optimized while longitudinal beam size is compressed by more than 8-fold. We demonstrated the high beam brightness and developed a technique to derive the beam parameters experimentally.

Work is supported by Brookhaven Science Associates, LLC under Contract No. DEAC0298-CH10886 with the U.S. Department of Energy, DOE NP office grant DEFOA-0000632.

REFERENCE

[1] V.N. Litvinenko *et.al.*, “Results of the Coherent Electron Cooling Experiment at RHIC”, presented at COOL’25, Stony Brook, NY, paper MOD3.
[2] Ji Qiang, IMPACT-T, A 3D Parallel Particle Tracking Code in Time Domain, `https://amac.lbl.gov/~jiqiang/IMPACT-T/index.htm`

ISBN: 978-3-95450-267-7 ISSN: 2226-0374 doi: 10.18429/JACoW-COOL2025-THA2

MULTIPLE-SLICE SIMULATIONS OF COHERENT ELECTRON COOLING PERFORMANCE WITH LOW BEAM CURRENT*

J. Ma†, Brookhaven National Laboratory, Upton, New York 11973, USA
Y. Jing, Brookhaven National Laboratory, Upton, New York 11973, USA
G. Wang, Brookhaven National Laboratory, Upton, New York 11973, USA
V. N. Litvinenko, Stony Brook University, Stony Brook, New York 11794, USA

Abstract

Coherent electron cooling (CeC) is a novel technique for rapidly cooling high-energy, high-intensity hadron beam. Plasma cascade amplifier (PCA) has been proposed for the CeC experiment in the Relativistic Heavy Ion Collider (RHIC) at Brookhaven National Laboratory (BNL). Cooling performance of PCA based CeC has been predicted in 3D start-to-end CeC simulations using code SPACE for multiple slices in the beam. The operation of low beam current provides more flexibilities for the CeC experiment.

INTRODUCTION

Coherent electron cooling (CeC) [1–3] is a promising technique for the rapid cooling of high-energy high-intensity hadron beams in modern accelerators. In this paper, we present simulation studies of the CeC with plasma cascade amplifier (PCA) [4, 5], which utilizes the plasma cascade instability (PCI) [6–9]. Our simulation tool, the SPACE code [10] has been used in the simulation studies for the mitigation effect by beam induced plasma [11], the modulation process in CeC [12–15], CeC with free electron laser (FEL) amplifier [16–19] and the CeC with PCA [20–23].

Figure1 shows the layout of the CeC system installed in the Relativistic Heavy Ion Collider (RHIC) at Brookhaven National Laboratory (BNL). Our simulation study is based on the CeC experiment and consists of four steps: 1) Design - perform CeC simulations including modulator, PCA, kicker to search for proper beam parameters; 2) Implement - perform beam dynamic simulation including superconducting radio frequency (SRF) gun, low energy beam transport (LEBT), SRF linac dogleg to match the required beam parameters at the entrance of modulator; 3) Predict - perform CeC simulations to predict cooling force with electron beam from beam dynamic simulation; 4) Verify - perform ion tracking simulation to predict ion beam evolution with the presence of CeC.

DESIGN

In the PCA-based CeC shown in Figure2, solenoids are used to modulate the transverse size of the electron beam and to excite the PCI. According to PCI theory, beam peak current and emittance should be carefully chosen to ensure high gain, as is shown in Figure3. Based on the PCI theory, two setups with high beam currents have been developed, as shown in Figure4. Recently, new setups with low beam current have been developed, which demonstrates high PCA gain, as is shown in Figure5.

IMPLEMENT

After a detailed studies on all setups, we have decided to perform beam dynamic simulations to match the low beam current setup, as this setup provides better chance to achieve key performance parameter (KPP) in the CeC experiment. Figure6 shows the beam parameters at the entrance modulator. The beam dynamics simulation is performed with code Impact-T [24].

PREDICT

To predict the cooling force, we have simulated multiple slices of the central beam, with slice duration 2.3 ps, through the PCA-based CeC section. Three PCA lattices have been developed to support the CeC experiment. In each setup, we have tracked the cooling force to ions with reference / off-reference energies, as well as with / without transverse offsets. Dependence of the cooling force amplitude on the transverse offset has been characterized. We have taken the weighted sum of cooling force at transverse offsets with corresponding 2D Gaussian distribution probability density function, to quantify overall cooling force. The ion beam is expected to have normal distribution in transverse plane with RMS beam size 1 mm. The cooling force from the three setups are presented in Figure 7, 8, 9.

VERIFY

Ion beam profile evolution has been tracked in simulations with / without the presence of CeC. Slice 24 to 30 of electron beam from setup 1 has been used to provide cooling. The cooling result is presented in Figure 10 and 11.

SUMMARY

Beam parameters of low peak current for PCA-based CeC have been established. PCA gain spectrum has been simulated, and agrees well with theoretical prediction. Beam dynamic simulation has achieved required beam parameters at the entrance of modulator, with low emittance, low energy spread, uniform β function and αfunction, good symmetry in transverse plane. CeC simulation has predicted strong cooling force because of good quality beam from beam dynamic simulation. Three PCA lattices have been designed

---

* Work supported by Brookhaven Science Associates, LLC under Contract No. DE-SC0012704 with the U.S. Department of Energy.

† jma1@bnl.gov

ISBN: 978-3-95450-267-7 ISSN: 2226-0374 doi: 10.18429/JACoW-COOL2025-THA2

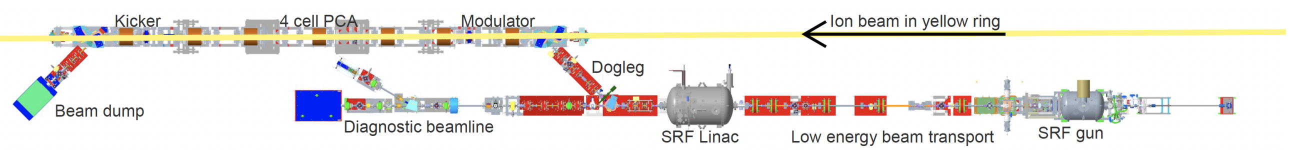

Figure 1: PCA-based CeC system installed at RHIC. The electron beam is generated in a 1.25 MV SRF photo-electron gun, accelerated to 14.56 million electronvolts (MeV), and merged to co-propagate with the 26.5 GeV/u ion beam circulating in RHIC's yellow ring.

Figure 2: Schematic of a CeC system with the PCA at BNL's RHIC.

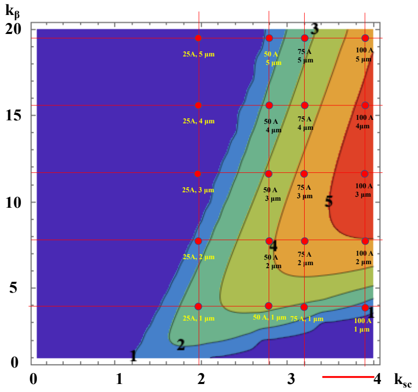

Figure 3: Contour plot of the absolute value of the growth rate in a PCA cell.

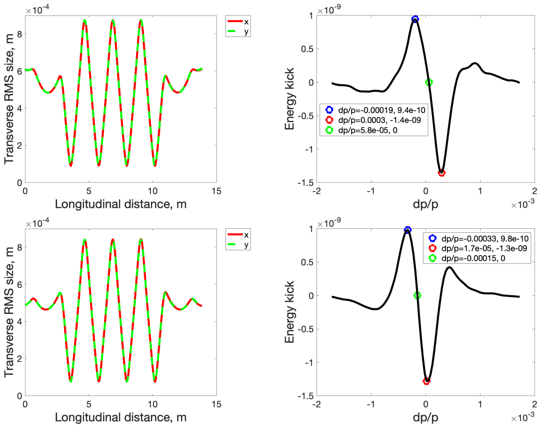

Figure 4: Evolution of the transverse RMS beam size (left) and energy kick to ions (right) for electron beam with peak current 75A and normalized RMS emittance 1.75 μm (top) and peak current 50A and normalized RMS emittance 1.5 μm (bottom).

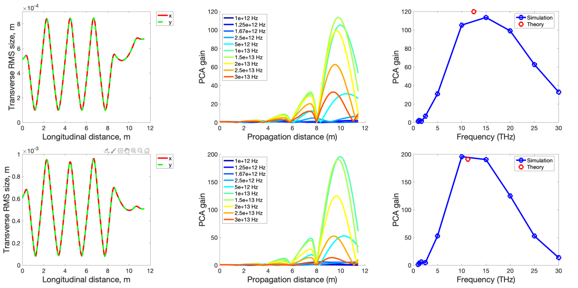

Figure 5: Evolution of the transverse RMS beam size (left column), evolution of PCA gain for various frequencies (middle column), and spectrum of PCA amplification (right column) for electron beam with peak current 25A and normalized RMS emittance 1.25 μm in two PCA lattices. The simulated PCA gain agrees well with the theoretical estimation from PCI theory.

to support the CeC experiment. Ion tracking simulation has confirmed observable effect on ion beam with the presence of CeC.

REFERENCES

[1] Y. S. Derbenev and V. Litvinenko, "FELs and High-energy Electron Cooling", in Proc. FEL'07, Novosi-birsk, Russia, Aug. 2007, paper TUCAU01, pp. 268-275.

[2] V. Litvinenko, "Coherent Electron Cooling", in Proc. PAC'09, Vancouver, Canada, May 2009, paper FR1GRI01, pp. 4236-4240.

[3] V. N. Litvinenko and Y. S. Derbenev, "Coherent Elec-tron Cooling," Phys. Rev. Lett., vol. 102, no. 11, Mar. 2009. doi:10.1103/physrevlett.102.114801

[4] V. N. Litvinenko et al., "Plasma-Cascade Micro-Bunching Amplifier and Coherent Electron Cooling of a Hadron Beams", arXiv:1802.08677, 2018.

[5] G. Wang, J. Ma, and V. N. Litvinenko. "Frequency Dependence of Plasma Cascade Amplification." In 12th International Particle Accelerator Conference (IPAC'21), Campinas, SP, Brazil, 24-28 May 2021, pp. 2672-2674. JACOW Publishing, Geneva, Switzerland, 2021.

ISBN: 978-3-95450-267-7 ISSN: 2226-0374 doi: 10.18429/JACoW-COOL2025-THA2

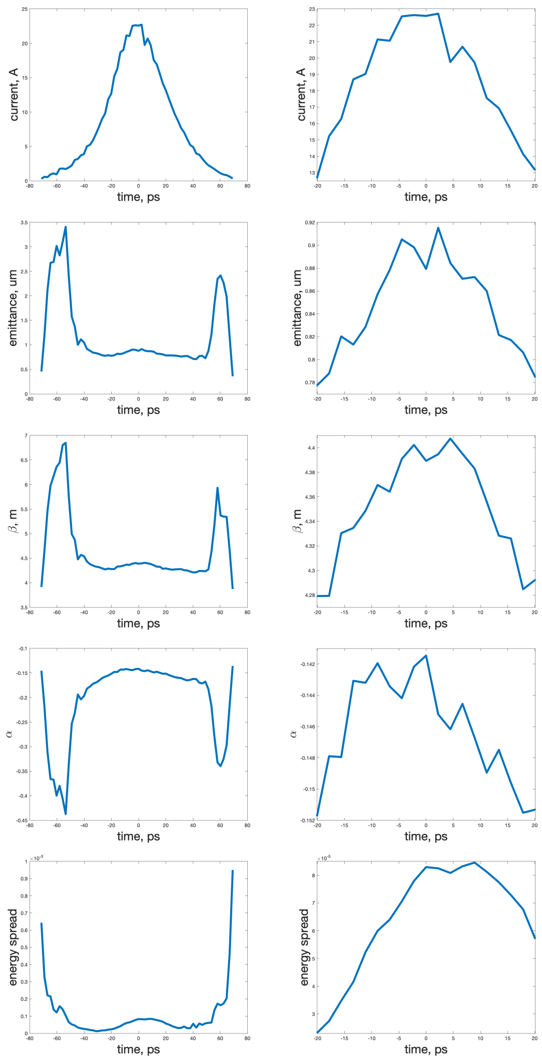

Figure 6: Beam current (1st row), normalized RMS emittance (2nd row), β function (3rd row), α function (4th row), RMS energy spread (5th row) of the entire beam (left column) and the central beam (right column) at the entrance of the modulator.

[6] V. N. Litvinenko et al., “Plasma-Cascade Instability” Physical Review Accelerators and Beams, vol. 24, no. 1, Jan. 2021. doi:10.1103/physrevaccelbeams.24.014402

[7] V. N. Litvinenko et al., “Plasma-Cascade Instability- Theory, Simulations and Experiment”, arXiv:1902.10846, 2019.

[8] V. N. Litvinenko., Y. Jing, J. Ma, I. Petrushina, K. Shih, and G. Wang. "3D theory of microscopic instabilities driven by space-charge forces." Physical Review Accelerators and Beams 26, no. 5 (2023): 054402.

[9] Y. Jing, V. N. Litvinenko, J. Ma, and G. Wang. "Relations between Shot Noise, Gain Bandwidth, and Saturation of Instabilities." Physics 6, no. 3 (2024): 921-944.

[10] K. Yu and V. Samulyak, “SPACE Code for Beam-Plasma Interaction”, in Proc. IPAC’15, Richmond, VA, USA, May 2015, pp. 728-730. doi:10.18429/JACoW-IPAC2015MOPMN012

[11] J. Ma, V. Samulyak, K. Yu, V. Litvinenko, and G. Wang, “Simulation of Beam-Induced Plasma for the Mitigation of Beam-Beam Effects”, in Proc. IPAC’15, Richmond, VA, USA, May 2015, pp. 734-736. doi:10.18429/JACoW-IPAC2015-MOPMN015

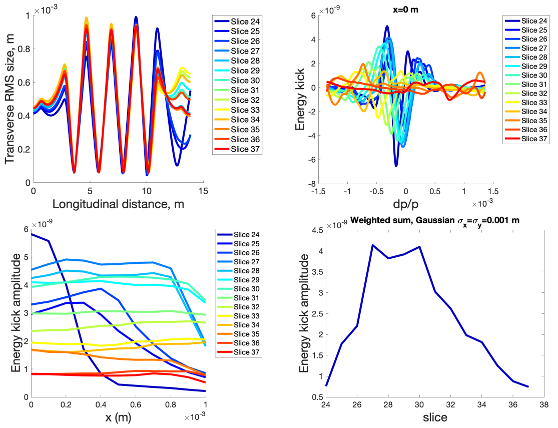

Figure 7: Evolution of the transverse RMS beam size (top left), cooling force to ions without transverse offsets (top right), cooling force amplitude to ions with transverse offsets (bottom left), weighted sum of cooling force amplitude with 2D Gaussian distribution probability density function (bottom right) using multiple slices of the central beam with PCA lattice setup 1.

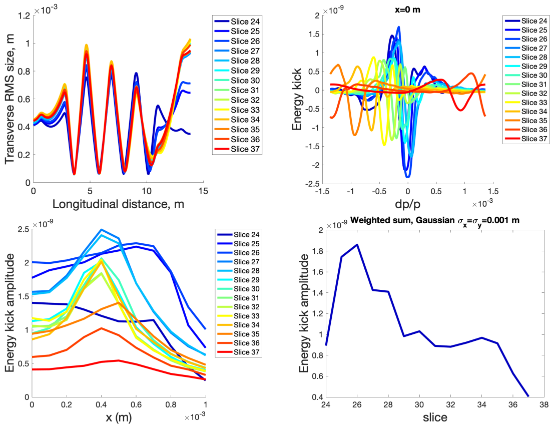

Figure 8: Evolution of the transverse RMS beam size (top left), cooling force to ions without transverse offsets (top right), cooling force amplitude to ions with transverse offsets (bottom left), weighted sum of cooling force amplitude with 2D Gaussian distribution probability density function (bottom right) using multiple slices of the central beam with PCA lattice setup 2.

[12] J. Ma, X. Wang, G. Wang, K. Yu, R. Samulyak, and V. Litvinenko, “Simulation studies of modulator for coherent electron cooling,” Phys. Rev. Accel. Beams, vol. 21, no. 11, Nov. 2018. doi:10.1103/physrevaccelbeams.21.111001

[13] J. Ma, “Numerical Algorithms for Vlasov-Poisson Equation and Applications to Coherent Electron Cooling”, Ph.D. thesis, Department of Applied Mathematics and Statistics, Stony Brook University, Stony Brook, New York, USA, 2017.

[14] J. Ma, V. Litvinenko, and G. Wang, “Simulations of Modulator for Coherent Electron Cooling”, in Proc. IPAC’18,

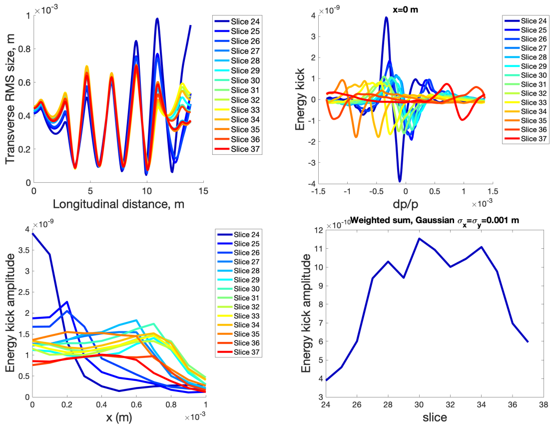

Figure 9: Evolution of the transverse RMS beam size (top left), cooling force to ions without transverse offsets (top right), cooling force amplitude to ions with transverse offsets (bottom left), weighted sum of cooling force amplitude with 2D Gaussian distribution probability density function (bottom right) using multiple slices of the central beam with PCA lattice setup 3.

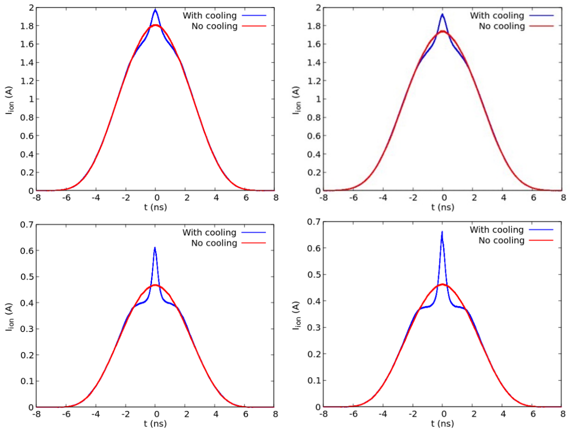

Figure 10: Evolution of the ion beam profile with intensity $8e+8$ (top) and $2e+8$ (bottom) after cooling time 4 minutes (left) and 8 minutes (right).

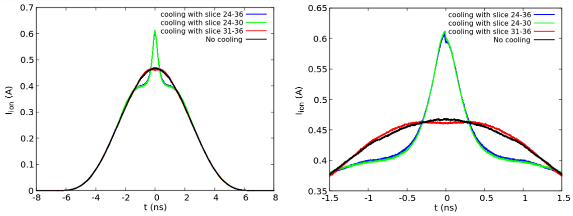

Figure 11: Evolution of the ion beam profile with intensity $2e+8$ after cooling time 4 minutes (left) and zoom in (right).

Vancouver, Canada, Apr.-May 2018, pp. 2953-2956. doi:10.18429/JACoW-IPAC2018-THPAF005

[15] J. Ma, X. Wang, V. Litvinenko, V. Samulyak, G. Wang, and K. Yu, “Modulator Simulations for Coherent Electron Cooling”, in Proc. NAPAC’16, Chicago, IL, USA, Oct. 2016, pp. 816-819. doi:10.18429/JACoW-NAPAC2016-WEPOA55

[16] J. Ma, G. Wang, and V. Litvinenko, “Simulations of coherent electron cooling with two types of amplifiers,” Int. J. Mod. Phys. A, vol. 34, no. 36, p. 1942029, Dec. 2019. doi:10.1142/s0217751x19420296

[17] J. Ma, V. Litvinenko, and G. Wang, “3d Start-to-End Simulations of the Coherent Electron Cooling”, in Proc. IPAC’19, Melbourne, Australia, May 2019, pp. 3329-3332. doi:10.18429/JACoW-IPAC2019-WEPTS092

[18] J. Ma, V. Litvinenko, and G. Wang, “Simulations of Coherent Electron Cooling With Free Electron Laser Amplifier and Plasma-Cascade Micro-Bunching Ampli-fier”, in Proc. ICAP’18, Key West, Florida, USA, Oct. 2018, pp. 52-58. doi:10.18429/JACoW-ICAP2018-SUPAF06

[19] J. Ma, V. Litvinenko, and G. Wang, “Simulations of Cooling Rate and Diffusion for Coherent Electron Cooling Experiment”, in Proc. IPAC’18, Vancouver, Canada, Apr.-May 2018, pp. 2957-2960. doi:10.18429/JACoW-IPAC2018-THPAF006

[20] J. Ma, V. Litvinenko, and G. Wang, “Simulations of Cooling Rate for Coherent Electron Cooling with Plasma Cascade Amplifier”, in Proc. IPAC’21, Campinas, Bra-zil, May 2021, pp. 3261-3264. doi:10.18429/JACoW-IPAC2021-WEPAB265

[21] J. Ma, V. Litvinenko, and G. Wang, “Simulation Studies of Plasma Cascade Amplifier”, in Proc. IPAC’21, Campinas, Brazil, May 2021, pp. 3265-3268. doi:10.18429/JACoW-IPAC2021-WEPAB266

[22] J. Ma, V. Litvinenko, and G. Wang, “Simulations of Coherent Electron Cooling with Orbit Deviation”, in Proc. IPAC’22, Bangkok, Thailand, Jun. 2022, pp. 2319-2322. doi:10.18429/JACoW-IPAC2022-WEPOMS032

[23] J. Ma, Y. Jing, G. Wang, and V. N. Litvinenko. "Simulations of Coherent Electron Cooling with Varied Beam Parameters". in Proc. IPAC’24, Nashville, Tennessee, USA, May 2024, pp. 1043-1046. doi:10.18429/JACoW-IPAC2024-TUPC18

[24] J. Qiang, IMPACT-T User Document Beta Version 1.7, Copyright the Regents of the University of California, LBNL-62326, 2007

ISBN: 978-3-95450-267-7 ISSN: 2226-0374 doi: 10.18429/JACoW-COOL2025-THA3

SIMULATION OF THE ION BUNCH IN THE PRESENCE OF THE CEC FOR THE NEW ENERGY SCHEME*

G. Wang[†,1], Y. Jing[1], V. N. Litvinenko[1,2], J. Ma[1], I. Pinayev[1]
[1]Brookhaven National Laboratory, Upton, NY, USA
[2]Stony Brook University, Stony Brook, NY, USA

Abstract

For RHIC run 25, the beam energy of the Coherent Electron Cooling (CeC) experiment will be reduced to achieve better cooling performance. For the new scheme, the distribution of the cooling electrons is obtained from beam dynamics simulation using Impact-T. A 3-D particle in cell (PIC) simulation code, SPACE, is then used to obtain the cooling force that acts both on the longitudinal and transverse location of the circulating ions. In this study, we track the ions in the presence of the cooling force and investigate how their distribution evolves during the cooling process.

INTRODUCTION

For the past decade, the demonstration experiment of the coherent electron cooling (CeC) has been actively pursued in the Relativistic Heavy Ion Collider (RHIC). To predict the evolution of the ion bunch in the presence of the cooling, a tracking code was developed and benchmarked with numerical solution of the Fokker-Planck equation [1]. The original code assumed a universal cooling force for all ions overlapping with the cooling electrons. If the properties of the electrons vary significantly within the bunch, the cooling force seen by an ion, in general, depends on its 3-D location within the electron bunch. Recently, we have improved the tracking code by implementing the dependence of the cooling force on the 3-D position of the ion.

In the next section, we show the beam parameters and cooling force obtained from the SPACE simulation. The evolution of the ion bunch profile as predicted by the tracking codes is shown in the section “Results of the Ion Tracking”.

PARAMETERS AND COOLING FORCE

Parameters

Before RHIC run 25, the beam energy for the plasma cascade amplifier (PCA) based CeC was γ=28.5 and the required peak current of the electron beam was 50 A [2]. Although the required beam parameter was achievable for some portion of the electron bunch, it was difficult to achieve a uniform region of 15 ps of duration with sufficient beam quality to satisfy the cooling requirement. As a result, a new scheme with beam energy of γ=19.5 was proposed. The new scheme requires 20 A of peak current with the normalized RMS slice emittance of 1.25 µm. After extensive simulation studies and experimental verification, it becomes clear that the new scheme is better suited to demonstrate CeC and it is currently the baseline for the CeC experiment in RHIC run 25. The parameters for the ion beam are shown in Table 1. Table 2 shows the targets for the parameters of the electron beam. Since the local parameters of the electrons vary along the bunch, the 6-D distribution of the electrons from the beam dynamic simulations are used in the single pass particle-in-cell (PIC) simulation to generate local cooling forces.

Table 1: Ion Beam Parameters for the CeC Experiment

Parameters	Ion beam
Energy, γ	19.5
Bunch intensity	2×10^8
RMS bunch length	2 ns
RMS emittance, normalized	2.5 µm
RF frequency	28 MHz
RF voltage	4.3 MV
Average beta function at IR2	11 m
Average RMS beam size	1.2 mm

Table 2: Electron Beam Parameters for the CeC Experiment

Parameters	Electron beam
Energy, γ	19.5
Bunch charge	0.8 nC
Peak current	20 A
RMS emittance, normalized	1.25 µm
RMS energy spread	$< 2 \times 10^{-4}$
Bunch repetition rate	78 kHz

Figure 1 shows the variation of the parameters of the electrons along the bunch as obtained from beam dynamic simulations [3]. While the energy spread and slice emittance are satisfactory, the variation of the peak current and the average energy of the electrons from different slices are significant. To understand the impacts of these variations to the cooling forces, we have conducted the PIC simulation with the code SPACE for each slice of the electrons.

---

* Work supported by Brookhaven Science Associates, LLC under Contract No. DE-SC0012704 with the U.S. Department of Energy.

† gawang@bnl.gov

ISBN: 978-3-95450-267-7 ISSN: 2226-0374 doi: 10.18429/JACoW-COOL2025-THA3

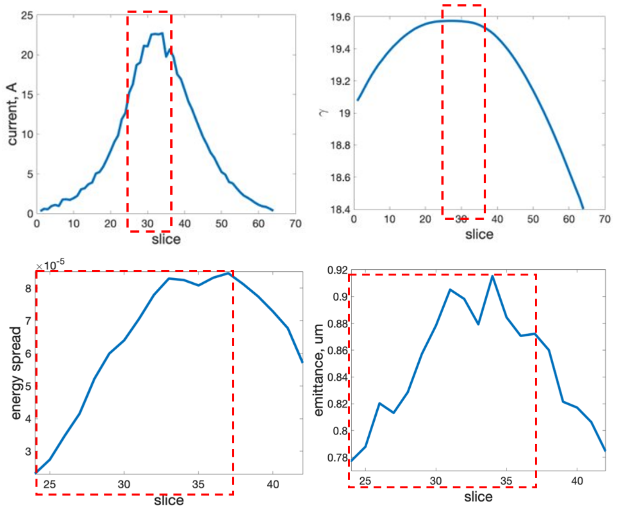

Figure 1: Parameters of the electrons along the bunch. The abscissa is the longitudinal position along the electron bunch in slice number and each slice has duration of 2.23 ps. The red box shows the region of slices used in the single pass cooling simulation with PIC code, SPACE.

Cooling Forces from the SPACE Simulation

For each slice of the electrons, the energy kick due to cooling depends on the energy deviation as well as the transverse offset of the ion. Figure 2 shows the cooling energy kick as a function of the relative energy deviation of an on-axis ion overlapping with various slices of the electrons [4]. Since the average energies of the electrons from slice 31 to slice 37 are significantly smaller than that of the ions, the ion overlapping with electrons in these slices tends to fall behind with respect to the cooling wake induced by itself in the modulator section.

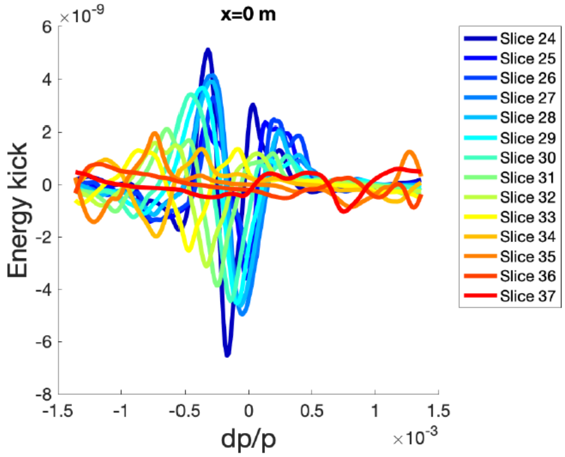

Figure 2: The energy kick due to cooling for an ion overlapping with different longitudinal slices of the electrons. The abscissa is the relative energy deviation of the ion and the ordinate is the relative energy kick received by the ion due to the cooling force. The ion is assumed to be on-axis for these plots.

It is worth noting that the cooling wakes for slices 31–37 tends to cancel each other and consequently, the net contribution from these slices is relatively small as shown in Fig. 3.

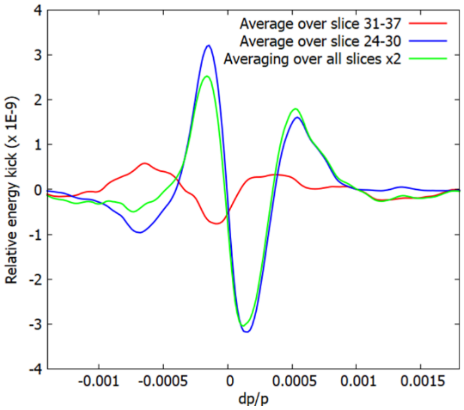

Figure 3: The averaged cooling energy kick for slices 24–30 and for slices 31–37. The cooling energy kick for each slice is taken from Fig. 2.

Figure 4 shows the cooling energy kick in slice 24 for an ion with various transverse offsets. The dependence of the cooling energy kick on transverse offset of the ion is determined by the transverse size of the electrons in the kicker section. Since the peak current, emittance and optical functions vary from slice to slice, the transverse sizes of the slices in the cooling section are also different.

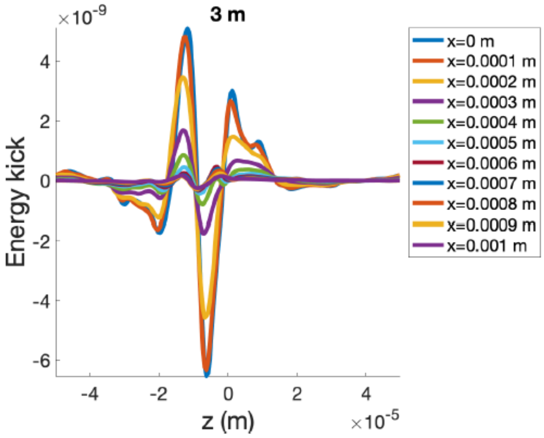

Figure 4: The cooling energy kick received by an ion overlapping with electrons in slice 24 and with various transverse offsets.

RESULTS OF THE ION TRACKING

The tracking code includes updates from the RF cavity, the betatron motion, the intra-beam scattering (IBS) and the energy kick due to the CeC process [1]. For the update in the cooling section, the cooling force is applied according to the ion's 3-D location in the electron bunch. The longitudinal location of the ion determines which slice of electrons it overlaps with, and the transverse location of the ion determines which two cooling wakes are to be used for calculating the cooling energy kick through linear interpolation. For the same initial distribution of the electrons at the entrance of the cooling section, we have investigated three setups of the solenoids' currents in the cooling sections.

The cooling forces shown in the previous section are obtained with the first setup. Figure 5 compares the longitudinal profiles of the ion bunch after 4 minutes of cooling with these three setups, which suggest that setup 1 should be used to achieve optimal cooling performance.

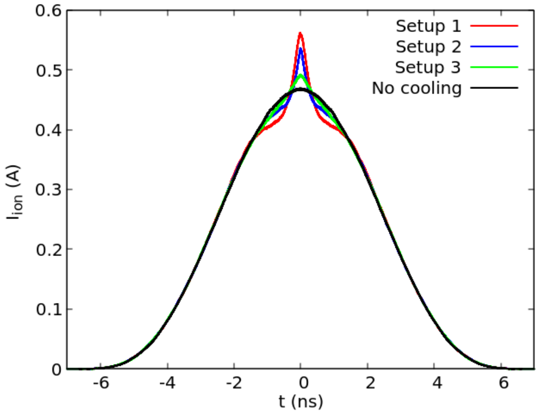

Figure 5: The longitudinal profiles of the ion bunch after being cooled for 4 minutes with the three setups of the solenoids' current in the cooling section.

In the CeC experiment, the energy jitter of the electron bunch has been observed, which is caused by the arrival time jitter of the laser pulses at the photocathode. Since the energy jitter of the electrons leads to extra offsets of the ions with respect to the cooling wakes in the kicker section, it reduces the cooling efficiency [5]. To investigate the impact of the energy jitter to the cooling performance, we have introduced the energy jitter into the tracking code. As shown in Fig. 6, the cooling effect is significantly reduced once the RMS energy jitter is greater than 10^{-4}.

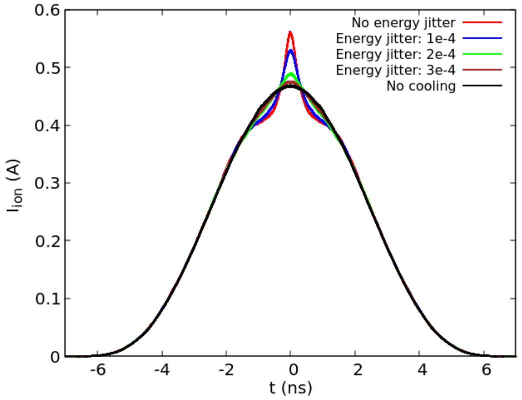

Figure 6: The longitudinal profiles of the ion bunch after being cooled for 4 minutes with various level of the RMS energy jitter of the cooling electrons.

Another adverse effect for the cooling performance is the excessive noise in the electron bunch [1]. Since the CeC process inevitably includes the diffusive kick from the neighbour electrons surrounding the ion, the excessive noise in the electron bunch leads to greater diffusion and hence slower cooling. To investigate the influences of the noise in the electrons on the cooling performance, we have increased the diffusive kick in the tracking to account for the excessive noise in the electron bunch. As shown in Fig. 7, the cooling effect reduces by a factor of 2 if the diffusive kick due to the shot noise in the electrons is increased by a factor of 4, which corresponds to an increase in the power of the shot noise by a factor of 16.

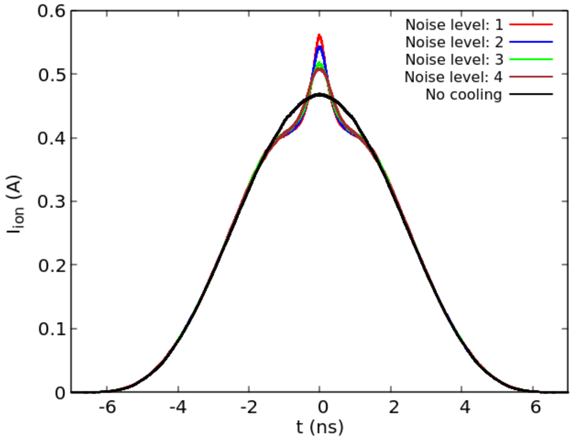

Figure 7: The longitudinal profiles of the ion bunch after being cooled for 4 minutes with various level of the diffusive kick of the cooling electron shot noise.

SUMMARY

In RHIC run 25, the CeC experiment adopted new scheme with reduced beam energy and peak current. For the new scheme, we have conducted beam dynamic simulation, single pass cooling simulation and ion tracking. The ion tracking results show that the cooling effects on the longitudinal profile of the ion bunch should be observable if the cooling force as simulated from the single pass simulation can be achieved. In addition, the energy jitter in the electron beam should be smaller than 10^{-4} and the excessive noise power in the electron bunch should stay below a factor of 16 to avoid significant reduction of the cooling performance.

REFERENCES

[1] G. Wang, "Evolution of ion bunch profile in the presence of longitudinal coherent electron cooling", *Phys. Rev. Accel. Beams,* 22, 111002, 2019. `doi:10.1103/PhysRevAccelBeams.22.111002`

[2] V. N. Litvinenko et al., "Results of the coherent electron cooling experiment at RHIC", in *Proc. COOL'25,* Stony Brook, USA, October 2025, paper MOD3, these proceedings.

[3] Y. Chao et al., "Electron beam dynamics simulation in coherent electron cooling", in *Proc. COOL'25,* Stony Brook, USA, October 2025, paper THA1, these proceedings.

[4] J. Ma et al., "Multiple-slice simulations of coherent electron cooling performance with low beam current", in *Proc. COOL'25,* Stony Brook, U.S.A., October 2025, paper THA2, these proceedings.

[5] G. Wang et al., "Influences of the energy jitter to the performance of the coherent electron cooling", in *Proc. IPAC'22,* Bangkok, Thailand, June 2022, pp. 115–117. `doi:10.18429/JACoW-IPAC2022-MOPOST026`

ISBN: 978-3-95450-267-7 ISSN: 2226-0374 doi: 10.18429/JACoW-COOL2025-THB1

DESIGN OF A MICROBUNCHED ELECTRON COOLER ENERGY RECOVERY LINAC

K. Deitrick*, S. Benson, B.R. Gamage, J. Guo, I. Neththikumara, R. Rimmer, T. Satogata,
N. Sereno, S. Setiniyaz, Thomas Jefferson National Accelerator Facility, Newport News, VA, USA
J. Conway, B. Dunham, R. Eichhorn, C. Gulliford, V. Kostroun,
C. Mayes, K. Smolenski, N. Taylor, Xelera Research LLC, Ithaca, NY, USA
W. Bergan, E. Wang, D. Xu, Brookhaven National Lab, Upton, NY, USA
N. Wang, Cornell University, Ithaca, NY, USA

Abstract

Microbunched electron Cooling (MBEC), a type of Coherent electron Cooling (CeC), is a possible way to cool high energy protons; such an electron cooler can be driven by an energy recovery linac (ERL). The beam parameters of this design are based on cooling 275 and 100 GeV protons at the Electron-Ion Collider (EIC), requiring 150 and 55 MeV electrons, respectively. If implemented, a high energy cooler would serve to increase the average luminosity of the collider by mitigating the emittance growth caused by various processes. This ERL is designed to deliver a bunch charge of 1 nC, an average current of 100 mA, and strict requirements on the transverse emittance, slice energy spread, and longitudinal distribution profile. This paper covers the current state of the design.

INTRODUCTION

The Electron-Ion Collider (EIC) is a partnership project between Brookhaven National Laboratory (BNL) and Thomas Jefferson National Accelerator Facility (TJNAF) to be constructed at BNL, using much of the existing infrastructure of the Relativistic Heavy Ion Collider (RHIC). Collisions occur between the hadrons in the Hadron Storage Ring (HSR) and the electrons supplied by the Electron Storage Ring (ESR); in order to maintain a high average polarization of the ESR, bunches are frequently replaced using the Rapid Cycling Synchrotron (RCS). While most of the magnets for the HSR are repurposed RHIC magnets, already installed in the existing tunnel, both the ESR and RCS will have to be installed. In the current scope of the EIC, only one interaction region (IR) is supported, sited at the current IR6 of RHIC; however, it is highly desired that a second IR may be supported at IR8 in the future, and design efforts support that eventuality [1].

The present EIC baseline only includes cooling of the injected hadron beam prior to ramping. However, it is possible that a future upgrade to improve the luminosity will be desired, requiring the hadron bunches to be cooled during collision in order to maintain the beam emittance [2].

MICROBUNCHED ELECTRON COOLING

Coherent electron cooling (CeC) uses an electron bunch to encode the density variations of the proton bunch, then uses the same electron bunch to apply corrective energy kicks to reduce the emittance of the proton bunch in the longitudinal and transverse directions. For the EIC, it is anticipated that the protons will be stored on the order of ten hours, but intrabeam scattering (IBS) and beam-beam effect will cause emittance growth on the order of two hours, reducing luminosity over the duration of the store. Consequently, to preserve the emittance of the proton beam and increase the average luminosity over the store, cooling during collisions is required to counteract emittance growth.

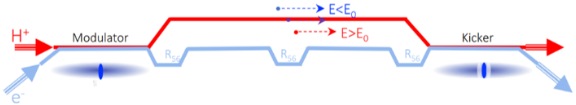

Figure 1: A representative layout of microbunched electron cooling. The protons and electrons co-propagate in the modulator section, separate into different lines, where the electron beam goes through a series of chicanes and drifts, before the electrons and protons once again co-propagate in the kicker section.

One type of coherent electron cooling is microbunched electron cooling (MBEC), the proposed mechanism for this ERL design to cool EIC protons during collisions. A representative diagram of this process is shown in Fig. 1. An electron bunch with the same relativistic gamma as the protons co-propagates with the proton bunch in the modulator, where the protons imprint on the electrons. Once separated, the electron bunch is sent through the amplifier, a series of chicanes and drifts which amplifies the energy modulation of the electron bunch that was induced by the protons; this energy modulation is converted into a density modulation. The protons and electrons co-propagate afterwards in the kicker, where the density modulation of the electrons provides a corrective kick to cool the protons. The necessary parameters for the electron beam and cooling section are shown in Table 1; further details of this cooling mechanism and these parameters can be found at [3].

Given the significant beam power necessary, it is clear that an energy recovery linac (ERL) is required - the operational power to produce the same beam parameters with a linac is prohibitive; additionally, using an ERL reduces the radiation considerations at the beam dump. Closed optics exist for both operational modes, shown in Fig. 2.

---

[*] kirstend@jlab.org

ISBN: 978-3-95450-267-7 ISSN: 2226-0374 doi: 10.18429/JACoW-COOL2025-THB1

Table 1: The parameters of the electron beam (top) and the cooling section geometry and optics (bottom) for the two proton beam energies of the EIC. The electron beam longitudinal distribution is assumed to be a supergaussian of order ~4.

Proton Energy	**100 GeV**	**275 GeV**
Gamma	107.6	294
Energy (MeV)	55	150
Bunch charge (nC)	1	
Rep. rate (MHz)	98.5	
Avg. current (mA)	98.5	
rms bunch length (mm)	9	7
Peak current (A)	10	13
Slice energy spread $dp/p(10^{-4})$	0.6–1.5	0.4–0.8
Norm. trans. emit. (mm−mrad)	2.8	
Modulator/Kicker Length (m)	33	
Number of Amplifier Drifts	2	
Amplifier Drift Length (m)	49	
β_x/β_y in Modulator (m)	20.0/20.0	21.4/21.4
β_x/β_y in Kicker (m)	29.7/4.09	7.89/7.89
β_x/β_y in Amplifier (m)	12.0/12.0	4.89/4.89
R_{56} in First Chicane (mm)	23.3	12.0
R_{56} in Second Chicane (mm)	-16.7	-6.66
R_{56} in Third Chicane (mm)	-18.2	-6.85

ERL DRIVER LAYOUT

A representative layout of the ERL is shown in Fig. 3. In beamline order during energy recovery, the sections are the injector, the merger, the booster, the bunch compressor and high energy bypass lines (PX), the main linac, the beam dump, the laser heater, transport to the cooling section, the cooling section (modulator, amplifier, and kicker), the first turnaround, the return line, and the second turnaround — after which, the beam begins energy recovery. Alternatively, the beam can be steered through the merger into the diagnostic line.

The injector consists of a photocathode DC gun and a cryomodule containing three superconducting radio frequency (SRF) cavities — two 197 MHz quarter-wave resonators (QWRs) and a 591 MHz single-cell cavity. The beam is accelerated to roughly 6 MeV and the accelerating cavities are run off-crest so that the bunch is chirped to allow for bunch compression later; the single cell cavity is at the third harmonic of the 197 MHz frequency and is used to linearize the longitudinal phase space.

The booster consists of two cryomodules, oriented so that the cavity order is two 197 MHz QWRs, two 591 MHz, and two 197 MHz QWRs. The beam energy is roughly 13 MeV, the bunch is significantly chirped, and the single cell cavities are again used to linearize the longitudinal phase space; however, the longitudinal phase space is evaluated after the bunch compressor in the following section.

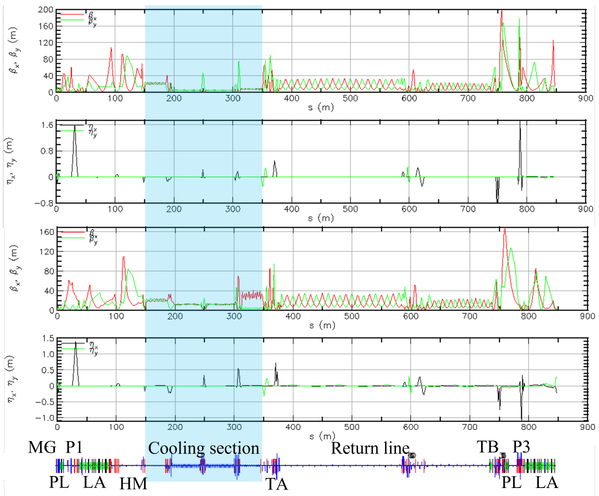

Figure 2: The preliminary designs of the 150 and 55 MeV electron coolers. Shown are the beta functions in meters (top) and dispersion in meters (bottom), all as a function of *s* in meters, with the upper and lower pair corresponding to the 150 MeV and 55 MeV design, respectively. Below the four plots is the component layout, with the various sections labeled.

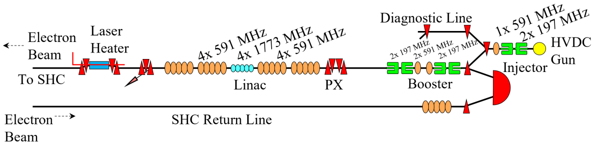

Figure 3: Represented is the injector, followed by the merger, going to either the diagnostic line or the booster, the bunch compressor and high energy bypass lines (PX), the main linac (Linac), the dump chicane, the laser heater, the transport to the cooling section, and the return line from the cooler, after which the beam energy recovers and is steered into the dump line.

Next, the beam enters the PX section, shown in Fig. 5, which consists of the P1, P2, and P3 lines. Each line is energy-specific and during the acceleration of both configurations, the 13 MeV beam goes down the P1 line, which compresses the bunch; bunch compression is tunable due to the quadrupole magnets included in the P1 line. A more in-depth description is in a later section.

Following the PX section is the main linac, consisting of eight 591 MHz five-cell SRF cavities and four 1773 MHz five-cell SRF cavities, with the 1773 MHz cavities placed in the center and four 591 MHz cavities on either side. The beam is accelerated to the top energy of either 150 or 55 MeV and is no longer chirped. Similar to the injector and booster, the longitudinal phase space is linearized with the 1773 MHz cavities.

The dump chicane and the laser heater chicane follow the main linac, after which the beam is transported to the cooling section, which consists of the modulator, amplifier,

ISBN: 978-3-95450-267-7 ISSN: 2226-0374 doi: 10.18429/JACoW-COOL2025-THB1

and kicker. After the cooling section, the beam separates from the HSR before entering a Bates bend and going down the return line.

At the end of the return line is a 591 MHz five-cell SRF cavity, which is run at the zero crossing and chirps the beam, minimizing the energy spread of the beam at the dump. Without this chirp cavity, the only way to minimize the energy spread is to have the beam energy at the dump to be significantly different than the 6 MeV injection energy.

After the return line is a second Bates bend — following this, the high energy line merges with the injection line, and the chirped beam begins deceleration and energy recovery. The beam is decelerated during the second pass through the booster, then enters the PX section. For the second pass through PX, the beam enters either the P2 or P3 beamline, corresponding to the 55 and 150 MeV modes, respectively. During the second pass through the linac, the beam decelerates to the injection energy and is transported to the beam dump.

LASER HEATER

Microbunched electron cooling is highly sensitive to the slice energy spread of the electron beam — for the EIC, this parameter needs to fall within the specified range, not just below a maximum value. While significant effort has been put into the design of the injector and booster to achieve a small slice energy spread, it is possible that the resulting value of this parameter will be too small at the exit of the linac and must be increased to fall within the target range before entering the cooling section. To increase the slice energy spread and provide an adjustable knob for this parameter downstream of the linac, a laser heater is located between the linac and the cooler [4]. The layout of the laser heater involves co-propagating a laser with the electron beam inside an undulator at the center of a chicane; a representative layout is shown in Fig. 4. The laser heater increases the slice energy spread by first applying a momentum modulation on the electron beam from the interaction with the laser within the undulator. This modulation is smeared out in the second half of the chicane [5].

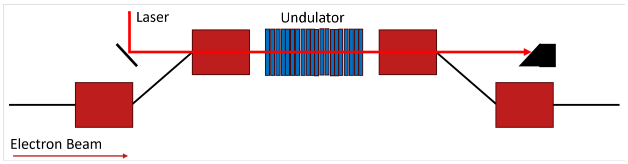

Figure 4: A representative layout of a laser heater, which involves co-propagating a laser with the electron beam inside an undulator at the center of a chicane.

TIME OF FLIGHT CONSIDERATIONS

Typically, ERLs have a single linac and consequently, only a single time of flight concern — the time of flight between the linac exit and the linac entrance. However, this machine has two accelerating sections, the booster and the linac, which means that there are two time of flight concerns. The first concern is the time of flight between the booster exit and the booster entrance; the second is the time of flight between the linac exit and the linac entrance.

The booster time of flight uses path length changes in the two Bates bends for flexibility, similar to the Jefferson Lab Free Electron Laser ERL drivers; correctors at the entrance and exit of the Bates bend allow for the beam to enter and exit on-axis, while the beam orbit through the magnet is off-axis, changing the path length through the Bates bend [6]. At the 197 MHz fundamental frequency of the booster and a 2.5 cm maximum orbit excursion at the center of the bend, this translates to a range of ±11.7° per Bates bend. However, the length of this machine introduces a complication — for a fixed path length on the order of 800 m, the time of flight for the two energies differs by roughly 8° at the booster frequency, but the time of flight between the booster exit and entrance is required to be the same for both modes. The second Bates bend was placed so that the relevant time of flight was roughly 4° from the requirement for both energies and by design, both energies travel through the second Bates bend off-axis to achieve the requisite time of flight.

The linac time of flight is controlled by the path length through the appropriate high energy PX line. Both P2 and P3 have moving stages in order to physically move two dipoles and change the on-axis path length through the lines, similar to the moving stages in the CBETA splitters [7, 8].

PX SECTION

The floor plan of the PX section, with the separate lines labeled, is shown in Fig. 5. The design of this section allows for the ERL to switch operational modes without requiring a change to the physical layout of the machine.

Each line in PX corresponds to a specific beam energy; P1, P2, and P3 are designed for beam energies of 13, 48, and 143 MeV, respectively. P1 compresses the accelerating beam for both modes, while P2 and P3 transport the decelerating beams for the top energies of 55 and 150 MeV, respectively. While all lines are achromats, none is isochronous; though it would be ideal for R_{56} to be zero in P2 and P3, it is more critical to close dispersion, dispersion prime, and control the transverse optics through these lines. Given that the decelerating beam is chirped, the non-zero R_{56} of these lines does mean that some bunch stretching occurs. If necessary, the R_{56} of the second Bates bend can be tuned to compress the bunch, so that the bunch length during the second pass the linac is sufficiently short.

In order for the time of flight requirement between the linac exit and entrance to be correct, the booster time of flight must be correct. This is driven by the limited range of the moving stages, i.e., the limited time of flight flexibility in the P2 and P3 lines, as well as the inherent geometry of the PX section; if the decelerating beam enters either high energy line at an energy significantly different than design, the beam will be lost on the beam pipe wall before

ISBN: 978-3-95450-267-7 ISSN: 2226-0374 doi: 10.18429/JACoW-COOL2025-THB1

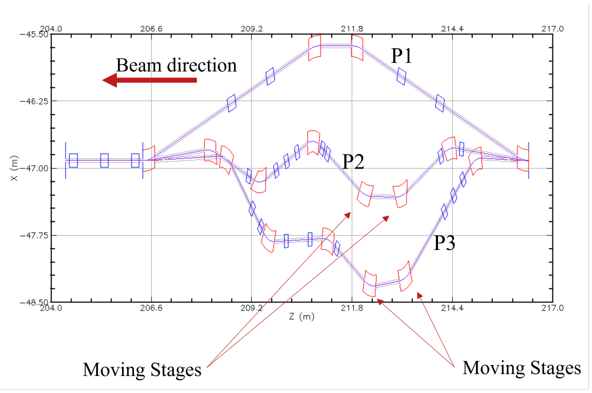

Figure 5: The floor layout of the PX section; the three separate lines are P1, P2, and P3, top to bottom (as labeled), which correspond to the beam energies of 13, 48, and 143 MeV, respectively. The "common" dipoles are the rightmost and leftmost dipoles, which is a common magnet for all three beam energies. In both the P2 and P3 lines, the second and third dipoles are on moving stages which can be remotely controlled to change the physical path length of the on-axis orbit.

reaching the first high energy dipole. While the 150 and 55 MeV configurations have very similar linac time of flight requirements, the P3 line has an extra wavelength of path length in order to remove geometry conflicts with the P2 line. As the two lines have different geometries, the time of flight flexibility is different. The P2 line has a range of ±35°, while the P3 line has a range of ±55°, both with respect to the 591 MHz fundamental frequency of the linac.

The design before the main linac, particularly the booster and PX sections, is motivated by the need to produce a super-gaussian longitudinal distribution, with small slice energy spread and transverse emittance. At present, we achieve this by producing a very long bunch at the gun, which controls both the slice energy spread and transverse emittance, until the beam is at a sufficiently high energy that when the bunch is compressed to the requisite bunch length, these parameters are relatively unperturbed through the compression process.

The inclusion of a bunch compressor within the accelerating section of an ERL is not a typical configuration, and its inclusion makes the design more complex. As a design alternative, the injector energy could be increased to 13 MeV and the bunch compressed before the merger. This would have the benefit of returning to a more simple ERL layout, with a single time of flight requirement and no need for higher-energy bypass lines to transport the decelerating beam around the compressor chicane. However, this design comes with other drawbacks — lower energy efficiency and higher shielding requirements at both the dump and the diagnostics line. Another alternative is to compress the 6 MeV bunch in the injector — however, this approach does not produce the required beam parameters.

ALTERNATE COOLING MECHANISM

Different high energy cooler designs are currently being considered for suitability in providing a potential future luminosity increase to the EIC. One concept proposed is an ERL driven circulating cooling ring (CCR), using bunched beam cooling. For an ERL driven CCR, an electron bunch is accelerated up to the desired energy, kicked into the cooling ring, circulated a small number of times to cool the protons, and is kicked out to be transported back to the linac to decelerate, be energy recovered, and transported to the beam dump. The beam parameters presented for this concept require a high-brightness, high-charge injector and ERL [9], which is similar to the design presented in this paper. Consequently, we believe that this work could serve as a starting point for the design of an ERL driver capable of achieving the necessary electron beam parameters.

CONCLUSION

We have developed a conceptual design for both energy modes of an ERL-driven cooler, which is capable of cooling high energy protons during collisions at the EIC. One critical success of this design is that the magnet layout is unchanged between configurations, so no vault access is required between switching energies. Though more complex than many ERLs, no show stoppers have been found. While it may be more feasible for the EIC parameters to consider a different cooling mechanism, this ERL design's ability to produce a high-charge, high-brightness electron beam makes it a good design starting point for future high energy cooling considerations.

ACKNOWLEDGMENTS

This work is supported by Jefferson Science Associates, LLC under U.S. DOE Contract DE-AC05-06OR23177 and Brookhaven Science Associates, LLC, Contract DE-SC0012704, while Xelera was supported by the U.S. DOE Small Business Innovation Research (SBIR) Phase II program under Federal Grant Number DE-SC0020514 during earlier stages of this work.

REFERENCES

[1] C. Montag *et al.*, "The EIC accelerator: design highlights and project status", in *Proc. IPAC'24*, Nashville, TN, May 2024, pp. 214–217. `doi:10.18429/JACoW-IPAC2024-MOPC67`

[2] K. Deitrick *et al.*, "Development of an ERL for coherent electron cooling at the Electron-Ion Collider", in *Proc. IPAC'24*, Nashville, TN, May 2024, pp. 3086–3089. `doi:10.18429/JACoW-IPAC2024-THPC40`

[3] W. Bergan *et al.*, "Coherent electron cooling physics for the EIC", in *Proc. IPAC'24*, Nashville, TN, May 2024, pp. 2937–2942. `doi:10.18429/JACoW-IPAC2024-THYD1`

[4] E. Wang *et al.*, "Generating Super-Gaussian distribution and uniform sliced energy spread bunch for EIC strong hadron cooling", in *Proc. IPAC'24*, Nashville, TN, May 2024, pp. 110–113. `doi:10.18429/JACoW-IPAC2024-MOPC23`

[5] Z. Huang *et al.*, "Measurements of the linac coherent light source laser heater and its impact on the x-ray free-electron laser performance", *Phys. Rev. ST Accel. Beams*, vol. 13, no. 2, p. 020703, 2010. `doi:10.1103/PhysRevSTAB.13.020703`

[6] D. Douglas, "Some features of the FEL upgrade π-bends", Rep. JLAB-TN-01-024, May 2001.

[7] G. H. Hoffstaetter *et al.*, "CBETA design report, Cornell-BNL ERL test accelerator", 2017, arXiv:1706.04245 [physics.acc-ph]. `doi:10.48550/arXiv.1706.04245`

[8] A. Bartnik *et al.*, "CBETA: first multipass superconducting linear accelerator with energy recovery", *Phys. Rev. Lett.*, vol. 125, p. 044803, 2020. `doi:10.1103/physrevlett.125.044803`

[9] D. Kayran, A. Fedotov, and S. Seletskiy, "Electron cooler for high-energy hadrons in the EIC based on ERL", presented at ERL'24, Tsukuba, Japan, Sep. 2024, paper THO04, unpublished. `https://conference-indico.kek.jp/event/225/contributions/5546/attachments/3907/5351/THO04.pdf`

ISBN: 978-3-95450-267-7 ISSN: 2226-0374 doi: 10.18429/JACoW-COOL2025-THB2

OPTICS DESIGN FOR A STORAGE RING BASED ELECTRON COOLER FOR COOLING AT HIGH ENERGIES

J. Kewisch [*][†], A. Fedotov, S. Seletskiy, D. Kayran, Y. Jing,
Brookhaven National Laboratory, Upton, NY, USA
J. Unger, Cornell University, Ithaca, NY, USA

Abstract

The Ring Electron Cooler (REC) is an option to provide beam cooling for the Electron Ion Collider (EIC) at high energies. Based on a storage ring this machine can provide the beam current necessary for cooling at higher energies. While the electrons cool the ions the electrons are cooled by radiation cooling, which is enhanced using strong wiggler magnets. The ring has a race track shape, where one straight section is used for ion cooling and the other includes the wigglers with a peak field of 2.4 T. In our solution the sextupoles and octupoles necessary for chromaticity correction are also located in the wiggler section, where the dispersion function is optimized in the multipoles without increasing the emittances too much through radiation excitation and intra beam scattering. A constant dispersion in the cooling section allows redistributing cooling power from the longitudinal to the transverse direction. A dispersion-free section is inserted into the arcs for RF cavities and injection.

INTRODUCTION

The idea of using an electron storage ring for electron cooling is not new. It was proposed nearly 50 years ago by D. Cline et al. [1]. Here the ion beam is cooled by the electrons and the electrons are kept cool through radiation damping. Wiggler magnets are employed to increase the radiation.

A storage ring eliminates the need for a high current electron gun, which would be necessary for sufficient cooling of the EIC beams at top energy using a linac or ERL based cooler.

While in a linac the beam emittance is naturally low, in a ring cooler the emittance is determined by the equilibrium of the radiation damping and the heating from

- quantum excitation in dipoles.
- intra-beam scattering (IBS) everywhere where the dispersion is nonzero.
- beam-beam (BBS) scattering in the cooling section.

As IBS and BBS are functions of the emittance itself the program GETRAD [3] is used. GETRAD calculates the emittances iteratively, starting from a guess, using:

$$\epsilon_{\text{new}} = \frac{(\lambda_{\text{rad}} + \lambda_{\text{IBS}}(\epsilon_{\text{old}}) + \lambda_{\text{BBS}}(\epsilon_{\text{old}}))}{\lambda_{\text{damping}}}$$

where the lambdas are the heating and damping rates.

GEOMETRIC AND OPTICAL CONSTRAINTS

The bunch frequency of the ion ring is 98.6 MHz. It is preferable that each ion bunch is always cooled by the same electron bunch, i.e. the ratio of the harmonic numbers of ions and electrons is an integer. This requirement allows a ring length of 255 m, 426 m or 576 m. The length of 255 m does not allow the full use of the 176 m long straight section for cooling; 576 m has a too large space charge tune shift.

The 426 m circumference allows the wiggler section to be longer than the cooling section, resulting in a trapezoid shape as shown in Fig. 1.

Figure 2 zooms into the arc region. The straight section inside of each 180° arc are dispersion-free and are used for the RF cavities and the injection.

The REC uses redistribution of cooling from the longitudinal to the horizontal direction. This requires a 1 m dispersion in the cooling section.

EMITTANCE AND CHROMATICITY

The major contribution in each of the three heating mechanisms comes from the coupling of longitudinal scattering into the transverse direction, which is described by the H-function:

$$H = \gamma D^2 + 2\alpha D D' + \beta D'^2 \quad \text{with} \quad \gamma = \frac{1+\alpha^2}{\beta}$$

The quantum excitation is exactly proportional to H, for IBS and BBS it is more complicated, but minimizing H is a recipe for a low emittance.

On the other hand we have to correct the chromaticity. For that purpose we need locations where the dispersion is large and the beta functions differ significantly. This requirement increases the H-function and leads to a larger emittance. The goal has to be to find a compromise between the two requirements and find suitable locations for the sextupoles.

The arcs are tiny compared to the rest of the machine. Placing the sextupoles in the arcs would concentrate them in two locations, which would harm the dynamic aperture. In the REC there is dispersion in the cooling section, but the beta functions are about equal, which does not allow effective chromaticity correction. The only place for sextupoles is therefore in the wiggler section.

---

[*] Work supported by Brookhaven Science Associates, LLC under Contract No. DE-SC0012704 with the U.S. Department of Energy.

[†] jorg@bnl.gov

ISBN: 978-3-95450-267-7 ISSN: 2226-0374 doi: 10.18429/JACoW-COOL2025-THB2

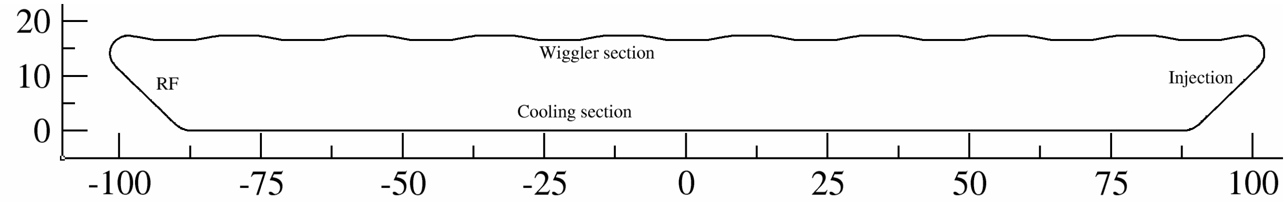

Figure 1: Layout of the ring cooler. The scale in x and y is the same, illustrating the true dimensions of the ring.

THE ARCS

The arcs employ a FODO lattice using 20 dipoles with a length of 20 cm per 180° arc. The phase advance per FODO cell is about 90° phase advance. The tune of the ring can be adjusted by modifying this phase advance.

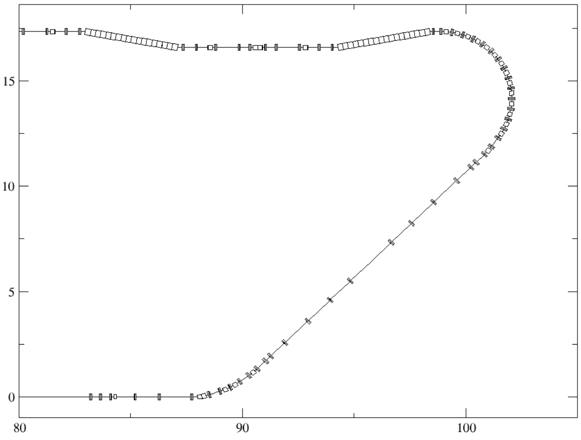

Figure 2: Top view of the arc. Dimensions in meters.

We tried a double-bend achromat lattice, but that did not improve the emittance. The reason is that IBS, unlike quantum excitation from dipoles, heats the beam in transverse direction everywhere where the dispersion is non-zero. A DBA lattice minimizes the H-function in the dipoles, but adds IBS in drifts and quadrupoles.

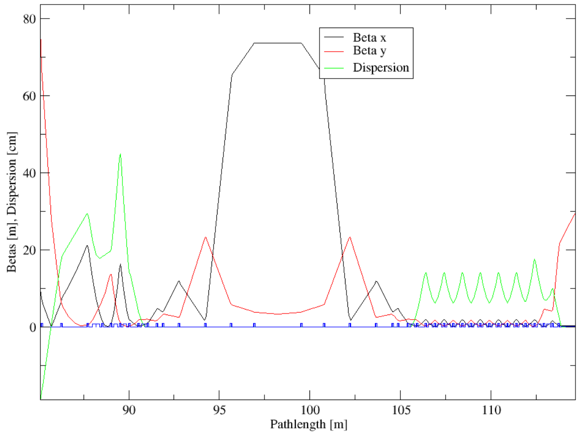

Figure 3: Twiss functions of the arc. The large beta function is necessary for the injection.

In the REC we need dispersion in the cooling section for cooling redistribution and in the wiggler section for chromaticity correction. The dispersion is therefore not compensated at both ends of the arc, but shaped to be used for those purposes. The Twiss functions of the arc are shown in Fig. 3.

The straight sections inside the arcs are made dispersion-free using a "missing magnet" configuration. These are the only places in the REC with zero dispersion, which is necessary for the RF and injection. A large horizontal beta function is required at the injection point.

THE WIGGLER SECTION

Usually wigglers have half-length periods at both ends to compensate the dispersion. Since we need dispersion in the sections between the wigglers, we use wigglers that end in a regular period and we tilt the wiggler relative to the incoming beam direction. The beam is bent by the first half wiggler period onto the wiggler axis. After a full period the beam will point into the incoming direction, but has a horizontal offset.

After 18 periods the offset is 75.4 cm. The following wiggler is tilted in the opposite direction, bringing the beam back to zero offset. A top view of the wiggler arrangement is shown in Fig. 4.

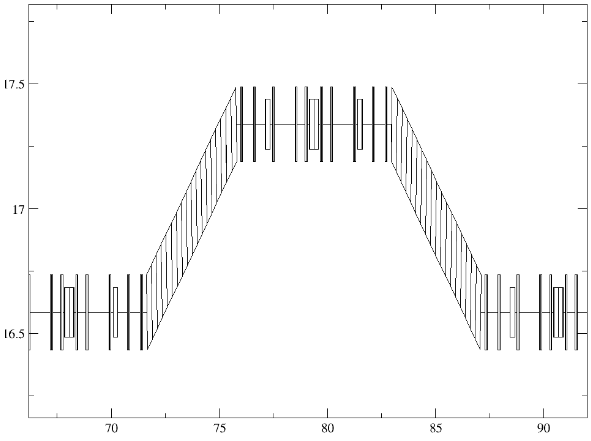

Figure 4: Top view of the wiggler arrangement.

In the same way the dispersion coming from the arc is matched to enter the wiggler with the same angle. The dispersion will then leave the wiggler with the same angle and is amplified in the section between wigglers to be used for chromaticity correction. The horizontal phase advance between wigglers is 180°, so that the dispersion enters the following wiggler with the correct slope. Figure 5 shows the optics of that section, and the wiggler specifications are summarized in Table 1.

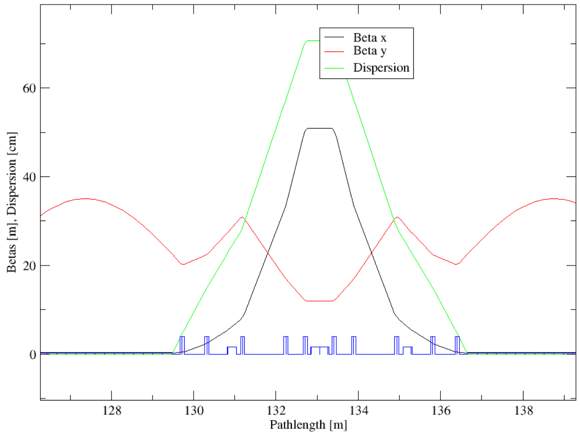

Figure 5: Twiss functions between wigglers.

Table 1: Wiggler Specifications

Number of wigglers	18
Wiggler total length	4.19 m
Number of wiggler periods	18
Period length	0.23279 m
Total gap height	2 cm
Peak field	2.385 T
Radiation power per wiggler	674 W
Beam injection angle	10.37°
k_x	26.990786
k_y	0.0073700
k_z	26.990787

We use a pole shape of the wigglers that produce a field described in [2]:

$$\begin{aligned} B_y &= B_0 && \cosh\left(k_x x\right)\cosh\left(k_y y\right)\sin\left(k_z z\right) \\ B_x &= B_0 \frac{k_x}{k_y} && \sinh\left(k_x x\right)\sinh\left(k_y y\right)\sin\left(k_z z\right) \\ B_z &= B_0 \frac{k_z}{k_y} && \cosh\left(k_x x\right)\sinh\left(k_y y\right)\cos\left(k_z z\right) \end{aligned} \quad (1)$$

where $k_z = \frac{2\pi}{\lambda}$ and λ is the length of the wiggler period. The variables k_x and k_y govern the focusing of the wigglers and obey $k_z^2 = k_x^2 + k_y^2$. We use a very small k_y, so that the wiggler focuses mainly in the horizontal direction. The periodic horizontal beta function is then close to the period length, i.e. about 23 cm. The vertical beta function can be selected arbitrarily. We used this parameter to vary the vertical phase advance from one wiggler to the next to optimize the dynamic aperture. The horizontal phase advance can be modified by varying the wiggler field.

Since the dispersion and the horizontal beta function is small, the H-function is small at the exit of the wiggler. H is a constant of motion outside dipoles, so it stays small between the wigglers.

The advantage of using a field as described in Eq. (1) is that it has on the central orbit a sextupole component that compensates the chromaticity introduced by the focusing of the wiggler. Since this sextupole is distributed over the length of the wiggler the dynamic aperture is not destroyed.

THE COOLING SECTION

Figure 6 shows the Twiss functions where the arc transitions into the cooling section, and REC cooling parameters are summarized in Table 2. The merging dipole injects the electron beam into the ions. We use a telescope with six quadrupoles to amplify the beta functions and dispersion.

We found that placing the telescope before the dipole causes a significant emittance growth from the quantum excitation in the dipole, caused by the increased dispersion. So the telescope is placed after the merging dipole. Unfortunately this arrangement reduces the active length of the cooling section because of the strong divergence of the electron beam in the telescope.

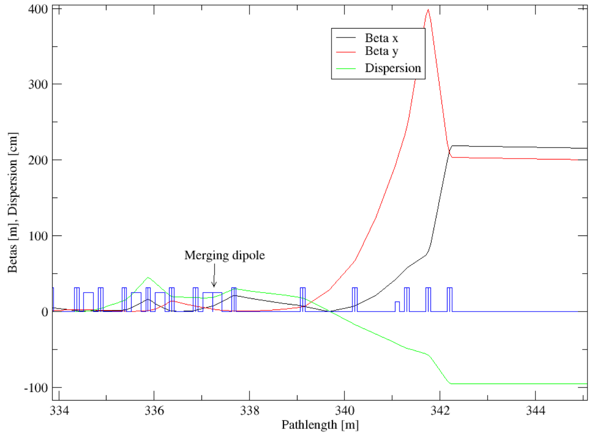

Figure 6: Twiss functions at the beginning of the cooling section.

Table 2: REC Cooling Parameters

Length of the active cooling section	166.3 m
Horizontal beta function in the center	180 m
Vertical beta function in the center	160 m
Horizontal beta function in the end	218.4 m
Vertical beta function in the end	203.2 m
Peak vertical beta function	203.2 m
Horizontal dispersion	1 m
Horizontal cooling time	2 h
Vertical cooling time	4 h
Longitudinal cooling time	3 h

CONCLUSION

We have created an optics layout for the REC that compromises between the need for small emittances and chromaticity correction. This was achieved by placing the sextupoles in the wiggler section instead of the arcs of the ring. Instead of compensating the dispersion inside the wigglers we amplified it to be used in the sextupole locations. The optics of the complete ring is shown in Fig. 7.

Together with a redistribution of the cooling from the longitudinal into the horizontal direction we achieved the required horizontal cooling time of 2 hours. More details are given in [4].

Table 3: Important Parameters of the REC

Energy	149.259 MeV
Gamma	293.093
Number of bunches	140
Number of electrons per bunch	$1.3 \cdot 10^{11}$
Charge per bunch	21 nC
Average current	2 A
Tunes	60.18 / 8.18
Chromaticity	-140 / -114
Geometric emittance	7.8 / 7.8 nm
Relative momentum spread	$9.7 \cdot 10^{-4}$
Momentum compaction	$-1.43 \cdot 10^{-3}$
FWHM bunch length	34 cm
Damping times	32.3/16.1 ms

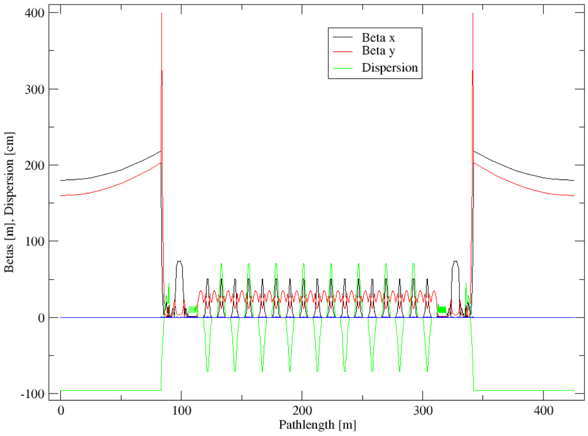

Figure 7: Twiss functions of the REC.

REFERENCES

[1] D. Cline, “High energy electron cooling to improve the luminosity and lifetime in colliding beam machines”, IEEE Trans. Nucl. Sci., Vol. NS-26, No. 3, June 1979

[2] R.P. Walker, “Wigglers,” in Proc. CERN Accelerator School: Synchrotron Radiation and Free Electron Lasers, CERN, Geneva, Switzerland, Rep. CERN-1995-006, 1995, pp. 807–834. doi:10.5170/CERN-1995-006.807

[3] M. Blaskiewicz, “Ring-based electron cooler for high energy beam cooling”, Phys. Rev. Accel. Beams 24, 043501 (2021). doi:10.1103/PhysRevAccelBeams.24.043501

[4] S. Seletskiy, “Development of storage ring electron cooler for high energy applications”, in *Proc. COOL’25*, Stony Brook, NY, USA, November 2025, paper MOB3.

A NEUTRAL HYDROGEN MONITOR FOR ELECTRON COOLING STUDIES OF H^- IONS IN ELENA

G A Tranquille*, CERN, Geneva, Switzerland

Abstract

H^- ions are routinely used for the recommissioning of the ELENA ring as well as for various machine studies. Because of the weak binding energy of the electron, these ions are stripped by the interaction with the residual gas molecules and the intense electron beam generated by the electron cooler after which they are lost on the vacuum chambers of the main machine dipoles.

A neutral hydrogen monitor is installed downstream from the electron cooling device in the extension of one of the dipole magnets and is used to study the above mentioned effects. This provides much information on the evolution of the beam size and position in the cooling section during the deceleration as well as the performance of the electron cooler.

INTRODUCTION

In ELENA [1,2] a dedicated linac, operating at an energy of 100 keV, allows the machine to be operated with H^- ions or protons when it is not sending antiprotons to the experiments. The proton mode of operation has never been used due to the complexity of changing the magnetic polarity of the ELENA ring resulting in a lengthy setting up. As the ELENA deceleration cycle lasts 15 seconds, up to seven "standard" cycles using H^- ions can be inserted between the antiproton cycles (repetition rate of 120 seconds) [3] in order to perform beam measurements and machine optimisation.

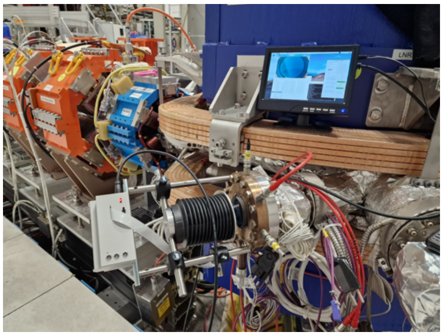

Figure 1: H0 monitor installation

HARDWARE

To measure the neutral hydrogen beam profile a detector (see Fig. 1), comprising of a chevron mounted micro-channel plate (MCP) coupled to a P43 phosphor screen, is installed in the vacuum extension of the 60° bending magnet approximately 3.14 m downstream from the centre of the electron cooler. The H0 atoms that are created travel straight towards the monitor and as they hit the MCP surface, electrons are produced and are amplified in the MCP before they are accelerated onto the phosphor screen. The image of the phosphor screen is acquired by a Raspberry Pi4 computer [4] using the Pi HQ camera mount with interchangeable lenses.

SOFTWARE

The high voltage for the MCP and P43 screen is provided by an iSeg THQ dual channel power supply. A Python script controls the voltage ramp that is applied to the MCP and screen. Camera control is also performed via a Python script which enables the user to adjust the camera settings (resolution, exposure etc.) and to select the acquisition mode. Continuous, single/multi-frame and video capture are available and can be triggered synchronously with events in the ELENA magnetic cycle. Once the signals are acquired, offline programs enable the evaluation of the beam parameters as well as their evolution. One feature that was implemented was the possibility to selectively analyse regions of the video images. This was essential as multiple beam spots can be observed during the deceleration cycle (see Fig. 2) caused by the offset of the circulating beam inside the cooler with respect to the rest of the straight section.

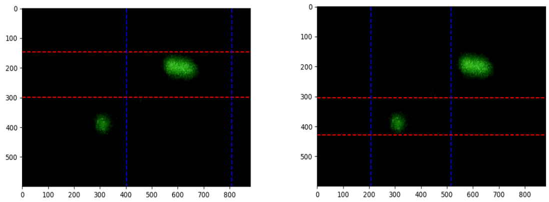

Figure 2: Signal cropping for selective analysis at 35 MeV/c

BEAM COOLING MEASUREMENTS

The alignment of the ion beam and the cooling electrons is essential in order to obtain the best cooling and hence reduce beam losses due to adiabatic blow-up and residual gas scattering. Beam position monitors can give information on the ion and electron beam trajectories but cannot give any indication on the efficiency of the cooling process. The effects of position and angle changes of the H^- beam on the cooling efficiency are directly observed on the H0 monitor and help to reduce the setting up time of the machine. The initial position and angle settings are shown on Table 1.

Position and Angle Scans at 35 MeV/c

At the first deceleration plateau of 35 MeV/c, a scan of the circulating beam trajectory and angle in the cooler section

---

* gerard.tranquille@cern.ch

ISBN: 978-3-95450-267-7 ISSN: 2226-0374 doi: 10.18429/JACoW-COOL2025-THC1

Table 1: Initial Settings

Momentum:	**35 MeV/c**	**13.75 MeV/c**
V_{cath} (V)	-368.86	-57.62
V_{grid} (V)	-300.00	-50.00
I_e (mA)	4.45	0.35
bump$_h$ (mm)	3.4	-0.4
angle$_h$ (mm)	1.4	-3.8
bump$_v$ (mrad)	4.0	4.2
angle$_v$ (mcrad)	0.5	-3.8

was performed to determine the best alignment for cooling. The horizontal position (bump$_h$) of the H^- beam was scanned from -5.6 mm to +7.4 mm and vertically (bump$_v$) from -5.0 mm to +5.0 mm. At the same time the change in cooling energy, obtained using the longitudinal Schottky monitor, was recorded to reconstruct the space-charge distribution of the electron beam (see Fig. 3 left). The programmed bump was also compared to the measured displacement measured on the H0 monitor (see Fig. 3 right).

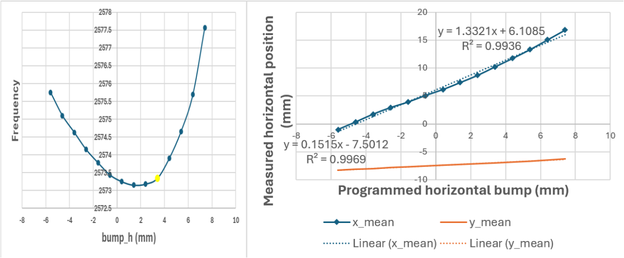

Figure 3: Revolution frequency (h=7) vs. horizontal bump (left) and Measured position vs. programmed bump (right)

Video data corresponding to the plateau (4.8 s to 7.2 s) was analysed to evaluate the evolution of the beam characteristics in the presence of the electrons. Figure 4 shows shows the effectiveness of the cooling at different horizontal positions of the circulating H- beam. One clearly sees a positive effect on the vertical beam size as the trajectory of the H^- ions is moved towards the exterior of the ring. However, no significant improvement on the horizontal size is observed and if the beam is moved towards the interior of the ring, the cooling becomes completely ineffective.

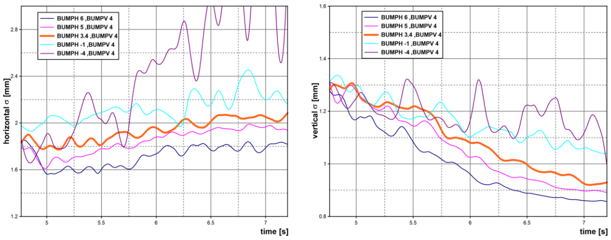

Figure 4: Horizontal (left) and vertical beam size evolution as a function of horizontal orbit bump

This is also illustrated in the electron stripping rates (see Fig. 5) where one observes a factor of three increase in the rate when the H^- beam is moved to the exterior. If steered in the other direction, the rate decreases indicating no cooling and possibly beam loss.

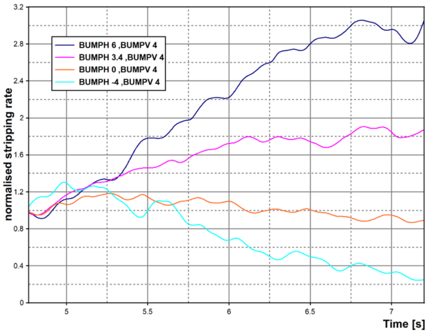

Figure 5: Normalised stripping rates at different orbit bumps

Scanning the vertical position of the H^- beam resulted in a significant improvement of the horizontal cooling when the ion beam is displaced downwards, with little or no effect in the vertical plane (see Fig. 6).

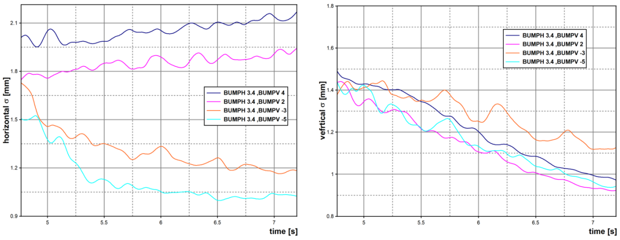

Figure 6: Horizontal (left) and vertical beam size evolution as a function of vertical orbit bump

A horizontal angle scan of ±2 mrad around the initial angle of 1.4 mrad (see Fig. 7) did not show any visible improvement in the cooling. The horizontal beam size did reduce slightly when a positive shift in the angle was made. However, in the vertical plane, cooling became less efficient. Similarly, scanning the vertical angle did not provide any major change in the cooling.

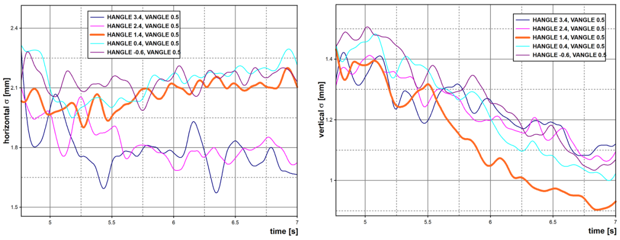

Figure 7: Horizontal (left) and vertical beam size evolution as a function of horizotal angle

ISBN: 978-3-95450-267-7 ISSN: 2226-0374 doi: 10.18429/JACoW-COOL2025-THC1

Measurements at 13.75 MeV/c

At the lower cooling plateau of 13.75 MeV/c (100 keV kinetic energy), the measurements were hindered by the fact that the signal coming from the neutral beam inside the cooler nearly overlapped the signal from the stripped H^- beam in the rest of the straight section (Fig. 8). It was decided to limit the alignment measurements and to concentrate on the influence of certain electron cooler parameters. Nevertheless the results of an angle scan did show a slightly better cooling performance if the horizontal angle of the electron beam is increased by 1 mrad. The position scans were difficult to interpret due to the coincidence of the H0 signals and will need to be revisited.

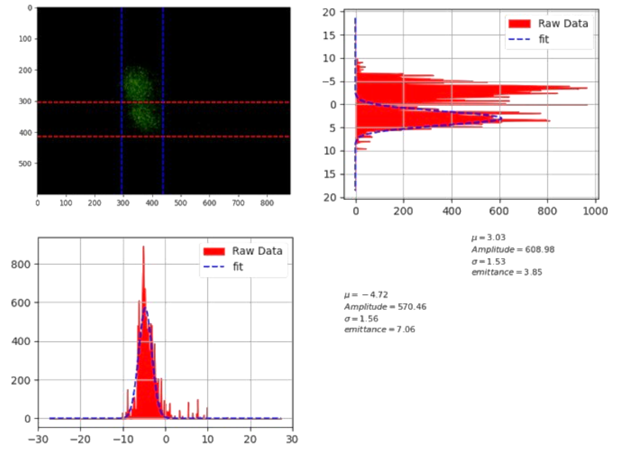

Figure 8: H0 signal at 13.75 MeV/c

Influence of the Electron Current I_e The cooling time is inversely proportional to the intensity of the cooling electrons [5]. By varying the voltage on the grid electrode, V_{grid}, thus increasing the potential difference between the cathode and the extracting electrode, the electron beam current can be adjusted. We varied the beam current between 0.34 mA and 1.46 mA to measure the effect on the H^- beam size. The evolution of the beam size was recorded and a linear approximation was applied to obtain a cooling gradient. Figure 9 shows the plot of the decrement in beam size as a function of the electron beam current. One clearly sees that, although the beam is cooled for all the settings, the best cooling is obtained with a lower current and more effectively in the horizontal plane. A possible reason for this unexpected result is that the increase in the electron beam current introduces a significant shift in cooling energy due to its space-charge. In a previous measurement the electron beam current was set to 0.75 mA and the energy increased to 60.32 V. For this setting the horizontal H0 size was reduced but the effect in the vertical plane was detrimental. It is clear that more investigations are need to fully understand how I_e affects the cooling, and this at both cooling plateaus.

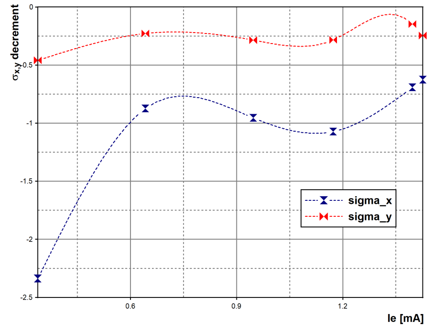

Figure 9: Beam size decrement as a function of I_e

Influence of Beam Expansion The ELENA cooler [6] is equipped with an expansion solenoid that can deliver a longitudinal field of 1000 G. This means that the electron beam radius r_e can be expanded from 8 mm to 25 mm with a reduction in the transverse temperature by a factor of 10. At present the expansion solenoid runs at a field of 290 G (expansion factor $k_{\text{exp}} = \sqrt{B/B_0} = 1.73$) resulting in an electron beam radius of 14 mm. For this set of measurements the expansion solenoid was varied up to 80 A (r_e= 20 mm) to determine the effectiveness of beam expansion. Figs. 10 and 11 show the evolution of the beam size for two values of the expansion factor. One sees that expanding the electron beam, a-priori, does not improve the cooling and even tends to blow up the beam.

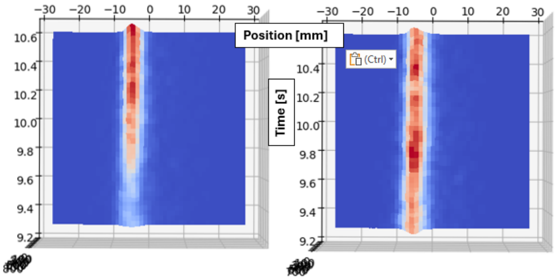

Figure 10: Horizontal beam size evolution with $k_{\text{exp}} = 1.73$ (left) and 2.44 (right)

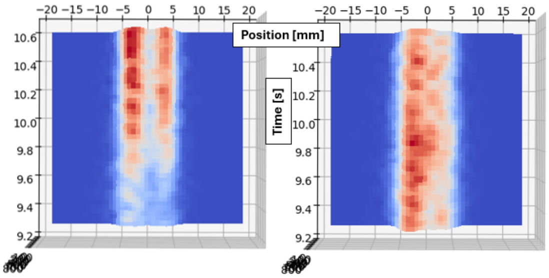

Figure 11: Vertical beam size evolution with $k_{\text{exp}} = 1.73$ (left) and 2.44 (right)

It is clear that the alignment could be one of the reasons why the cooling is not enhanced. The field from the expansion solenoid permeates into the toroid where the ion

ISBN: 978-3-95450-267-7 ISSN: 2226-0374 doi: 10.18429/JACoW-COOL2025-THC1

beam enters the cooling section and hence can modify the deflecting field experienced by the ions. Further studies will be made to elucidate this point.

Electron Detachment of the H- Beam In a previous machine development session [7] an attempt was made to estimate the electron detachment cross-section [8, 9] for H^- ions at low energy. The experiment consisted of three stages (see Fig. 12):

- electron cooling for the normal operational duration
- beam bunching for intensity measurement
- switch on electron beam at different energies and record the beam intensity

As the electron cooler gun and collector voltages cannot be modified for different magnetic cycles, the 35 MeV/c parameters were adjusted for the lower energy and had their timings modified to allow the electrons to be switched on again once the beam had been re-bunched.

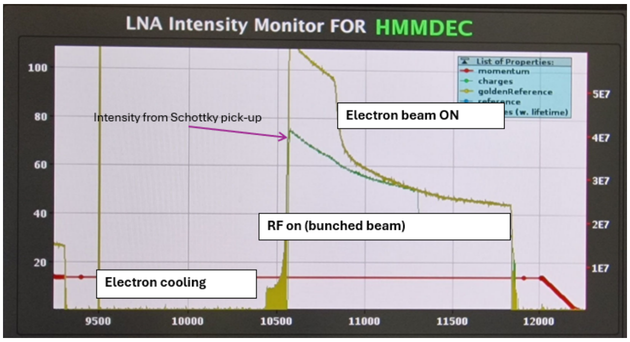

Figure 12: Electron detachment cross-section measurement sequence

For this measurement the same sequence was used and the stripping rate was evaluated from the H0 signal measured on the monitor. The results (see Fig. 13) obtained contradict somewhat the previous measurements and seem to indicate that the main reason for the beam loss is due to the electron intensity. Scanning the intensity around a fixed energy E_e (see Fig. 14) reinforces this observation as we clearly see that beam survives until a certain electron current is reached after which the H^- beam is completely lost. This was true for all energies that were used for these measurements.

Whilst making these measurements it also came to our attention that the electron gun was not producing the intensity as anticipated. Normally the generation of an electron beam follows Child's Law, $I_e = \mu V^{3/2}$, where the perveance, μ, is a geometrical constant dependent on the ratio of the cathode radius and the cathode to anode distance. From Fig. 15, where the beam current I_e is plotted against the cathode to anode (or "grid") voltage difference raised to the power 3/2, one expects to obtain a straight line, the gradient of which gives the perveance. However, this is not the case and we see a clear influence of the cathode voltage on the gun perveance. The calculated perveances range from 2.53 to 4.12 μP. A measurement made at the 35 MeV/c plateau gave a higher value of 4.73 μP.

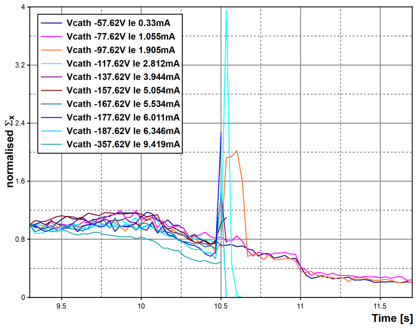

Figure 13: H^- stripping rates as a function of E_e

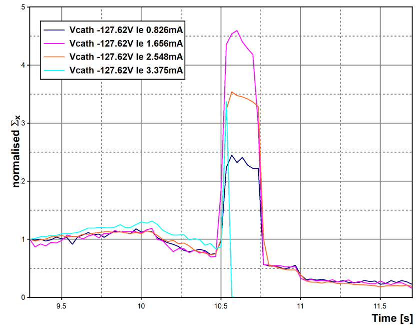

Figure 14: H^- stripping rates as a function of I_e for $E_e = 127eV$

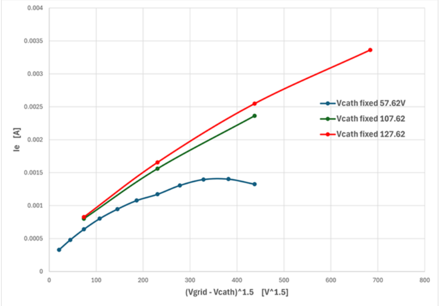

Figure 15: I_e vs. $(V_{\text{grid}} - V_{\text{cath}})^{3/2}$

CONCLUSION

The neutral hydrogen monitor is a useful instrument to, not only help a speedy (re)commissioning of the ELENA ring, but also investigate in more detail the interaction of electrons on the circulating ion beam. The cooling performance over the complete deceleration cycle can be evaluated in one shot and any improvement after adjustment of the machine parameters is immediately visible. The measurements that have been performed have brought to light an unexpected behaviour of the cooler which will require further studies.

REFERENCES

[1] G. Tranquille et al., “ELENA: From the first ideas to the project”, in Proc. IPAC’12, New Orleans, LA 2012, pp.3764. https://accelconf.web.cern.ch/IPAC2012/papers/THPPP017.pdf

[2] V. Chohan et al., “Extra Low ENergy Antiproton (ELENA) ring and its Transfer Lines: Design Report”, http://dx.doi.org/10.5170/CERN-2014-002

[3] L. Ponce et al., “The CERN antimatter factory: performance and perspectives”, in proc. COOL’25, Stony Brook, New York, 2026, paper MOA2.

[4] Raspberry Pi 4, https://www.raspberrypi.com

[5] H. Poth. “Electron cooling: Theory, experiment, application.”, in Physics Reports 196.3 (1990), pp. 135–297. doi:https://doi.org/10.1016/0370-1573(90)90040-9

[6] G. Tranquille et al., “The ELENA electron cooler”, in proc. IPAC’16, Busan, Korea, May 2016, https://doi.org/10.18429/JACoW-IPAC2016-TUPMR006

[7] D. Gamba. “Beam Instrumentation Requirements for AD”, https://indico.cern.ch/event/1411240/

[8] U. Narain and N.K. Jain, “Electron detachment cross sections of H-”, J. Phys. B: Atom. Molec. Phys. **9**, No. 6, 1976, https://doi.org/10.1088/0022-3700/9/6/015

[9] H.C.Bryant et al. “Observation of Resonances near 11 eV in the Photodetachment Cross Section of the H- Ion”, https://journals.aps.org/prl/pdf/10.1103/PhysRevLett.38.228

ISBN: 978-3-95450-267-7 ISSN: 2226-0374 doi: 10.18429/JACoW-COOL2025-THC2

TRANSVERSE BBU SUPPRESSION WITH FEEDBACK FOR ENERGY RECOVERY LINACS

S. Setiniyaz*, N. Sereno, I. Neththikumara, K. Deitrick, Jefferson Lab, Newport News, VA, USA

Abstract

In this study, we present beam dynamics simulations of the Strong Hadron Cooling (SHC) Energy Recovery Linac (ERL) that incorporate a feedback (FB) system designed to mitigate Beam Breakup (BBU) instabilities. The FB effectively suppresses BBU and increases the threshold current by roughly an order of magnitude. Our analysis revealed the aliasing behavior of the dominant higher-order mode (HOM) and its suppression by the FB, as evident from the power spectral density (PSD) of the beam centroid's horizontal motion at the exit of the final linac section. Although the FB system— even when affected by noise—successfully reduced the BBU peak, it also amplified the PSD at other frequencies. These results provide important insights into BBU suppression and threshold current enhancement in ERLs.

INTRODUCTION

The Electron-Ion Collider (EIC) is a state-of-the-art, high-luminosity particle accelerator designed to collide highly polarized electrons with ions [1, 2]. To be constructed at Brookhaven National Laboratory (BNL) in collaboration with Thomas Jefferson National Accelerator Facility (JLab), the EIC originally planned to achieve its unprecedented luminosity through an innovative beam cooling technique known as Coherent electron Cooling (CeC) [3].

An Energy Recovery Linac (ERL) serves as the backbone of the CeC system, allowing the recovery of the electron beam's energy after cooling. This approach greatly improves energy efficiency, as the recovered energy minimizes the power deposited in the beam dump, thereby reducing both radiation concerns and the need for extensive cooling infrastructure. Detailed descriptions and design considerations of the ERL can be found in Refs. [4–6].

The general framework for ERL feedback (FB) systems has been discussed in Refs. [7, 8]. A schematic layout of the Strong Hadron Cooling (SHC) ERL incorporating an FB system is shown in Fig. 1. The injector accelerates the electron beam to 6 MeV before it enters the recirculating section of the ERL. The beam then passes sequentially through two single-cell 197 MHz cavities, two quarter-wave 591 MHz cavities, and another pair of 197 MHz cavities, reaching an energy of approximately 13 MeV. Subsequently, it traverses five 5-cell 591 MHz, four 5-cell 1773 MHz, and four additional 5-cell 591 MHz cavities, providing final energies of 55 MeV in Mode-B and 150 MeV in Mode-A operation. For detailed simulation studies of BBU effects in the EIC Cooler ERL, the reader is referred to Ref. [9].

HIGHER ORDER MODES

When the beam passes through the cavities, part of its wakefields are trapped inside long enough to impact the subsequent bunches in present and later passes. These trapped modes generated what is referred to as long-range wakefields, which have high Q-factors and act like narrow band resonator. The cutoff frequency is inversely related to the cavity iris size. Monopole modes produce longitudinal wakefields that may cause energy and timing fluctuations in the beam. However, their effect on beam instabilities is minor and can be mitigated by employing off-crest acceleration or deceleration. On the other hand, dipole modes generate transverse wakefields, which can deflect the beam and lead to transverse BBU (Beam Breakup) instabilities. This study specifically focuses on dipole HOMs (Higher Order Modes) and transverse BBU instability, as these are the dominant factors. For more details on the HOMs are given in Ref. [9].

FB SYSTEM SETUP

The feedback (FB) system consists of two BPMs located near the accelerating cavities (downstream of the laser heater) and four kickers positioned in the return line, as illustrated in Fig. 1. The kickers are placed such that the beam travels approximately 520 m (1.73 μs) downstream in the beamline between the BPMs and the kickers. As shown in Fig. 2, the kickers are positioned approximately 5–10 m apart, corresponding to a temporal separation of about 20–30 ns. This spacing provides sufficient latency within the FB loop for bunch-to-bunch correction.

The four kickers allow for independent correction of both beam angle and position in the horizontal and vertical planes. The feedback loops in each plane operate independently but can influence one another through transverse coupling between the planes. The coupling effects between the horizontal and vertical planes, resulting from magnet tilts and misalignment, are neglected. Similarly, delays in the feedback response are not considered in this initial analysis of the BBU feedback performance.

THRESHOLD CURRENT WITH FEEDBACK

The cavities used in these BBU tracking simulations are BNL-type cavities, and the corresponding HOM parameters are provided in Ref. [9]. A total of 30 dominant HOMs were included in the study—15 horizontal and 15 vertical modes. The threshold current without the feedback (FB) system is determined to be 229 mA, as shown in Fig. 3. At 230 mA, the HOM voltage grows exponentially, while at 229 mA, it remains stable and low.

---

* saitiniy@jlab.org

ISBN: 978-3-95450-267-7 ISSN: 2226-0374 doi: 10.18429/JACoW-COOL2025-THC2

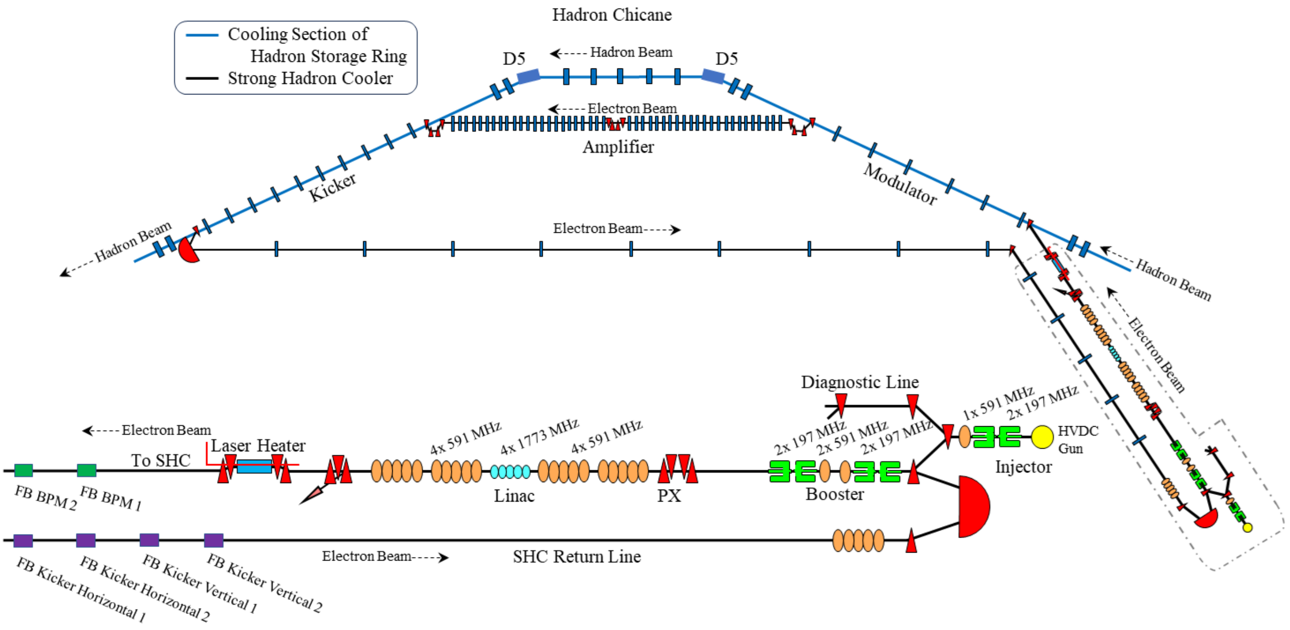

Figure 1: Schematic layout of the SHC-ERL with the feedback system.

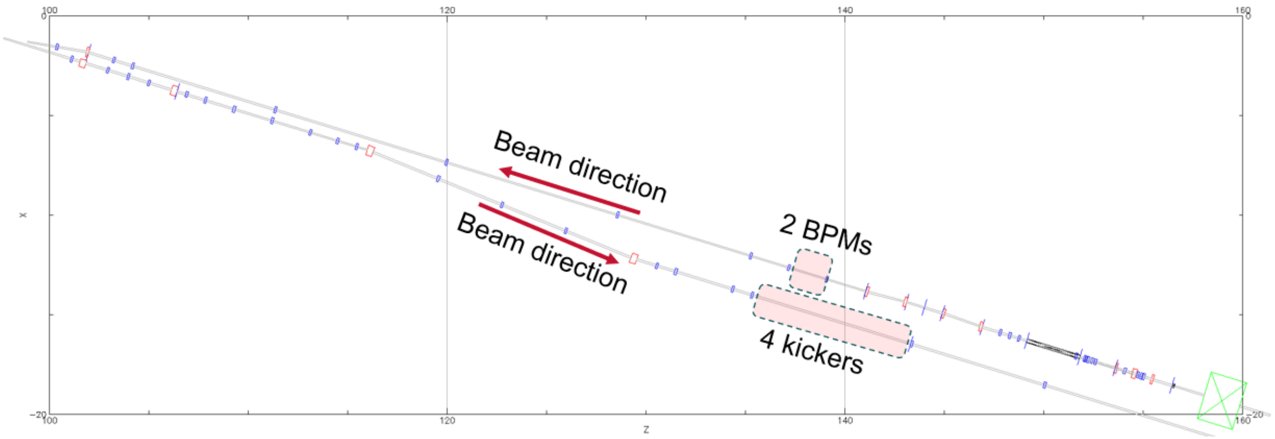

Figure 2: Physical locations of the BPMs and kickers along the beamline.

A substantial increase in the threshold current was observed when the FB system was activated. In the absence of BPM and kicker noise, the threshold current rose to 9.72 A, representing a 42-fold improvement, as shown in Fig. 4. The most dominant mode in this case is mode No. 13, a horizontal mode with a frequency of 846.1337 MHz.

NOISE SENSITIVITY OF THE FEEDBACK SYSTEM

So far, noise in both the BPMs and the kickers has not been included in the analysis. Such noise can adversely affect the FB system's performance and reduce the threshold current. Another factor not yet considered is the variation of HOM frequencies among cavities due to manufacturing imperfections. These variations introduce a frequency spread — typically a few MHz — that follows a Gaussian distribution. To account for this effect in the simulations, tracking was performed multiple times with the cavity frequencies varied according to a relative RMS frequency spread of $\sigma_f/f = 10^{-3}$. Consequently, the simulations yield a distribution of threshold currents rather than a single deterministic value.

Figure 5 presents the threshold current scan results with and without BPM and kicker noise. Each subplot corresponds to a different BPM noise level, as indicated, while the different colors represent scans performed with various kicker noise levels. For each scan, the HOM frequencies were varied to generate the corresponding distribution of threshold currents.

As shown in the results, the threshold current ranges from 7–11 A in the absence of FB noise, while the inclusion of FB noise significantly reduces it. Nevertheless, the threshold current remains on the order of several amperes—an order of magnitude higher than the case without feedback. All

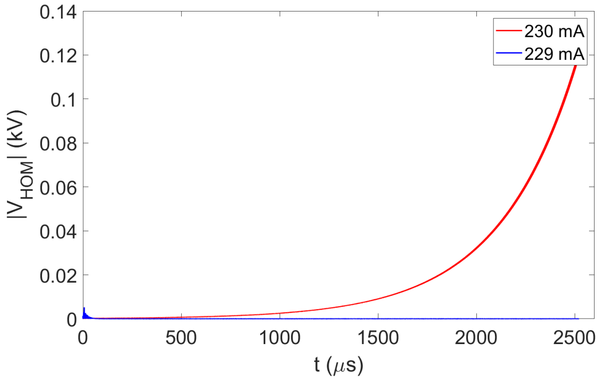

Figure 3: Higher-order mode voltage of the most dominant mode without FB when the test current is at 229 mA (blue line) and 230 mA (red line).

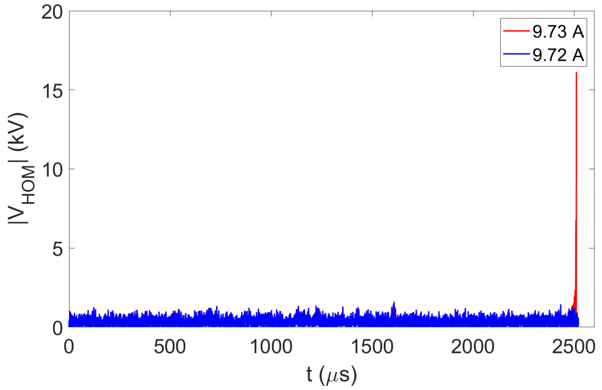

Figure 4: Higher-order mode voltage of the most dominant mode without BPM and kicker noise with the FB system, when the test current is at 9.72 A (blue line) and 9.73 A (red line).

results are summarized in Fig. 6. The system is observed to be more sensitive to BPM noise than to kicker noise, as expected from feedback theory, where the readback noise is amplified by the feedback loop.

POWER SPECTRAL DENSITY OF BEAM MOTION

The horizontal position of the bunch centroid, recorded at the end of the linac section, is used to compute the Power Spectral Density (PSD), as shown in Fig. 7. In this case, no FB noise is applied. While a time-domain analysis reveals how a signal evolves over time, the PSD characterizes how the signal's total power is distributed across frequencies. As seen in the plot, the spectral peak around 58 MHz is strongly suppressed by the FB system. The frequency of this peak, $f_{\text{PSD, peak}} = 58.1151$ MHz, corresponds to the alias frequency of the dominant mode at $f_{\text{maxHOM}} = 846.1151$ MHz. The beam injection frequency is $f_{\text{inj}} = 98.5$ MHz, and the relationship among these frequencies is given by

$$f_{\text{PSD, peak}} = f_{\text{maxHOM}} - 8 \times f_{\text{inj}}. \tag{1}$$

As shown in Fig. 8, when noise is introduced, the same HOM peak remains suppressed by the FB system; however, the PSD at other frequencies increases significantly. This occurs because the BPM and kicker noises are primarily broadband random sources—arising from position measurement errors and kick-angle fluctuations—which are amplified by the feedback loop. Future work will focus on mitigating this noise using optimized filtering schemes and adaptive algorithms that can anticipate and suppress the onset of instability in individual HOMs.

CONCLUSION

We have simulated a feedback (FB) system designed to suppress beam breakup (BBU) instabilities in the EIC Cooler ERL. The results demonstrate that the FB system effectively suppresses BBU and substantially increases the threshold current. In the absence of noise, the threshold current rises by nearly two orders of magnitude, while the inclusion of BPM and kicker noise reduces it but still maintains roughly an order of magnitude improvement over the no-feedback case.

Our analysis also revealed aliasing of the dominant higher-order mode (HOM) and its suppression by the FB system, as observed in the power spectral density (PSD) of the beam centroid motion. Although the FB system with noise successfully reduced the BBU peak, it simultaneously amplified the PSD at other frequencies.

Future studies will focus on implementing filtering and adaptive algorithms capable of detecting, from beam motion, when a particular HOM is approaching instability. We will also incorporate realistic component frequency responses, system delays, and transverse coupling effects. These results provide valuable insight into transverse BBU suppression and threshold current enhancement in energy recovery linacs.

ACKNOWLEDGMENTS

The authors thank W. Bergan and E. Wang of Brookhaven National Laboratory, and N. Wang of the Cornell University for productive collaboration on SHC-ERL physics design. Similarly, we are grateful to S. Benson, Z. Conway, J. Guo, R. Rimmer, and T. Satogata for helpful comments and guidance dating back to the conception of the SHC-ERL. The authors appreciate several good discussions on feedback theory as applied to the BBU feedback system problem with P. Sirisha Kallakuri of Argonne National Laboratory (Advanced Photon Source). This work was produced in part by Jefferson Science Associates, LLC under Contract No. DE-AC05-06OR23177 and Brookhaven Science Associates, LLC, Contract DE-SC0012704 with the U.S. Department of Energy.

REFERENCES

[1] R. Abdul Khalek *et al.*, “Snowmass 2021 White Paper: Electron Ion Collider for High Energy Physics”, arXiv preprint

ISBN: 978-3-95450-267-7 ISSN: 2226-0374 doi: 10.18429/JACoW-COOL2025-THC2

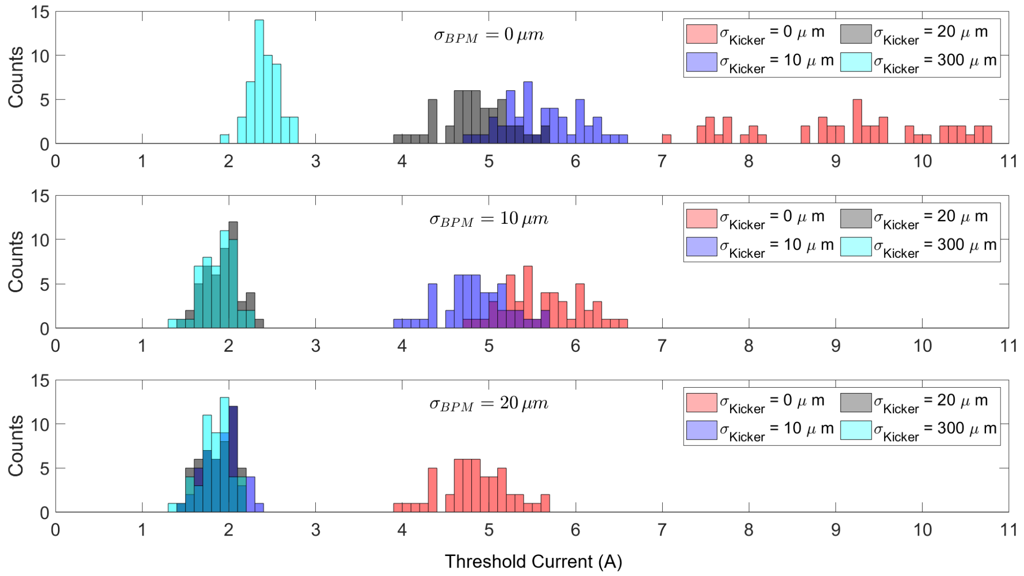

Figure 5: Threshold current scan results with and without BPM noises.

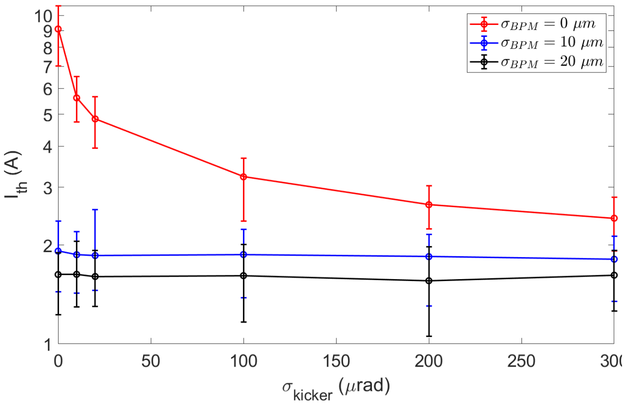

Figure 6: Noise sensitivity of the FB system.

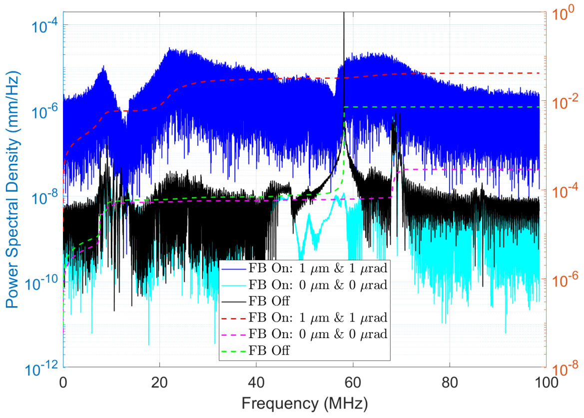

Figure 8: PSD at 230 mA with and without noise applied.

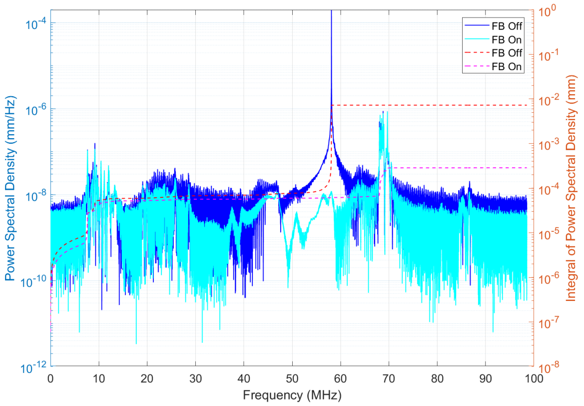

Figure 7: Power spectral density (PSD) of the bunch centroid at 230 mA—1 mA above the threshold current—with and without the feedback (FB) system. FB noise not included.

arXiv:2203.13199, 2022.
`doi:10.48550/arXiv.2203.13199`

[2] F. Willeke, “Electron Ion Collider Conceptual Design Report 2021,” Rep. BNL-221006-2021-FORE, Brookhaven National Laboratory, Upton, NY, USA, 2021.
`doi:10.2172/1765663`

[3] E. Wang *et al.*, “Electron Ion Collider Strong Hadron Cooling Injector and ERL”, in *Proc. LINAC’22*, Liverpool, UK, Aug.-Sep. 2022, pp. 7–12.
`doi:10.18429/JACoW-LINAC2022-MO2AA04`

[4] N. Sereno *et al.*, “SHC ERL Precooling and Main Linac RF System Parameter Setup Without Space Charge”, JLAB-TN-24-041 and EIC-SHC-TN-24-002.

[5] N. Wang *et al.*, “Optimization of cooling distribution of the EIC SHC cooler ERL”, in *Proc. IPAC’24*, Nashville, TN, USA, May 2024, pp. 1104–1107.
`doi:10.18429/JACoW-IPAC2024-TUPC43`

ISBN: 978-3-95450-267-7 ISSN: 2226-0374 doi: 10.18429/JACoW-COOL2025-THC2

[6] K. E. Deitrick *et al.*, “Development of an ERL for Coherent Electron Cooling at the Electron-Ion Collider”, in *Proc. COOL2023*, Montreux, Switzerland, Oct. 2023, pp. 87–90. `doi:10.18429/JACoW-COOL2023-THPOSRP17`

[7] C. D. Tennant, "Suppression of beam breakup in energy recovering linacs," Ph.D. dissertation, College of William and Mary, Williamsburg, VA, USA, 2006. `doi:10.21220/s2-9ga7-4826`

[8] C. D. Tennant, “Modeling a transverse feedback system for an energy recovery linac", Tech note JLAB-TN-03-045, 12 November 2003.

[9] S. Setiniyaz *et al.*, “A preliminary feasibility study on multi-cavity cryomodule integration for the Electron Ion Collider energy recovery linac cooler”, in *Proc. IPAC’24*, Nashville, TN, USA, May 2024, pp. 1111–1114. `doi:10.18429/JACoW-IPAC2024-TUPC45`

ISBN: 978-3-95450-267-7 ISSN: 2226-0374 doi: 10.18429/JACoW-COOL2025-THC3

BEAM POSITION MONITORING FOR LOW ENERGY COOLING SECTION*

I. Pinayev† and S. Seletskiy, Brookhaven National Laboratory, Upton, NY, USA

Abstract

The Electron-Ion Collider is being constructed at Brookhaven National Laboratory. To achieve the required luminosity the hadron beam will be cooled at the injection energy to reduce its vertical emittance. This paper describes the beam position monitors for the cooling section.

INTRODUCTION

The Electron-Ion Collider (EIC) will employ Low Energy Cooler (LEC) dedicated to cooling proton bunches at injection energy ($\gamma \approx 25$) [1,2]. LEC utilizes a 170 m long cooling section (CS), which is a straight section of the EIC hadron storage ring where electron and hadron bunches co-propagate. The 14 beam position monitors (BPM) installed in the CS should be capable to measure the positions of the electron and hadron independently. The hadron BPMs should measure beam position for the wide variety of bunch shapes as well. The signals from the pick-up electrodes will have large dynamic range due to the substantial variation of the bunch charges and length. The cable attenuation can also vary strongly.

The orbits of the hadron and electron beams should be transversely aligned to the accuracy better than 35 microns. The relative angular misalignments between the electron and proton trajectories in the CS must be kept below 15 microradians [3]. The mechanism for the measurement of the BPMs offsets between two BPM systems should be also developed.

BEAM PARAMETERS

The hadron beam parameters vary greatly from the Au^{+78} ions pilot bunch of 5 nC and bunch length of 4.2 ns to protons at store with 31 nC bunch charge and 200 ps bunch length. During ramp the proton bunch charge can be as great as 45 nC with same short length of 200 ps.

The cooling will happen at injection energy with relativistic factor of γ=25.4 (proton energy 23.8 GeV and electron energy 12.5 MeV). The proton beam during cooling will be stretched using harmonic RF cavity to the flat top of 3 ns. The profiles of the electron and proton beams are shown in Fig. 1.

The hadron BPM electronics should be able to handle signals from all set-ups. This will require thorough modelling of the analogue chain and digital processing.

The electron beam used for cooling will consist of the train of 24.625 MHz macrobunches, with each macrobunch containing three bunches separated by 5.1 ns (197 MHz RF system). Each electron bunch has a charge of 1.2 nC and r.m.s. length of 170 ps. Repeatable parameters of the beam make the design of the receivers easier.

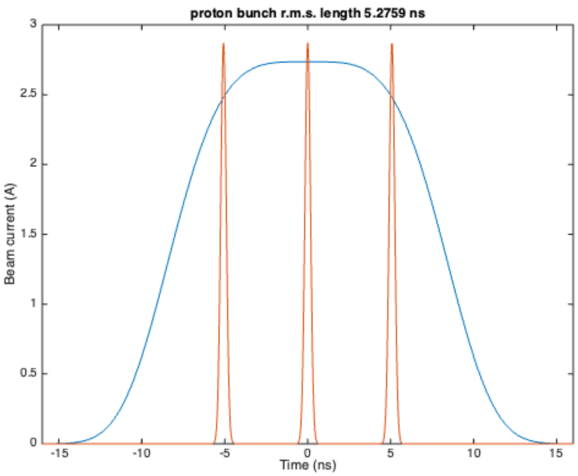

Figure 1: The profiles of the proton bunch (blue) and the electron beam (red). The r.m.s. proton bunch length is 5.3 ns.

SIGNAL PROCESSING

Conventional signal path includes a) cable connecting the pick-up electrode with BPM, b) RF front end conditioning the signal, eliminating the unwanted frequencies, and reducing the signal level to an acceptable level, c) controllable attenuator normalizing the signal and preventing overload, d) pre-amplifier, e) main filter providing the final frequency response of the analogue chain, f) the second amplifier compensating losses in the main filter, g) analogue-to-digital converter (ADC). ADC digitizes the signal and provides the stream of data for digital processing.

The electron beam generates 3 V peak signal on the 30 mm diameter button in the 127 mm diameter beampipe. The spectrum of the signal is shown in Fig. 2.

The weakest signal for the hadron BPM will be generated by a gold ion pilot bunch. Its amplitude at the button will be only 20 mV. The strongest signal is generated by the proton bunch of 45 nC during ramp when bunch length reaches 200 ps. The button signal will be on 70 V peak. The propagation of the signal through a cable reduces the amplitude to 40 V which still too high for the electronics. An RF front end with 3rd order low-pass filter of 150 MHz will reduce the amplitude to 3 V and can be further decreased by the attenuator (see Fig. 3).

---

* Work supported by Brookhaven Science Associates, LLC under contract No. DE-SC0012794 with the U.S. Department of Energy.

† pinayev@bnl.gov

ISBN: 978-3-95450-267-7 ISSN: 2226-0374 doi: 10.18429/JACoW-COOL2025-THC3

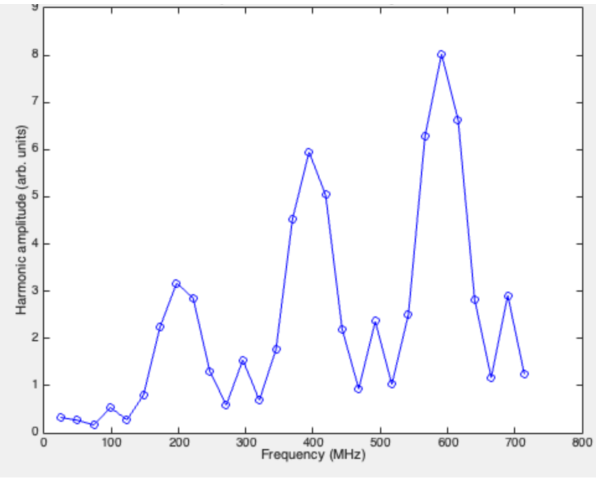

Figure 2: Spectrum of the electron beam signal.

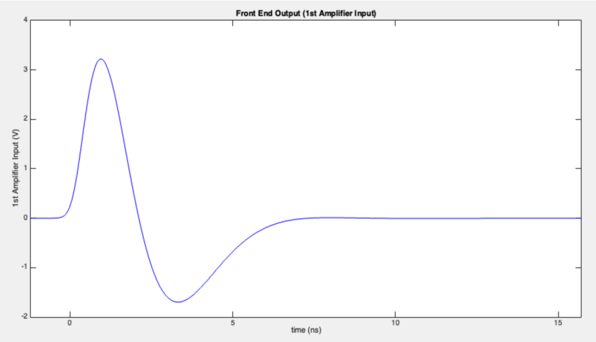

Figure 3: The proton bunch signal after the front-end low-pass filter.

During cooling the proton bunch will have flat top and the signal induced on the button is shown in Fig. 4.

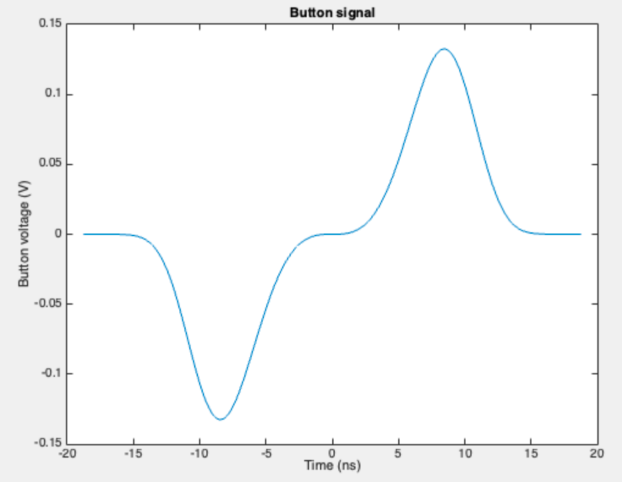

Figure 4: Signal on the button from the cooled proton bunch.

The spectrum of the cooled bunch is shown in Fig. 5. Spectral power decreases with frequency because the bunch length is large. There are also two dips at 49.25 and 221.6 MHz due to the interference of negative and positive pulses shown in Fig. 4. The frequency dip value as well at its position will depend on the proton bunch length and can vary during the cooling process.

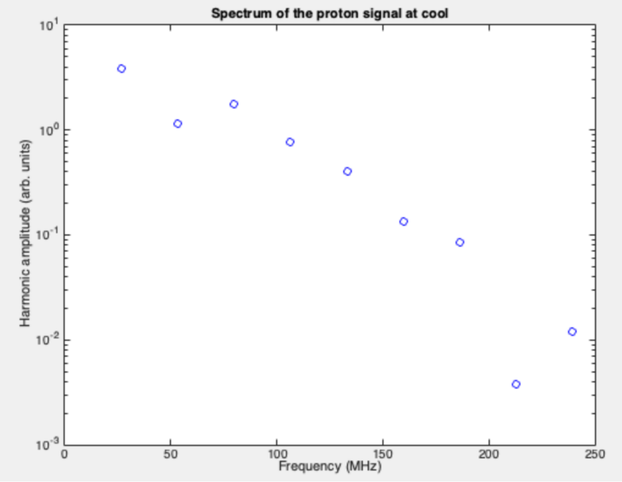

Figure 5: Spectrum of the cooled beam signal.

At store with 1000 bunches the lowest harmonic of the beam signal will be 98.5 MHz equal to the bunch repetition rate. The spectrum is shown in Fig. 6.

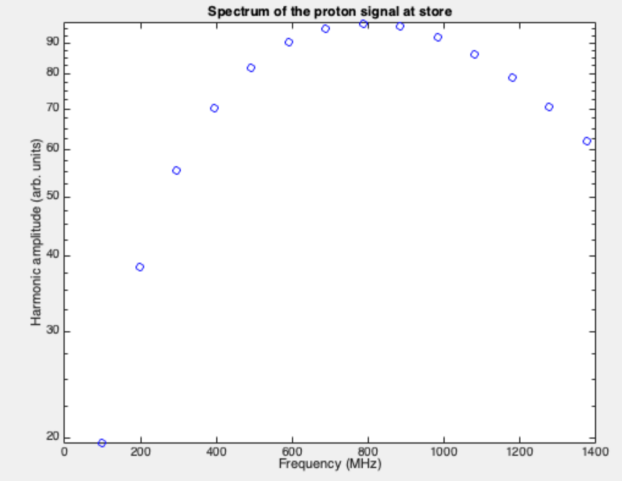

Figure 6: Spectrum of hadron beam signal at store.

The electron beam signal can be processed in the narrow band around 600 MHz where the induced signal has largest amplitude and hadron signal is small during the cooling process.

Narrowband processing does not look suitable for the hadron beam since it can not be warranted that signal will be present at all operational modes. It can disappear completely during RF gymnastics when splitting single bunch into four. The sampling on the top of the pulse presently employed at RHIC will require continuous monitoring of the peak location and can have substantial noise due to the ADC clock jitter since the bunches will be much shorter.

We propose to utilize low-pass filter with cut off frequency around 150 MHz in the analogue chain to suppress the electron beam contribution. The square root of the sum of ADC readings squared will be used for the evaluation of

ISBN: 978-3-95450-267-7 ISSN: 2226-0374 doi: 10.18429/JACoW-COOL2025-THC3

the strength of the beam signal. Such procedure is much less sensitive to the shape of the bunch and will not require changes in the parameters during operational cycle.

NOISE EVALUATION

For the electron beam with a current of 88 mA (3.6 nC, 24.6 MHz), the signal level after 130 meters of LMR-240 cable is 5 mV r.m.s. This estimate is for 10 MHz bandwidth of the filter.

The amplifier with a noise figure of 2.6 dB has a thermal noise level of 4 µV in the 10 MHz bandwidth, The corresponding signal-to-noise ratio (SNR) is 61.9 dB. For the 600 MHz frequency ADC clock jitter of 70 fs will provide SNR of 71.7 dB which is better than thermal noise. The ADC with 11.4 effective number of bits corresponds to 68.4 dB SNR which is also better than thermal noise.

The scaling factor defined by the diameter of vacuum chamber is 32 mm, and noise jitter for a single bunch train is 30 microns. Averaging over 260 bunches (1 turn) reduces the position noise to 2 microns. Further filtering of the signal to 10 kHz required for the orbit feedback will bring noise below 1 micron.

Noise estimation for the hadron BPM was performed with MATLAB script which evaluates the signal level and adds thermal noise, ADC clock jitter, and noise corresponding to the effective number of bits. The screenshot of the application is shown in Fig. 7.

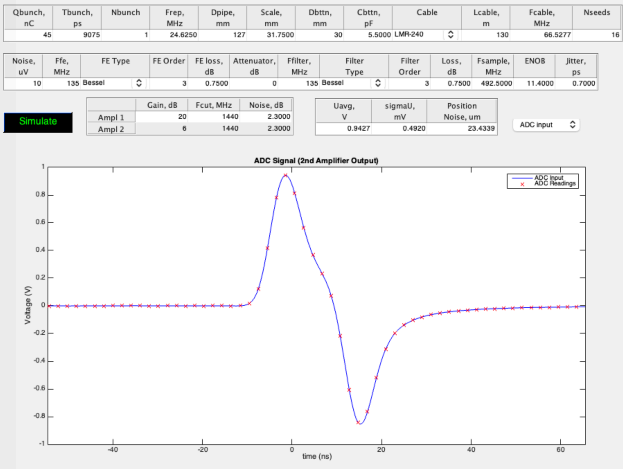

Qbunch, nC	Tbunch, ps	Nbunch	Frep, MHz	Dpipe, mm	Scale, mm	Dbttn, mm	Cbttn, pF	Cable	Lcable, m	Fcable, MHz	Nseeds
45	9075	1	24.6250	127	31.7500	30	5.5000	LMR-240	130	66.5277	16

Noise, uV	Ffe, MHz	FE Type	FE Order	FE loss, dB	Attenuator, dB	Ffilter, MHz	Filter Type	Filter Order	Loss, dB	Fsample, MHz	ENOB	Jitter, ps
10	135	Bessel	3	0.7500	0	135	Bessel	3	0.7500	492.5000	11.4000	0.7000

	Gain, dB	Fcut, MHz	Noise, dB
Ampl 1	20	1440	2.3000
Ampl 2	6	1440	2.3000

Uavg, V	sigmaU, mV	Position Noise, um
0.9427	0.4920	23.4339

Figure 7: Screenshot of the MATLAB application for the modelling of the hadron BPM.

For the single proton bunch with 45 nC charge the expected noise in the position measurement is 20 microns. The averaging for the one turn 260 bunches the noise in the position measurement will be 1.25 microns.

As we showed the errors in the position measurements are well below the requirement of 35 microns. The angular deviation is defined by the noise in position and distance between BPMs, which is about 13 meters. Contribution of the BPMs will be below 100 nanoradians.

OFFSET CALIBRATION

While both electron and hadron BPMs provide sufficiently low noise measurements, the transverse alignment of two beams requires compensation of the systematic errors such as different attenuation in the cables, varying gains and losses in the analogue chains of the BPMs.

The cross calibration of the BPM offsets can be performed when only one beam is present and its position is measured by both types of the BPMs. Even the electron beam can generate sufficient level signal for the hadrons as shown in Fig. 8.

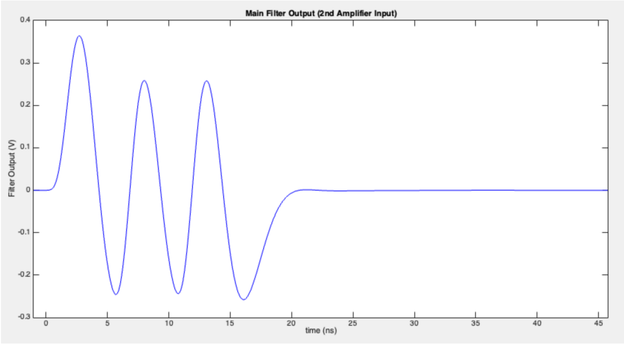

Figure 8: The signal from the electron beam at the input of the hadron BPM ADC.

The proton beam at store generates factor 10 stronger signal as it can be seen from Fig. 6. It will be the preferred way to calibrate the system. Another advantage of using the hadron beam is that it travels in a straight path in the cooling section.

CONCLUSION

We have provided a possible technical solution for the beam position monitors located in the cooling section of the Low Energy Cooler for the Electron-Ion Collider. The performance of the BPMs satisfies the requirements.

REFERENCES

[1] S. Nagaitsev, "Design Overview of the Electron Ion Collider," presented at COOL2025, Stony Brook, NY, USA, Jun. 2026, paper MOA1, this conference.

[2] A.V. Fedotov et al., “Accelerator Physics Requirements and Challenges of RF-Based Electron Cooler for EIC Injection Inergy”, in Proc. NAPAC’25, Sacramento, CA, USA, Aug. 2025, pp. 346–349. `doi:10.18429/JACoW-NAPAC2025-TUP003`

[3] S. Seletskiy et al., “Requirements for Equipment in Cooling Section of EIC Low Energy Cooler, ” in Proc. IBIC'25, Liverpool, UK, Sep. 2025, paper TUPCO26. `doi:10.18429/JACoW-IBIC2025-TUPCO26`

TIME DOMAIN STOCHASTIC COOLING SIMULATIONS: TRANSVERSE AND FILTER COOLING

V. Tsiantis, Aristotle University of Thessaloniki, Thessaloniki, Greece
C. Carli, D. Gamba, W. Höfle, S. Rey, D. Sittard, CERN, Meyrin, Switzerland

Abstract

Stochastic cooling is a technique for reducing the phase space volume of particle beams in accelerators improving the experimental conditions for facilities like the Antiproton Decelerator at CERN. We present a stochastic cooling simulation model, for the transverse and longitudinal planes. This work studies the cooling performance of particle beams under different scenarios, like different gains or number of particles, applying a feedback mechanism for the longitudinal plane called filter cooling. Some cases of emittance and momentum spread reduction are presented, as well as some interesting scenarios of unsuccessful cooling.

INTRODUCTION

Stochastic cooling [1–3] is applied to the beam in the CERN Antiproton Decelerator (AD) in both transverse and longitudinal planes during two plateaus, at 3.57 GeV/c and at 2.0 GeV/c. Specifically for the longitudinal phase space filter cooling [4, 5] using a notch filter is applied (Fig. 1).

The work presented in this paper, is a simplified time-domain simulation framework that models coasting beam stochastic cooling, for a smaller number of macro-particles. Both longitudinal and one transverse planes are included in this framework and filter cooling [3, 6] is applied in the longitudinal plane. Results are compared for different parameters, such as noise, gain and number of particles, illustrating scaling laws and the system's performance.

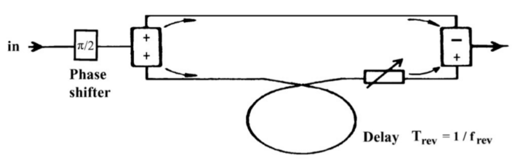

Figure 1: Diagram of a typical notch filter, consisting of a phase-shifter, a splitter, a short and a long transmission line and a "subtractor".

MODELING APPROACH

One of the challenges for the modeling of coasting beam stochastic cooling is the seamless computation of correction to be applied at the kicker. The approach applied is to divide the macro-particles into two groups labeled *red* and *blue* and to track them alternately as sketched in Fig. 2. The (absolute) time increases from left to right. Particles within one group are described by the relative arrival time τ roughly within a time interval $\tau_H/2 \leq \tau \leq \tau_H/2$ with τ_H being half of the revolution time. The following steps are applied starting with particle coordinates at the position of the Pick-Ups (PU):

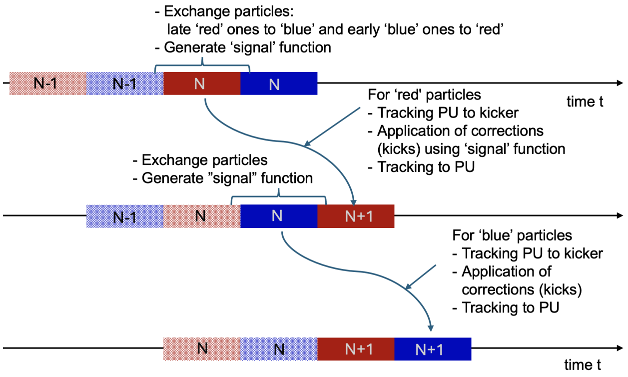

Figure 2: Alternate tracking of two groups of macro-particles. Iterations increase from the top to the bottom.

- To ensure that particles are within the relevant group and as first step of the procedure (see top of Fig. 2), particles of the red group with $\tau \geq \tau_H/2$ (blue group with $\tau \leq -\tau_H/2$) are moved to the blue (red) group.
- Then "signal functions" describing the correction to be applied are computed for the "red" particles. The coordinates of all particles are available and are first binned in relative arrival time τ with a sufficient resolution. For the transverse plane, the sum of the positions is determined for each bin and used to compute the "signal function" at sufficient discrete times using a "response function" given in Eq. 1. The procedure for the longitudinal plane is similar with using the number of particles per bin instead of the sum of the positions and the requirement to use as well the "signal function" from a turn earlier for the implementation of filter cooling. The window, for which the "signal function" is computed extends from $-\tau_H/2 - \tau_{\text{ovlap}}$ to $\tau_H/2 + \tau_{\text{ovlap}}$ with τ_{ovlap} given in Eq. 2 to ensure that the correction to be applied can be computed for all macro-particles.
- The "red" particles are tracked to the position of the kicker by multiplication of the phase space vector with a transfer matrix determined from the Twiss parameters, the phase advances and the momentum compaction factor.
- The corrections from the stochastic cooling system are applied. Kicks applied are the product of a gain factor

ISBN: 978-3-95450-267-7 ISSN: 2226-0374 doi: 10.18429/JACoW-COOL2025-FRA2

with the "signal function" (spline through the discrete values determined before) evaluated at the particles relative arrival time.

- Tracking from the kicker to the PU again by multiplication of the particles phase space vector with a linear transfer matrix leading to the situation in the middle row in Fig. 2.

This is followed by analogous procedure applied to the "blue" particles to propagate the whole beam for one turn.

The quantities of interest, transverse rms emittance and rms momentum spread [7, 8], are calculated at the tracking points. Both wanted and unwanted mixing is taken into account by delays of the particles calculated from their momentum offset, the revolution period and the momentum compaction factor η from pickup to kicker and from kicker to pickup [9, 10].

Response Functions, Binning and "Signal Function"

In the real stochastic cooling system, each element (PU, head amplifier, signal treatment) has its own unique response that affects the signal traveling from pickup to kicker. In order to calculate the total contribution of all the elements between pickup and kicker, all responses have to be convoluted. In our model, we defined one response function in each plane that describes the total response function. The formulas used are educated guesses based on the real system's bandwidth. They are good approximations for first studies, but should be further refined based on the properties of the AD stochastic cooling system. These response functions are defined in a small time window $(-w, w)$ with $w = 1.6\,\text{ns}$. Outside this time window, the response functions are zero. Inside the time window, the longitudinal R_L and transverse R_H response functions are:

$$
\begin{aligned}
R_L &= \left(\frac{63}{\text{ns}}t\right)\left(1-\frac{6.5}{\text{ns}^2}t^2\right)\left(1-\frac{1.55}{\text{ns}^2}t^2\right)\left(1-\frac{t^2}{w^2}\right)^8,\\
R_H &= \left(1-\frac{27\,t^2}{\text{ns}^2}\right)\left(1-\frac{3\,t^2}{\text{ns}^2}\right)\left(1-\frac{1.15\,t^2}{\text{ns}^2}\right)\left(1-\frac{t^2}{w^2}\right)^7.
\end{aligned}
\tag{1}
$$

Since longitudinal positions τ change from the PU to the kicker turn, a particle within the interval $\pm\tau_H/2$ at the PU location may be outside this interval at the kicker. To ensure that the correction can be computed for all particles, the time interval or the "signal function" is extended on both sides by an overlap time region T_{ovlap}, chosen large enough to include the fastest and slowest particles given by:

$$
T_{\text{ovlap}} = 4 \times \sigma_\delta(\eta_{pu->K} + \eta_{K->pu})T_{\text{rev}} \tag{2}
$$

where σ_δ is the rms momentum spread.

For each iteration (tracking either the red or the blue macro-particle group around the ring), a "signal function" is computed based on the coordinates at the PU and then used to determine the kicks applied to macro-particles at the kicker location. The "signal functions" are computed at discrete longitudinal positions τ_k. The spacing between τ_k values has to be fine enough such that the variations of the response function remain small. To this end, particle positions are binned around times τ_i with a smaller spacing. For each bin, the particle number N_i and average positions $\bar{x}_i$ are determined. Electronic noise with a spectral density equal to the Fourier transform of the response function can be added by adding random values to the quantities N_i and $\bar{x}_i$ for the longitudinal and transverse plane. The convolution with the longitudinal R_L and transverse R_H response functions given in Eq. 1 to compute the "signal" functions is approximated by:

$$
\begin{aligned}
S_L(\tau_k) &= \sum_i R_L(\tau_k - \tau_i)N_i\\
S_H(\tau_k) &= \sum_i R_H(\tau_k - \tau_i)N_i\,\bar{x}_i
\end{aligned}
\tag{3}
$$

which is implemented as matrix multiplication with the matrix evaluated only once at the beginning of the simulation.

The kicks to be applied to particles at the location of the kicker are computed by a second order spline through the data points of the "signal function" multiplied with a gain factor G.

Table 1: Parameters of the Simulation Software

Parameter(unit)	**Default value**
Simulation window T_H(s)	$T_{\text{rev}}/2$
Revolution time T_{rev} (ns)	620.9
Beta function $\beta_{\text{pu}}, \beta_K$	1.3, 0.8
Alpha function a_{pu}, a_K	−0.9, 0.6
One turn phase advance μ_T (rad)	$2\pi \times 1.34$
Phase advance PU-kicker $\mu_{pu->K}$ (rad)	$\pi/2$
Slipping factors $\eta_{pu->K}, \eta_{K->pu}$	−0.01, −0.01
Standard deviation of dp/p σ_δ	0.004
Number of time bins N_b	25000

NUMERICAL RESULTS

Below a few numerical results are presented. Default values used for the presented simulations are given in Table 1.

Scaling Law

The simulations cannot reach the AD intensity which decelerates $\approx 6 \times 10^7$ particles. We felt the necessity to test Van der Meer's scaling law [3], which holds for small values of η (like our case) and optimal gain, and which, for the longitudinal case, can be simplified as solving the differential equation:

$$
\frac{d\sigma_\delta}{dt} = -\underbrace{AG\,\sigma_\delta}_{\text{Cooling term}} + \underbrace{BNG^2}_{\text{Heating term}} \tag{4}
$$

where A and B are some scaling factors dependent on cooling system properties such as bandwidth and particle mixing rates, N is the number of particles, G is the gain, σ_δ is the RMS momentum spread. The solution of Eq. 4 can be written as:

$$\sigma_\delta(t) = \sigma_{\delta 0}\, e^{-A(NG)t/N} + \sigma_{\delta,\mathrm{eq}}\left(1 - e^{-A(NG)t/N}\right) \quad (5)$$

where $\sigma_{\delta 0}$ and $\sigma_{\delta,\mathrm{eq}}$ are the initial and final equilibrium RMS momentum spreads, respectively. The indicator used is the time T_h needed for the rms momentum spread to halve, i.e. $\sigma_\delta(T_h) = \sigma_{\delta 0}/2$, and which using Eq. 5 can be written as:

$$\frac{T_h}{N} = \frac{1}{A\,(N\,G)} \ln\left(\frac{\sigma_{\delta 0} - (N\,G)(B/A)}{\frac{1}{2}\sigma_{\delta 0} - (N\,G)(B/A)}\right) \quad (6)$$

The result from several simulations varying the number of macro-particles is shown in Fig. 3. We observe very good agreement for different number of particles until $G_L \times N \approx 0.42$, which is very close to the optimal gain. Larger gains lead to rms momentum spread blow up for all simulations with $N < 50000$, so that most curves have no point above this gain. The theoretical model's fit is not satisfying, with Normalized RMS Error (NRMSE) ~ 0.1. A possible explanation for this discrepancy is that the assumption that the distribution remains Gaussian does not hold. The fit deviates from the data points as under the action of the cooling system the distributions deviate significantly from a Gaussian.

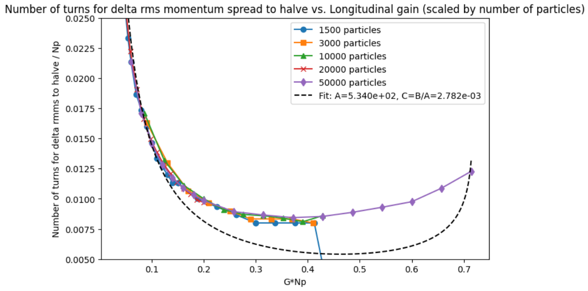

Figure 3: Time needed for the rms momentum spread to halve (expressed in number of full revolutions around the machine divided by the number of particles) for different gains and different number of particles. An attempt to fit the data according to Eq. 6 is also shown.

We also plotted the rms momentum spread over normalized time (Fig. 4) for $G_L N = 0.5$. We observe very good agreement, especially early in the simulation. As the simulation proceeds, we observe artifacts for a small number of particles. For lower gains the agreement is better throughout the whole simulation.

Below we give the results of the exponential fit for $G_L N = 0.5$ (Table 2). We observe that the exponential model is satisfying to explain the data of our simulations. This holds for $G_L N = 0.2$ and $G_L N = 0.8$ as well. Also for an increasing number of particles and decreasing $G_L N$, the cooling time T_c is increasing.

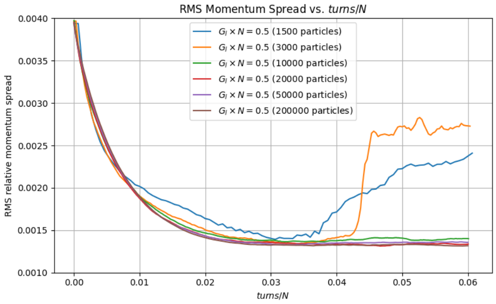

Figure 4: RMS momentum spread as a function of number of turns divided by the number of macro-particles t/N for $G_L N = 0.5$ and different numbers of macro-particles.

Table 2: NRMSE and Cooling Times for $G_L N = 0.5$ for Different Number of Particles

$G_L N = 0.5$		
No. of particles	NRMS error (%)	T_c(s)
10000	1.356	3.89×10^{-5}
20000	0.663	7.99×10^{-5}
50000	0.928	19.68×10^{-5}
200000	0.911	81.38×10^{-5}

Electronic Noise and High Initial σ_δ Artifacts

Some results for different levels of electronic noise are presented, for $G_L N = 0.5$ for 10000 particles. The noise follows a Gaussian distribution and is added to each time bin. The Noise to Signal Ratio (NSR) is given by:

$$NSR = \frac{\sigma^2_{\mathrm{electronic}}}{\sigma^2_{\mathrm{beam}}} \quad \text{with} \quad \sigma^2_{\mathrm{beam}} = \frac{1}{N_{\mathrm{bins}}} \sum_{i=1}^{N_{\mathrm{bins}}} (n_i - \bar{\mathrm{n}})^2 \quad (7)$$

We can clearly observe that for higher levels of NSR, we have a higher equilibrium emittance, in comparison to the cases of low or no noise at all. This is what the theory predicts [2].

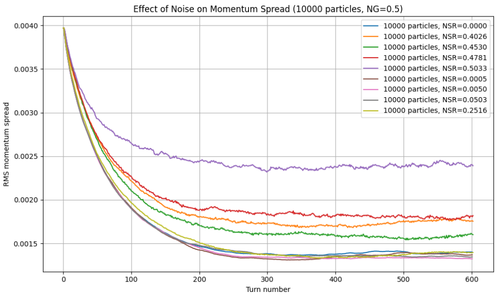

Figure 5: RMS momentum spread over turns for NG = 0.5 for 10000 particles for different levels of NSR.

The initial momentum spread in AD is of the order of $\sigma_\delta \approx 0.004$. This large value for RMS momentum spread

ISBN: 978-3-95450-267-7 ISSN: 2226-0374 doi: 10.18429/JACoW-COOL2025-FRA2

combined with the bandwidth of AD stochastic cooling system and the momentum compaction factor as specified in Table 1, led to various features in the longitudinal phase space as shown in Fig. 6. We can clearly see three lines forming in phase space, at $\sigma_\delta = -6.57 \times 10^{-3},\ 0,\ 6.5 \times 10^{-3}$. This is compatible with typical observations in the AD.

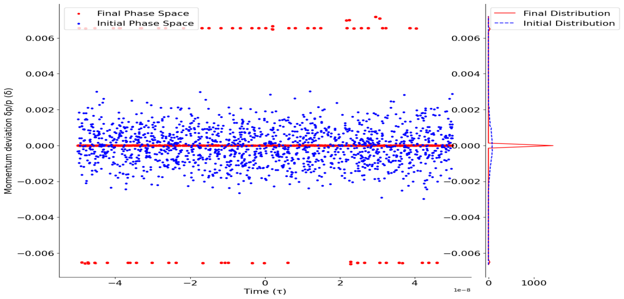

Figure 6: Longitudinal phase space for 1500 particles. We can clearly see three 'lines' forming in the phase space at discrete momentum offsets *delta*.

In order to understand, why this is the case, we have to look at the longitudinal signal used for the kick (Fig. 7), which is produced by the filter method. The blue dots marked in the plot are the stable points of the signal, which are the zero crossings with a positive slope. Particles with high momenta escape the zero stable region and they end up to some other stable region of no correction. If we increase the initial σ_δ even more, we observe 5 stable regions and if we use the wrong sign for the kick (flipping the signal essentially) we observe 2.

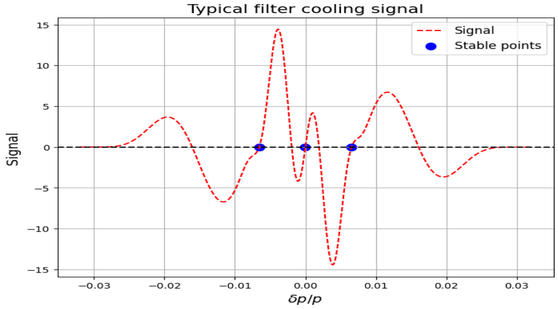

Figure 7: Energy change experienced by a particle due to the signals generated by itself (without heating due to other particles) in a filter cooling system. The curve is the superposition of the signals due to two passages at the PU, the current turn's signal minus the previous turn one.

DISCUSSION AND IMPROVEMENTS

A time domain stochastic cooling code has been developed and tested.

Scaling laws to extrapolate from simulations with a smaller number of macro-particles than in a real machine have been carried out. The results produced for longitudinal cooling were satisfying. Some artifacts as initial cooling followed by very fast momentum spread increase have been observed in simulations with large gains and small number of macro-particles. Increasing the number of macro-particles allowed to cure this artifact.

For transverse cooling, we followed the same procedure, but artificial sudden emittance increase after initial cooling made the interpretation of the results difficult. Contrary to our expectations, we observed faster emittance blow up for an increasing number of macro-particles, which needs to be understood.

An important future improvement of the code would be to use response functions that are obtained by measurements and electro-magnetic simulations of the stochastic cooling hardware of the AD. Possible future improvements comprise the implementation of gain variations along the machine cycle (as used in practice in AD), and to take into account non-linear effects for tracking the macro-particles.

REFERENCES

[1] S. van der Meer, "Stochastic Damping of Betatron Oscillations in the ISR," CERN-ISR-PO-72-31, CERN, Geneva, 1972.

[2] D. Möhl, *Stochastic Cooling of Particle Beams*, Lecture Notes in Physics, vol. 866. Springer, 2013. `doi:10.1007/978-3-642-34979-9`

[3] S. van der Meer, "Stochastic Cooling Theory and Devices," in *Proceedings of the Workshop on Producing High Luminosity Proton-Antiproton Storage Rings*, eConf C7803272 (1978), pp. 73–77, CERN, 1978.

[4] G. Carron and L. Thorndahl, "Stochastic Cooling of Momentum Spread by Filter Techniques," CERN-ISR-RF-78-12, CERN, Dec. 1978.

[5] L. Thorndahl, "A Differential Equation for Stochastic Cooling of Momentum Spread with the Filter Method," CERN ISR-RF/LT/PS Technical Note, 10 May 1977.

[6] J. Marriner, "Stochastic Cooling Overview," *Nucl. Instrum. Methods Phys. Res., Sect. A*, vol. 532, no. 1, pp. 11–18, 2004. `doi:10.1016/j.nima.2004.06.025`

[7] H. Wiedemann, *Particle Accelerator Physics*, 3rd ed. Springer, 2007. `doi:10.1007/978-3-319-18317-6`

[8] E. D. Courant and H. S. Snyder, "Theory of the Alternating-Gradient Synchrotron," *Ann. Phys.*, vol. 3, no. 1, pp. 1–48, 1958. `doi:10.1016/0003-4916(58)90012-5`

[9] M. Sands, "The Physics of Electron Storage Rings: An Introduction," SLAC-121, SLAC, 1970. `doi:10.2172/1453884`

[10] R. Appleby, G. Burt, J. Clarke, and H. Owen, *The Science and Technology of Particle Accelerators*. Chapman & Hall, 2020. `doi:10.1201/9781351007962`

ISBN: 978-3-95450-267-7 ISSN: 2226-0374 doi: 10.18429/JACoW-COOL2025-FRA3

A CHARGE-AGNOSTIC DESIGN FOR 6D MUON IONIZATION COOLING

C. Riggall*, R. Ganesan, L. Lee, T. Holmes, University of Tennessee, Knoxville, TN
K. Yonehara, D. Stratakis, D. Neuffer, Fermi National Accelerator Laboratory, Batavia, IL
M. Palmer, Brookhaven National Laboratory, Upton, NY

Abstract

A muon collider presents a compelling path forward for high-energy physics, offering both energy reach and precision. The notable challenge in realizing the target luminosities for a muon collider is in the development of a sufficiently fast beam cooling scheme – one capable of several orders of magnitude in emittance reduction with minimal decay losses. Ionization cooling is the only proposed scheme to fit this criterion. Traditional ionization cooling channels are characterized by a solenoid-based lattice for beam focusing and a low-Z absorbing material wherein the beam deposits energy via ionization. Dipole fields are used to generate dispersion such that higher-momentum muons pass through more absorbing material, enabling 6D cooling by leveraging emittance exchange. The problem with this approach is the charge-specificity of the dispersion function, necessitating separate channels for μ^+ and μ^-. Here, the Helical FOFO Snake (HFOFO) is presented as an alternative approach to 6D cooling that can handle both signs of muon, enabling a single cooling channel.

INTRODUCTION

Confronted with myriad unsolved problems not addressed by the Standard Model, a muon collider presents an opportunity for both precision measurements and discovery potential at the 10 TeV scale [1]. However, the finite lifetime of the muon necessitates considerable R&D to make such a collider realizable. Notably, established cooling approaches are not fast enough for muons; ionization cooling, as demonstrated by MICE [2] and Muon g-2 [3], is a promising alternative.

The concept of ionization cooling is captured by

$$\frac{d\varepsilon_n}{ds} = -\frac{1}{\beta^2}\frac{dE_\mu}{ds}\frac{\varepsilon_n}{E_\mu} + \frac{1}{\beta^3}\frac{\beta_\perp (0.014)^2}{2E_\mu m_\mu X_0} \tag{1}$$

where ε_n is the normalized emittance, s is the path length, β is the velocity, E_μ is the energy of the muon beam, $\beta_\perp$ is the transverse beta value, m_μ is the mass of the muon, and X_0 is the radiation length of the absorbing material. The first term on the right describes cooling via ionization, while the second is a heating term due to multiple scattering.

To achieve ionization cooling in all six dimensions of phase space, the prescription is as follows: first leverage emittance exchange to (conservatively) increase the transverse emittance. Then induce dispersion via a dipole field to correlate position and momentum. Next pass the beam through a low-Z absorbing material in the shape of a wedge, facilitating momentum-dependent cooling, with higher-momentum particles passing through more material and hence losing more energy. Ionization deposition in the material acts as the nonconservative process required to shrink the momentum distribution. Longitudinal momentum can subsequently be restored via RF cavities.

The principal disadvantage of this approach is the requirement of a dipole field, which enforces the need for charge-specificity. To apply this scheme at a μ^+-μ^- collider, this implies two separate cooling channels are necessary, and charge separation must be performed immediately after the front-end [4]. However, considering the large initial phase space of the beam post-pion decay, charge separation at this stage will result in significant losses. Additionally, duplicate channels require increased construction costs. In this paper, we present an alternative: the Helical FOFO Snake (HFOFO), a charge-agnostic design to serve as an initial 6D cooling stage before charge separation. HFOFO was first proposed by Yuri Alexahin during the Muon Accelerator Program (MAP), but received little attention after the conclusion of the program [5]. Our recent efforts to revive and optimize the design will be detailed here.

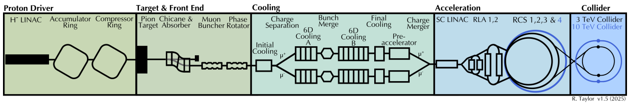

Figure 1: A proposed design for the muon collider accelerator complex, including HFOFO as the initial cooling section [4].

LATTICE DESIGN

The HFOFO lattice is composed of alternating-polarity, inclined solenoids for focusing and dispersion generation, as well as RF cavities and LiH wedge absorbers. The defining parameters of each of these elements are given in Table 1. One period in the lattice is defined as six focusing elements and the subsequent gaps, as depicted in Figure 2. The construction is such that the minima of the beta function align with the absorbers to maximize cooling. Nominally, the initial cooling channel would comprise 30 periods, plus a section at the start for matching, making for a total length of ~132 m. For a reference momentum of 221.8 MeV/c, as matched to the full channel ignoring stochastic effects, we would expect about 9% beam loss due to decays over this length.

Where HFOFO differs from standard ionization cooling channel designs is in the application of rotations about both the x- and z-axes, which we have defined by pitches and rolls, respectively. A constant x-rotation of 2.5 mrad is applied to every coil, inducing a dipole field and thereby dispersion.

---

[*] criggall@tennessee.edu

ISBN: 978-3-95450-267-7 ISSN: 2226-0374 doi: 10.18429/JACoW-COOL2025-FRA3

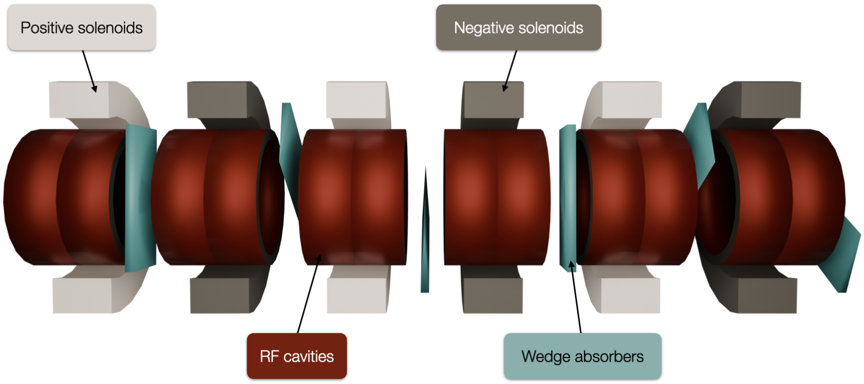

Figure 2: A model of one period in the HFOFO lattice.

Table 1: Lattice Element Parameters

Parameter	Unit	Value
Period length	mm	4200
Coil length	mm	300
Coil inner radius	mm	420
Coil outer radius	mm	600
Spacing between coil centers	mm	700
RF frequency	MHz	325
RF length	mm	249
RF gradient	MV/m	25
GH_2 density	g/cm^3	0.014

The successive z-rotations are periodic, advancing by 120° per solenoid as shown in Table 2.

Table 2: Periodic Parameters

Position of unit in period	Periodic coil rolls [deg]	Periodic wedge angles [deg]
1	240	333
2	0	93
3	120	213
4	240	333
5	0	93
6	120	213

The effect of these second rotations is the generation of a rotating dipole field. Leveraging the alternating polarity of the FOFO lattice structure to have the first half of the period mirrored in the second half, this design yields identical, longitudinally-offset orbits for μ^+ and μ^- – compatible with the bunch timing structure of the two beams exiting the front-end. As shown in Figure 3, these orbits are dominated by Larmor motion, hence its (leading-order) namesake helical behavior.

Another unique feature of the HFOFO design is the operation near a resonance. When the beta tune is close to an integer value, the momentum compaction factor,

$$\alpha_c = \frac{\Delta L/L}{\Delta p/p} \qquad (2)$$

is positive – that is, dispersion is large. This closeness to a resonance enables increased cooling efficiency, potentially at some expense of momentum acceptance.

The novel beam trajectory apparent in HFOFO requires dedicated matching. A matching section is placed at the start of the main lattice and serves to modulate the beam envelope to optimal shape and size to guide the beam into the design trajectory and minimize beam loss. This consists of nine solenoids of alternating polarities and RF cavities placed as in Figure 2. There are naturally no absorbers in this section. The parameters for these elements, however, vary greatly from those in Table 1, with each element having unique values. The fitting procedure originally performed to find these specific parameters requires further study. It is essential that the process of determining the matching section lattice parameters for any HFOFO design trajectory can be replicated.

At the start of the channel, muons exiting the front-end have an average momentum of about 250 MeV/c. Given the ideal operating momentum for ionization cooling is around 200 MeV/c, the HFOFO channel is designed to decrease the average of the distribution to this value over the length of the channel. The thickness and radii of the RF cavities' Be windows coarsely decrease along the channel, while the solenoid current, wedge absorber angle, and RF timing offset are reduced in finer increments. The solenoid current begins around 94.5 A/mm^2 and ends around 85 A/mm^2, corresponding also to a reduction in the on-axis magnetic field strength. Ending the initial cooling section at 200 MeV/c optimally prepares the beam for subsequent stages of the cooling complex.

PERFORMANCE IN SIMULATION

We use G4beamline to simulate and study the performance of the HFOFO channel [6]. Because the design has not yet been adjusted to reflect post-MAP changes to the

ISBN: 978-3-95450-267-7 ISSN: 2226-0374 doi: 10.18429/JACoW-COOL2025-FRA3

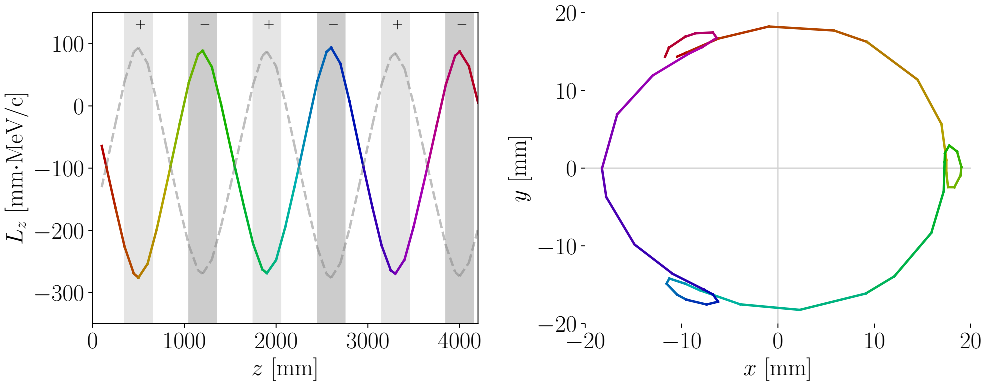

Figure 3: Orbit of a reference μ^+ at 200 MeV/c.

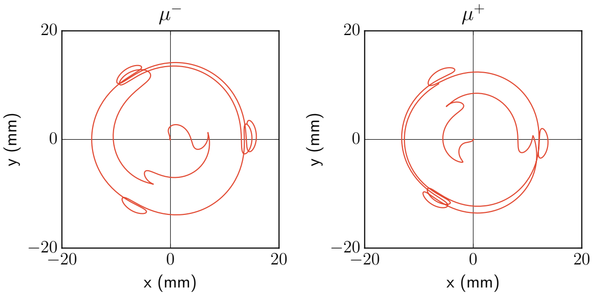

Figure 4: Trajectories of 225 MeV/c reference μ^- (left) and μ^+ (right) in the matching section.

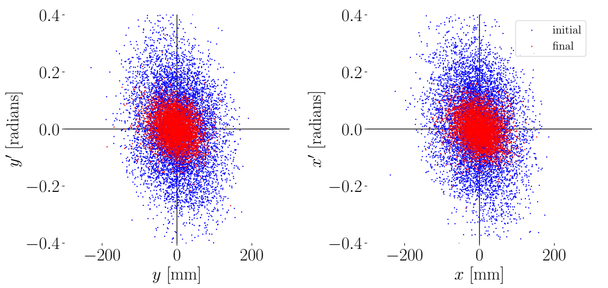

Figure 5: Phase space distributions at the start (blue) and end (red) of the simulated HFOFO channel, using a MAP-era front-end μ^+ beam as input.

front-end system, the results given here are generated from an input beam distribution produced by a simulated MAP-era front-end. Investigations with more contemporary beam files have yielded diminished performance, demonstrating the need for modernization of the HFOFO design. Note also that all results shown here are with a μ^+ beam; performance with μ^- is similar.

Figure 5 shows the initial and final distributions in xx'- and yy'-space. The shrinking distribution evidences cooling, which is echoed by the emittances given in Figure 6 and Table 3. Due to the lack of azimuthal symmetry in the HFOFO system – from the rotated solenoid fields – we used the *emitcalc* program included in the ICOOL toolkit [7]. This computes the eigenemittances, which were found to roughly correspond to one longitudinal mode and two transverse modes (linear combinations of x and y). From these normal mode emittances, we calculated the longitudinal and transverse values reported here.

Given the significant losses expected when cooling muons, it is often pragmatic to consider only the portion of the beam distribution which we expect to survive the entirety of the channel. Unless otherwise specified, it is implied that we have applied a cut such that momentum values fall within the range $150 < p < 350$ MeV/c. As reported in Table 3, we observe a transmission rate (including decays) through the full channel of 47% without this cut and 67% with the cut.

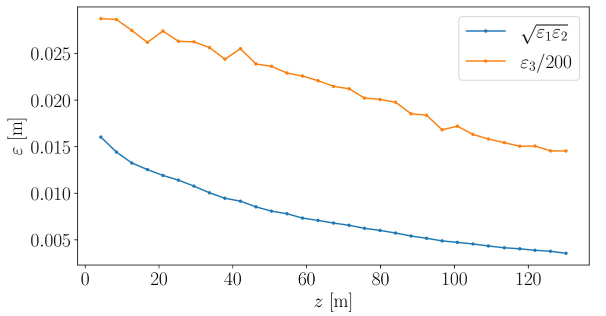

Figure 6: Longitudinal (orange) and transverse (blue) emittances along the simulated HFOFO channel.

To investigate how the transmission rate evolves along the channel, see Figure 7. From decays alone, we would expect around 91% transmission at a reference momentum of 221.8 MeV/c. The observed transmission of 67% suggests there are significant beam losses due to mismatching. Near resonance, it is crucial to understand how much this can be mitigated by improving the momentum acceptance.

ISBN: 978-3-95450-267-7 ISSN: 2226-0374 doi: 10.18429/JACoW-COOL2025-FRA3

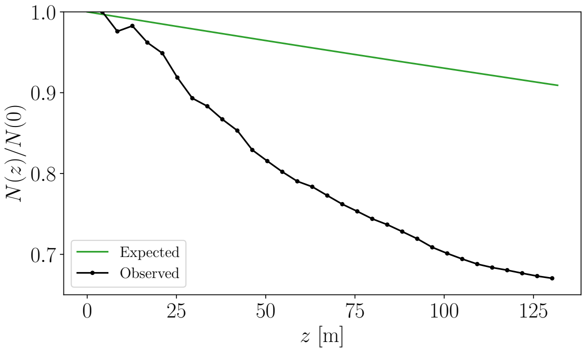

Figure 7: Transmission along the simulated HFOFO channel. The expected decay rate is derived from a 221.8 MeV/c reference particle, as matched to the full channel with stochastic effects disabled.

We report in Table 3 a factor of 4.46 in transverse emittance reduction and 1.98 in longitudinal – making the total 6D emittance reduction a factor of around 40.

Table 3: Current Performance

	N_{total}	N_{cut}	$\varepsilon_\perp$ [m]	$\varepsilon_\perp$ [m]
Initial	11 452	7666	0.016 04	5.748
Final	5348	5139	0.003 595	2.908
Ratio	47%	67%	0.2241	0.5059

SUMMARY AND OUTLOOK

While we are presently seeing an order of magnitude in 6D cooling with reasonable survival rate, there is obvious room for improvement. Continued work focuses primarily on optimizing the design to achieve lower final emittance and higher transmission.

To highlight one of these ideas, we are currently investigating the possibility of replacing the solenoid rotations with multipole components. Motivated both by considerations of physical realizability and by a desire for an analytic description of the field structure and beam dynamics, our preliminary studies have yielded a promising proof of concept. Figures 7 and 8 show the magnitude and phase (respectively) of the complex coefficients in a multipole expansion of the residual field – that is, the difference between the HFOFO field and a FOFO fieldmap, effectively isolating the contributions of the solenoid tilts. We see the expansion is dominated by a dipole term, suggesting the higher-order effects might be sufficiently minimal that a dipole (or even dipole+quadrupole) lattice could replace the solenoid rotations.

Our future plans to improve the design include:

- Reducing the length of lattice elements along the channel (while simultaneously increasing the solenoid current to preserve the transverse beta tune), enabling a reduction in channel length and thereby minimizing decay losses.

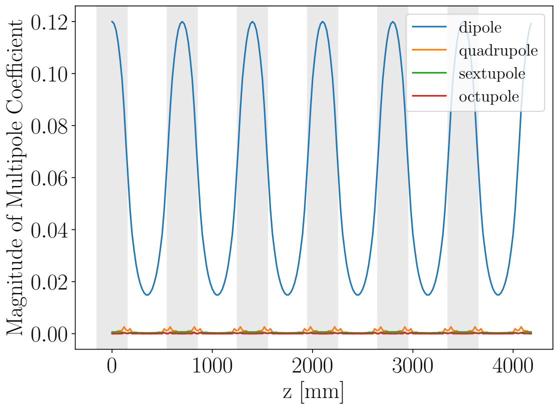

Figure 8: Magnitude of coefficients in the multipole expansion of the residual field over one period. The shaded regions indicate the longitudinal positions of the solenoids.

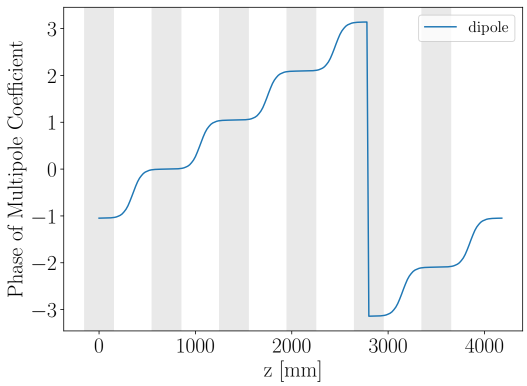

Figure 9: Phase of dipole term in the multipole expansion of the residual field over one period.

- Increasing the betatron phase for each focusing unit to reduce the beta function at the minima, yielding improved cooling performance.
- Optimizing lattice parameters via, for example, a genetic algorithm [8].
- Constructing a Hamiltonian from an analytic approximation of the multipole-expanded field, facilitating analytic optimization of focusing elements to achieve ideal beam dynamics.
- Experimenting with gas densities and alternative absorbing materials (e.g. vacuum- or gas-only designs, as opposed to the current hybrid design).

ACKNOWLEDGMENTS

This work has been supported by the Research Corporation for Science Advancement under two Cottrell Scholar Awards and by Brookhaven National Lab. This work was

ISBN: 978-3-95450-267-7 ISSN: 2226-0374 doi: 10.18429/JACoW-COOL2025-FRA3

also supported by the U.S. Department of Energy, Office of Science, Office of High Energy Physics, through the Fermi National Accelerator Laboratory (Fermilab), which is operated by the Fermi Research Alliance, LLC, under Contract No. DE-AC02-07CH11359.

REFERENCES

[1] C. Accettura, D. Adams, R. Agarwal, C. Ahdida, C. Aimè, N. Amapane, D. Amorim, P. Andreetto, F. Anulli and R. Appleby, *et al.* "Towards a muon collider," Eur. Phys. J. C **83**, no.9, 864 (2023) [erratum: Eur. Phys. J. C **84**, no.1, 36 (2024)] doi:10.1140/epjc/s10052-023-11889-x [arXiv:2303.08533 [physics.acc-ph]].

[2] MICE collaboration. Demonstration of cooling by the Muon Ionization Cooling Experiment. Nature 578, 53–59 (2020). doi:10.1038/s41586-020-1958-9

[3] D. Stratakis. Application of absorbers for performance improvement of the Fermilab Muon g-2 Experiment (2021). `https://indico.cern.ch/event/1031354/contributions/4330757/attachments/2230926/3780136/Stratakis_Cooling.pdf`

[4] R. Taylor *et al.* [MuCoL], "MuCol Milestone Report No. 7: Consolidated Parameters," doi:10.5281/zenodo.17476875 [arXiv:2510.27437 [physics.acc-ph]].

[5] Y. Alexahin, "Helical FOFO Snake for Initial Six-Dimensional Cooling of Muons," JINST **13**, no.08, P08013 (2018) doi:10.1088/1748-0221/13/08/P08013 [arXiv:1806.07517 [physics.acc-ph]].

[6] T. J. Roberts and D. M. Kaplan, "G4Beamline Simulation Program for Matter dominated Beamlines," Conf. Proc. C **070625**, 3468 (2007) doi:10.1109/PAC.2007.4440461

[7] R. C. Fernow. "ICOOL: A Simulation Code for Ionization Cooling of Muon Beams". *1999 Particle Accelerator Conference* (1999). `https://proceedings.jacow.org/p99/PAPERS/THP31.PDF`

[8] R. Taylor and B. Stechauner. "Genetic algorithms for muon cooling lattice design" (2025). `https://indico.cern.ch/event/1512734/contributions/6365917/attachments/3026406/5342353/CEI_Meeting_GA_Cooling.pdf`